Mathematical models of pathological oscillatory activity and effects of deep brain stimulation in movement disorders

Benoît Duchet

Brasenose College

University of Oxford

A thesis submitted for the degree of

Doctor of Philosophy

Trinity 2020

Supervised by Prof. Rafal Bogacz and Dr. Christian Bick

Acknowledgements

I am indebted to my supervisors, Prof. Rafal Bogacz and Dr. Christian Bick, who helped me shape this work with their invaluable feedback, insights, and enthusiasm. I am very grateful for the freedom I had to explore my ideas, for opportunities to present my work, and generally for their support in helping me to grow as a researcher.

I would like to express my sincere thanks to Prof. Peter Brown for his thoughtful feedback and for crucial opportunities to share my work with the experimental neurology group. Interacting with present and past members of the Brown, Tan, and Cagnan groups in formal and informal settings has been a constant source of inspiration. In particular, many thanks to Dr. Gerd Tinkhauser and Dr. Haryiye Cagnan for stimulating discussions and for sharing patient data.

I could not have done this work without the support of the Bogacz group. In particular, I wish to show my gratitude to Dr. Gihan Weerasinghe for sharing his knowledge of global optimisation with me, and for so many thought-provoking conversations. Special thanks to Filippo Ghezzi for his dedication and talent as my first cosupervised master student.

Funding from the Medical Research Council and Brasenose College was instrumental to this work. I would like to acknowledge the use of the University of Oxford Advanced Research Computing facility in carrying out this work, and the helpful assistance of Yassamine Mather. I would like to recognize the contribution of Prof. Chris Keylock for sharing code to compute gradual wavelet reconstruction surrogates.

Another heartfelt thank you goes to mentors who helped me develop as an engineer and a researcher before Oxford, in particular Prof. Paulo Monteiro, Prof. Thomas Pashuck, and my EOS colleagues.

Friends from all over the world whom I met in Oxford, Berkeley, London, and France have been an essential source of inspiration. Hunter, your love and support have been vital to this work. Finally, I would like to express my deepest gratitude to my family, who have stood behind me every step of the way.

Abstract

Essential tremor and Parkinson's disease are the most common movement disorders affecting patients globally. When pharmacological treatment options have been exhausted, continuous, high-frequency deep brain stimulation (DBS) is an effective therapy option. Despite its success, DBS is limited by side effects such as speech and motor impairment, as well as impulsivity. Closed-loop DBS could address these limitations by stimulating in a way that is more parsimonious and by targeting the pathology more selectively to spare physiological processing. In closed-loop DBS, pathological activity is recorded, and stimulation is delivered based on the current state and knowledge of its association with symptoms. Experimental closed-loop strategies include phase-locked DBS in essential tremor and adaptive DBS in Parkinson's disease. In phase-locked DBS, a precise understanding of the phase-dependence of the response to stimulation is difficult to attain experimentally because of patient fatigue. In Parkinson's disease, refining adaptive DBS likely requires a better understanding of the dynamics of bursts in the recorded beta band activity (13-35 Hz), which have been implicated in motor symptoms. To inform closed-loop DBS strategies, we use patient data as a starting point to formulate and constrain mathematical models of pathological oscillatory activity and of the effects of DBS. In Chapter 2, we model the effects of phase-locked stimulation in essential tremor patient data. Models fitted to patient data can be used to optimise DBS in silico, and provide insights into the pathophysiology of the disease. In Chapter 3, we relate changes in beta oscillation temporal patterning between medication states in Parkinson's disease to changes in dynamical properties of the system generating beta bursts. In particular, we show that the system generating beta oscillations is more non-linear in the pathological state, which has implications for closed-loop DBS. In Chapter 4, we compare two definitions of amplitude to measure the effects of phase-locked DBS, and to optimise stimulation in models. We demonstrate that a dynamical measure of amplitude, isostable amplitude, can in some cases be more beneficial to optimise stimulation than envelope amplitude. Together, this thesis sheds light on key aspects of Parkinson's disease and essential tremor, and contributes to advancing closed-loop DBS.

Contents

List of Figures

List of Tables

List of Abbreviations

ABC . . . . . approximate Bayesian computation.

aDBS . . . . . adaptive deep brain stimulation.

ARC . . . . . amplitude response curve.

ARMA . . . . auto-regressive moving average.

BG . . . . . basal ganglia.

BDDLS . . . . burst duration distance to linear surrogates.

CDF . . . . . cumulative distribution function.

DBI . . . . . dynamical Bayesian inference.

DBS . . . . . deep brain stimulation.

DCN . . . . . deep cerebellar nuclei.

EEG . . . . . electroencephalogram.

EMG . . . . . electromyography.

ET . . . . . essential tremor.

FDL . . . . . flexor digitorum longus.

FDR . . . . . false discovery rate.

FT . . . . . Fourier transform.

GABA . . . . . gamma aminobutyric acid.

GPe . . . . . globus pallidus pars externa.

GWR . . . . . gradual wavelet reconstruction.

IAAFT . . . . iterated amplitude adjusted Fourier transform.

LFP . . . . . local field potentials.

LOWESS . . . locally weighted scatterplot smoothing.

MFPT . . . . . mean first passage time.

MODWT . . . maximal overlap discrete wavelet transform.

nRT . . . . . reticular nucleus.

OU . . . . . Ornstein-Uhlenbeck.

PD . . . . . Parkinson's disease.

PDF . . . . . probability density function.

PING . . . . . pyramidal-interneuron gamma.

PRC . . . . . phase response curve.

PSD . . . . . power spectrum density.

QIF . . . . . quadratic integrate and fire.

sem . . . . . standard error of the mean.

SNc . . . . . substantia nigra pars compacta.

STN . . . . . subthalamic nucleus.

tACS . . . . . transcranial alternating-current stimulation.

TEED . . . . . total electrical energy delivered.

UPDRS . . . . unified Parkinson's disease rating scale.

VIM . . . . . ventral intermediate nucleus.

WC . . . . . Wilson-Cowan.

1

General introduction

Contents

1.1 Thesis overview

Essential tremor and Parkinson's disease are the most common movement disorders, affecting 0.9% and 0.08% of the world population, respectively (Louis and Ferreira 2010; Hay et al. 2017). While essential tremor predominantly manifests as a tremor of the upper limbs, neurodegeneration in Parkinson's disease causes a broad range of motor and non-motor symptoms. When pharmacological treatment options have been exhausted, deep brain stimulation (DBS) is an effective therapy option. Clinically available DBS continuously delivers high-frequency electrical stimulation to deep structures within the brain. Despite its success, the therapy is limited by side effects – most commonly speech impairment, but also motor and cognitive side effects, as well as impulsivity (Børretzen et al. 2014; Rodriguez-Oroz et al. 2005; Benabid et al. 2009). Additionally, DBS efficacy tends to decrease over time in essential tremor (Fasano and Helmich 2019). These factors are the primary motivations to improve DBS. It is thought that closed-loop DBS could address these limitations by stimulating in a way that is more parsimonious and by targeting the pathology more selectively to spare physiological processing. In closed-loop DBS, pathological activity is recorded directly from the stimulation electrode or from peripheral sensors, and stimulation is delivered based on the current state and knowledge of its association with symptoms.

An experimental approach called phase-locked DBS seeks to preserve physiological activity by only stimulating at specific phases of on-going pathological oscillations (Brittain et al. 2013; Cagnan et al. 2017). This approach has been pioneered in essential tremor (Cagnan et al. 2017). To measure the effect of stimulating at different phases of the tremor, patients are asked to assume a tremor provoking posture. Because patients get tired quickly, only short recordings can be obtained. Optimising phase-locked DBS requires a precise understanding of the phase-dependence of the response to stimulation, which is not available experimentally. Additionally, detailed knowledge of how ET comes about is missing, and insights into the generation of tremor rhythms could potentially contribute to better therapies.

In Parkinson's disease, heightened oscillatory activity in the beta band (13-35 Hz) in the basal ganglia has been correlated with worsening of slowness of movement and rigidity, the cardinal symptoms of the disease (Kuhn et al. 2006; Kühn et al. 2008; Kühn et al. 2009; Tan et al. 2013; Steiner et al. 2017). Based on this association, an experimental DBS protocol called adaptive DBS only provides stimulation when the amplitude of beta oscillations is greater than a threshold (Little et al. 2013; Little et al. 2016; Rosa et al. 2017a; Arlotti et al. 2018; Velisar et al. 2019). There is some evidence that adaptive DBS would maintain clinical efficacy and reduce side-effects (Little et al. 2016; Rosa et al. 2017a; Arlotti et al. 2018). However, beta activity in the basal ganglia has a physiological role and beta amplitude only discriminates pathological from physiological activity in a very coarse manner. In fact, beta oscillations come in bursts of activity, and the duration of these bursts has been associated with motor symptoms (Tinkhauser et al. 2017a; Tinkhauser et al. 2017b). Further insights into the dynamics of beta bursting may be key to refining DBS in Parkinson's disease.

When optimising DBS from the perspective of suppressing pathological oscillations, envelope amplitude or oscillatory power are typically used as measures of rhythm amplitude. Such measures of amplitude are instantaneous, and do not carry any information about future evolution of the system. In contrast, isostable amplitude is a measure of convergence time to the attractor, defined for a large class of dynamical systems (Mauroy et al. 2013; Wilson and Moehlis 2016a; Shirasaka et al. 2017; Mauroy and Mezić 2018). This dynamical measure of amplitude has been applied successfully to control the state of systems in various contexts (Mauroy et al. 2014; Wilson and Moehlis 2015; Wilson and Moehlis 2016b; Wilson and Djouadi 2019). How a dynamical measure of amplitude compares to commonly used envelope amplitude has not been investigated in model-based DBS research.

Taken together, the phase-dependence of response to stimulation in essential tremor, the temporal patterning of beta oscillations in Parkinson's disease, and oscillation amplitude are notions believed to be central to advancing closed-loop DBS. Improving our understanding of these notions is called for to make headway

with closed-loop stimulation. To this end, we use patient data as a starting point to formulate and constrain mathematical models of pathological oscillatory activity and of the effects of DBS.

In Chapter 2, we analyse phase-locked DBS essential tremor recordings and identify datasets where there is a statistically significant dependence of the response to stimulation on stimulation phase. We fit a simple model representing interacting excitatory and inhibitory neuronal populations to these datasets. The fits reveal that this simple model can reproduce both tremor dynamics and the phase dependence of the response to phase-locked stimulation. We approximate analytically the relationship between phase and amplitude response in a linearisation of the model.

In Chapter 3, we analyse basal ganglia recordings of Parkinsonian patients to get insights into the dynamics of beta bursting and inform closed-loop DBS in Parkinson's disease. We demonstrate a relationship between the temporal patterning of beta oscillations, the dynamics of the underlying system, and motor impairment. In particular, we show that the system generating beta oscillations acts in a more non-linear regime in the pathological state (when patients are withdrawn from medication). We further narrow-down dynamical changes in models fitted to data, and show that envelope dynamics can be extracted from a measure of beta oscillation temporal patterning.

Using the models fitted to essential tremor patients, we relate in Chapter 4 isostable amplitude response to a measure of amplitude response used in phase-locked DBS experiments. We demonstrate that a simple model-based closed-loop stimulation strategy is in most cases on par or at a slight advantage compared to stimulation based on envelope amplitude.

In essential tremor, the ability of a simple two-population model to reproduce tremor dynamics and the response to phase-locked DBS implies that tremor generation may not require continuous interactions between the many brain populations in the tremor pathway. At any given time, two coupled populations may suffice to generate tremor. In Parkinson's disease, our findings shed light on the success

of burst duration as a marker of pathology. The correlation between greater nonlinearity and motor symptoms may pave the way for more specific ways of targeting the pathology with DBS. More broadly, the generality of our linear analysis of phase-dependent stimulation suggests that various systems may be approximately bound by the relationship found between phase and amplitude responses. We anticipate that isostable amplitude could be beneficial to model-based approaches aiming at suppressing pathological oscillations in various disorders. Our envelope model extraction method for time series may find applications in other fields.

1.2 Background

In this thesis, I will develop mathematical models of the effects of DBS in essential tremor, and of pathological oscillatory activity in Parkinson's disease. To clarify what these models could bring to the field, I will therefore provide a clinical review of Parkinson's disease, essential tremor, and of the current state of clinical and experimental DBS. To motivate our modelling choices, I will review applicable modelling approaches, and different perspectives on measuring the effects of stimulation.

1.2.1 Most common movement disorders

Essential tremor and Parkinson's disease are the two most common movement disorders. In addition to general background, I will examine in this section pathological signals associated with the disorders, which are key to refining stimulation therapies.

1.2.1.1 Essential tremor

Essential tremor (ET) is the most common movement disorder, affecting 0.9% of the world population (Louis and Ferreira 2010), which is an order of magnitude more than Parkinson's disease (PD). Approximately 5% of individuals over 40 have ET (Louis 2005). Tremor is defined as "an involuntary, rhythmic, oscillatory movement of a body part" (Bhatia et al. 2018). ET predominantly manifests as a tremor of the upper limbs, and can severely affect daily-life. The condition is characterised by an action tremor, which intensifies with voluntary movements such as writing, pouring,

and eating. Postural tremor, which is a tremor occurring with sustained muscle tone (for example holding outstretched arms), can also be seen in severe cases. ET is a progressive neurological disorder, and both genetic factors and environmental factors (toxins) are believed to cause the disease (Louis 2005).

Treatments No cure exists, and treatment can be pharmacological or surgical. There are no drugs specific to ET, and beta-blockers or anti-epileptic drugs can be prescribed in the first instance. When medications are ineffective or not tolerated, thalamic DBS is an effective therapy option (Koller et al. 2001; Sydow et al. 2003; Pahwa et al. 2006). Unilateral thalamic DBS improved tremor scores by 75% at a 5-year follow-up (Pahwa et al. 2006). Clinically available DBS continuously delivers high-frequency (about 130 Hz) electrical stimulation to deep structures within the brain via an electrode connected to a pulse generator implanted in the chest (Figure 1.1, panel A). For ET, the most common stimulation site is the ventral intermediate nucleus (VIM) of the thalamus. Alternatively, a recently introduced technique called magnetic resonance-guided focused ultrasound allows unilateral thalamotomy (ablation of the thalamus) without opening the skull. Indirect comparison with high frequency DBS shows that tremor improvement may be somewhat comparable (Harary et al. 2019), however lesioning is irreversible and no adjustment is possible.

Pathological signals Neurophysiologists have found signals in the thalamus closely related to tremor in ET. Outside the brain, tremor can be measured with an accelerometer attached to the tremulous limb, or invasively using electromyography (EMG). The latter technique records muscle activity from a needle inserted into the muscle. During essential tremor episodes, a proportion of VIM neurons fires bursts of spikes at tremor frequency (around 5 Hz), and this activity is coherent with peripheral muscle activity driving the tremor (Hua et al. 1998; Hua and Lenz 2005). This is also true of Parkinsonian tremor (Zirh et al. 1998). Local field potentials (LFPs) recorded from the VIM display theta frequency oscillations (4 to

7 Hz) which are coherent with forearm flexor and extensor activity during essential tremor (Pedrosa et al. 2014), see Figure 1.1, panels B to D.

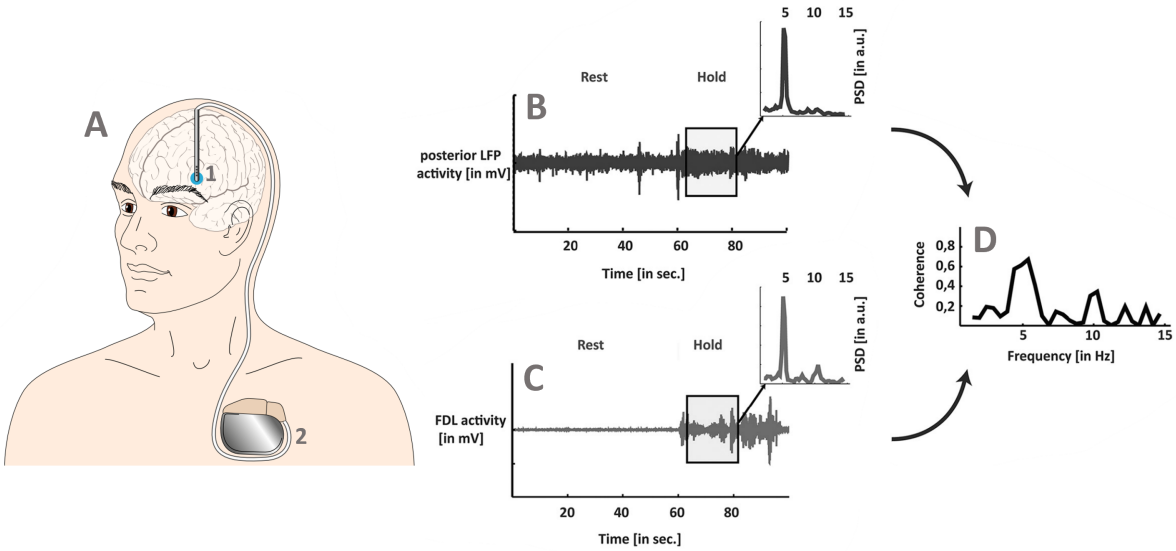

Figure 1.1: Implanted DBS device, and coherence between ET pathological signals. Clinically available DBS continuously delivers high-frequency electrical stimulation to deep structures within the brain via an electrode (A1) connected to a pulse generator implanted in the chest (A2). LFP recorded from the VIM (B) and forearm flexor digitorum longus (FDL) EMG (C) are coherent at tremor frequency around 5 Hz (D). Panel A was adapted from (Cagnan et al. 2019b), panels B to D from (Pedrosa et al. 2014).

Pathophysiology Detailed knowledge of how ET comes about is missing. It is believed that the disorder originates in the cerebellar-thalamic-cortical pathway (Schnitzler et al. 2009). The correlations mentioned between thalamic activity and tremor muscle activity do not necessarily imply a thalamic origin of tremor. One hypothesis is that the GABAergic system (system producing the neurotransmitter Gamma aminobutyric acid or GABA) is disrupted in the cerebellum following neurodegeneration. This would cause an increase in the deep cerebellar input to the thalamus, triggering rhythmic activity in the thalamus. This elevated thalamic activity would then propagate through the motor system and give rise to tremor. The evidence supporting this so-called GABA hypothesis is mixed, as reviewed in (Gironell 2014). Regardless, it is likely that the thalamus plays an important role in generating tremor. The fact that tremor frequency stimulation of the VIM

can entrain tremor (Cagnan et al. 2013) demonstrates that the thalamus is not simply relaying established oscillations (Cagnan et al. 2014).

1.2.1.2 Parkinson's disease

Parkinson's disease (PD) is an age-related neurodegenerative disease which affected 0.08% of the world population in 2015 (6.2 million patients, Hay et al. 2017). PD is the second most common neurodegenerative disease to Alzheimer's Disease (de Lau and Breteler 2006), and the second most common movement disorder. The cardinal motor symptoms of PD are slowness of movement (bradykinesia) or even inability to initiate movements, as well as rigidity due to increased muscle tone. Other motor symptoms include tremor at rest (as opposed to ET action tremor), a stooped posture, balance problems, and freezing of gait. Patients also experience non-motor symptoms, such as sleep disorders, depression, cognitive impairment, and dementia (Kalia and Lang 2015). PD is believed to be caused by the progressive death of dopaminergic neurons in the substantia nigra pars compacta (SNc) located in the basal ganglia (BG). The ensuing dopamine deficit results in dynamic changes in the BG network favouring movement inhibition. By symptom onset, cell death has already occurred in a substantial proportion of SNc dopaminergic neurons. Estimates range from 30% to 70% (Kordower et al. 2013; Cheng et al. 2010). Aggregates of the protein α-synuclein are found to have spread in the brain of PD patients, and it is hypothesised that α-synuclein may be a key player in dopaminergic neuron death (Venda et al. 2010; Mor et al. 2019). Mathematical modelling supports the theory that these aggregates spread as prions (proteinaceous infectious particles), and suggests that this spreading mechanism would be common to other neurodegenerative diseases such as Alzheimer disease (Weickenmeier et al. 2018; Weickenmeier et al. 2019). PD has been related to genetic factors in a minority of cases, and the disease aetiology is generally unclear.

Treatments There is no cure for the disease but symptoms can be successfully managed for a number of years by pharmacological treatment, and in a subset of advanced cases, surgical intervention. The principal drug is a precursor of

dopamine called Levodopa which, as opposed to dopamine, can cross the blood-brain barrier. Levodopa is transformed into dopamine in the brain, and thereby alleviates the dopamine deficit. Whilst Levodopa can initially manage motor symptoms successfully, motor side effects of the drug called dyskinesia tend to get worse after years of treatment (Marconi et al. 1994). Dyskinesias are uncontrollable, involuntary movements that may involve only one limb or the entire body and can become debilitating. Additionally, as the disease progresses, medication effects last for shorter and shorter periods of time, causing unpredictable fluctuations in motor symptoms (Nutt and Holford 1996). Debilitating dyskinesia and motor symptom fluctuations are the main indications for DBS surgery in PD. The most common stimulation target is the subthalamic nucleus (STN) in the BG. Similarly to DBS for ET, stimulation is delivered at high frequency (about 130 Hz) in clinically available devices. High frequency DBS for PD is a well established, effective treatment (Rodriguez-Oroz et al. 2005; Deuschl et al. 2006; Benabid et al. 2009).

Beta oscillations Elevated oscillatory activity in the beta band (13-35 Hz) is found in the BG of PD patients withdrawn from medication (in the "OFF" medication state). Generally, beta oscillations have been associated with motor control. A reduction in beta power is observed during voluntary movement initiation and execution and is followed by a rebound in beta power both at the cortical (Miller et al. 2009; Tan et al. 2014; Torrecillos et al. 2015; Fischer et al. 2016) and BG level (Cassidy et al. 2002; Kühn et al. 2004; Hebb et al. 2012). In this sense, beta oscillations can be thought of as anti-kinetic. In PD, as suggested by Brown (2003), increased beta oscillatory activity in the BG has been correlated with worsening of motor symptoms, in particular bradykinesia and rigidity but not tremor (Kuhn et al. 2006; Kühn et al. 2008; Kühn et al. 2009; Tan et al. 2013; Steiner et al. 2017). This elevated beta activity is reduced by medication (Brown et al. 2001; Neumann et al. 2017) and high frequency DBS (Eusebio et al. 2011; Neumann et al. 2016, see Figure 1.2, panels A and B). It is believed that heightened synchrony in the beta band decreases the information coding capacity of the cortico-basal

ganglia network (Hammond et al. 2007; Brittain and Brown 2014), as recently confirmed (Khawaldeh et al. 2020). This would contribute to motor impairment in PD. However, the potential causal role of elevated beta oscillations in giving rise to motor impairment in PD is still debated. A direct evidence for a causal role of beta in suppressing movement was given by increasing cortical beta synchrony with transcranial alternating-current stimulation (tACS) in healthy subjects, which induced slowing of movement (Pogosyan et al. 2009).

Recent studies suggest that beta activity is of phasic (transient) nature and comes in bursts. This was first reported in physiological beta activity in the cortex (Feingold et al. 2015; Sherman et al. 2016; Shin et al. 2017), and cortical beta bursts have been related to motor preparation before movement (Little et al. 2019; Wessel 2020). Beta burst are commonly defined as events corresponding to the beta envelope being above a predefined threshold (see Figure 1.2, panels C and D). In PD, besides the average level of beta synchrony, the temporal patterning of beta activity has been shown to be of importance. Specifically, the proportion of longer bursts of activity in the beta band of STN LFPs OFF medication has been correlated with motor impairment (Tinkhauser et al. 2017b), and it was found that motor symptoms can be ameliorated by shortening beta bursts of longer duration with STN adaptive deep brain stimulation (Tinkhauser et al. 2017a). Since then, STN bursts in PD patients have been shown to impact motor performance at the single trial level (Torrecillos et al. 2018). In another task, the percentage of time spent in beta bursts has been shown to be a better predictor of bradykinesia than average beta power (Lofredi et al. 2019), and it has been argued that temporal synchrony patterning may be more sensitive to clinical changes than average synchrony (Ahn et al. 2018). The clinical relevance of temporal synchrony patterning may extend to other PD motor symptoms, and STN beta burst duration has also been suggested as a potential biomarker for freezing of gait in PD (Anidi et al. 2018).

Pathophysiology How exactly dopamine depletion causes PD symptoms is still debated. Albin's "rate model" (Albin et al. 1989) explains motor symptoms by the

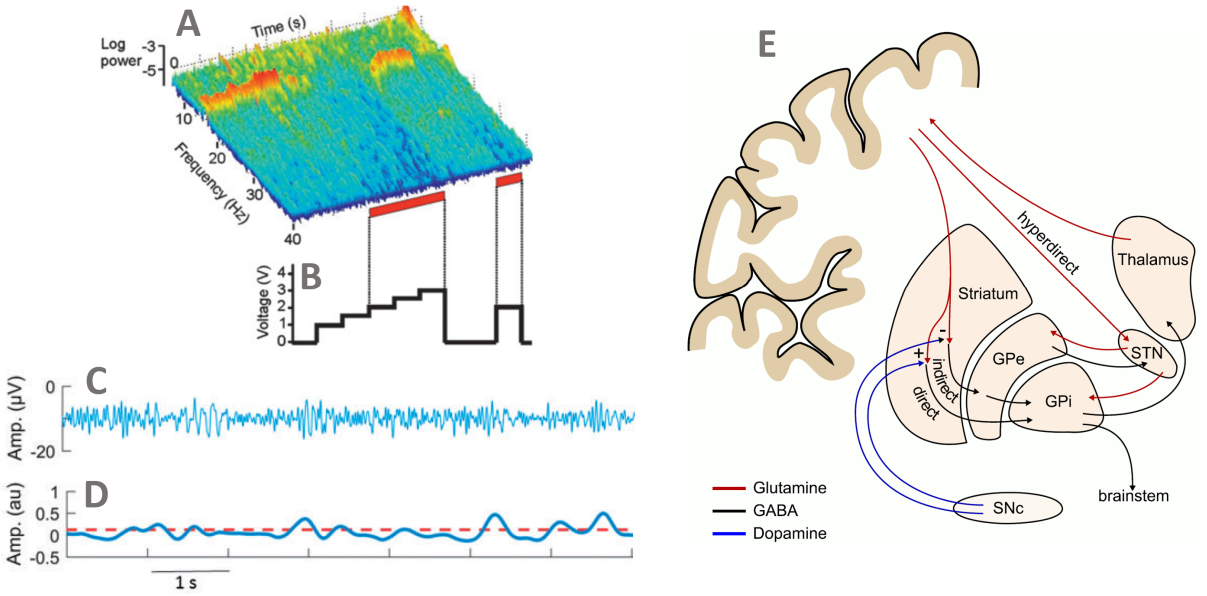

Figure 1.2: Beta oscillations in PD, and BG pathways. Beta power is suppressed (A) as DBS voltage is increased (B). Beta bursts can be identified by filtering the raw LFP (C) around its beta peak, and thresholding the beta envelope obtained from the Hilbert amplitude of the filtered signal (D). Albin's rate model is based on the competition between BG direct and indirect pathways (E). Excitatory connections are shown in red, inhibitory connections in black. The effect of dopamine on the direct and indirect pathways is indicated by plus and minus signs. Panels A and B were adapted from (Eusebio et al. 2011), panels C and D from (Tinkhauser et al. 2017b), and panel E from (Brittain and Brown 2014).

effect of dopamine depletion on the competition between BG direct and indirect pathways (Figure 1.2, panel E). While the direct pathway promotes movement by disinhibiting the thalamus, the indirect pathway prevents movement by inhibiting the thalamus. Dopamine normally promotes movement by its antagonistic action on the two pathways at the level of the striatum. Specifically, dopamine is believed to drive the direct (pro-kinetic) pathway, and hold back the indirect (anti-kinetic) pathway. With low dopamine levels, the drive to the pro-kinetic pathway is reduced, and the strength of the anti-kinetic pathway is increased, resulting in difficulties to move. Although very influential, the rate model has been criticised for a lack of interaction and coordination between the pathways (Calabresi et al. 2014).

The implication of beta oscillations and beta bursts in the disease has shifted the focus from the output rates of the direct and indirect pathways to investigating how excessive beta oscillations arise in the BG and might cause the pathology.

No consensus has been reached, and as reviewed in (Schroll and Hamker 2016), several mechanisms have been identified as potential causes of exaggerated beta oscillations in PD and may not be exclusive. The feedback loop formed by the reciprocally connected STN and globus pallidus pars externa (GPe) is one candidate (Terman et al. 2002; Holgado et al. 2010; Tachibana et al. 2011; Pavlides et al. 2012). Exaggerated beta oscillations could also arise from the longer cortico-BG-thalamic loop (Leblois et al. 2006; Pavlides et al. 2015), or directly within interconnected populations of striatal neurons (McCarthy et al. 2011).

1.2.2 From high-frequency to closed-loop deep brain stimulation

Although high-frequency DBS is an effective treatment for PD and ET, there is a need to refine the therapy. It is thought that the way forward is to provide stimulation in a closed-loop fashion.

1.2.2.1 High frequency deep brain stimulation

The first DBS surgery was performed for ET by Benabid and colleagues in (1987), and since then, over 150 000 DBS surgeries have been performed for PD alone (Hariz 2017). As mentioned previously high frequency DBS is an effective treatment for ET and PD. It has also been applied successfully to other "oscillopathies" (i.e. disorders where symptoms are correlated with elevated oscillatory neural activity) such as dystonia (Kiss 2007; Volkmann et al. 2014) and epilepsy (Salanova et al. 2015; Klinger and Mittal 2016; Li and Cook 2018). The therapy has been tested with varying degrees of success in other neurological and psychiatric diseases such as Tourette syndrome, major depression, Alzheimer's disease, and anorexia nervosa (see Cagnan et al. 2019b; Lozano et al. 2019, for recent reviews).

The mechanisms of action of high-frequency DBS are still debated in the research community (McIntyre and Anderson 2016; Cagnan et al. 2019b; Lozano et al. 2019). In the case of PD, an influential view is that high frequency DBS induces a partial "information lesion" in the stimulated network, thereby blocking the propagation of pathological oscillations (Grill et al. 2004). This might be mediated by DBS induced

entrainment of axonal firing and inhibition of firing in the soma of neurons (McIntyre et al. 2004). However, Rosenbaum and colleagues (2014) proposed that DBS induced axonal and synaptic failures play a major role in causing an information lesion.

High frequency DBS is an effective treatment for a number of oscillopathies, but it is believed there is room for improvement in terms of efficacy, decrease in power usage, and most importantly reduction of side effects (Kumar et al. 2003). Reported side effects of high-frequency thalamic DBS include speech impairment, gait disorders, and abnormal dermal sensations (Børretzen et al. 2014). In addition to these, dyskinesia, balance problems, cognitive impairment, and impulsivity have been observed in STN DBS (Rodriguez-Oroz et al. 2005; Benabid et al. 2009). Habituation, where the benefit of stimulation diminishes considerably over the years in some patients, is another significant downside of high-frequency DBS, mostly in ET (Fasano and Helmich 2019). Habituation is often addressed by changing stimulation parameters, but surgery is required in some cases to re-position the stimulation electrode or implant a new one (Fasano and Helmich 2019).

1.2.2.2 Closed-loop deep brain stimulation

Taken together, the above-mentioned limitations are the motivation to improve DBS by stimulating in a way that targets the pathology more selectively and delivers less energy to the brain than continuous, high frequency stimulation. As an example, minimising the energy delivered in STN and thalamic DBS would limit how much current spreads to the internal capsule's fiber tracts adjacent to the target. Stimulation spreading to these fiber tracts may be the cause of speech impairment (Mücke et al. 2018), one of the most common side effect in STN and thalamic DBS. Additionally, STN DBS has been shown to interfere in perceptual decision making tasks (Herz et al. 2018) and value-based choice tasks (Frank et al. 2007). Stimulating in a way that preserves more of the STN physiological processing may reduce impulsivity induced by DBS in some PD patients (Cagnan et al. 2019b). Furthermore, reducing power consumption would be desirable to increase the time

between battery replacement surgeries. This is however becoming less critical with the advent of wireless charging.

To reduce side effects and habituation while maintaining or even improving efficacy, some experimental stimulation strategies do not rely on feedback signals to adjust stimulation and are labelled "open-loop", but most do and are labelled "closed-loop". An innovative open-loop DBS approach for PD is coordinated reset, in which neural populations are entrained with different delays at several locations in space (electrode contacts), thereby reducing synchronisation between those sites (Tass 2003; Adamchic et al. 2014). In closed-loop strategies, a function of the feedback signal called "biomarker" and chosen for its correlation with symptom severity is often used to adapt stimulation. Closed-loop feedback signals can be measured directly in the brain (stimulation electrodes can record LFPs from non-stimulation contacts, but additional electrodes could also be used), or peripherally via wearable sensors. However, using wearable sensors in a chronic setting rather than an implanted electrode is likely to bring additional challenges, chief of which is patient compliance (Cagnan et al. 2019b). A proof of concept in a non-human primate model of PD has shown that closed-loop DBS is more effective than high frequency DBS in reducing motor impairment (Rosin et al. 2011). In this study, stimulation was triggered by spiking activity in motor cortex after a constant delay. Since then, various biomarkers have been considered for closed-loop stimulation strategies, such as beta oscillation amplitude or phase amplitude coupling in the case of PD, and tremor frequency activity in the thalamus or even peripheral tremor amplitude and phase directly measured via a wearable sensor for ET (reviewed in Hoang et al. 2017). Additionally, machine learning techniques have been applied to predict tremor episodes from brain signals in PD and ET, opening the door to on-demand stimulation for tremor (Houston et al. 2017; Tan et al. 2019; Yao et al. 2020).

Adaptive deep brain stimulation A particular class of closed-loop stimulation strategies called adaptive DBS (aDBS) delivers 130 Hz stimulation when pathological oscillation amplitude exceeds a given threshold (Figure 1.3, panel A). Note that

stimulation provided above the threshold is high frequency, but in this thesis we use the term high frequency DBS to refer to clinically available continuous high frequency DBS described earlier. Adaptive DBS has been tested in PD patients in acute trials, but not chronically so far. As recently reviewed (Little and Brown 2020), these acute studies have demonstrated that aDBS is at least as effective as high frequency DBS (Little et al. 2013; Little et al. 2016; Herz et al. 2018), and delivers approximately half the energy to the brain (Little et al. 2013; Rosa et al. 2017a; Velisar et al. 2019). Early evidence indicates that aDBS would reduce side-effects such as speech impairment and dyskinesia compared to high frequency DBS (Little et al. 2016; Rosa et al. 2017a; Arlotti et al. 2018). In PD, "fast" aDBS has been implemented based on beta oscillation amplitude averaged over 300 ms (Little et al. 2013; Little et al. 2016; Herz et al. 2018), and "slow" aDBS based on beta oscillation amplitude averaged over 50 s (Rosa et al. 2017a; Arlotti et al. 2018). Preliminary evidence suggests that the former approach would be more effective (Little and Brown 2020). This is in line with the fact that fast aDBS allows stimulation to interact with the bursty nature of beta oscillations. Specifically, longer bursts of beta activity believed to be implicated in motor impairment (as reviewed earlier) can be shortened (Tinkhauser et al. 2017a). Beta bursts are rarely longer than one second (Tinkhauser et al. 2017b), and averaging over 50 s masks beta bursts.

In its current form, aDBS specificity in targeting the pathology could still be improved. Because aDBS cuts high levels of beta oscillations, it may impact beta rebound at the end of movements, potentially delaying termination of movements, and impacting motor learning (Little and Brown 2020). Refining aDBS will require to further clarify the relationship between burst dynamics and motor impairment to interact with beta dynamics in a subtler way.

Phase-locked deep brain stimulation Another class of stimulation strategies termed phase-locked DBS locks stimulation to pathological oscillation phase. Because aDBS intermittently provides stimulation at about 130 Hz, physiological activity such as activity related to movement in PD could still be disrupted (Holt

et al. 2019; Little and Brown 2020). In phase-locked DBS, it is hypothesised that rhythmic physiological activity not directly phase-locked to the stimulation will be preserved (Cagnan et al. 2013). In part because of the added challenge of estimating oscillation phase in real time, fewer phase-locked DBS studies have been conducted so far than aDBS studies. Tremor rhythm is slower than beta oscillations (around 5 Hz versus around 20 Hz), making ET a natural candidate to test phase-locked stimulation.

The potential of phase-dependent stimulation to suppress tremor has been demonstrated non-invasively in Parkinsonian tremor using transcranial alternating current stimulation (Brittain et al. 2013), and in ET using thalamic DBS (Cagnan et al. 2013). Phase-dependent STN DBS has been investigated more recently to suppress beta oscillations in PD (Holt et al. 2019). In these studies, stimulation is provided at the pathological rhythm average frequency such that the phase of stimulation slowly drifts over time. Several consecutive periods with similar stimulation phases are available, allowing to estimate stimulation effects on pathological oscillations as a function of stimulation phase. Up to 30% tremor suppression was achieved in (Cagnan et al. 2013), and up to 40% beta amplitude suppression in (Holt et al. 2019). Most amplifying and most suppressing phases were found in (Cagnan et al. 2013) to be 180 degrees apart. This suggests that the change in tremor amplitude as a function of stimulation phase, called amplitude response curves (ARC), might be sinusoidal (Cagnan et al. 2013).

Sustained phase-locked stimulation is more effective than slowly drifting stimulation at tremor frequency. Using the most suppressive stimulation phase, Parkinsonian tremor was suppressed by up to 53% (Brittain et al. 2013), and essential tremor by up to 87%, while delivering to the thalamus half the energy of high frequency DBS (Cagnan et al. 2017). In the latter study, thalamic DBS was delivered locked to the phase of tremor acceleration recorded from an accelerometer fitted to patients (Figure 1.3, panel B1). The efficacy of stimulating at different phases of the tremor cycle was quantified using ARCs (see Figure 1.3, panels B2 to B4). We will return to this notion, and to how the response was precisely measured in this study.

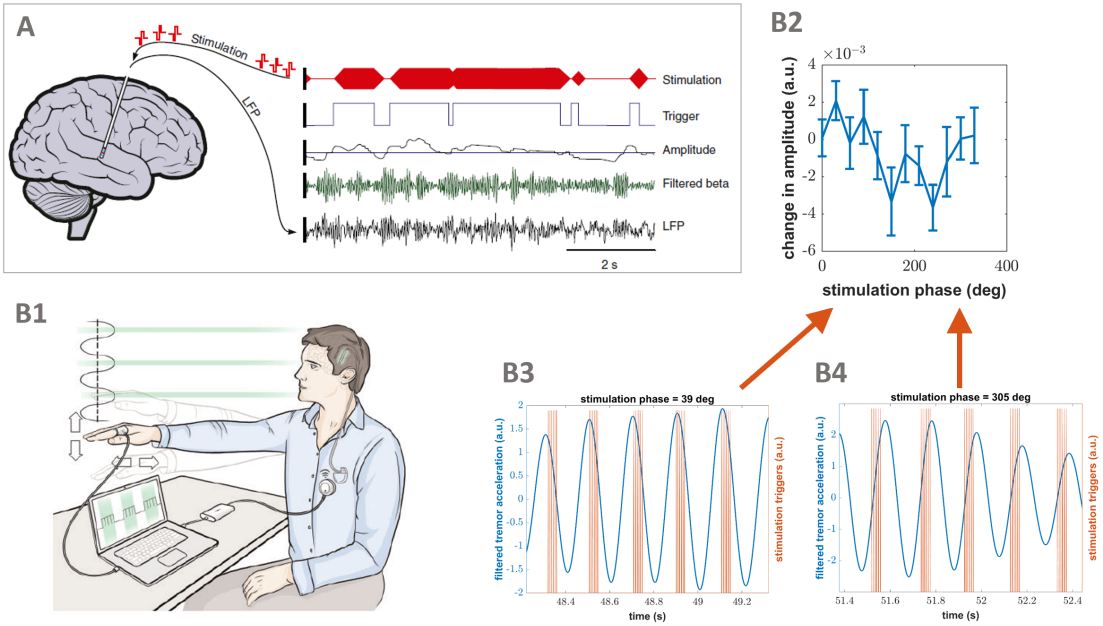

Figure 1.3: Experimental closed-loop DBS: aDBS in PD and phase-locked DBS in ET. In aDBS, 130 Hz stimulation is triggered when beta amplitude obtained from the recorded LFP exceeds a given threshold (A). In (Cagnan et al. 2017), tremor acceleration is recorded by an accelerometer, and stimulation is provided phase-locked to tremor acceleration via the DBS electrode (B1). The effect of phase-locked stimulation on tremor amplitude is measured by the ARC (B2). Panels B3 and B4 show phase-locked stimulation early and late in the tremor cycle, respectively (tremor shown in blue, stimulation triggers in red). The ARC is constructed from the amplitude responses to blocks of phase-locked DBS at stimulation phases spanning $[0, 2\pi)$. Panel A was adapted from (Little et al. 2013), panel B1 from (Cagnan et al. 2013).

1.2.3 Modelling approaches

Computational studies can further our understanding of movement disorder pathophysiology (Schroll and Hamker 2016). In addition, they are also a crucial tool in developing better therapies. For practical reasons, experimental exploration of stimulation strategies is limited to only a few selected case studies, while the space of stimulation parameters is infinite. To understand how phase-locked DBS affects tremor (Cagnan et al. 2017), patients are asked to assume tremor provoking positions, which is very tiring for them. Thus, only short recordings are available, which is not enough to optimise the therapy. Large amount of synthetic data can be generated from models and be used as a testbed for stimulation strategies. In general, individualised patient models could help speed up the lengthy DBS

parameter tuning process currently done manually by neurologists (Yousif et al. 2020). Computational simulations offer a natural complement to experiments by providing the experimentalists with hand-picked scenarios and predictions that can be realistically tested (Schroll and Hamker 2016).

Oscillations in LFPs are believed to represent synchronous activity of large neuron populations, which can be modelled in various ways. While large networks of detailed neuron models can be used, neural mass models (also known as population models) are specifically designed to describe synchronous mesoscale activity. Because of the intricate physiology of an individual neuron and the sheer number of units involved, neuron level models are computationally expensive and hard to constrain. This topic will be revisited in Section 1.2.3.3. Mesoscale models have much fewer parameters than neuron level models and are therefore less prone to overfitting. Owing to their low dimensionality and relatively low number of parameters, they are more easily constrained by data, and can even in some cases be analysed mathematically.

Before reviewing models of pathological oscillations and models of DBS in PD and ET, I will provide more background on selected mesoscale models. In particular, I will introduce the Wilson-Cowan (WC) population model, and a phenomenological model that can be reduced to a mesoscale mean-field, the Kuramoto model. A general review of neuron level models can be found in (Ashwin et al. 2016).

1.2.3.1 The Wilson-Cowan model

In their seminal work, Wilson and Cowan heuristically derived mean-field equations for the proportion of neurons firing (also called activity) in reciprocally coupled inhibitory and excitatory populations (Wilson and Cowan 1972). They assumed that neurons receive the same number of excitatory and inhibitory afferents within each population, and that these numbers are large enough that neurons experience the same average inputs. They showed that if neurons have a unimodal distribution of their firing thresholds, the activation function of each population will be sigmoidal. The final step in their derivation is to average activities over a short time scale

(time coarse graining). Since then, Galtier and Touboul (2013) have shown that WC-type equations are obtained when applying stochastic network reduction to a wide class of spiking neuron models.

We present a generic version of the WC model, where we assume that the duration of neuron refractory period is negligible. The excitatory and inhibitory populations interact via reciprocal connections, and entertain within population connections (see Figure 1.4). The activity E of the excitatory population, and the activity I of the inhibitory population are described by the differential equations

$$\begin{cases} \tau_E \frac{dE}{dt} = -E + f(\theta_E + w_{EE}E - w_{IE}I), \\ \tau_I \frac{dI}{dt} = -I + f(\theta_I + w_{EI}E - w_{II}I), \end{cases} \tag{1.1}$$

with w_{PR} the weight of the projection from population "P" to population "R", θ_P the constant input to population "P", and τ_P the time constant of population "P". The activation function f is a sigmoid such as

$$f(x) = \frac{1}{1 + e^{-\beta(x-1)}}$$

parametrized by a steepness parameter β. This is the same activation function as used in (Onslow et al. 2014), and corresponds to allowing spontaneous population spiking in the absence of inputs. While inhibitory and excitatory populations can have different activation functions and the position of the maximum slope on the sigmoid can be parametrised (as in Wilson and Cowan 1972), we choose to limit the number of model parameters.

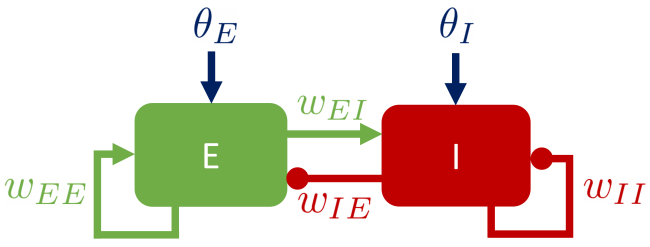

Figure 1.4: Connections in a generic two population WC model. The excitatory population is denoted by E and the inhibitory population by I. Arrows represent excitatory connections or inputs, whereas circles denote inhibitory connections.

While mathematically relatively simple, the WC model exhibit rich dynamics, which is one reason for its enduring success (Chow and Karimipanah 2020). The

WC model can oscillate when connections are strong enough via interactions akin to a PING mechanism (pyramidal-interneuron gamma, see Tiesinga and Sejnowski 2009) where excitation precedes inhibition. A rise in E caused by self-excitation in the excitatory population will trigger an increase in I which will subsequently inhibit E, and the cycle will repeat. Limit cycle dynamics cannot be observed in the absence of self-excitation of the excitatory population, unless connections between populations have delays (Holgado et al. 2010). As shown in (Borisyuk and Kirillov 1992; Merrison-Hort et al. 2013), the WC model can also display bistability, where a stable fixed point and a stable limit-cycle coexist. Coupling WC models can lead to more multistability and chaos (Borisyuk et al. 1995; Ueta and Chen 2003; Wilson 2019). Besides movement disorders and DBS (see Sections 1.2.3.3 and 1.2.3.4), the WC model and its spatial extension (Wilson and Cowan 1973) have recently been applied to investigate cognition and memory (Rabinovich et al. 2008; Liu et al. 2017; Pina et al. 2018), travelling waves (Harris and Ermentrout 2018; Roberts et al. 2019), vision (Bressloff et al. 2002; Chossat 2020), whole brain dynamics (Atasoy et al. 2016), cortical resonance (Lea-Carnall et al. 2016), phase-amplitude coupling (Onslow et al. 2014), pain (Crodelle et al. 2019), epilepsy (Wang et al. 2017), and obsessive compulsive disorder (Radulescu et al. 2017) to name a few.

Examples of more complex population models include the Jansen-Rit model, which considers a population of pyramidal neurons in addition to one excitatory and one inhibitory population (Jansen and Rit 1995). Each population is associated with a second order differential equation, bringing the dimensionality of the model to six. The increase in complexity enables the model to generate evoked potentials seen in electroencephalogram (EEG) recordings (Jansen and Rit 1995) and realistic seizure-like activity when models are coupled (Wendling et al. 2000). However we will not be modelling this type of signals, and the increase in the number of parameters and in the dimensionality of the model makes it less suitable to be fitted to data.

1.2.3.2 The Kuramoto model

Synchronous activity can also be modelled using coupled oscillator models, such as the Kuramoto model (Kuramoto 1975). A phenomenological model, the Kuramoto model does not model interacting populations of neurons, but describes the synchronisation of weakly coupled oscillators. These oscillators can be interpreted as neurons or micro-circuits (Weerasinghe et al. 2019). They are only defined by their phases, and interact via sinusoidal functions of pairwise phase differences. For N oscillators, oscillator phases θ_l, $l \in \{1, .., N\}$ evolve according to

$$\frac{d\theta_l}{dt} = \omega_l + \frac{k}{N} \sum_{n=1}^{N} \sin(\theta_n - \theta_l), \tag{1.2}$$

where ω_l is the natural frequency of oscillator l, and k represents the (constant) coupling strength between oscillator pairs. Oscillator synchrony is measured by the modulus ρ of the Kuramoto order parameter r defined as

$$r = \rho e^{i\psi} = \frac{1}{N} \sum_{n=1}^{N} e^{i\theta_n}. \tag{1.3}$$

In the thermodynamic limit ($N \to +\infty$) and under certain assumptions about the distribution of oscillator natural frequencies, Ott and Antonsen mean field reduction can be applied to reduce the N dimensional system described by equation (1.2) to a two-dimensional system describing the evolution of r (Ott and Antonsen 2008; Bick et al. 2020).

Besides applications to DBS (see Section 1.2.3.4), some recent applications of the Kuramoto model to neuroscience include investigations of structural and functional connectivity (Cabral et al. 2014; Schmidt et al. 2015; Finger et al. 2016), criticality (Kitzbichler et al. 2009), and resting state activity (Ponce-Alvarez et al. 2015).

1.2.3.3 Modelling pathological oscillations in Parkinson's disease and essential tremor

Models of various levels of complexity have been put forward to generate pathological oscillations in PD and ET. Here, we put in perspective population models and neuron level models describing pathological oscillations in PD and ET. Motivated

by the recent implication of bursting activity in motor impairment in PD (see Section 1.2.1.2), we highlight gaps in modelling of transient synchrony in PD.

Population models The BG network is a prime example of excitatory/inhibitory architecture, in particular in the STN-GPe loop. Glutamatergic (excitatory) connections project from STN to GPe, while connections from GPe to STN are GABAergic (inhibitory). In line with this, the WC model or close variants have been a popular choice to model the BG. In particular, a number of studies have shown that the STN-GPe loop could play a predominant role in the generation of heightened sustained beta oscillations in PD, and identified conditions for such oscillations to appear (Gillies et al. 2002; Holgado et al. 2010; Pavlides et al. 2012; Nevado-Holgado et al. 2014). Representing segregated STN-GPe channels by WC models coupled at the GPe level, Merrison-Hort and colleagues (2013) showed that Parkinsonian beta oscillations can be generated when between-channel coupling is strong enough. Considering a single channel, they found a bistable region in parameter space where a stable limit cycle encloses a stable fixed point. The authors hypothesised that transient inputs can selectively switch individual channels from oscillatory activity to steady state to enable movement. This mechanism could account for the beta suppression seen during movement. It was suggested that PD could shrink the basin of attraction of the stable fixed point, which would impair movement.

Motivated by the evidence for a role of the cortex in the generation of beta oscillations in the primate literature, the WC STN-GPe loop model was extended with populations representing cortical oscillators in (Pavlides et al. 2015). In addition to the cortex, thalamic and cerebellar populations were also considered in a network of WC populations (Yousif et al. 2020). The network could reproduce beta frequency oscillations for a broad range of parameters. Similarly to earlier work based on a smaller WC network not including the BG (Yousif et al. 2017), tremor frequency oscillations could also be generated. These rhythms could all be suppressed by high frequency DBS.

Neuron level models Models based on detailed representations of individual neurons have been used to reproduce oscillations in the BG. A STN-GPe circuit with 3000 leaky integrate and fire neurons (Kumar et al. 2011) showed that the strength of inhibitory striatal input to GPe is central to the generation of beta oscillations. The Hahn and McIntyre (2010) STN/GPe/GPi model is more complex and employs 500 Hodgkin-Huxley single-compartment neurons. Related conductance-based models were also used in (Terman et al. 2002; Rubin and Terman 2004; Popovych et al. 2017; McCarthy et al. 2011). In ET, a spatially extended part of the VIM was modelled with multi-compartment neurons (Lee et al. 2019).

These complex models require a large number of parameters, which are often chosen so the model reproduces the data to some degree, or are taken from past studies. With short, noisy datasets, it is very likely that for complex models, most parameters will not be identifiable, i.e. a "true" unique value cannot be estimated for these parameters (Bellman and Åström 1970; Hines et al. 2014). Non identifiability and a high dimensional parameter space imply that a very large number of parameter sets could likely reproduce the data at least as well. Additionally, how the model behaves in a high dimensional parameter space cannot be extensively studied in most cases (this is usually achieved in low-dimensional models using bifurcation analysis). Therefore, it is very difficult to say whether insights obtained for an arbitrary set of parameters (such as the strength of a pathway controlling the generation of pathological oscillations) are likely to generalise to other sets of parameters also reproducing the data. This limits the applicability of such insights and may explain some the heterogeneity found in BG model literature (Rubin 2017). Mean field approaches such as the WC model benefit from a low number of parameters while retaining some level of description of a microscopic biological reality. These models might therefore be better suited to model short pathological oscillation recordings obtained from a single recording site.

Transient beta synchrony As reviewed earlier in this subsection, many modelling studies have reported the generation of sustained beta oscillations in the

context of PD. However, despite the recent implication of bursting activity in motor impairment in PD (see Section 1.2.1.2), reproducing the temporal patterning of beta oscillations has received little attention. It has been shown that models of the STN-GPe loop can generate realistic transient beta oscillations in response to beta frequency inputs from PD patient EEG recordings (Ahn et al. 2016), and in response to biologically inspired input patterns in healthy animals (Mirzaei et al. 2017). Whether models of the STN-GPe loop could be capable of reproducing transient beta in the absence of correlated inputs is unknown. Without changing inputs, which dynamical changes could account for changes in the temporal patterning of beta oscillations between the healthy and pathological states has not been investigated either. This could be key to refining aDBS since the temporal patterning of beta oscillations is related with symptoms in PD.

1.2.3.4 Optimising deep brain stimulation

Model-based approaches to improve DBS based on control theory and approaches based on coupled oscillator models have been particularly influential. We will review some of these in this section, with a focus on coupled oscillator models which have moved forward phase-dependent stimulation. We will argue that the WC model is a complementary candidate to model closed-loop DBS.

Control theory Control theory has been used in model based approaches to suppress pathological oscillations. A WC model of the STN-GPe loop was subjected to stimulation determined by proportional feedback with a low pass filter for robustness to measurement delays (Haidar et al. 2016). In (Su et al. 2019), an input-output linear autoregressive model of an underlying conductance based model of the cortex, thalamus, and BG was identified to apply proportional integral feedback. Delayed feedback has also been investigated in various forms (Popovych et al. 2006; Popovych et al. 2017). However these approaches aim at indiscriminately reducing oscillations. It might be possible to spare more physiological processing by better understanding beta dynamics and how these dynamics are related to

motor impairment in PD. When practical, phase-locked stimulation may also be less disruptive to rhythms not perfectly phase-locked to.

Coupled oscillators Coupled oscillator models have spearheaded the development of innovative stimulation strategies based on oscillator sensitivity to the phase of stimulation. Coordinated reset was first simulated with a Kuramoto model, where stimulation affects an oscillator by shifting its phase (Tass 2003). The sensitivity of a single oscillator to stimulation depends on the phase at which it is stimulated via its individual phase response curve (PRC). How to optimally desynchronise coupled oscillators with the knowledge of their individual PRCs was studied in (Wilson and Moehlis 2014).

Weerasinghe and colleagues (2019) further elucidated the dependence of the effects of stimulation on stimulation phase in a Kuramoto model. Specifically, population PRCs and ARCs were derived from individual oscillator PRCs using Ott and Antonsen mean field reduction (2008). A subset of ET patient datasets were found to follow the predictions made by the model, in particular that the response to phase-locked stimulation should be greater when pathological oscillation amplitude is low. A hybrid DBS strategy was therefore put forward, whereby high-frequency DBS would be applied at higher amplitudes and phase-locked stimulation at lower amplitudes, where its efficacy is greater. How to best provide phase-locked stimulation was also investigated computationally in (Holt et al. 2016) in the context of PD. The STN and GPe were viewed as oscillators, and a phase-locked stimulus was derived from STN and GPe individual PRCs.

A common prediction made in (Wilson and Moehlis 2014; Holt et al. 2016; Weerasinghe et al. 2019) is that the best phase to stimulate is in under certain conditions close to the phase at which the derivative of the PRC is maximum. These studies are based on the knowledge of individual oscillator PRCs, which are difficult to obtain in patients. Additionally, they do not model interacting neural populations with distinct properties, or if they do, only population phases are considered, not population amplitudes (Holt et al. 2016). For mesoscale populations,

this is a coarse approximation. Thus, a complementary approach with population models such as the WC model is called for.

Wilson-Cowan populations Wilson-Cowan equations have been successfully employed to investigate high frequency DBS, implying that the WC model may also be a good choice to study closed-loop DBS strategies. In (Velarde et al. 2017), the therapeutic range of high frequency DBS predicted by a WC-type model matches PD experimental data. In silico experiments performed in ET (Yousif et al. 2017; Yousif et al. 2020) and in PD (Yousif et al. 2020) revealed that the impact of varying stimulation frequency in the model is consistent with data. Periodic forcing has been approached in the WC model (Pollina et al. 2003), but not in the context of DBS, and without attending to dependence on the phase of stimulation. Modelling phase-locked DBS with WC populations has not been investigated.

1.2.4 Amplitude, phase, and response curves

Refining aDBS requires to work with the notion of amplitude, and quantifying the effects of phase-locked DBS involves phase and amplitude. These notions are routinely defined differently in neurophysiology and in the field of dynamical system. In this thesis, because we are fitting models to data, we will favour definitions preferred in neurophysiology. However, an asymptotic definition of amplitude imported from dynamical systems, isostable amplitude, could benefit DBS research. Here we will contrast these definitions, and review how they relate to different types of PRCs and ARCs.

1.2.4.1 Amplitude definitions

Hilbert amplitude One of the most commonly used measures of instantaneous amplitude in neurophysiological data is the Hilbert amplitude (Barnikol et al. 2008; Cagnan et al. 2013; Brittain et al. 2015; Cagnan et al. 2017; Tinkhauser et al. 2017a; Holt et al. 2019). The Hilbert amplitude is defined as the modulus of the

analytic signal, and is meaningful for narrow band signals. Considering a narrow band signal $\text{sig}(t)$, the associated analytic signal is defined as

$$\widehat{\text{sig}}(t) = \text{sig}(t) + i\mathcal{H}(\text{sig}(t)), \tag{1.4}$$

where $\mathcal{H}$ denotes the Hilbert transform. The Hilbert transform is defined as

$$\mathcal{H}(\text{sig}(t)) = \frac{1}{\pi}\text{p.v.}\int_{-\infty}^{+\infty}\frac{\text{sig}(\tau)}{t-\tau}d\tau \tag{1.5}$$

when the integral exists, and where p.v. denotes the Cauchy principal value. In practice however, the analytic signal is computed using the fast Fourier transform and its inverse (Lawrence Marple 1999). The Hilbert amplitude $|\widehat{\text{sig}}(t)|$ describes the envelope of $\text{sig}(t)$ and is also called Hilbert envelope. The Hilbert amplitude will be used extensively throughout this thesis to describe the severity of tremor in ET, as well the envelope of beta oscillations in PD. In some previous studies (Tinkhauser et al. 2017a; Tinkhauser et al. 2017b), the beta envelope has been obtained from wavelet amplitude. Amplitudes obtained from Hilbert and wavelet analysis are believed to be equivalent in most practical situations (Bruns 2004). It has been reported that bursts characteristics derived using wavelet amplitude or filtering and Hilbert amplitude are similar (Schmidt et al. 2019).

Isostable amplitude From the perspective of coupled oscillators, synchronisation problems in the presence of perturbations are commonly approached by assuming a phase description of each oscillator given by phase reduction techniques (for recent reviews, see Ashwin et al. 2016; Pietras and Daffertshofer 2019). Individual oscillators are assumed to evolve on a limit cycle, and for infinitesimal perturbations, oscillator amplitude can be neglected. The response of an individual oscillator to infinitesimal perturbations can therefore be described solely by its phase response. To measure this phase response, the asymptotic phase on the limit cycle is used. We provide more details on asymptotic phase, also known as isochronal phase, in the next subsection. In this thesis, we are not considering coupled phase oscillators, but interacting mesoscale populations of neurons. Instead of using asymptotic phase to

infer synchronisation properties, we will therefore directly study the amplitude of the activity generated by mesoscale populations. Thus, the amplitude counterpart of isochronal phase, isostable amplitude, will be more relevant.

Isostable amplitude is given by isostables, which are sets of points approaching the attractor synchronously, i.e. crossing successive isostables at the same time (Mauroy et al. 2013; Shirasaka et al. 2017). The notion of isostable amplitude is therefore related to convergence time to the attractor. A precise mathematical definition of isostables and isostable amplitude for fixed point dynamics in $\mathbb{R}^2$ is given in Chapter 4. Isostables were first defined in the basin of attraction of fixed points (Mauroy et al. 2013). The concept was later extended to the basin of attraction of limit cycles (Wilson and Moehlis 2016a; Wilson and Ermentrout 2017; Shirasaka et al. 2017; Mauroy and Mezić 2018). Alternative definitions of amplitude associated with augmented phase reduction include methods based on the euclidean distance to the attractor (Wedgwood et al. 2013), and on a transverse variable obtained from parametrising isochrons (Castejón et al. 2013). In this thesis, the tremor data we fitted to are best represented by stochastic models giving rise to fixed point dynamics, and these alternative methods are only applicable when the attractor is a limit cycle. We will therefore rely on the definition of isostables for fixed point dynamics given in (Mauroy et al. 2013).

The model-based approaches to improving DBS mentioned in Section 1.2.3.4 are based on the Hilbert amplitude of the pathological signal or equivalent (such as oscillatory power or the Kuramoto order parameter). How Hilbert amplitude relates to isostable amplitude is unclear, and isostable amplitude may be complementary to Hilbert amplitude in the context of model-based optimisation of DBS. This hypothesis is substantiated by the fact that isostable amplitude includes knowledge about convergence time to the attractor, and by successful applications of the isostable framework to control the state of various systems. Outside of neuroscience, examples include stopping cardiac alternans (Wilson and Moehlis 2015), controlling non-linear flows (Wilson and Djouadi 2019), and optimal convergence to a stable fixed point (Mauroy 2014). In coupled oscillators modelling pathological oscillations

in PD, an external stimulation was designed based on isostable reduction to desynchronise neurons (Wilson and Moehlis 2016b). However the performance of the strategy was not compared to a more naive approach based on Hilbert amplitude or equivalent.

1.2.4.2 Phase definitions

Central to phase-locked DBS, phase can be defined in various ways. Phase definitions preferred by experimentalists when analysing signals differ from phase definitions more common in dynamical systems such as asymptotic phase. We review distinct phase definitions used for different purposes relevant to this thesis.

Definitions preferred by experimentalists Phase dependent activity is believed to play a key role in physiological information processing (Engel et al. 2013; Fries 2015), and phase is routinely extracted from neurophysiological signals. Similarly to Hilbert amplitude, the Hilbert phase is one of the most common measures of instantaneous phase in neurophysiological data analysis (Palva et al. 2005; Yang et al. 2012; Brittain et al. 2013; Cagnan et al. 2015; Cagnan et al. 2017). A typical signal only has one component, and the Hilbert transform provides a convenient way of reconstructing a phase from a single component. For narrow band signals, the Hilbert phase is defined as the argument of the associated analytic signal (given by equation 1.4). In real time, the simplest way to obtain the phase of an oscillation is to track positive or negative zero-crossings of the signal and assume a constant frequency between them. This method is used to deliver phase-locked stimulation to ET patients in (Cagnan et al. 2017). For noisy signals, suitable thresholds around zero help prevent failures of the tracking caused by noisy fluctuations around zero. An implementation example used in Chapter 2 is described in more details in Appendix A.7.

Definitions preferred in dynamical systems When studying dynamical systems, phase can be defined in various ways. In the phase-space of a two-dimensional system, the polar angle between a suitable reference and the current state can be

used to define a simple geometric phase (this definition will be used for simplicity in Chapter 4). The displacement of the velocity vector can also be used (Pereira et al. 2007). However, owing to the success of phase reduction methods, the most ubiquitous phase definition in dynamical systems is perhaps isochronal phase. Isochrons can be defined as sets of initial conditions resulting in oscillations sharing the same asymptotic phase (Guckenheimer 1975; Winfree 2001). This definition is typically intended for limit cycle dynamics, where the limit cycle can be parametrised by a phase evolving linearly with time called asymptotic phase. In the case of a stable focus, isochrons have not been studied as much but can similarly be defined as "isochronous sections" invariant under a T return map (Sabatini 2003; Giné and Grau 2005), where $T = \frac{2\pi}{\omega}$, with ω the imaginary part of the complex eigenvalues of the Jacobian at the fixed point.

These phase definitions are markedly different, and isochronal phase stands out in particular as the only non-instantaneous phase. To make meaningful predictions, one challenge associated with modelling phase-locked DBS will be to approximate in a population model the Hilbert phase, which is the phase used to analyse clinical recordings.

1.2.4.3 Measuring phase-dependent response to stimulation

The effects of stimulating at a given phase of the on-going oscillations can be quantified using phase and amplitude response curves. Because we directly consider the activity generated by mesoscale populations rather than synchronisation arising from coupled oscillators, the ARC will be representative of stimulation clinical efficacy (i.e. reduction in tremor in the case of ET models), and we will not use PRCs to predict synchronisation.

Asymptotic response curves In keeping with the prevalence of isochronal phase in the phase reduction literature, response curves have mostly been defined as the asymptotic response to infinitesimal perturbations on a limit cycle or close to it (Winfree 2001; Brown et al. 2004; Izhikevich 2007; Guillamon and Huguet

2009; Castejón et al. 2013; Ashwin et al. 2016). The infinitesimal asymptotic PRC is the gradient of isochronal phase and is classically obtained numerically as the solution to an adjoint problem (Brown et al. 2004; Izhikevich 2007; Ashwin et al. 2016). Analytical solutions have been found for some normal forms and one-dimensional neuron models (Brown et al. 2004). To improve the precision of phase reduction in the vicinity of the limit cycle, infinitesimal isostable response curves have later been introduced (Wilson and Moehlis 2016a). Related amplitude response functions have also been obtained from parametrising isochrons (Castejón et al. 2013). Isostable response curves can be determined far from the attractor and for large perturbations with global methods, which can compute isostables anywhere in the basin of attraction (Mauroy et al. 2013; Shirasaka et al. 2017; Mauroy and Mezić 2018). Isostable response will be investigated in Chapter 4.

Finite time response curves Instead of basing response curves on asymptotic quantities such as isochronal phase and isostable amplitude, they can be defined using notions of phase and amplitude common to data analysis, and the response can be measured in finite time. So-called first order PRCs and ARCs measure the difference in phase and amplitude between the stimulated trajectory and a reference trajectory at the end of the period where stimulation was applied. The first order phase response is also called first order phase resetting (Achuthan and Canavier 2009), and will be a useful tool in Chapter 2. Another definition of response curves follows (Cagnan et al. 2017). The phase and amplitude response to a block of several periods of phase-locked stimulation is determined using what we call the "block method". It is based on the Hilbert phase and amplitude, and the phase and amplitude response are quantified by comparing the Hilbert phase and amplitude at the end of the block to reference values obtained before the block. The block method will be described in greater details in Chapter 2.

These techniques differ in when response to stimulation is measured: asymptotically, at the end of the stimulation period (first order response), or after several periods (block method). The block method is adapted to the phase-locked ET

data used in this thesis, and how other phase and amplitude response measurement techniques relate to it is unknown.

1.3 Thesis outline

It emerged from our review of the literature that phase-locked DBS and aDBS are promising improvements to clinically available high-frequency DBS in PD and ET. Key to advancing phase-locked DBS is the phase-dependent response to stimulation, which is quantified by PRCs and ARCs. The experimental success of aDBS in PD hinges on interrupting events of high beta oscillation amplitude. However, this strategy does not target pathological activity very selectively. Beyond beta amplitude, we outlined how burst temporal dynamics are related to motor symptoms, and may be key to refining aDBS. Optimising closed-loop DBS in oscillopathies has been translated to altering (often suppressing) the amplitude of a pathological signal, and could benefit from a dynamical definition of amplitude, isostable amplitude. In this sense, response curves, burst temporal dynamics, and amplitude are concepts central to closed-loop DBS. From this perspective, the overall aim of the thesis is

to better our understanding of concepts key to closed-loop DBS using mathematical modelling, in order to get insights into underlying pathologies and inform next-generation closed-loop DBS.

To model the phase-dependence of the response to phase-locked DBS in ET, a canonical, mesoscale model describing the populations involved in the generation of ET is a natural choice, since detailed knowledge of how ET comes about is missing. In Chapter 2, I therefore ask the question

"Can the effects of phase-locked stimulation seen in ET patient data be accounted for by a canonical WC model?"

While Chapter 2 focuses on phase, Chapter 3 is concerned with amplitude phenomena called bursts. In PD, mounting evidence suggests it is the duration of beta burst that is of clinical importance. To get insights into burst generation, I ask in Chapter 3

"Can we relate observed changes in beta oscillation temporal patterning in PD between the ON and OFF medication states to changes in dynamical properties of the system generating beta oscillations?"

Bursts are defined in Chapter 3 based on Hilbert amplitude, which is a typical measure of synchrony used to optimise closed-loop DBS. Similarly, the amplitude response to stimulation in Chapter 2 is measured with Hilbert amplitude. As a dynamical measure of amplitude, isostable amplitude is a prime candidate to assist in optimising DBS. However, how isostable amplitude compares to Hilbert amplitude in the context of closed-loop DBS is unknown. In Chapter 4, I therefore raise the question

"How does isostable amplitude compare to Hilbert amplitude in fitted patient models when measuring the effects of phase-locked DBS, and when delivering stimulation in phase-space?"

I conclude the thesis with a general discussion (Chapter 5), which includes a summary of the clinical and theoretical contributions of this work (Section 5.1). Figure 1.5 illustrates how the key notions studied in this thesis relate to closed-loop stimulation strategies.

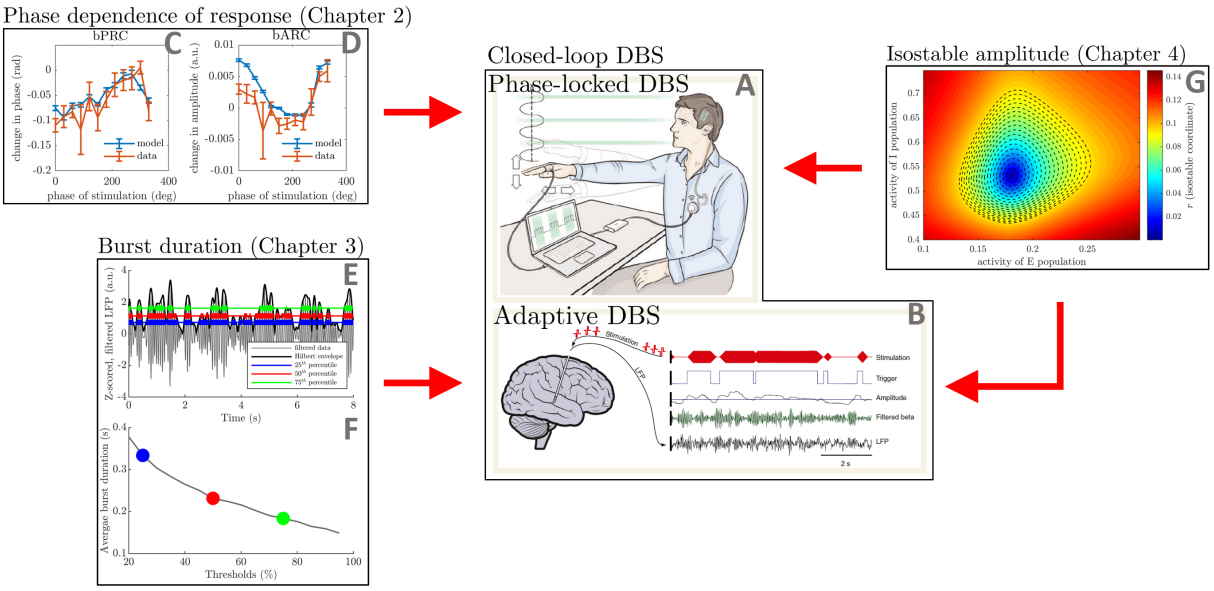

Figure 1.5: Relevance of key concepts studied in this thesis to phase-locked DBS and aDBS. Red arrows mean "has implications for". Two influential closed-loop DBS strategies are represented in panel A (adapted from Cagnan et al. 2017) and panel B (adapted from (Little et al. 2013)). In phase-locked DBS for ET (panel A), stimulation is provided according to the phase of the ongoing tremor. In aDBS for PD (panel B), stimulation is triggered when beta amplitude exceeds a threshold. The key concepts studied in Chapter 2, namely PRCs and ARCs, describe the dependence of the response to DBS on the phase of stimulation. Panels C and D show the PRCs and ARCs obtained from the block method for one patient and the corresponding model fit. The focus of Chapter 3 is average burst duration profiles (panel F), which are obtained by computing beta envelope average burst duration for a range of thresholds (panel E). Isostable amplitude is introduced in Chapter 4 (isostable amplitude field of a patient fit shown in panel G).

Publications Chapter 2 is adapted from (Duchet et al. 2020b), and Chapter 3 from (Duchet et al. 2020a). My contribution to (Weerasinghe et al. 2019), an analysis of the dependence of the response to single pulses of stimulation on tremor amplitude in patient data, is not included in this thesis.

B. Duchet, F. Ghezzi, G. Weerasinghe, G. Tinkhauser, A. A. Kuhn, P. Brown, C. Bick, and R. Bogacz (Apr. 2020a). "Average beta burst duration profiles provide a signature of dynamical changes between the ON and OFF medication states in Parkinson's disease". In: *bioRxiv*, p. 2020.04.27.064246. DOI: 10.1101/2020.04.27.064246.

B. Duchet, G. Weerasinghe, H. Cagnan, P. Brown, C. Bick, and R. Bogacz (2020b). "Phase-dependence of response curves to deep brain stimulation and their relationship: from essential tremor patient data to a Wilson–Cowan model". In: *The Journal of Mathematical Neuroscience* 10.1, p. 4. DOI: 10.1186/s13408-020-00081-0.

G. Weerasinghe, B. Duchet, H. Cagnan, P. Brown, C. Bick, and R. Bogacz (Aug. 2019). "Predicting the effects of deep brain stimulation using a reduced coupled oscillator model". In: *PLOS Computational Biology* 15.8. Ed. by J. Rubin, e1006575. DOI: 10.1371/journal.pcbi.1006575.

2

Phase-dependence of response curves to deep brain stimulation and their relationship: from essential tremor patient data to a Wilson–Cowan model

Contents

2.1 Abstract

Essential tremor manifests predominantly as a tremor of the upper limbs. One therapy option is high-frequency deep brain stimulation, which continuously delivers electrical stimulation to the ventral intermediate nucleus of the thalamus at about 130 Hz. Constant stimulation can lead to side effects, it is therefore desirable to find ways to stimulate less while maintaining clinical efficacy. One strategy, phase-locked deep brain stimulation, consists of stimulating according to the phase of the tremor. To advance methods to optimise deep brain stimulation while providing insights into tremor circuits, we ask the question: can the effects of phase-locked stimulation be accounted for by a canonical Wilson-Cowan model? We first analyse patient data, and identify in half of the datasets significant dependence of the effects of stimulation on the phase at which stimulation is provided. The full non-linear Wilson-Cowan model is fitted to datasets identified as statistically significant, and we show that in each case the model can fit to the dynamics of patient tremor as well as to the phase response curve. The vast majority of top fits are stable foci. The model provides satisfactory prediction of how patient tremor will react to phase-locked stimulation by predicting patient amplitude response curves although they were not explicitly fitted. We also approximate response curves of the significant datasets by providing analytical results for the linearisation of a stable focus model, a simplification of the Wilson-Cowan model in the stable focus regime. We report that the non-linear Wilson-Cowan model is able to describe response to stimulation more precisely than the linearisation.

2.2 Introduction

As detailed in Section 1.2.2, thalamic high-frequency DBS in ET is limited by side effects and habituation. Building on previous studies reviewed earlier (Brittain et al. 2013; Cagnan et al. 2013; Holt et al. 2016), phase-locked DBS in ET has recently been investigated to address these challenges (Cagnan et al. 2017). Hand tremor is recorded, and the reduction in energy delivered comes from stimulating

with a burst of pulses according to the phase of tremor, only once per tremor cycle rather than continuously. This way, physiological activity not phase-locked to stimulation might be relatively spared (Cagnan et al. 2013). In some patients, the strategy only requires half the energy delivered by high-frequency DBS for the same effect (Cagnan et al. 2017).

Optimising phase-locked DBS requires a detailed understanding of the phase-dependence of the response to stimulation across patients. However, data collection from phase-locked stimulation experiments has been restricted so far to small datasets because patients fatigue quickly in tremor provoking postures. While direct analysis of the data has proven insightful (Cagnan et al. 2017), modelling phase-locked stimulation would allow predictions to be made from analytic and computational studies regarding the phase-dependence of the response to stimulation, and would open the door to supplement scarcely available patient data with synthetic data. The ability to easily generate large amounts of synthetic data could come in handy to help devise and test control algorithms. It could also be useful when trying to predict an effect that, because of noise in recordings, can only be deciphered when a large number of trials is available.

We outlined in Section 1.2.1.1 that tremulous hand movements are closely related to thalamic activity (Hua et al. 1998; Hua and Lenz 2005; Pedrosa et al. 2014, and see Figure 1.1, panels B to D). It is thought that ET originates in the cerebellar-thalamic-cortical pathway (Schnitzler et al. 2009). However detailed knowledge of how ET comes about is missing, which makes simple, canonical models natural candidates to study ET. Recently, phase-locked DBS was studied using Kuramoto phase oscillators (Weerasinghe et al. 2019, reviewed in Section 1.2.3.4). However, this model does not describe interacting neural populations with distinct properties. To model neural populations, we base this chapter on the WC model introduced in Section 1.2.3.1. The architecture of the WC model can be mapped onto neural populations thought to be involved in the generation of ET, and allows for strong coupling between the populations. Additionally, stimulation can be delivered in the model to the most common stimulation site for ET, the VIM. As

highlighted before, the WC model only has a few parameters, which makes it less prone to overfitting and significantly easier to constrain than more detailed models. Moreover, the WC model has been shown to be adept at describing oscillations in PD and ET, as well as the effects of high-frequency DBS (more details in Section 1.2.3.3 and 1.2.3.4). To advance phase-locked DBS, the present work will focus on reproducing the phase-dependent effects of phase-locked DBS measured in human data in (Cagnan et al. 2017) with a WC model.

Stimulation changes the phase and the amplitude of tremor and the dependence of these changes on the phase of stimulation can be quantified by the PRC (in this study change in tremor phase as a function of tremor phase) and the ARC (in this study change in tremor amplitude as a function of tremor phase). The ARC directly measures the change in tremor, hence the change in patient handicap, but both the ARC and the PRC are important to understand the effects of phase-locked DBS and potentially optimise the stimulation pattern. We have reviewed in Section 1.2.4.3 that in dynamical systems, PRCs and ARCs have mostly been defined in the context of limit cycle models concerned with asymptotic response to infinitesimal perturbations (Winfree 2001; Brown et al. 2004; Izhikevich 2007; Guillamon and Huguet 2009; Wedgwood et al. 2013; Castejón et al. 2013). In patients, DBS stimulation is not infinitesimal, and tremor data is very variable so stimulation happens in transient states. Therefore rather than considering an asymptotic description of the changes in phase and amplitude, we will be focusing on a close variant of the experimental response curve measurement methodology applied to blocks of stimulation in (Cagnan et al. 2017), the "block method". It provides a finite time response to finite perturbations and relies on the changes in the Hilbert phase and amplitude of the tremor signal following blocks of phase-locked stimulation (more details in Section 2.3.1). The only exception to this will be in analytical derivations (Section 2.5), where a first order measurement of the response curves (i.e. measurement at the end of the stimulation period) will be used for tractability, as a simplified first approach to the model. For coherence with the experimental response curve measurement methodology, the notion of

phase and amplitude used throughout will be the Hilbert phase and amplitude or approximately equivalent. It should also be noted that we are considering population response curves and not single neuron response curves. The vast majority of best performing WC models in reproducing patient data are found in this work to give rise to stable foci, where tremor dynamics are being reproduced by adding noise to the system, so we restrict our analytical considerations to stable foci.

Starting with the data, the narrative of this chapter will be guided by the following questions. How do patient responses to phase-locked deep brain stimulation depend on phase? How do patient phase and amplitude response curves relate to one other? Can patient response curves and their relationship be described analytically in a simple linear model? Can we model patient tremor and better model response to phase-locked deep brain stimulation with a non-linear WC model? The main contributions of this chapter are as follows. We first focus on the data and analyse patient response curves, identify a subset of datasets passing appropriate statistical tests, and characterise the relationship between PRC and ARC in these patients (Section 2.3). Following the introduction of our biologically motivated WC model (Section 2.4), we derive approximate analytical expressions that delineate the response to stimulation of a 2D dynamical system described by a linearised focus, with the goals of better understanding the constraints built in the model and of providing a first level of description of the data (Section 2.5). The derived response curves are close to sinusoidal, and a relationship between them is found, revealing similarities in shape and phase shift with patients who have statistically significant PRCs and ARCs. We then show that for these patients, the WC model can be fitted to the data and can reproduce the dependence of the effects of stimulation on the phase of stimulation. The model is fitted to the PRC and can reasonably predict the ARC, and notably what is approximately the best phase to stimulate (Section 2.6). We then proceed to compare the relationship between response curves in the linearised and the full model and conclude that non-linearity is important to better reproduce the relationship found in patients (Section 2.7). Finally a discussion is provided (Section 2.8).

2.3 Patient response curves and their phase relationship

In order to assess phase-dependence of the effects of DBS in patients, we extract PRCs and ARCs from patient's tremor data, provide a statistical analysis of the response curves, and analyse their phase relationship when applicable. This data characterisation will inform our modelling approaches of the next sections, and we also introduce relevant concepts.

2.3.1 Analysis method

We extract response curves from tremor acceleration data presented in (Cagnan et al. 2017), and available as (Cagnan et al. 2019a). The experimental paradigm in (Cagnan et al. 2017) is as follows. ET patients are fitted with an accelerometer to record their tremor acceleration, and DBS locked to the phase of tremor acceleration is provided in blocks of 5 s to the VIM of the thalamus, with 1 s without stimulation between blocks. An example of one such block of stimulation is shown in Figure 2.1 in light blue, with the 1 s period without stimulation before the block highlighted in light orange (reference period). Each block targets a stimulation phase randomly selected out of 12 tremor phases (e.g. 120 degrees for the block shown in Figure 2.1). Stimulation is delivered once per period at the target phase, in the form of a burst of 4 to 6 pulses at high frequency (130 Hz or higher). By burst we mean in this chapter a quick succession of stimulation pulses (not to be confused with the bursts of beta activity studied in Chapter 3). Details of the pulses making up a burst can be seen in the zoomed-in insert in Figure 2.1. Tremor frequency being around 5 Hz and stimulation blocks lasting 5 s, there are about 25 bursts of stimulation at the same target phase per stimulation block. There are about 10 trials available per phase bin so about 120 stimulation blocks per patient (12 phase bins times around 10 trials per phase). The method described in (Cagnan et al. 2017) to obtain patient's response curves was specifically developed for this type of data, and we closely follow it and provide additional statistical analysis of the phase-dependence. We refer to our version of the method as the "block method" and denote the response

curves obtained by bPRC and bARC, "b" standing for block. More specifically, we define the bPRC and the bARC according to the following procedure.

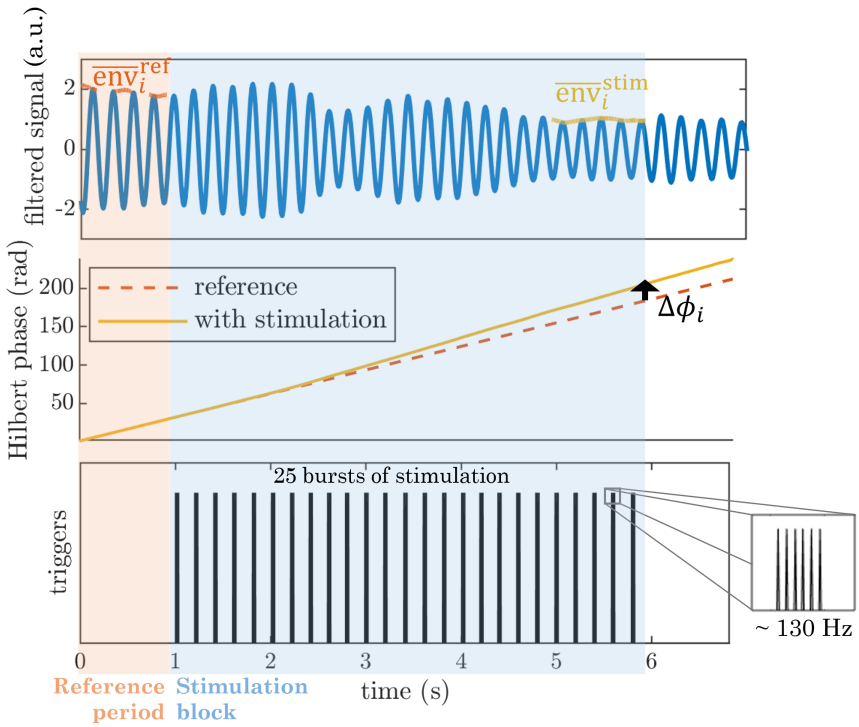

Figure 2.1: Example showing the block method applied to a block of stimulation. The three panels share the same horizontal axis. The reference period without stimulation before the block is highlighted in light orange, and the stimulation block itself in light blue. The filtered tremor is shown in blue in the upper panel. Stimulation triggers are shown in black in the lower panel and are provided at the same target phase of the tremor. The 25 bursts of stimulation are each composed of a number of individual pulses at high frequency as shown in the zoomed-in insert. As shown in the middle panel, the change in phase $\Delta\phi_i$ due to the block of stimulation is obtained by comparing at the end of the block the actual Hilbert phase to a linear phase obtained by a straight line fit to the phase evolution 1 s before the block (reference period). The change in amplitude is given by the difference between the means $\overline{\text{env}}_i^{\text{stim}}$ and $\overline{\text{env}}_i^{\text{ref}}$ (top panel). Both the phase and amplitude responses are later normalised by the number of pulses in the block (not shown here).

The dominant axis tremor acceleration recordings are bandpass-filtered (4 Hz band encompassing the patient tremor frequency content) and z-scored. The filter used is a Butterworth second order filter, which provides a maximally flat response in the passband (Butterworth 1930). Because this study focuses on phase, we perform zero-phase filtering by applying our filter in the forward and backward directions to avoid phase distortions. Since the resulting signal is narrow-band,

the instantaneous phase $\phi(t)$ and amplitude $\text{env}(t)$ are obtained as the Hilbert phase and amplitude of the processed tremor acceleration. The Hilbert phase and amplitude have been introduced in Sections 1.2.4.2 and 1.2.4.1, respectively.

Obtaining the change in phase (bPRC) For each block (we index blocks by the subscript i), a straight line $\widehat{\phi}_i^{\text{ref}}(t)$ is fitted to the evolution of the Hilbert phase $\phi_i(t)$ during the 1 s period without stimulation before the block (reference period, see middle panel in Figure 2.1). The change in phase $\Delta\phi_i$ due to block i is given by the difference between the actual Hilbert phase at the end of the block and the phase of the fitted reference line evaluated at the end of the block (see middle panel in Figure 2.1), i.e.

$$\Delta\phi_i = \phi_i(t_i^{\text{end}}) - \widehat{\phi}_i^{\text{ref}}(t_i^{\text{end}}), \tag{2.1}$$

where t_i^{end} is the time of the end of block i. This phase response is divided by the number of pulses in blocks n_{pulses} (on the basis of 4 pulses per burst for patient 4R and 4L, and 6 pulses per burst for the rest), which gives an average response for one pulse. The target phase at which the closed-loop stimulation system aims to deliver stimulation is known for each block. However, phase tracking not being perfect, the actual Hilbert phase at which stimulation occurred is determined for each burst of stimulation as the circular mean of the Hilbert phase during the burst (unlike in the original study, Cagnan et al. 2017, where target phase is directly used). We take the circular mean of these burst angles for a given block as the actual mean phase of stimulation for the block, and denote it Φ_i^{stim} for block i. These values are then binned into 12 phases bins, and the change in phase is averaged within bins to obtain the bPRC. Put another way,

$$\text{bPRC}(\Phi_j^{\text{bin}}) = \frac{1}{n_{\text{pulses}} n_{\text{bin}_j}} \sum_{\Phi_i^{\text{stim}} \in \text{bin}_j} \Delta\phi_i, \tag{2.2}$$

where Φ_j^{bin} is the center phase of bin j, and n_{bin_j} is the number of blocks with Φ_i^{stim} falling in bin_j.

Obtaining the change in amplitude (bARC) For each block i, the change in amplitude Δenv_i is given by the difference between the mean of the Hilbert amplitude during the last second of the block $\overline{\text{env}}_i^{\text{stim}}$ and the mean of the Hilbert amplitude during the one second without stimulation before the block $\overline{\text{env}}_i^{\text{ref}}$ (see top panel in Figure 2.1).

$$\Delta\text{env}_i = \overline{\text{env}}_i^{\text{stim}} - \overline{\text{env}}_i^{\text{ref}}. \tag{2.3}$$

Similarly to the change in phase, this amplitude response is divided by the number of pulses in the block, and averaged across blocks in the same phase bin to obtain the bARC. Explicitly, we have

$$\text{bARC}(\Phi_j^{\text{bin}}) = \frac{1}{n_{\text{pulses}} n_{\text{bin}_j}} \sum_{\Phi_i^{\text{stim}} \in \text{bin}_j} \Delta\text{env}_i. \tag{2.4}$$

Measuring response curves significance and PRC-ARC phase shift In order to identify significant patient's response curves, we performed two statistical analyses. First, bPRCs and bARCs were tested for a main effect of phase by means of a Kruskal-Wallis ANOVA (12 phase bins) to differentiate patients' response curves that may be dominated by noise (which could be due to a lack of phase-dependent response or our inability to measure it, possibly because of an insufficient amount of data). Second, since we are expecting response curves to have a dominant first harmonic as mentioned in Section 1.2.2.2, the cosine model $y = c_1 + |c_2|\cos(x + c_3)$ was fitted to patients' phase response and amplitude response curves. We assessed via F-tests whether the cosine model was better at describing the data than a horizontal line at the mean ($y = c_1$, where c_1 is the mean change in phase or the mean change in amplitude). Including the less specific ANOVA test allows for more generality, as we do not wish to exclude patients with significant, but non-sinusoidal response curves. On the other hand, the cosine test is more likely to detect phase-dependent effects of stimulation in patients which indeed have sinusoidal response curves. We therefore define the following criterion for selection of a patient for further study in the rest of the chapter.

Significance criterion: *having both bPRC and bARC deemed significant under FDR control (see below) by at least one of the two tests – ANOVA test for a main effect of phase or cosine model F-test.*

In both cases, we address the multiple testing problem by controlling the false discovery rate (FDR) at 5%, which guarantees that the expectation of the number of false positives over the total number of positives is less than 5%. Because of the high number of rejections of the null hypotheses compared to the number of tests (5 out of 12 for the ANOVA, 6 out of 12 for the F-test, see Table 2.1), the total number of tests is a very poor estimator of the number of true null hypotheses, which is needed when controlling the FDR. Instead, we used a better estimator $\hat{m}_0$ of the number of true null hypothesis given by Storey et al. (Storey et al. 2004) which we take as

$$\hat{m}_0 = \frac{m + 1 - r_{5\%}}{1 - 5\%}, \tag{2.5}$$

where m is the total number of tests and $r_{5\%}$ is the number of rejections at the 5% confidence level (without FDR control). Based on this estimator, we applied the adaptive linear step-up FDR control procedure (reviewed in Benjamini et al. 2006).

Additionally, in datasets where both bPRC and bARC are significant according to the cosine F-test, the relationship between bPRC and bARC is quantified by the shift in phase between the cosine model fits to the bPRC and the bARC. In these datasets, the PRC-ARC shift between the bPRC and bARC is calculated as

$$\phi_{PRC} - \phi_{ARC} \equiv c_3^{\mathrm{PRC}} - c_3^{\mathrm{ARC}} \pmod{2\pi}, \tag{2.6}$$

with $\phi_{PRC} - \phi_{ARC} \in [0, 2\pi)$. Calculating a PRC-ARC shift in other cases is not meaningful. The PRC-ARC phase shift is an important quantity. Indeed, for PRCs and ARCs with a dominant first harmonic (close to sine curves), the ARC will be close to a scaled version of the PRC shifted in phase. The extent of the shift is given by the PRC-ARC phase shift. In other words, the minimum of the ARC (best phase to stimulate) will be at the minimum of the PRC plus the PRC-ARC shift. The shift highlights the difference in the phases of maximum sensitivity of the system in terms of its phase response and in terms of its amplitude response.

As we will see later, the PRC-ARC shift will be a key differentiator between the non-linear WC model and its linearisation in terms of their ability to describe the effects of phase-locked stimulation seen in data.

2.3.2 Results of the analysis

Analysing six datasets from the five patients included in (Cagnan et al. 2019a) (datasets 4R and 4L are for the right and left upper limbs of the same patient) shows that half of the datasets satisfy our significance criterion. bPRCs and bARCs obtained are shown in Supplementary Figure A.2 in Appendix A.9, and results of the statistical tests are presented in Table 2.1. Based on the significance criterion defined in the previous section, patients 1, 5 and 6 are selected for further study, as both their bPRCs and bARCs are found significant by the cosine F-test under FDR control. We note that patient 5 also has both his response curves deemed significant by the ANOVA test under FDR control. Response curves corresponding to datasets meeting our significance criterion are highlighted in green in Supplementary Figure A.2). Datasets 3, 4R and 4L do not satisfy our significance criterion. In other words, for both tests, an effect of stimulation phase could not be found in at least one of their response curves (in most cases for both response curves, as

Patient	Type	ANOVA p-value	F-test p-value
1 **	bPRC	**0.0113**	**0.00993**
	bARC	0.1733	**0.0365**
3	bPRC	0.1097	0.448
	bARC	0.1591	0.500
4R	bPRC	0.3463	0.581
	bARC	0.2064	0.057
4L	bPRC	0.2895	0.352
	bARC	**0.0077**	0.200
5 **	bPRC	**4.925e-04**	**0.00906**
	bARC	**4.012e-06**	**0.00142**
6 **	bPRC	**4.815e-04**	**0.0122**
	bARC	0.0527	**0.0341**

Table 2.1: P-values of both statistical tests performed on patients' response curves: Kruskal-Wallis ANOVAs testing a main effect for phase in patients' response curves (third column), and cosine model F-tests (fourth column). P-values in bold are deemed significant with FDR control at the 5% level (separate FDR analyses per test type, $\hat{m}_0 \approx 8.42$ for the ANOVAs and $\hat{m}_0 \approx 7.37$ for the F-tests). Double stars indicate datasets satisfying our significance criterion as defined in Section 2.3.1.

seen in Table 2.1). In Figure 2.2, the PRC-ARC shift $\phi_{PRC} - \phi_{ARC}$ is plotted for patients for whom the cosine model was deemed significant in describing both their bPRC and bARC (which happens to be the same subset as patients satisfying our significance criterion). Figure 2.2 shows that the PRC-ARC shift in significant datasets is in $\left[\frac{\pi}{2}, \pi\right]$, patients 5 and 6 being quite close to $\frac{\pi}{2}$.

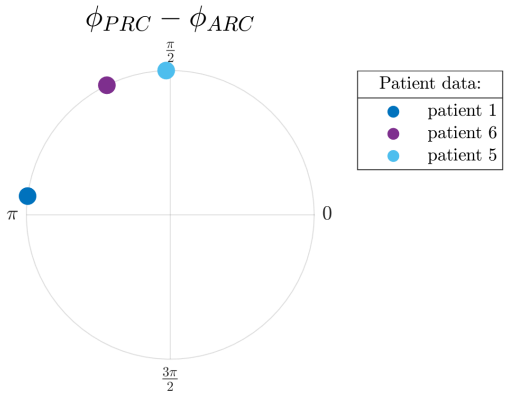

Figure 2.2: PRC-ARC shift in patients. Only showing patients with significant cosine model F-test for bPRC and bARC under FDR control. The calculated PRC-ARC shifts are in $\left[\frac{\pi}{2}, \pi\right]$.

2.4 Implementation of the Wilson Cowan model for essential tremor DBS

To model the experimental data described in the previous section, in particular the shape of the response curves and the PRC-ARC shift, we use a version of the WC model introduced in Section 1.2.3.1. Specifically, we map a two-population WC model without delays as described in (Onslow et al. 2014) onto the connectivity structure of the thalamus (Figure 2.3). The circuit we are about to describe is a good candidate, but not the only biologically plausible mapping of an excitatory/inhibitory loop in the context of tremor. In our candidate mapping, the VIM is modelled as an excitatory population, connected to an inhibitory population of the thalamus, the reticular nucleus (nRT). We model tremor by the activity of the excitatory population, and this is justified by the high coherence between ventral thalamic activity and electromyographic recording of the contralateral wrist flexors (Hua et al.

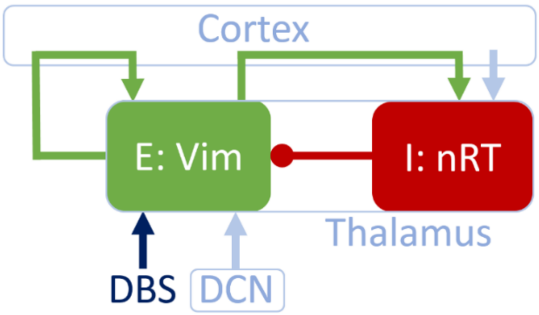

Figure 2.3: The WC model can describe the populations thought to be involved in the generation of ET. The excitatory population E and the inhibitory population I model respectively the VIM and the nRT of the thalamus. Arrows denote excitatory connections or inputs, whereas circles denote inhibitory connections. The VIM is the target of DBS and also receives an input from the DCN. The self-excitatory loop of the VIM, as well as the excitatory connection from VIM to nRT are via cortex.

1998; Hua and Lenz 2005; Pedrosa et al. 2014). The VIM and nRT are reciprocally connected (the excitatory projections from VIM to nRT are via cortex). The VIM receives a constant input from the deep cerebellar nuclei (DCN) and is part of a self-excitatory loop via cortex. The nRT receives a constant cortical input. We add Gaussian white noise to this two-population WC, and the activity of the VIM, E, and the activity of the nRT, I, are described by the stochastic differential equations

$$\begin{cases} dE = F_1(E,I)dt + \zeta dW_E, \\ dI = F_2(E,I)dt + \zeta dW_I, \end{cases} \tag{2.7}$$

where dW_E and dW_I are Wiener processes, and ζ the noise standard deviation. We define

$$F_1(E,I) = \frac{1}{\tau}\left(-E + f(\theta_E + w_{EE}E - w_{IE}I)\right),$$
$$F_2(E,I) = \frac{1}{\tau}\left(-I + f(\theta_I + w_{EI}E)\right),$$

with w_{PR} the weight of the projection from population "P" to population "R", θ_P the constant input to population "P", τ a time constant (assumed to be the same for both populations to reduce the number of model parameters), and f the sigmoid function introduced in Section 1.2.3.1 and parametrized by a steepness parameter β. Because the VIM is the most common target of DBS for ET, we model stimulation as a direct increase in E. Analytical expressions for response

curves are out of reach for the full non-linear model, which is why we study next a linearisation of a deterministic stable focus model to approximate the full model response, and get a better understanding of the shape of its phase response curves and their relationship. This will provide a first level of description of the data.

2.5 Response curves and their relationship in a focus model

This section aims to provide a basis for understanding how the effects of stimulation on phase and amplitude are coupled in the WC model, and for comparison with experimental data. We therefore derive approximate analytical expressions for the first order phase and amplitude responses to one pulse of stimulation in the linearisation of a 2D dynamical system described by a (stable) focus. Such a linearisation can be applied to the deterministic WC model given by equation (2.7) with $\zeta = 0$ in the focus regime. We follow the previous section in modelling the tremor signal as the first coordinate of the dynamical system, and in providing stimulation pulses along the first dimension.

2.5.1 Linearisation of a focus

To distinguish scalars and vectors more easily, vectors will be denoted in bold. Let $\dot{\mathbf{Z}} = F(\mathbf{Z})$ be a dynamical system, where $\mathbf{Z} \in \mathbb{R}^2$ and F is differentiable. The Jacobian of F is

$$J = \begin{bmatrix} \frac{\partial F_1}{\partial Z_1} & \frac{\partial F_1}{\partial Z_2} \\ \frac{\partial F_2}{\partial Z_1} & \frac{\partial F_2}{\partial Z_2} \end{bmatrix}. \tag{2.8}$$

Let $\mathbf{Z}^*$ be a fixed point of F. If it is hyperbolic, the dynamics of $\mathbf{X} = \mathbf{Z} - \mathbf{Z}^*$ are approximated in the vicinity of the equilibrium $\mathbf{X} = \mathbf{0}$ by the linear equation

$$\dot{\mathbf{X}} = J(\mathbf{Z}^*)\mathbf{X} \tag{2.9}$$

where $J(\mathbf{Z}^*)$ is the Jacobian evaluated at the fixed point. We will treat the case of Jacobians having complex conjugate eigenvalues $\lambda_\pm = \sigma \pm i\omega$. In particular, we are interested in stable hyperbolic foci, which imply $\sigma < 0$ and $\omega > 0$. The

WC model can operate in that regime (Borisyuk and Kirillov 1992; Onslow et al. 2014). The nonhyperbolic case of the linearisation having purely imaginary complex conjugate eigenvalues will also be described for didactic purposes, although it is of little interest for patient fits. If $\mathbf{k} = \mathbf{a} + i\mathbf{b}$ is the right eigenvector associated with λ_+, and K and K' coefficients determined according to initial conditions, the general real valued solution of (2.9) reads

$$\mathbf{X}(t) = \{K(\mathbf{a}\cos\omega t - \mathbf{b}\sin\omega t) + K'(\mathbf{a}\sin\omega t + \mathbf{b}\cos\omega t)\}e^{\sigma t}. \tag{2.10}$$

We will be using the following notations for the coordinates of the eigenvector:

$$\mathbf{k} = \begin{bmatrix} a_1 + ib_1 \\ a_2 + ib_2 \end{bmatrix}. \tag{2.11}$$

Equation (2.10) and what follows are not valid in the case of real eigenvalues, which are of no interest for our purposes (no rotation).

2.5.2 Phase definition

The notion of phase is central to phase-locked stimulation, and in this section we define phase in a way that is approximately equivalent to the Hilbert phase. Because the Hilbert phase is widely used to analyse experimental data (see review in Section 1.2.4.2) including in (Cagnan et al. 2017), we are relying on the Hilbert phase in the other sections of this chapter to make meaningful predictions. This is the reason why we choose in our linearised system a phase definition approximately equivalent to the Hilbert phase. We define a phase as $\phi = \omega t$ with a zero phase point defined as the maximum of $X_1(t)$ (similarly to the Hilbert phase), which is therefore on the nullcline of the first coordinate. This phase definition is different from other common definitions in dynamical systems such as the trajectory polar angle in the phase plane of a 2D system, or isochronal (asymptotic) phase (see review in Section 1.2.4.2). We demonstrate next that it is very close to the Hilbert phase of X_1 for slow decay compared to the rotation (this condition is verified in patient fits presented in Section 2.6.2, see Supplementary Table A.2). It should be noted that this is generally only true for the linearisation. As the Hilbert

phase is also the phase definition used in the other sections of this chapter, the following proof ensures consistency.

We now establish equivalence of our phase definition with the Hilbert phase of X_1. Recall that we denote the Hilbert transform by $\mathcal{H}$. The Hilbert phase of X_1 is given by

$$\phi^{Hilbert} = \arctan \frac{\mathcal{H}(X_1(t))}{X_1(t)}. \tag{2.12}$$

A first step is to calculate the Hilbert transform of the signal $X_1(t)$. The Hilbert transform is a linear operator, and $X_1(t)$ is a linear combination of $s(t)s_c(t)$ and $s(t)s_n(t)$ with $s(t) = e^{\sigma|t|}$, $s_c(t) = \cos\omega t$, and $s_n(t) = \sin\omega t$ (see equation (2.10)). We show in Appendix A.1 that the Hilbert transform $\mathcal{H}(s(t)s_j(t))$ can be approximated by $s(t)\mathcal{H}(s_j(t))$ for $j = c, n$. The Hilbert phase of X_1 is therefore given by

$$\phi^{Hilbert} = \arctan \frac{\mathcal{H}(X_1(t))}{X_1(t)} \approx \arctan \frac{\sqrt{\alpha^2+\beta^2}\sin\left(\omega t - \arctan\frac{\alpha}{\beta}\right)}{\sqrt{\alpha^2+\beta^2}\sin\left(\omega t + \frac{\pi}{2} - \arctan\frac{\alpha}{\beta}\right)}, \tag{2.13}$$

where

$$\alpha = K'a_1 - Kb_1,$$
$$\beta = Ka_1 + K'b_1.$$

Using trigonometric identities, we obtain

$$\phi^{Hilbert} \approx \omega t - \arctan\frac{\alpha}{\beta}. \tag{2.14}$$

In our setting, trajectories start at $t = 0$ at the maximum of $X_1(t)$, and we have $\frac{\alpha}{\beta} = -\frac{\sigma}{\omega}$ (immediate with the coefficients of the reference trajectory K_{ref} and K'_{ref} introduced in equation (2.15) and given in Appendix A.2). Hence if $\omega \gg |\sigma|$, equation (2.14) yields $\phi^{Hilbert} \approx \omega t$, which matches with our definition of phase ϕ (including our choice of zero-phase reference).

2.5.3 Reference trajectory and stimulated trajectory

In order to calculate first order response curves for our phase definition, we will consider a reference trajectory without stimulation, and a trajectory that underwent an instantaneous stimulation pulse δX_1 at a stimulation phase ϕ_0. The effects of stimulation on phase and amplitude will be measured at the next maximum of X_1 for both trajectories. We will denote these hPRC$^{(1)}$ and hARC$^{(1)}$ as they are first order responses based on a phase definition approximately equivalent to the Hilbert phase. A sketch of the method is provided in Figure 2.4.

Expressions for the coefficients K_{ref} and K'_{ref} of the reference trajectory are derived in Appendix A.2. We want to study the effects of stimulating at phase ϕ_0. The point of stimulation $\mathbf{X^{1^-}}$ at phase ϕ_0 is expressed as

$$\mathbf{X^{1^-}} = \left\{ K_{ref} \left(\mathbf{a} \cos \phi_0 - \mathbf{b} \sin \phi_0 \right) + K'_{ref} \left(\mathbf{a} \sin \phi_0 + \mathbf{b} \cos \phi_0 \right) \right\} e^{\sigma \frac{\phi_0}{\omega}}. \tag{2.15}$$

An instantaneous stimulation δX_1 is applied at $\mathbf{X^{1^-}}$ as

$$\mathbf{X^{1^+}} = (X_1^{1^+}, X_2^{1^+}) = (X_1^{1^-} + \delta X_1, X_2^{1^-}). \tag{2.16}$$

The trajectory after stimulation is still constrained by the dynamics given by equation (2.10), which allows for expressions for the coefficients on this new trajectory K_{stim} and K'_{stim} to be found (see Appendix A.3). To measure the change in phase and amplitude between the next peaks of the stimulated trajectory and the reference trajectory, the phase of the next maximum of the first coordinate on the stimulated trajectory X_1^{stim} is needed. We denote this phase $\phi_{max} + 2\pi$, and a derivation for ϕ_{max} is provided in Appendix A.4. The phase of the next maximum of X_1 on the reference trajectory will also be used and is simply 2π.

2.5.4 Phase response

The first order phase response curve can be calculated based on the reference trajectory period T_0 and the stimulated trajectory period T_{stim}, which is given by

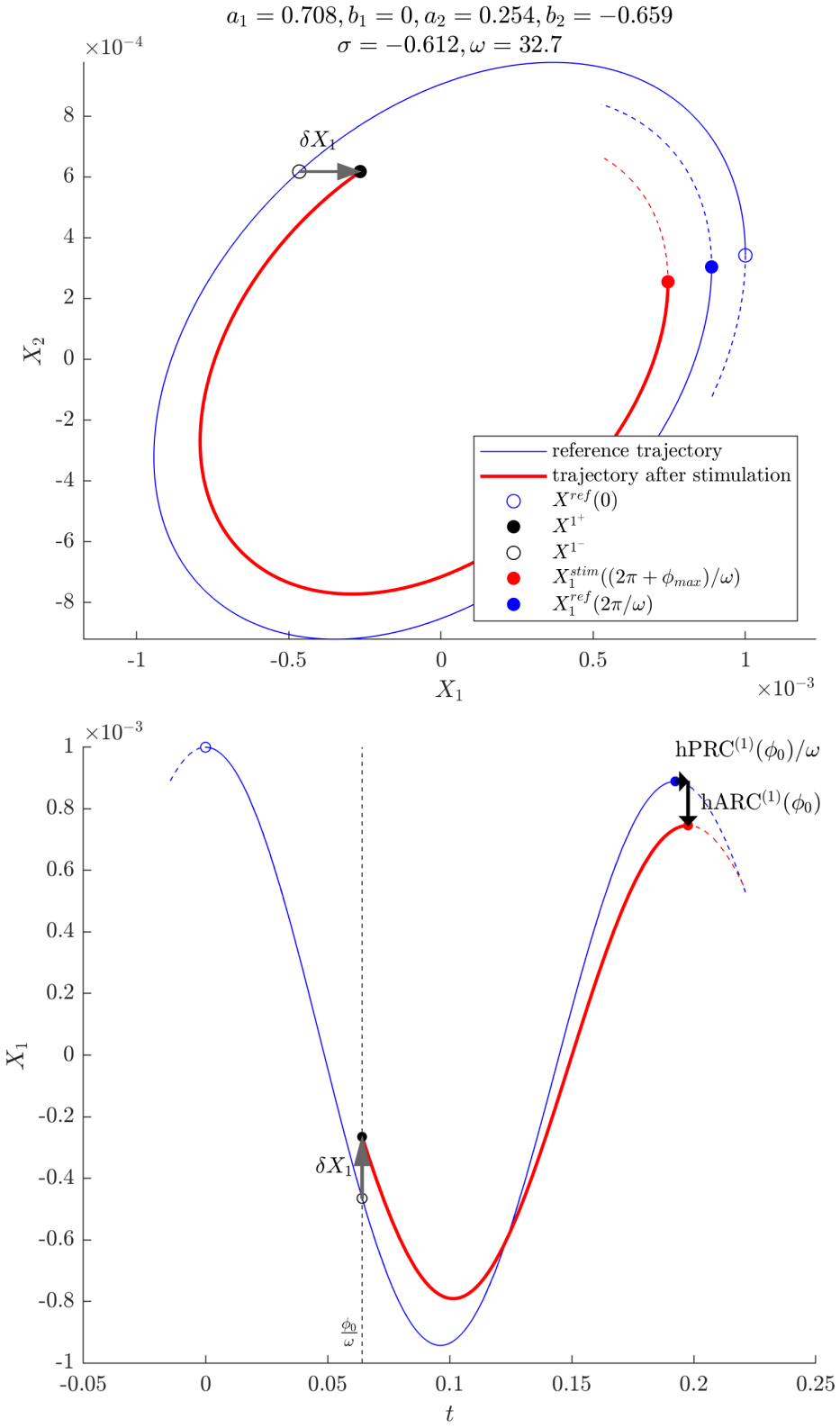

Figure 2.4: Illustration of the approach taken to derive expressions for the phase and amplitude responses in the linearisation of a 2D focus model. Top: phase plane, bottom: time-series of X_1. The tremor is modelled by X_1, and the stimulation δX_1 is applied to X_1. The system shown corresponds to the linearised fit of patient 1 as described in Section 2.7.1.

the sum of the time spent on the reference trajectory before stimulation and the time spent on the new trajectory after stimulation:

$$T_0 = \frac{2\pi}{\omega},$$
$$T_{stim} = \frac{(\phi_0 - 0) + (2\pi + \phi_{max} - \phi_0)}{\omega} = \frac{2\pi + \phi_{max}}{\omega}.$$

For a phase response curve in radian, we obtain

$$\text{hPRC}^{(1)}(\phi_0) = 2\pi \frac{T_0 - T_{stim}}{T_0} = -\phi_{max}(\delta X_1), \tag{2.17}$$

where the phase ϕ_{max} depends on the stimulation magnitude δX_1 (see equation (2.16)). The dependency enters through K_{stim} and K'_{stim} (see equation (A.17) in Appendix A.4 and equations (A.13) and (A.15) in Appendix A.3). A Taylor expansion around $\delta X_1 = 0$ yields, to lowest order in δX_1 (for weak stimulation),

$$\text{hPRC}^{(1)}(\phi_0) \approx \frac{\delta X_1}{X_1^0} \left(A \cos\phi_0 - B \sin\phi_0\right) C e^{-\sigma \frac{\phi_0}{\omega}} \tag{2.18}$$

with

$$A = (a_1 a_2 + b_1 b_2)\omega - (a_1 b_2 - a_2 b_1)\sigma,$$
$$B = (a_1 b_2 - a_2 b_1)\omega + (a_1 a_2 + b_1 b_2)\sigma,$$
$$C = \frac{\omega}{(\omega^2 + \sigma^2)(a_1 b_2 - a_2 b_1)}.$$

Although we are omitting the amplitude dependence in our notations for convenience in equations (2.17) and (2.18), the first order PRC is found to be proportional to the inverse of X_1^0 (the peak amplitude of the oscillations at the beginning of the stimulation period). It is also directly proportional to the stimulation amplitude δX_1, and directly depends on phase via sinusoidal functions and a factor related to the decay. But unlike in the cosine test (Section 2.3), no assumption was made on a dominant first harmonic in our derivation. The constants A, B, and C only depend on the real and imaginary parts of the eigenvalue λ_+ (decay and rotation) and the associated eigenvector $\mathbf{k}$. We note that $a_1 b_2 - a_2 b_1$ cannot be zero (otherwise the trajectory would be constrained to a straight line).

2.5.5 Amplitude response

For our purposes we are interested in the amplitude of the first coordinate, and the first order ARC is obtained as the difference in first coordinates between the stimulated and the reference trajectories evaluated at their respective next peak after stimulation. It should be noted this is approximately equivalent to a first order change in Hilbert amplitude, at least for $\omega \gg |\sigma|$. The first order ARC is calculated as

$$\mathrm{hARC}^{(1)}(\phi_0) = X_1^{stim}\left(\frac{2\pi + \phi_{max}(\delta X_1)}{\omega}\right) - X_1^{ref}\left(\frac{2\pi}{\omega}\right). \tag{2.19}$$

A Taylor expansion around 0 yields, to lowest order in δX_1,

$$\mathrm{hARC}^{(1)}(\phi_0) \approx \delta X_1 \left(\cos\phi_0 + D\sin\phi_0\right) e^{-\sigma\frac{\phi_0 - 2\pi}{\omega}} \tag{2.20}$$

with

$$D = \frac{a_1a_2 + b_1b_2}{a_1b_2 - a_2b_1}.$$

Interestingly, the first order ARC close to the fixed point does not depend on the amplitude of the oscillations X_1^0. As expected, the first order ARC is directly proportional to the stimulation amplitude δX_1. Similarly to the first order PRC, it directly depends on phase via sinusoidal functions and a factor related to the decay, and the constant D only depends on $\mathbf{k}$. The obvious similarities between the first order PRC and ARC suggest there may be a relationship between the two.

2.5.6 Relationship between first order PRC and ARC

We seek a relationship involving the derivative of the first order PRC, which, based on equation (2.18), is given by

$$-\frac{d\mathrm{hPRC}^{(1)}(\phi_0)}{d\phi_0} \approx \frac{\delta X_1}{F X_1^0}(\cos\phi_0 + G\sin\phi_0)e^{-\sigma\frac{\phi_0 - 2\pi}{\omega}} \tag{2.21}$$

with

$$F = \frac{(a_1b_2 - a_2b_1)(\omega^2 + \sigma^2)}{(a_1b_2 - a_2b_1)(\omega^2 - \sigma^2) + 2(a_1a_2 + b_1b_2)\omega\sigma} e^{\frac{2\pi\sigma}{\omega}},$$
$$G = \frac{(a_1a_2 + b_1b_2)(\omega^2 - \sigma^2) - 2(a_1b_2 - a_2b_1)\omega\sigma}{(a_1b_2 - a_2b_1)(\omega^2 - \sigma^2) + 2(a_1a_2 + b_1b_2)\omega\sigma}.$$

For $\omega \gg |\sigma|$, we have

$$F = \frac{(a_1b_2 - a_2b_1)\left(1 + \left(\frac{\sigma}{\omega}\right)^2\right)}{(a_1b_2 - a_2b_1)\left(1 - \left(\frac{\sigma}{\omega}\right)^2\right) + 2\left(a_1a_2 + b_1b_2\right)\frac{\sigma}{\omega}} e^{\frac{2\pi\sigma}{\omega}} \approx 1 - 2(D - \pi)\frac{\sigma}{\omega} \approx 1,$$

$$G = \frac{(a_1a_2 + b_1b_2)\left(1 - \left(\frac{\sigma}{\omega}\right)^2\right) - 2(a_1b_2 - a_2b_1)\left(\frac{\sigma}{\omega}\right)}{(a_1b_2 - a_2b_1)\left(1 - \left(\frac{\sigma}{\omega}\right)^2\right) + 2(a_1a_2 + b_1b_2)\left(\frac{\sigma}{\omega}\right)} \approx D - 2(1 + D^2)\frac{\sigma}{\omega} \approx D.$$

Therefore in that case the first order ARC is approximately the opposite of the derivative of the first order PRC scaled by the peak amplitude at the beginning of the stimulation period (in general, the scaling factor is FX_1^0):

$$-X_1^0 \frac{d\text{hPRC}^{(1)}(\phi_0)}{d\phi_0} \approx \text{hARC}^{(1)}(\phi_0). \tag{2.22}$$

For a slow decay compared to the rotation, the PRC-ARC shift in the linearisation of a focus will therefore be close to $\frac{\pi}{2}$, which is the value observed for patient 5 (see Figure 2.2). A detailed analysis of the PRC-ARC shift in the model is provided in Section 2.7.

2.5.7 Applications to simple systems

We turn to simple examples of linear systems to illustrate the results of the previous sections, in particular how the strength of the decay affects the sinusoidal character of the response curves and the PRC-ARC shift, and how a tilted ellipsoid flow impacts the response curves. Additionally, links to the WC model are provided when possible. In what follows, response curves are given for $\delta X_1 = 2 \times 10^{-4}$ and $X_1^0 = 10^{-3}$, X_1^0 being a maximum of X_1 as a function of time (these only act as scaling factors of the response curves and will not change their shape).

Circular flow without decay As an introductory example, let us consider a simple circular flow for which the J matrix is

$$J_{circ} = \begin{bmatrix} 0 & -1 \\ 1 & 0 \end{bmatrix}.$$

The eigenvalues of J_{circ} are $\pm i$ so the results of the previous sections can be applied. Equations (2.18) and (2.20) are plotted for this system with our choice of δX_1

and X_1^0. The result for the first order PRC is shown in Figure 2.5, panel A2, and for the first order ARC in panel A3. For this system, $\sigma = 0$, and $\text{hPRC}^{(1)}$ is simply the opposite of a sine, $\text{hARC}^{(1)}$ simply a cosine. Moreover, $G = D$ (see Section 2.5.6) and equation (2.22) is exact, as exemplified in Figure 2.5, panel A3. The amplitude response curve $\text{hARC}^{(1)}$ is obtained by only scaling the derivative of $\text{hPRC}^{(1)}$ by $-X_1^0$ as $a_2 = b_1 = 0$ and $F = 1$. Note that WC parameters for which the system's Jacobian at the fixed point is J_{circ} cannot be found as the second diagonal term cannot be 0, at least in the version of the WC model used in this work (see equation (A.20) in Appendix A.5).

Circular flow with decay We can introduce a slow decay (Figure 2.5, panel B) and then a fast decay (Figure 2.5, panel C) in the circular flow. We choose the J matrices

$$J_{circ}^{slow} = \begin{bmatrix} -5\times10^{-3} & -1 \\ 1 & -5\times10^{-3} \end{bmatrix}, \qquad J_{circ}^{fast} = \begin{bmatrix} -2\times10^{-1} & -1 \\ 1 & -2\times10^{-1} \end{bmatrix}.$$

The slow decay leads to a scaling factor $F \approx 1$, and the approximation of equation (2.22) is very good, as $\omega \gg |\sigma|$ (see Figure 2.5, panel B3, close match of the ARC and the scaled derivative of the PRC, hence a shift close to $\frac{\pi}{2}$). The case of the fast decay corresponds to $\omega = 5|\sigma|$. The first order PRC and ARC no longer look like pure sinusoids and the approximation relating the response curves is less accurate ($\omega = 200|\sigma|$, see Figure 2.5, panel C3), highlighting a shift different from $\frac{\pi}{2}$. It is also more obvious that the first order response curves are not periodic due to the measurement of the changes in phase and amplitude at the end of the stimulation period. It is possible to find WC parameters for which the system's Jacobian at the fixed point is J_{circ}^{slow} or J_{circ}^{fast}. How such parameters are found is explained in Appendix A.5, and the results are presented in Supplementary Table A.1 in Appendix A.10. In both cases, $w_{IE} = w_{IE}$, and $w_{EE} = 0$.

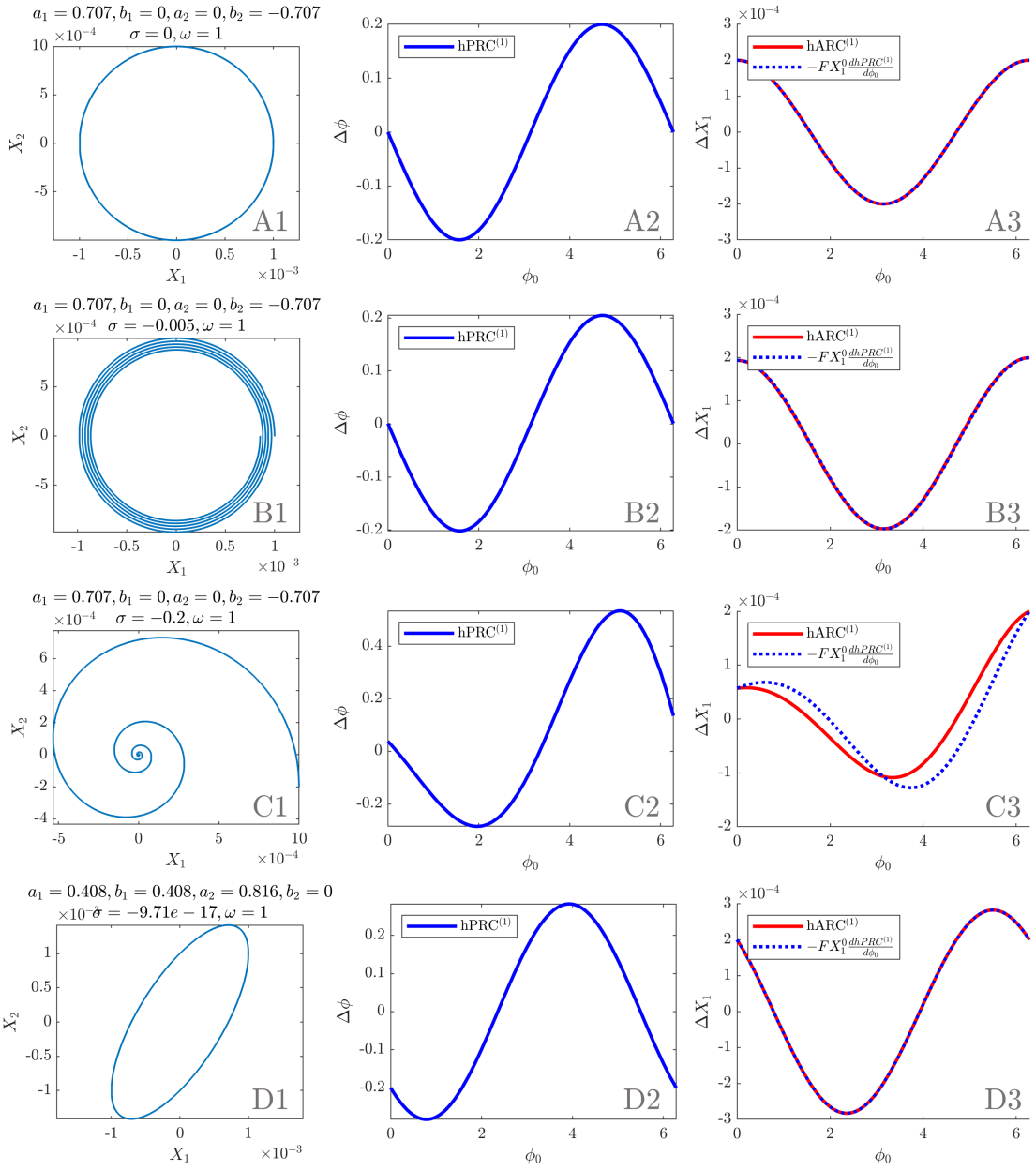

Figure 2.5: Analytical results in simple systems (initial conditions as in the main text). First column: phase space. Second column: first order PRC as per equation (2.18) (scaling valid for the first cycle). Third column: first order ARC as per equation (2.20) and opposite of the derivative of the first order PRC scaled by FX_1^0. Panel A corresponds to J_{circ} (circular flow, no decay), panel B to J_{circ}^{slow} (circular flow, slow decay), panel C to J_{circ}^{fast} (circular flow, fast decay), and panel D to J_{ellip} (tilted elliptic flow, no decay).

Tilted elliptic flow without decay The tilted elliptic flow without decay of Figure 2.5, panel D, corresponds to the J matrix

$$J_{ellip} = \begin{bmatrix} 1 & -1 \\ 2 & -1 \end{bmatrix}.$$

The first order PRC and ARC are sums of a sine and a cosine, which brings a horizontal shift in phase for both curves compared to a circular flow without decay. The eigenvalues are still purely imaginary, but F is no longer one. Because $\sigma = 0$, the relationship of equation (2.22) is still exact (see Figure 2.5, panel D3). It is possible to find WC parameters for which the system's Jacobian at the fixed point is J_{ellip} (see Supplementary Table (A.1) in Appendix A.10). Patient fits fall in the category of (potentially tilted) elliptic flows with decay, and will be dealt with in Section 2.7.1.

For a slow decay compared to the rotation, the linearised stable focus model exhibits close to sinusoidal response curves and a PRC-ARC shift close to $\frac{\pi}{2}$ as shown by equation (2.22). This is verified in Figure 2.5, as the scaled first order PRC derivatives very closely match the corresponding ARCs (except in panel C where the decay is fast). When contrasted with patient data (response curves passing the cosine model F test and PRC-ARC shifts in $\left[\frac{\pi}{2}, \pi\right]$ as shown in Figure 2.2), these results already provide a good level of description of the data, but also a strong motivation to fit the more complex non-linear WC model to data.

2.6 Fitting the full Wilson Cowan model to patient data and response to phase-locked stimulation

2.6.1 Fitting procedure

With the insights on the linearised stable focus response curves given by the previous section in mind and to provide a more accurate level of description of the data in particular in terms of PRC-ARC shift, we now turn to fitting our stochastic neural mass model introduced in Section 2.4 (equation (2.7)) to patient data. The model is fitted to features (also known as summary statistics) extracted from patient tremor recordings. The parameters we fit are shown in Table 2.2, and include model parameters, stimulation magnitude, and stimulation delay (time between when the stimulation trigger is recorded and when stimulation is actually provided to the E population, more about its interpretation in Section 2.8). Stimulation is implemented directly in our Euler-Maruyama integration scheme. We aim at reproducing tremor

dynamics and fit to three dynamical features: the power spectrum density (PSD) of the data, its Hilbert envelope probability density function (PDF), and its Hilbert envelope PSD. While the envelope PDF captures the range of amplitudes present in the tremor, the envelope PSD describes how quickly tremor amplitude changes. But we also aim at reproducing response to stimulation, and fit to the patient bPRC. The data dynamical features are obtained after filtering and z-scoring the data as described in Section 2.3.1. The data bPRC is obtained as described in Section 2.3.1.

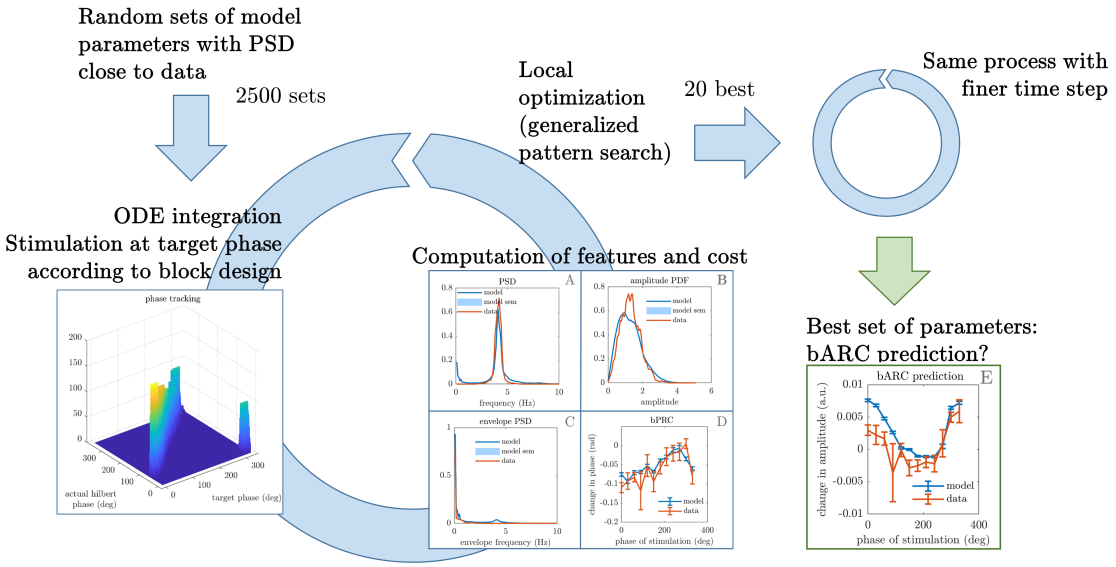

Figure 2.6: The fitting procedure involves 2500 local optimisations for each patient. The simulation of the model at each optimisation step requires to track the zero-crossing phase in order to provide stimulation at the right phase. The phase-tracking ability of the scheme is satisfactory when compared to the actual Hilbert phase (left, detailed in Supplementary Figure A.3 in Appendix A.9). The optimiser minimises a cost function that includes the comparison of three tremor dynamics features (tremor PSD, tremor envelope PSD, tremor envelope PDF) plus the bPRC against the data (middle). Response curves are obtained the same way for the data and the model. Following a second optimisation of the 20 best results with a finer time step, a best set of parameters comes out of the procedure, and the model bARC can be compared against the data bARC. More details on the fitting procedure are given in Appendix A.6.

The fitting procedure is summarized in Figure 2.6. Local optimisations are carried out using gradient free optimisation, specifically a direct search algorithm called the generalized pattern search algorithm (more details are given in Appendix A.6). In order to measure response to stimulation as in the data, each local optimisation step needs to simulate the model with phase-locked blocks of stimulation. This

requires integrating the differential equations of the model while tracking the phase and providing stimulation at the right time, which is done by monitoring the zero-crossing phase alongside a Euler–Maruyama integration scheme. Appendix A.7 details implementation of the simulator. The four features (PSD, envelope PDF, envelope PSD, bPRC) are computed on the model output at each optimisation step. The same method is used as for the data features, with three differences. The first is that for increased stability of the optimisation, the model bPRC is averaged over a much greater number of trials (600 trials), while the more robust dynamical features are obtained from nine trials only to reduce computation cost. The second is that the model output is not filtered to compute the dynamical features (only z-scored), as we want the model output to primarily generate the filtered tremor signal (a model generating mostly 1Hz oscillations but reproducing patient tremor when filtered at 5Hz would not be desirable). Computing the bPRC still requires filtering, as it relies on the Hilbert transform. The third difference is that the filtering window for the bPRC cannot be adjusted manually in optimisation steps, so a 4Hz band centered on the model PSD peak is used. As for the data bPRC and bARC, the actual Hilbert phase at which stimulation occurred is used to compute response curves via the re-binning process described in Section 2.3.1, and the zero-crossing phase is only needed to enable phase-locked stimulation in the model. Phase-tracking performance is illustrated in Supplementary Figure A.3 in Appendix.

At each step, once the four features have been computed on the model output, the optimiser returns the cost

$$c = \frac{1}{N_f} \sum_{n=1}^{N_f} \left(\frac{\sum_{i=1}^{N_n} \left(y_{n,i}^{data} - y_{n,i}^{model} \right)^2}{\sum_{i=1}^{N_n} \left(y_{n,i}^{data} - \overline{y_n^{data}} \right)^2} \right), \tag{2.23}$$

with $y_n, n \in \{1, ..., N_f\}$ being the features considered (here, $N_f = 4$), N_n the length of y_n, and $\overline{y_n^{data}}$ the mean of data feature n. At the end of the procedure, the fit with the highest $R^2 = 1 - c$ for each patient is deemed the best fit. In case of a tie (difference in mean costs lower than standard error of the mean), foci are preferred over limit cycles. The bifurcation structure of the original WC model has been studied in (Borisyuk and Kirillov 1992), but we simply differentiate between

parameters giving rise to stable foci and limit cycles by forward simulating the model without noise, and exploring the region of phase space that is occupied by the system with noise.

2.6.2 Results of the fits

Patients with both of their response curves statistically significant (see significance criterion in Section 2.3), in other words with meaningful response curves, are fitted to. For these patients, namely patient 1, 5, and 6, we find that the model successfully reproduces tremor dynamics, including tremors with sudden bursts, and can fit to patient phase response to stimulation. Recall from Section 2.4 that tremor is highly coherent with thalamic activity, which is why we model tremor using a neural population model. The best fits obtained upon completion of the optimisation procedure are shown in Figures 2.7, 2.8, and 2.9. In addition to reproducing tremor dynamics and being able to fit to patient bPRCs, the model seems to be able to reasonably predict patient bARCs (obtained as in Section 2.3.1, but not fitted to), and in particular which phases are approximately the best phases to stimulate, i.e. the phases at which the maximum decrease in tremor happens. Because of averaging across 600 trials, the model bPRC and bARC error bars are small compared to the data error bars (only about 10 trials per phase bin).

Parameter	Symbol	Best fit values		
		Patient 1	Patient 5	Patient 6
I to E weight	w_{IE}	9.4014	26.048	5.2064
E to I weight	w_{EI}	9.6306	25.3384	24.4813
E to E weight	w_{EE}	6.7541	1.548	2.7514
Sigmoid steepness parameter	β	1.1853	2.4234	4.1933
Time constant (s)	τ	0.0758	0.29984	0.2513
Constant input to E	θ_E	1.4240	22.8621	2.9127
Constant input to I	θ_I	-3.2345	-9.9279	-3.4008
Noise standard deviation	ζ	0.0457	0.013707	0.0263
Stimulation magnitude	δE	0.001684	0.00598	0.001686
Stimulation delay (ms)	Δt_{stim}	138.8366	444.1573	183.4711

Table 2.2: Best parameters for the 3 fitted patients.

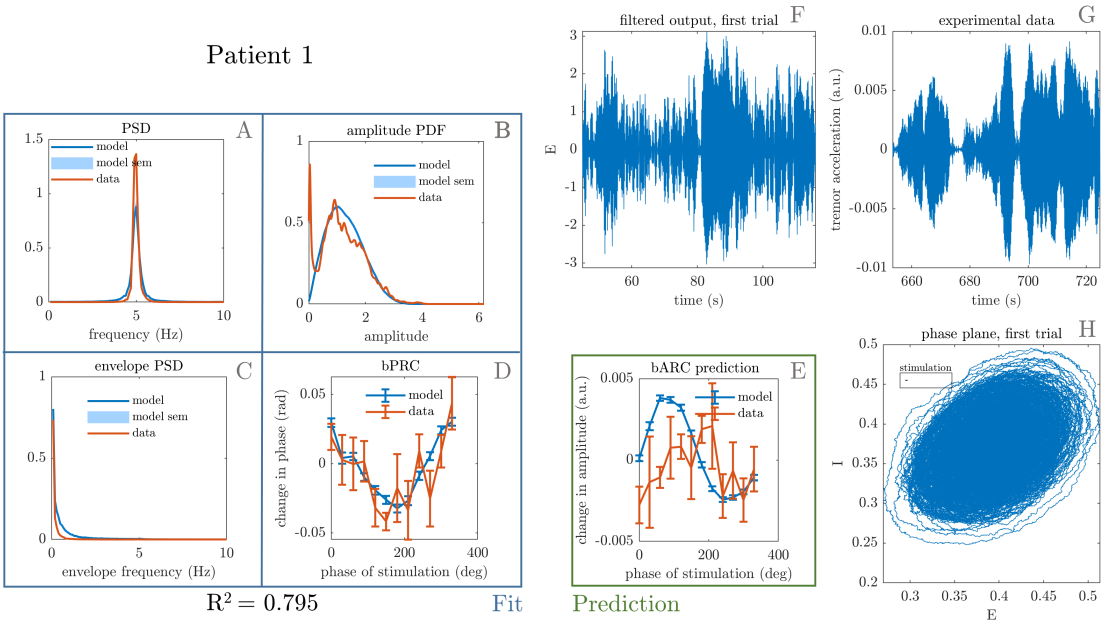

Figure 2.7: Best fit to patient 1. The four features that were included in the cost function are shown on the left, namely tremor PSD (A), tremor envelope PDF (B), tremor envelope PSD (C) and bPRC (D). The R^2 for the model fit to these features is 0.795, and the model reasonably predicts the data bARC (E). The model phase plane is shown in H, and the model tremor time-series (F) is shown next to the patient tremor time series (G). The framed black bar in H indicates the fitted stimulation magnitude to scale.

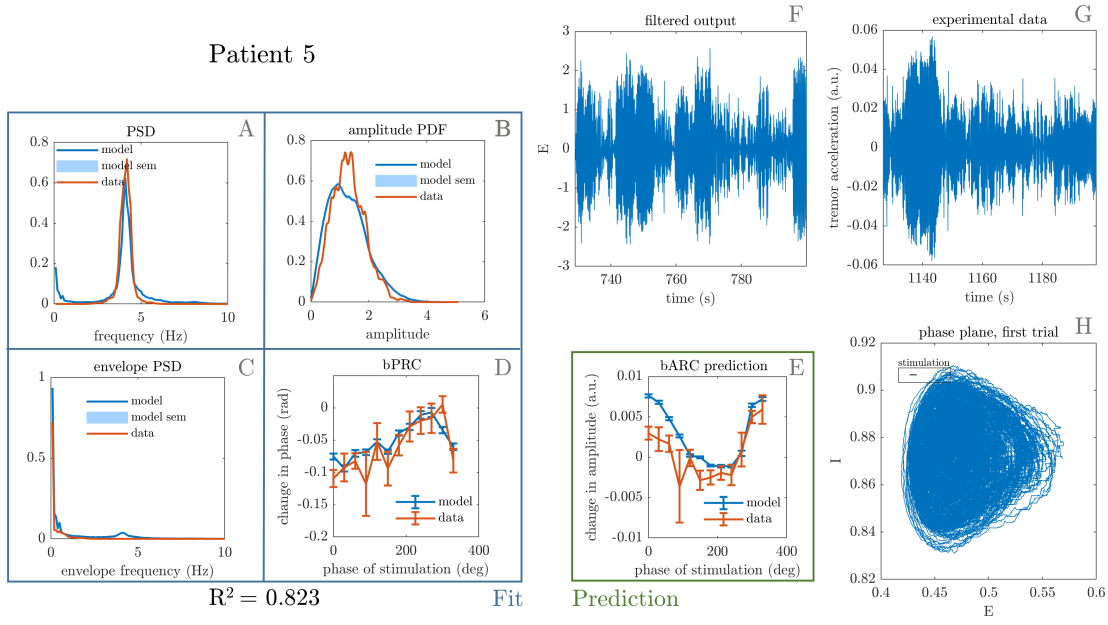

Figure 2.8: Best fit to patient 5. The four features that were included in the cost function are shown on the left, namely tremor PSD (A), tremor envelope PDF (B), tremor envelope PSD (C) and bPRC (D). The R^2 for the model fit to these features is 0.823, and the model predicts the data bARC (E). The model phase plane is shown in H, and the model tremor time-series (F) is shown next to the patient tremor time series (G). The framed black bar in H indicates the fitted stimulation magnitude to scale.

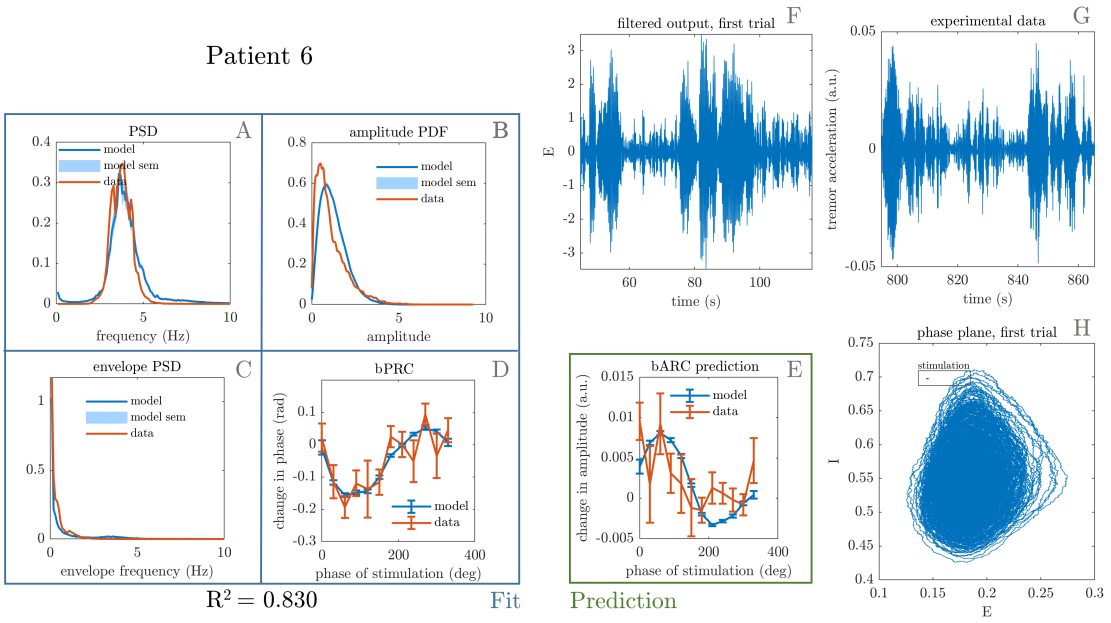

Figure 2.9: Best fit to patient 6. The four features that were included in the cost function are shown on the left, namely tremor PSD (A), tremor envelope PDF (B), tremor envelope PSD (C) and bPRC (D). The R^2 for the model fit to these features is 0.830, and the model reasonably predicts the data bARC (E). The model phase plane is shown in H, and the model tremor time-series (F) is shown next to the patient tremor time series (G). The framed black bar in H indicates the fitted stimulation magnitude to scale.

Validating fitted stimulation magnitude As Cagnan and colleagues (2017) report what the device settings are, and in particular the total electrical energy delivered (TEED) per unit time for each patient, we can valide fitted stimulation magnitudes against these values. We build an equivalent quantity Ξ for the model that we call "model effective stimulation per unit time", and that should scale with the TEED per unit time. We define Ξ as

$$\Xi = \frac{\delta E}{E_\sigma} \overline{f_E}, \tag{2.24}$$

where E_σ is the standard deviation of the non z-scored first dimension of the model output, and $\overline{f_E}$ is the mean frequency of the first dimension of the model output. Since stimulation in the model is a direct increase in E, δE should be scaled the same way, which is the purpose of the division by E_σ. And since bursts are delivered once per period, the multiplication by $\overline{f_E}$ ensures that Ξ is defined per unit time (the number of pulses per burst is the same for the three patients). Figure 2.10

shows the model effective stimulation per unit time for the 15 best performing fits against the TEED per unit time for each patient (correlation coefficient for fit averages $r = 0.98$). Under the assumption that patient intrinsic sensitivities to stimulation are somewhat similar, we can conclude from the correlation that the fitting procedure successfully captures the scale of stimulation across patients.

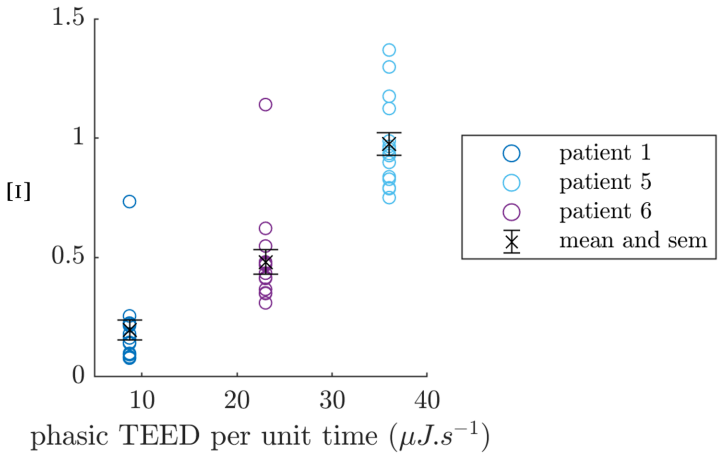

Figure 2.10: Model effective stimulation per unit time Ξ versus total electrical energy delivered per unit time by the device, for the three fitted patients. Showing the 15 best performing models for each patient, along with the mean and standard error of the mean error bars for each patient in black.

PRC-ARC shift in WC synthetic data The PRC-ARC shift is computed on WC synthetic data with phased-locked blocks of stimulation generated by the full model fitted to each patient. This time we can take full advantage of the model and compute bPRCs and bARCs from more trials than for patient data or model data in optimisation steps, and perform 10 repeats of 600 trials for the top 15 fits for each patient. The PRC-ARC shift is then measured as in Section 2.3.1 for each of the 10 repeats, and shown in Figure 2.11. The large filled circles represent the mean of the 10 repeats for each patient fit. It appears that the PRC-ARC shifts obtained for synthetic data of top patient fits mostly lie in the upper-left quadrant of the unit circle for all three patients $\left(\left[\frac{\pi}{2}, \pi\right]\right)$, similarly to patient data. One fit to patient 6 is an outlier in terms of its shift, due to high model effective stimulation (defined in the previous section). While the non-linear model can allow

for a larger shift than $\frac{\pi}{2}$, this is not the case for the linearised model, and the difference is the focus of the next section.

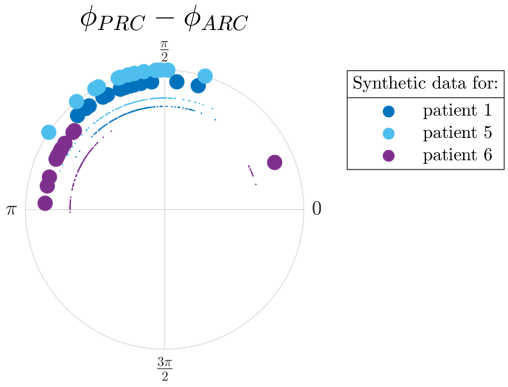

Figure 2.11: PRC-ARC shift in synthetic data (full WC model fitted to patients). For each patient, the shift for all 10 repeats of the top 15 fits is shown (smaller circles), as well as the repeat mean for each fit (larger circles). One repeat corresponds to 600 trials.

2.7 PRC-ARC shift in the model

The analytical expressions for the linearised model make different predictions for patient response curves than synthetic data generated by the full model and analysed with the block method, in particular in terms of PRC-ARC shift. The present section will look at the deterministic linearisation of patient fits, and then contrast it with the full model with noise.

2.7.1 Relationship between analytic response curves in the linearised fitted WC models

The first order PRC and ARC expressions derived in Section 2.5 can be applied to the linearisation of the best WC models fitted to data from the three patients statisfying our significance criterion. The Jacobians at the fixed points are

$$J_1 = \begin{bmatrix} 11.9723 & -35.0323 \\ 34.9513 & -13.1953 \end{bmatrix}, \qquad J_5 = \begin{bmatrix} -0.2252 & -52.3293 \\ 23.2880 & -3.3351 \end{bmatrix},$$
$$J_6 = \begin{bmatrix} 2.8269 & -12.8784 \\ 101.6943 & -3.9789 \end{bmatrix},$$

where J_i corresponds to patient i. The response curves obtained are shown in Figure 2.12. The same values as in Section 2.5.7 are used for X_1^0 and δX_1. Note that the stimulation delay Δt_{stim} is not shown – it affects both the PRC and the ARC and does not play a role in the PRC-ARC shift. More interestingly, we observe that $\omega \gg |\sigma|$ in the 3 fits (see Supplementary Table A.2 in Appendix A.10), suggesting that the response curves' relationship described by equation (2.22) should approximately hold. This is indeed the case as shown in the third column of Figure 2.12, which tells us that the PRC-ARC shift should be close to $\frac{\pi}{2}$. The decay is higher for patient 5 (about 5% of the rotation versus less than 2% for the other two patients) and as expected, the approximation is slightly worse for this patient (panel B3 in Figure 2.12). For small stimulation and close to the fixed point, the deterministic picture with patient parameters is that the PRC-ARC shift should be close to $\frac{\pi}{2}$. In what follows, we investigate the difference between this idealised picture and what is observed in synthetic data.

2.7.2 Accounting for the difference in shift between focus model analytic expressions and WC synthetic data

Four factors could account for the difference in PRC-ARC shift between the idealised picture given by analytic response curves with patient parameters (previous section) and what is observed in WC synthetic data (Section 2.6.2). First, stimulation may be large enough that the Taylor expansions used to derive the analytic PRC and ARC expressions are no longer approximately valid. Second, tremor in patient fits may correspond to a regime where trajectories are not so close to the fixed point, compromising the linearisation validity. Third, the introduction of noise in the model may result in effects on the PRC-ARC shift that do not average out to zero. Fourth, in synthetic data, the response to stimulation is measured by the block method, which differs from the first order approach taken in our derivations. We next show that for the three best fits considered, non-linearity is the main driver.

Ten repeats of 600 trials of synthetic data are generated for the linearisation of the best fits to each patient. The integration scheme with live phase tracking

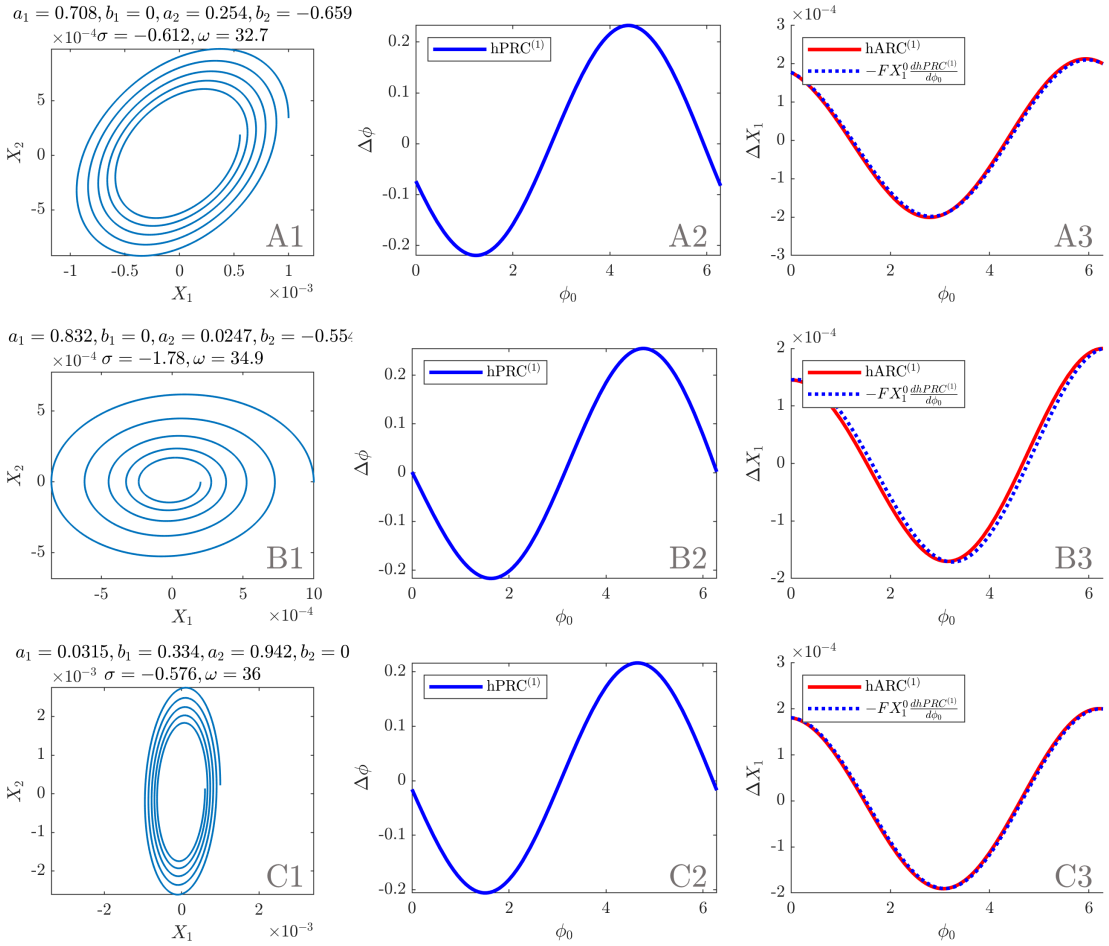

Figure 2.12: Analytical results for linearised patient fits (initial conditions as in the main text). First column: phase space. Second column: first order PRC as per equation (2.18) (scaling valid for the first cycle). Third column: first order ARC as per equation (2.20) and opposite of the derivative of the first order PRC scaled by FX_1^0. Panel A, B, and C correspond to patient 1, 5, and 6, respectively.

and stimulation is the same as described in Section 2.6.1, only the stochastic differential equations are now

$$\begin{bmatrix} dE \\ dI \end{bmatrix} = J \begin{bmatrix} E - E^* \\ I - I^* \end{bmatrix} dt + \zeta \begin{bmatrix} dW_E \\ dW_I \end{bmatrix}, \tag{2.25}$$

where dW_E and dW_I are Wiener processes, ζ the noise standard deviation (same values as in the non-linear case), E^* and I^* are the coordinates of the fixed point, and J is the Jacobian at the fixed point of the patient fit. The same values as in the non-linear case are used for the stimulation magnitude and delay, with the exception of patient 5, for whom the stimulation magnitude is set to a fifth of its

value in the non-linear case, as higher values were seen to cause a breakdown of phase tracking, and result in unreliable response curves.

For each patient and for each of the 10 repeats, bPRCs and bARCs are obtained, and the PRC-ARC shift is then measured as in Section 2.3.1. The results are shown in Figure 2.13 (middle), alongside the shifts measured from the response curves presented in Section 2.7.1 (left), and the shifts measured in the full WC model (right). It can be seen that going from the analytic response curves to the linearised model (i.e. adding noise, measuring the response to stimulation via the block method and not a first order method, and using a finite stimulation magnitude rather than an infinitesimal stimulation), doesn't affect the shift much (compare the left and middle panels of Figure 2.13). However, a substantial increase in the shift is obtained by introducing the non-linearity (compare the middle and right panels of Figure 2.13), which brings the shift in the upper-left quadrant, where patient data lie. The PRC-ARC shift can be modulated in the non-linear model in a way that is not available in the linearisation.

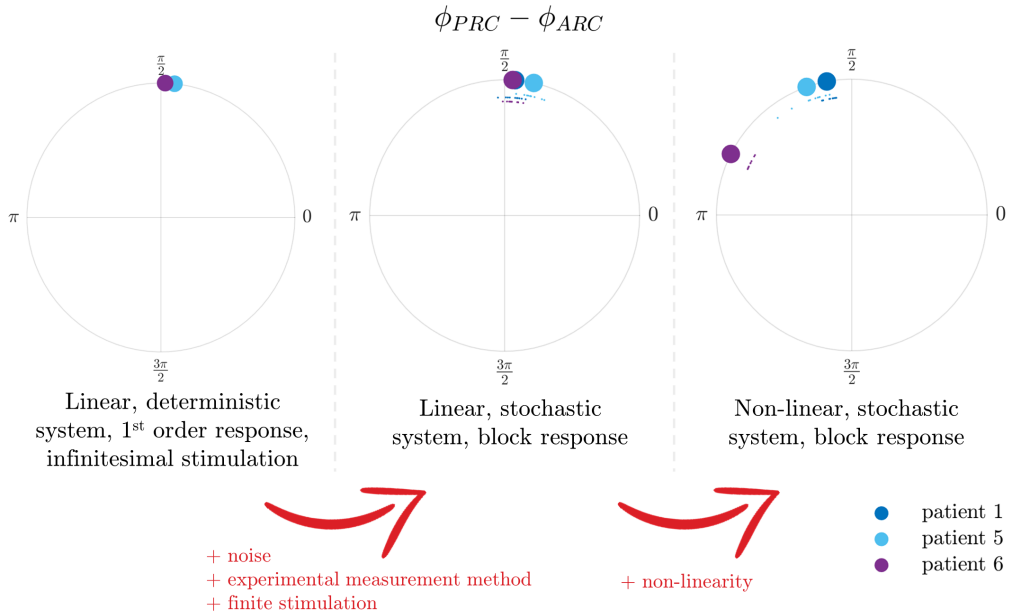

Figure 2.13: Non-linearity accounts for most of the difference in PRC-ARC shift seen in synthetic data (middle and right), when compared to the PRC-ARC shift derived in the focus model (left). When computed from synthetic data, the PRC-ARC shift of all 10 repeats is shown (smaller circles), as well as the repeat mean (larger circles). One repeat corresponds to 600 trials, only showing best fit for each patient.

2.8 Discussion

We showed that in a 2D linearised stable focus model, the first order PRC and ARC based on a phase definition approximately equivalent to the Hilbert phase are close to sinusoidal for small decay. Moreover, the PRC-ARC shift is close to $\frac{\pi}{2}$. Half of the patients in our dataset had significant sinusoidal bPRCs and bARCs (an effect of stimulation phase could not be found in other patients in at least one of their response curves), and the significant patients have a PRC-ARC shift in the interval $\left[\frac{\pi}{2}, \pi\right]$. A full WC model can be fitted to tremor dynamics features and to the bPRC for these patients, and as hinted at by the similarities seen in the linearised focus model and the data, the best fits – a vast majority of stable foci – can reproduce the dependence of the effects of stimulation on the phase of stimulation. The best fits also reasonably predict the bARC, and notably what is approximately the best phase to stimulate. Compared to the 2D linearised focus, the non-linearities of the full WC model allow for a better reproduction of the phase-dependence found in patient data, in particular as far as the PRC-ARC shift is concerned. Our full model can capture the behaviour of neural populations plausibly involved in the generation of tremor, which, together with its success in reproducing phase response and predicting amplitude response in patients, makes it a strong candidate for further study of phase-locked DBS.

Phase definition While asymptotic phase definitions are common in theoretical studies, experimental studies tend to favour instantaneous phase definitions such as the Hilbert phase (see review in Section 1.2.4.2). To reproduce the data, an instantaneous phase seems more appropriate than an asymptotic phase, as there is no indication of stimulation happening on or close to an attractor. It has been shown recently in (Wilson and Ermentrout 2018) how an operational definition of the phase can describe transient spiking, when an asymptotic phase does not capture the phase-dependence of transients. Moreover, stimulation is assumed to be small in our analytical expressions (Section 2.5), but not in the full model, contrary to standard asymptotic phase reduction strategies.

In this study, our phase definition is the Hilbert phase of the tremor data or approximately equivalent. It is therefore referenced to the maximum of the tremor oscillations (represented by the first coordinate of the dynamical system in our models), and does not require a limit cycle. The Hilbert phase is an angle in the analytic signal space, it does not generally grow linearly with time, and is a protophase (Kralemann et al. 2008). This is not a concern from the perspective of describing patient data, as this is the observable choice we are making for both the data and the model. Commonly used with data, the Hilbert transform has also been proposed as a robust method to measure steady state PRCs in single neuron models (Oprisan 2017).

Linearisation The response curves derived for the linearisation of a 2D focus in Section 2.5 can be related to previously published expressions. In particular, the infinitesimal PRC for radial isochron clocks has been derived in (Glass and Mackey 1988), and has been recently included in (Monga et al. 2018) under the larger umbrella of general radial isochron clocks. The radial clock case ($K(\phi) = \omega$ in (Monga et al. 2018)) perturbed along the first dimension agrees with our equation (2.18) for the case of a circular flow (see Section 2.5.7). For this simple system, the asymptotic phase response is the same as the first order Hilbert phase response.

Moreover, we demonstrated that in the linearisation of a 2D focus, the best phase to stimulate (i.e. the minimum of the ARC), corresponds to the maximum positive slope of the first order PRC (see equation (2.22)). This is valid for small decay compared to the rotation, for the phase and amplitude definitions given in Section 4.2 (phase approximately equivalent to the Hilbert phase, amplitude defined as the first coordinate), and for a small stimulation magnitude. In fact, the first order ARC is simply a scaled version of the opposite of the first order PRC derivative. As mentioned in Chapter 1 (Section 1.2.3.4), a similar relationship has been first reported in a theoretical study in the context of an individual oscillator (Wilson and Moehlis 2014), and more recently in (Weerasinghe et al. 2019) in the context

of population responses arising from the individual responses of coupled phase oscillators, whose time evolution follows Kuramoto equations, and where the level of synchrony takes the role of amplitude. The results in (Weerasinghe et al. 2019) also assume particular distributions of oscillator frequencies. It is noteworthy that we found a similar result with very few assumptions on the dynamics: our result is valid for the linearisation of any 2D focus with slow decay, i.e. any linearisation obeying equation (2.10) with slow decay. This applies in particular for the linearisation of the WC model, another popular neuroscience model very different in essence from coupled oscillator models. Recall from Section 1.2.3.2 that in the thermodynamic limit and under certain assumptions about the distribution of oscillator frequencies, the Kuramoto model can be reduced to a two-dimensional system (Ott and Antonsen 2008; Bick et al. 2020). Our results are applicable to the linearisation of a fully desynchronised reduced Kuramoto model observed through $X_1 = \rho \cos\theta$ where $\mathbf{r} = \rho e^{i\theta}$ is the order parameter (ρ is the modulus and θ the angle in the complex plane). Such a system therefore satisfies equation (2.22) as well (for small decay).

Our derivations do not assume proximity to a limit cycle, and this allows the study of the dependence of the response to stimulation on the amplitude of the oscillations for a given model (limit cycles do not have an amplitude variable in the case of infinitesimal perturbations). In the linearisation, the PRC is found to be inversely proportional to the amplitude of the oscillations before stimulation (see X_1^0 term in equation (2.18)), while the ARC does not depend on it.

Because the block method phase and amplitude response used in the rest of the chapter are normalised by the number of pulses and blocks are only about 25 period long, it seems legitimate to think that, although they are different objects, the first order response to a single pulse ($\mathrm{hPRC}^{(1)}$ and $\mathrm{hARC}^{(1)}$) and the block method response (bPRC and bARC) could be related, and in particular that they might share similar PRC-ARC relationships. Part of the connection hinges on our proof that the phase definition in the linearisation of the focus model matches with the Hilbert phase when the decay is small compared to the rotation (Section 2.5.2). And indeed, the PRC-ARC shift predicted by our expressions derived for the first order

response to one pulse of stimulation in a linearised focus is very close to the shift obtained by the block method on linearised WC synthetic data (compare the left and middle panels of Figure 2.13). Our analytical derivations provide a rationale to fit the full WC model to data and an intuition for why the model can predict patient ARC, but do not offer an exact analytic treatment of the block method. Specifically, individual pulses in a block may have different effects depending on where they are located in the block and depending on stimulation history within the block (Cagnan et al. 2017). Another method to approximate bARCs will be presented in Chapter 4.

To the best of our knowledge, there is no simple way of getting analytical PRCs and ARCs based on Hilbert phase and amplitude or equivalent in the non-linear system, making the analytical expressions for the linearisation more valuable. It is also of interest to understand what can be achieved with a simple, linear model before adding more complexity. In fact, realising that the linear model can already explain the data to some extent is a motivation to fit the non-linear model, which is an expensive endeavour.

Fitting procedure Fits of the non-linear WC model were performed using the generalized pattern search algorithm on many sets of random initial parameters. This approach was chosen for its robustness and computational efficiency in a non-smooth, non-convex landscape with four non-linear features and 10 parameters, despite requiring the use of a supercomputer. In particular it has been deemed superior to the simplex algorithm in finding better fits. The implementation used also has the additional benefit of being able to handle failed simulations (which occasionally happen as response curves with 12 phase bins cannot be obtained for some parameter sets with noise values too high compared to the vector field). However the fitting procedure results in many "good" local optima. What these "good" sets of parameters have in common and what they can tell us about the patients we are fitting to is not easily addressed with our current fitting strategy. Even real biological networks may have redundancies, and may exhibit the same behavior under different network configurations. However more work is needed to

understand whether parameter non-identifiability comes from the model and the choice of summary statistics, or is a feature of the underlying biology.

A limitation of our fitting method is related to the integration scheme: to reduce computation cost, the Euler step used in the first optimisation process is 1 ms. The top 20 best fits are then re-optimised based on a Euler step of 0.1 ms, and results are produced with this finer time step, as dynamics can be qualitatively different (further reduction in the Euler step has not been seen to change the dynamics). While the need to track the phase at each integration step to decide if stimulation has to be applied precludes the direct use of built-in, powerful integration schemes, a more advanced custom event-based stochastic integration scheme could remove the need for a second optimisation while keeping the computation cost down. The performance of our simple phase-tracking strategy is good for patient 1 and 6 and satisfactory for patient 5 (see Supplementary Figure A.3 in Appendix A). Response curves are obtained based on the actual Hilbert phase of stimulation in a post-hoc manner, which makes up for the reduced performance observed for patient 5. Still, more accurate algorithms could be explored. Our simple live phase estimation strategy is based on a linear phase evolution between zero-crossings of E (details in Appendix A.7), and would benefit from a better frequency estimate for the current period (currently simply based on the duration of the previous period) and more robustness to noise. Even better live estimates of the Hilbert phase could be obtained thanks to autoregressive forward prediction (Chen et al. 2013), but at the expense of a higher computational cost, and of a need to adjust hyper parameters for each time series.

Non-linear WC model The fitting procedure discussed above was applied to fit to data the full WC model with Gaussian white noise (equation (2.7)). The best performing fits are stable foci for all three patients, and very few limit cycles are found in the top 15 fits for all three patients. One is found for patient 1 (shares the 1st place with a stable focus - distance between mean costs only 30% of the standard error of the mean), one for patient 5, and none for patient 6.

In the stable focus regime, noise brings the system away from the stable fixed point, and the interaction of the noise with the dynamics of the system makes the reproduction of patient tremor possible. In our study, noise corresponds to contributions that are not modelled by either the E/I populations or the inputs to these populations. We are considering that these contributions have no explanatory power, and model them with uncorrelated noise. While in the absence of noise, the system would converge to the stable fixed point and no tremor would be generated, Gaussian white noise alone cannot reproduce the dynamical features of tremor time series. Symptoms in the model depend just as much on the noise as on the other parameters of the model. This is shown in Appendix A.8 where an expression is obtained for the stationary standard deviation of the linearisation of the WC model. The standard deviation is dependent on the noise, but also on the other parameters of the model via the Jacobian at the fixed point. A limitation of our approach is that comparison of the fitted weights or fitted inputs across patients may be difficult when noise levels are not comparable. Enforcing a constant level of noise in the fits or limiting noise to the minimum level required to reproduce the data may address this point. Instead of noise, tremor-like activity may be obtained by exploiting chaotic dynamics arising from coupling several WC models together (Borisyuk et al. 1995; Ueta and Chen 2003), but this would significantly increase the complexity of the model (more on increasing complexity in the last part of this section).

Contrary to weights, stimulation delays can more easily be compared across patients, and the fitted values obtained deserve some discussion. In fitting our thalamic model to tremor acceleration, we are assuming thalamic activity and tremor are directly related as mentioned before (see Section 2.6.1). Tremor activity is however expected to lag thalamic activity due to conduction delays. The accelerometer used to measure tremor is also expected to introduce an electromechanical coupling delay. In the model, we allow for a stimulation delay Δt_{stim} between the stimulation trigger and the time when stimulation is actually delivered to the excitatory population. This parameter is fitted to the data, and gives the model the ability to shift its bPRC in phase. Fitted stimulation delays are hundreds of milliseconds, and conduction

and accelerometer delays (tens of milliseconds) only account for a small part. The higher fitted values are required by the model to match data bPRCs. With our candidate VIM/nRT mapping in mind, the higher fitted values remain unexplained on the biology side, although as mentioned before tremor generation and ET DBS are not fully understood. It is interesting to note that the stimulation delay of the best performing model for patient 5 is longer than one period (see Table 2.2). This is found consistently in the top three best fits, and reducing the delay to its value modulo the average period substantially reduces the quality of the bPRC fit. Besides this short term delay, our model does not include medium or long term plasticity effects, which are not expected to be strongly present in the recordings as stimulation is only delivered for periods of 5 seconds in a row. In our model, stimulation is provided to the E population via a direct increase in the population activity. While stimulation is provided via the sigmoid function of the excitatory population in other studies (Yousif et al. 2017), we found this approach too restrictive due to sigmoid saturation, and inadequate to reproduce the full extent of the response to phase-locked DBS in some patients. As a reminder, the choice of stimulating the excitatory population rather than the inhibitory population is made for biological consistency, as the VIM is the most common stimulation target in ET DBS.

The success of the non-linear WC model in predicting patient ARCs when fitted to their PRCs is partially explained by its ability to modulate the PRC-ARC shift. The PRC-ARC shift in the full model can reach the range found in patients while the linearised version of the WC is limited to the close vicinity of $\frac{\pi}{2}$. The response curves of the full WC model are also better at reproducing the data and can deviate from pure sinusoids. However there is still some room for improvement in reproducing the shift, in particular as far as patient 1 is concerned (patient shift quite a bit larger than the model). The model can allow for a larger shift as shown by a fit hand-picked in the top 15 shown in Supplementary Figure A.4 in Appendix A.9. While the troughs of the model bPRCs are roughly aligned with the troughs of the data bPRCs in Supplementary Figure A.4 and in our best fit in Figure 2.7, it is apparent that the peaks of the model bARCs are closer to the

peaks of the data bARCs in Supplementary Figure A.4 than in Figure 2.7. This highlights that the PRC-ARC shift of the model is closer to that of the data in Supplementary Figure A.4 than in Figure 2.7. The PRC-ARC shift could be selected as an additional feature to fit to in order to improve ARC reproduction. Moreover, the model's ability to describe all patients with both response curves statistically significant in at least one of our tests should be re-assessed as more data becomes available, both in terms of number of patients and recording length.

In its two-population version, the suggested mapping of the excitatory and inhibitory populations (VIM and nRT) is not the only possibility. Other candidates include antidromically stimulated structures at the cerebellar level or below, such as DCN as the inhibitory population, and the inferior olive as the excitatory population. The model could also be extended by including more populations. With our current mapping in mind, the cortex and the DCN could be turned into populations of their own, which would make the model four-dimensional. As suggested by Yousif and colleagues (2017), the inferior olive which provides input to the DCN could also be modelled, and the spatial extent of the VIM could be accounted for by splitting it in two populations or more. Increasing the number of populations would however increase the number of parameters of the model, and make the optimisation process more computationally intensive, and the model more prone to over-fitting. In contrast, the incorporation of additional loops in the model architecture may help explain the inertia in stimulation effects discussed above. Nevertheless, the model seems to be able to reproduce the data in its current state, which suggests an increase in complexity is not warranted. Our study positions the WC as a strong candidate to model the effects of phase-locked DBS. It is remarkable that one excitatory/inhibitory loop seems to be enough to model the phase-dependent effects of ET DBS in the datasets available with statistically significant response curves. It gives some support to the hypothesis that sub-circuits of the central tremor network may behave as individual oscillators entraining each other (Raethjen and Deuschl 2012). This will be discussed in greater details in Chapter 5 (Section 5.4).

3

Average beta burst duration profiles provide a signature of dynamical changes between the ON and OFF medication states in Parkinson's disease

Contents

3.1 Abstract

Parkinson's disease motor symptoms are associated with an increase in subthalamic nucleus beta band oscillatory power. But these oscillations are phasic, and there is a growing body of evidence suggesting that beta burst duration may be of critical importance to motor symptoms. This makes insights into the dynamics of beta bursting generation valuable, in particular to refine closed-loop deep brain stimulation in Parkinson's disease. In this study, we ask the question "Can average burst duration reveal how dynamics change between the ON and OFF medication states?". Our analysis of local field potentials from the subthalamic nucleus demonstrates using linear surrogates that the system generating beta oscillations acts in a more non-linear regime OFF medication and that the change in the degree of non-linearity is correlated with motor impairment. Further, we pinpoint specific dynamical changes responsible for changes in the temporal patterning of beta oscillations between medication states by fitting to data biologically inspired models, and simpler beta envelope models. Finally, we show that the non-linearity can be directly extracted from average burst duration profiles under the assumption of constant noise in envelope models. This reveals that average burst duration profiles provide a window into burst dynamics, which may underlie the success of burst duration as a biomarker. In summary, we demonstrate a relationship between average burst duration profiles, dynamics of the system generating beta oscillations, and motor impairment, which puts us in a better position to understand the pathology and improve therapies such as deep brain stimulation.

3.2 Introduction

We outlined in Chapter 1 that in PD, elevated beta oscillatory activity in the STN has been correlated with worsening of motor symptoms, in particular bradykinesia and rigidity but not tremor (Kuhn et al. 2006; Kühn et al. 2008; Kühn et al. 2009; Tan et al. 2013; Steiner et al. 2017, see Section 1.2.1.2). This association motivated the development of aDBS, where stimulation is provided when beta oscillation

amplitude is above a given threshold. As detailed in Section 1.2.2.2, aDBS has been tested chronically in patients (Little et al. 2013; Little et al. 2016; Rosa et al. 2017a; Arlotti et al. 2018; Velisar et al. 2019). Several of these studies have provided evidence that aDBS would reduce side-effects while maintaining clinical efficacy (Little et al. 2016; Rosa et al. 2017a; Arlotti et al. 2018).

However, besides average beta synchrony, the temporal patterning of beta activity has more recently been shown to be of importance to PD symptoms. In particular, the proportion of longer bursts of activity in the beta band of STN LFPs OFF medication has been correlated with motor impairment (Tinkhauser et al. 2017b), leading to the hypothesis that longer bursts are more likely to be pathological. Other studies have implicated beta burst temporal patterning in motor performance in PD (Anidi et al. 2018; Ahn et al. 2018; Lofredi et al. 2019, reviewed in Section 1.2.1.2). Torrecillos and colleagues (2018) demonstrated that STN beta bursts play a physiological role. As such, beta amplitude thresholding as done in aDBS discriminates pathological from physiological activity in a very coarse manner (although it might suppress on average more longer bursts, see Tinkhauser et al. 2017a). Further insights into the dynamics of beta bursting are thus needed to refine closed-loop DBS in PD. In this study, we therefore ask the following question: can we relate observed changes in beta oscillation temporal patterning in PD between the ON and OFF medication states to changes in dynamical properties of the system generating beta oscillations?

In previous studies, STN beta bursts have been mostly studied based on one arbitrary threshold of the beta envelope as events above the threshold, potentially with a minimum duration condition (examples of various thresholds shown in Figure 3.1, panel A). Average burst duration and amplitude profiles describing the average burst duration and amplitude for a range of thresholds (see Figure 3.1, panel A and B for an illustration of average burst duration profiles) have been introduced (Tinkhauser et al. 2017b; Tinkhauser et al. 2017a). However, they played a minor role and have not been considered systematically on an individual patient basis. Here, we leave behind the arbitrary choice of a threshold by relying on profiles

across thresholds to provide an unbiased characterisation of beta oscillation temporal patterning. It has been established that STN beta burst duration is a better metric than burst amplitude to distinguish between the healthy and pathological states in an animal model of PD (Deffains et al. 2018). We begin our study by investigating in STN recordings of PD patients whether average burst duration profiles are better at distinguishing between the ON and OFF medication states than average burst amplitude profiles. We only observe changes in temporal patterning of beta oscillations in average burst duration profiles, and come to the conclusion that burst duration is the better metric as in (Deffains et al. 2018). We introduce a burst duration specific measure of non-linearity based on linear surrogates, and show that non-linearity is increasing from the ON to the OFF state, thereby presenting a first level of description of the dynamical changes associated with changes in the temporal patterning of beta oscillations. To support the relevance of these changes, we study the correlation of our non-linearity measure with motor symptoms.

Many modelling studies have reported the generation of sustained beta oscillations in the context of PD, and identified several potential sources of exaggerated beta oscillations (see Section 1.2.3.3). However, reproducing the temporal patterning of beta oscillations has been limited to STN-GPe models receiving complex, correlated inputs (Ahn et al. 2016; Mirzaei et al. 2017, reviewed in Section 1.2.3.3). How model dynamics would need to change in the absence of correlated inputs to account for changes observed in the temporal patterning of beta oscillations in patients ON and OFF medication has not been reported. To confirm that more non-linearity is present OFF medication and delineate which types of circuit dynamics are associated with average burst duration profiles ON and OFF medication, we fit time discretized WC models of increasing complexity with uncorrelated inputs to selected patient data.

The time discretization of one dimensional stochastic processes can be used to simulate the Hilbert envelope of beta oscillations (see Figure 3.1, panels C and D). We call these models "envelope models". Powanwe and Longtin (2019) showed that under simplifying assumptions, the envelope of a linear WC model can be described by a particular envelope model. While the WC model is biologically inspired and

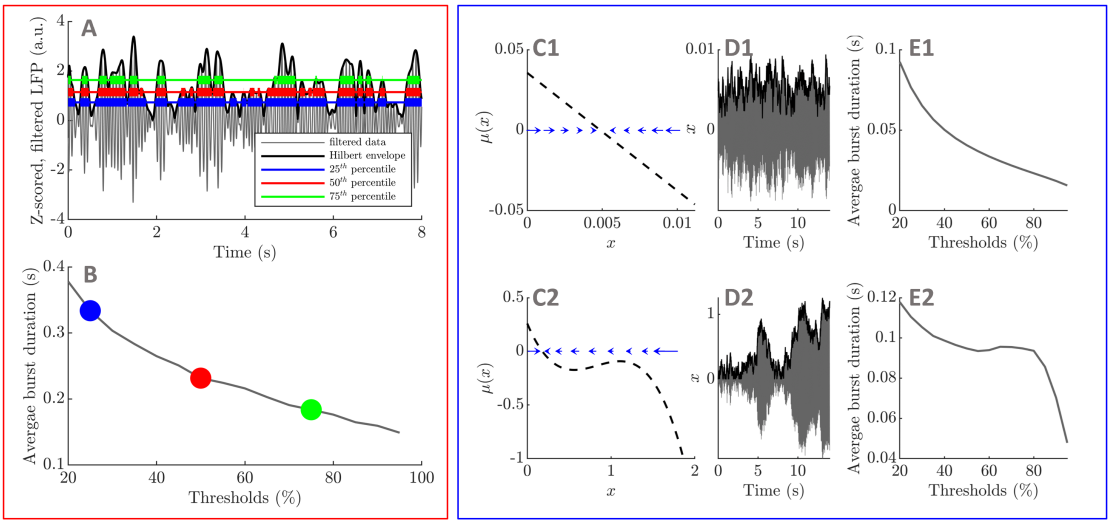

Figure 3.1: Introducing average burst duration profiles. Average burst duration profiles are obtained by computing beta envelope average burst duration for a range of thresholds. An example is provided for three thresholds, where thick lines highlight the duration of individual bursts for the three thresholds in panel A, and the corresponding averages are identified with the same colour in panel B. Considering the time discretization of simple envelope models of the form $dx_t = -\mu(x_t)dt + \zeta dW_t$, where μ is the drift function, W is a Wiener process, and ζ is a constant noise parameter, we illustrate with two example drift functions the link between envelope dynamics (panels C1 and C2, one-dimensional vector field also sketched with blue arrows) and average burst duration profiles (panels E1 and E2). The envelope models produce the black envelopes in panels D1 and D2, and beta oscillations (shown in grey in panels D1 and D2) can be obtained by adding a constant frequency phase equation. In C1, when x moves away from the fixed point, it will be strongly attracted back. By contrast, in the case of C2, if x is around 1, there is weak attraction towards the fixed point, allowing x to stay at an elevated level for longer.

describes the STN-GPe circuit, envelope models are simpler, can reproduce average burst duration profiles, and summarize the essence of the underlying dynamics. We use this to our advantage to pinpoint the simplest polynomial forms of envelope drift function representative of the ON and OFF medication states, and to derive an analytical expression for average burst duration profiles by identifying a first passage problem. Based on this result, we relate changes in average burst duration to changes in one specific parameter in the linear case.

Different envelope dynamics result in different average burst duration profiles (this is illustrated in Figure 3.1, panels C to E). To fully relate temporal patterning of beta oscillations to dynamics, we establish a mathematical link under general assumptions from average burst duration profile to envelope dynamics. This suggests

that average burst duration profiles are a direct signature of envelope dynamics, and may be one reason why beta burst duration is found to be an important marker of pathology in experimental studies of PD. Further, we illustrate the relationship between burst duration and dynamics by recovering envelope dynamics in envelope model synthetic data, and in examples of patient data. This envelope dynamics inference method may find applications in other contexts, as it can be applied to any envelope time series.

Starting with the data, the chapter's narrative will be guided by the following questions. Is non-linearity increasing from the ON to the OFF state (surrogate analysis, neural mass model, and envelope model sections)? Can the change in the degree of non-linearity help predict motor impairment (surrogate analysis section)? Which type of non-linearity is required to explain experimental average burst duration profiles (neural mass model and envelope model section)? How can we directly extract this non-linearity from average burst duration profiles (dynamics inference section)? The surrogate analysis is based on a statistical method which makes the least assumptions about the system, and is used to link dynamical changes with motor impairment. While the biologically inspired neural mass models describe the STN-GPe circuit, envelope models are particularly insightful as they can be used to study the dependence of average burst duration on model parameters, and provide a direct link from average burst duration to drift function. To clarify the exposition, some methodological and derivation details are presented in Appendix B rather than in this chapter.

3.3 Comparing bursting features ON and OFF medication

3.3.1 Choice of bursting features

The activity at beta frequency comes in the shape of bursts, and several features could be analysed to capture the difference in beta bursting dynamics between medication state in STN LFPs. In addition to the power spectrum, we will consider the average burst duration profile, the average burst amplitude profile, and the

envelope PDF. Bursts are commonly defined as events corresponding to the envelope being above a predefined threshold for more than 100 ms (Tinkhauser et al. 2017b; Tinkhauser et al. 2017a). Burst profiles across thresholds do not depend on an arbitrary threshold choice. Additionally, given a short time series, they make more efficient use of the data available than the burst distribution at a single threshold. This is because they rely on a mean value for a given threshold and the same time series is reused for all thresholds. Importantly, dynamical properties of the system are revealed by average burst duration profiles as will be detailed later.

3.3.2 Extracting bursting features

We extracted the PSD and the three features mentioned above from bilateral STN LFP recordings of 8 patients ON and OFF Levodopa (Kuhn et al. 2006). Recording duration ranged from 137 s to 366 s (mean duration 233 s). For a given patient and hemisphere, the channel with the highest beta peak was selected, and both the ON and OFF medication data were band-pass filtered $\pm$ 3 Hz around the beta peak found in the OFF state (defined as the power spectrum maximum in the 13 to 35 Hz range). Power spectra were directly obtained from the filtered data. Next, the filtered data were individually z-scored to remove amplitude differences that could arise simply from a difference in mean beta power between the ON and OFF states, and highlight instead any possible differences in the temporal dynamics of beta amplitude (this z-scoring step has no effect on burst duration profiles as thresholds considered are individual to each time series). Beta envelopes were obtained as the smoothed Hilbert amplitude of the filtered, z-scored data (smoothing span of 5 ms, about a tenth of a beta cycle). To allow for statistical analysis, time-series were then divided into five parts of equal length. For each segment, beta envelope PDFs were estimated, and burst duration and burst amplitude profiles were built as the average burst duration and amplitude for thresholds ranging from the 20^{th} to the 95^{th} percentiles of the envelope in steps of 5%. We used the definition of bursts given above (including the minimum burst duration of 100 ms), and burst amplitude was defined as the maximum amplitude recorded during a burst.

3.3.3 Average burst duration profile is the relevant feature to discriminate bursting dynamics ON and OFF medication

Our statistical analysis reveals that average burst duration profile is the most powerful of the features analysed to discriminate bursting dynamics between conditions. Significant differences in mean burst duration and mean burst amplitude between the ON and OFF states were assessed by paired t-tests with FDR control at 5% (we used the same FDR procedure as in Section 2.3.1). We evaluated significant differences in envelope PDFs between the ON and OFF conditions using cluster-based permutation testing (10^6 permutations). The power spectra and the three bursting features are shown for the right hemispheres of the 8 patients in our dataset in Figure 3.2. Besides differences in the power spectra which are known to be statistically significant, only burst duration profiles exhibit significant differences after FDR correction between the ON and OFF states. These significant differences are seen in most patients, although they are consistent across thresholds only for half the datasets. Besides a difference in mean power removed by z-scoring, amplitude statistics were not found to be significantly different ON and OFF medication as exemplified by the lack of significant differences in both average burst amplitude profiles and envelope PDFs for all patients. A similar picture is seen in left hemisphere LFPs (see Supplementary Figure B.2 in Appendix B.6). We show in Supplementary Figure B.3 and B.4 in Appendix B.6 that profiles obtained ON medication are different from similarly filtered white noise for the majority of hemispheres. This confirms that ON profiles are physiologically meaningful, despite the choice of filtering windows always centered on the beta peak OFF medication. We will therefore focus on average burst duration profiles in the rest of the chapter, and we start with a linear surrogate analysis of the changes in these profiles.

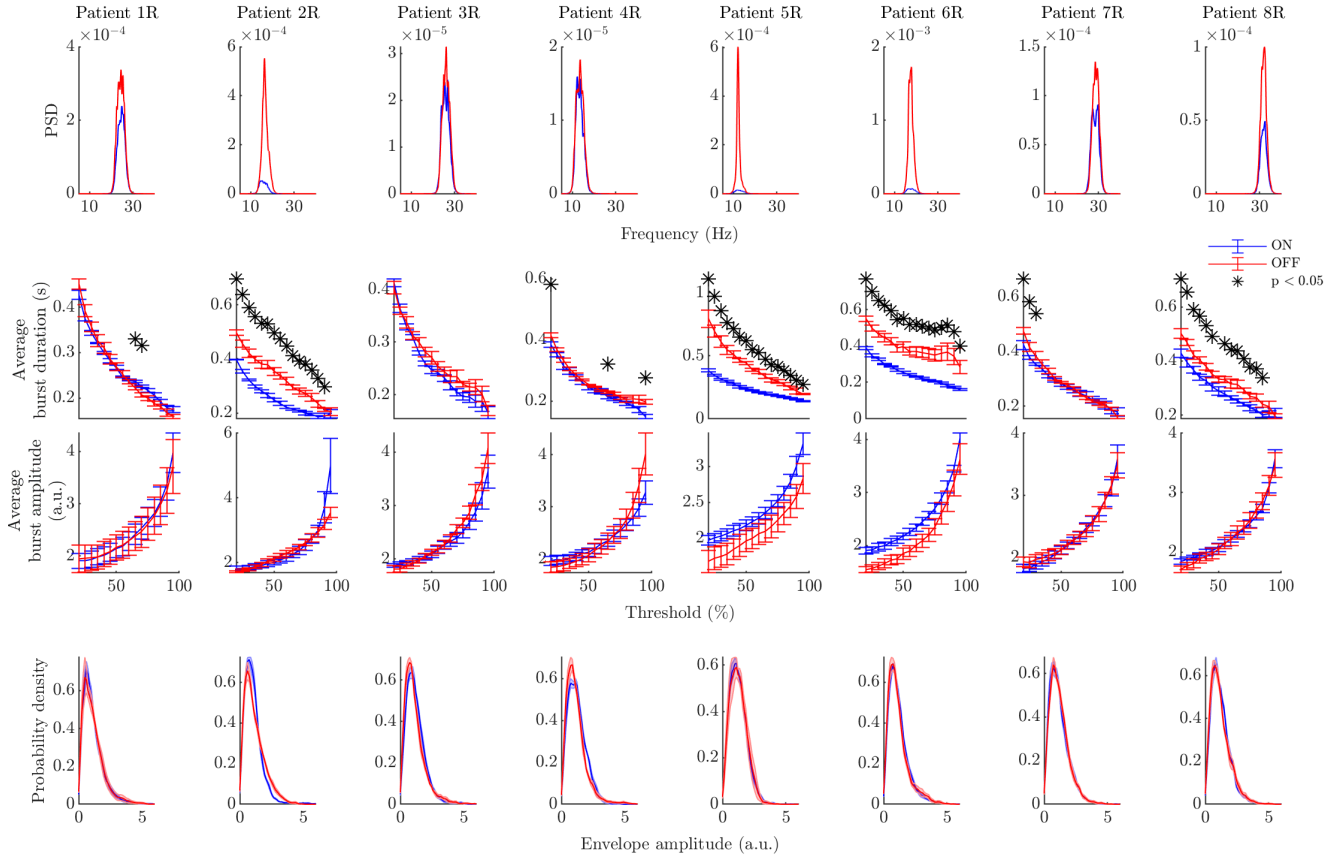

Figure 3.2: Power spectra and bursting features ON and OFF Levodopa (right hemispheres). Each column corresponds to the right hemisphere of one of the eight patients. Each row corresponds to a bursting feature, the ON state is always in blue, and the OFF state in red. The first row shows power spectra, the second row average burst duration profiles, the third row average burst amplitude profiles, and last row envelope amplitude PDFs. Statistically significant differences under FDR control are indicated by black stars (three bursting features only).

3.4 Approaching dynamical changes using a linear surrogate analysis of average burst duration profiles

Our first approach to relating changes in the temporal patterning of beta oscillations between the ON and OFF states to dynamical changes is to consider the degree of non-linearity in the ON and OFF states. It is obtained by comparing average burst duration profiles ON and OFF medication to the profiles of their respective linear surrogates. In addition, we provide support for the relevance of these changes

by reporting correlations with motor impairment.

3.4.1 Linear surrogates

Linear surrogates provide a way of testing for the presence of non-linearity in the system that generated an observed time-series (Theiler et al. 1992). Here linear system refers to a stationary linear stochastic process, an example of which is a stationary linear Gaussian process (in discrete time an auto-regressive moving average model or ARMA model). As a reminder, an ARMA(p,q) model can be described as

$$y_n = \sum_{i=1}^{p} a_i y_{n-i} + \sum_{i=0}^{q} b_i \epsilon_{n-i}, \tag{3.1}$$

where ϵ_i are independent Gaussian white noise increments. The value at time n is a linear combination of past values and noise terms.

Linear surrogates preserve the linear properties of the data (linear correlations) but erase any potential non-linear structure. Besides the mean and standard deviation, linear properties are limited to the auto-correlation at all lags in the time domain, which is equivalent to the power spectrum in the frequency domain via the Wiener-Khinchin theorem. Fourier transform (FT) surrogates are the most straightforward implementation of this idea: the Fourier phases of the data Fourier transform are randomized, but its Fourier amplitudes are kept, which ensures that upon inverse Fourier transform, the generated time series will share the same linear properties as the data but none of their potential non-linear properties. This corresponds to generating surrogates according to a stationary linear Gaussian process (ARMA in discrete time) that shares the same power spectrum as the data. Note that the coefficients and the order of the model need not be estimated and are not determined by the procedure.

Iterated amplitude adjusted Fourier transform (IAAFT) surrogates improve on FT surrogates by providing an exact match of the values in the surrogates and the values present in the data (Schreiber and Schmitz 1996). This corresponds to

generating surrogates according to a stationary linear Gaussian process rescaled by an invertible, time-independent, non-linear measurement function:

$$y_n = h(z_n), \tag{3.2}$$

where h is the measurement function, z_n an ARMA model as described above, and y_n is constrained by the procedure to have the same PDF as the data, and approximately the same power spectrum. Thanks to h, the requirement that y_n has a Gaussian noise structure is relaxed. The IAAFT surrogate method in particular, but also a number of other methods, have been successfully applied in various fields. For in-depths reviews of the methods available and their applications, see (Schreiber and Schmitz 2000; Lancaster et al. 2018; Keylock 2019).

Both FT and IAAFT surrogates assume the data is stationary, which should be questioned in LFP recordings. In this work, even if the recordings used are short (on the order of 250 s), we rely on gradual wavelet reconstruction (GWR) surrogates, which can mitigate the nonstationarity issue. At the same time, GWR surrogates can quantify the strength of an effect by providing surrogates along a continuum parametrised by ρ, where $\rho = 0$ corresponds to IAAFT surrogates, and $\rho = 1$ corresponds to the data (Keylock 2010). More details on the GWR method can be found in Section B.1 in Appendix B. Nineteen GWR surrogates were computed from the filtered data for each patient and hemisphere, ON and OFF medication, and for each ρ levels ranging from 0 to 0.9 in steps of 0.1 with an additional value at 0.99 (as close to the data as possible). A range of surrogates are shown in Figure B.1 in Appendix B. Fixing the largest wavelet coefficients up to 10% of the total wavelet energy to the data values ($\rho = 0.1$) includes most of the data temporal variability in surrogates.

3.4.2 Change in a burst duration specific measure of non-linearity in the ON and OFF states

To evaluate dynamical changes between the ON and OFF states, we define a burst duration specific measure of non-linearity based on linear surrogates, and show that it is significantly greater OFF than ON medication.

We obtain average burst duration profiles and PSD from the filtered data and surrogates as in Section 3.3.2, except that no segmentation is done and the surrogates are not filtered (as they already reproduce the spectrum of the filtered data). Average burst duration profiles of linear surrogates and filtered data are shown for the right hemispheres of the eight patients in Figure 3.4 for $\rho = 0$. Similar figures are provided for a range of ρ levels for both hemispheres (Supplementary Figure B.5 and B.6 in Appendix B.6), and show that surrogates PSDs very closely match the data PSDs as expected.

As shown in Figure 3.3, panel A, we define a non-linearity measure specific to burst duration profiles as the sum of the squared differences between filtered data and linear surrogate average burst duration profiles, relative to the square of the mean value of surrogate average burst duration profile. We refer to this measure as BDDLS, which stands for burst duration distance to linear surrogates. We call the difference in BDDLS OFF and ON medication BDDLSdiff.

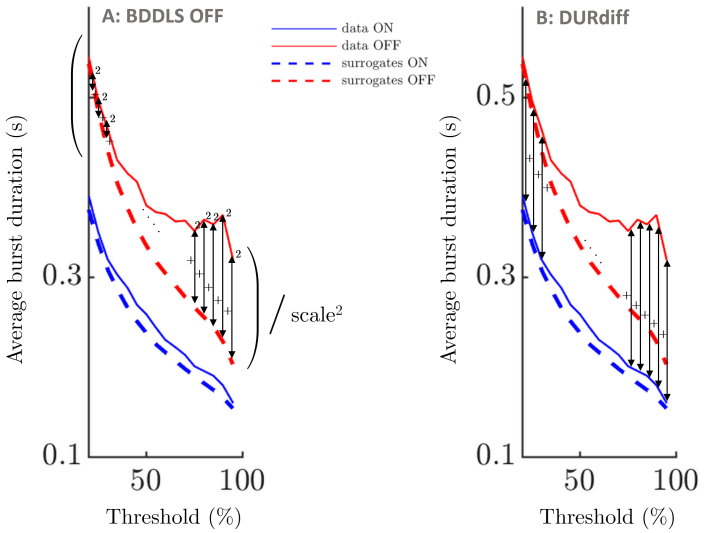

Figure 3.3: Sketch of burst duration metrics. A: illustration of burst duration distance to linear surrogates in the OFF state (BDDLS OFF). BDDLS OFF is defined as the sum of squared differences between data and linear surrogate average burst duration profiles for the OFF condition divided by the square of a scale. The scale is taken as the mean value of the OFF linear surrogate average burst duration profile. BDDLS ON is defined in a similar way, and BDDLSdiff is BDDLS OFF medication minus BDDLS ON medication. B: DURdiff is defined as the sum of the differences across thresholds between average burst duration profiles OFF and ON medication.

Our burst duration specific measure of non-linearity, BDDLS, was found significantly greater OFF than ON medication from $\rho = 0$ up to $\rho = 0.6$ under FDR correction as shown in Table 3.1 (one-tailed Wilcoxon signed rank test, all patients and hemispheres). The BDDLS measures include a scaling by the square of the mean value of the surrogate average burst duration profile which ensures that the effect is not due to the profiles of data and surrogates having overall larger values OFF medication. Two conclusions can be drawn from the effect being significant up to $\rho = 0.6$. Firstly, the effect is not due to nonstationarity in the data (as mentioned earlier, GWR surrogates at $\rho = 0.1$ already look very similar to the data, and thus capture the major non-stationary features that may be present). Secondly, significance up to $\rho = 0.6$ implies that a limited amount of phase randomization in the surrogates is enough to start seeing a significant difference between BDDLS OFF and ON medication, hinting at a strong effect. More details on ρ can be found in Section B.1 in Appendix B.

As a control, we calculated BDDLS OFF and ON medication for data band-pass filtered $\pm$ 3 Hz around 35Hz, for $\rho = 0$. The control is here to show that there is no difference between BDDLS OFF and ON medication in another frequency band, and the choice of ρ is therefore conservative (it is more likely to find a difference when the surrogates are the most different from the data). No effect of medication state on BDDLS was found (p = 0.449, and see Supplementary Figure B.7 and B.8 in Appendix B.6). This further suggests the effect does not come from differences in signal to noise ratio, as PSDs still vary considerably between the OFF and ON states in the controls. As BDDLS is greater in the pathological state, it is natural to ask whether BDDLSdiff correlates with motor impairment, which is what we focus on next.

ρ	0	0.1	0.2	0.3	0.4	0.5	0.6	0.7	0.8	0.99
p-val	**0.0010**	**0.0009**	**0.0010**	**0.0009**	**0.0003**	**0.0081**	**0.0012**	0.259	0.510	0.330

Table 3.1: Statistical significance of medication state effect on BDDLS. Showing p-values for the test that BDDLS is greater OFF than ON medication (sign rank test, all patients, both hemispheres) as a function of the GWR surrogate parameter ρ. P-values in bold are smaller than 5%, while green indicates significance under FDR correction.

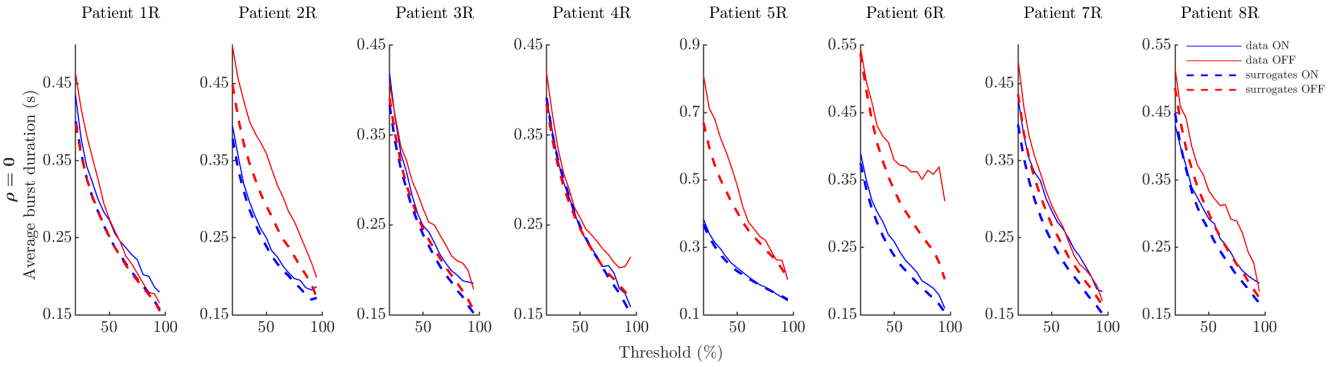

Figure 3.4: Average burst duration profiles ON and OFF medication for data and GWR surrogates at $\rho = 0$ (right hemispheres). In all panels, data profiles are solid lines, while linear surrogate profiles are dashed lines. The OFF medication state is indicated in red, and the ON state in blue.

3.4.3 Clinical correlations

To show that the difference in BDDLS OFF and ON medication, BDDLSdiff, is indicative of motor impairment, we also consider two other metrics as possible predictors of motor impairment. The first one is the relative difference between PSD OFF and ON medication called PSDdiff (the difference has to be relative to allow an analysis across patients as PSD levels vary greatly), and the second one is the sum of the differences between burst duration profiles OFF and ON medication across thresholds called DURdiff (similar scale across patients). DURdiff is illustrated in Figure 3.3, panel B. We measure motor impairment using the total unified Parkinson's disease rating scale (UPDRS) OFF medication. The correlations we report are for predictors and total UPDRS OFF averaged across sides.

BDDLSdiff correlates with total UPDRS OFF. The correlation is statistically significant under FDR correction from $\rho = 0.1$ to $\rho = 0.5$ (Spearman's correlation coefficients and associated p-values are shown in Table 3.2). This suggests a robust effect as explained previously. The other factors of interest PSDdiff (relative change in PSD) and DURdiff (change in burst duration) are also correlated with total UPDRS OFF medication (Spearman's correlation of 0.500, p = 0.216, and of 0.476, p = 0.243, respectively). The lack of significance for these factors is likely due to

the small sample size (8 subjects). The relationship between predictors and changes in clinical scores is plotted in Supplementary Figure B.9 in Appendix B.6.

ρ	0	0.1	0.2	0.3	0.4	0.5	0.6	0.7	0.8	0.99
correlation	0.571	0.738	0.810	0.929	0.833	0.810	0.333	-0.048	-0.571	0.595
p-val	0.1511	**0.0485**	**0.0218**	**0.0022**	**0.0154**	**0.0218**	0.428	0.935	0.151	0.132

Table 3.2: Spearman's correlations between BDDLSdiff and total UPDRS score OFF medication. Values presented as a function of the GWR surrogate level ρ. P-values in bold are smaller than 5%, while green indicates significance under FDR correction.

The three predictors considered are correlated (Spearman's correlations are 0.500, p = 0.216 between BDDLSdiff for $\rho = 0.2$ and PSDdiff, 0.476, p = 0.243 between BDDLSdiff for $\rho = 0.2$ and DURdiff, and 0.952, p = 0.001 between DURdiff and PSDdiff). However, scaling BDDLS by the mean value of surrogate average burst duration profile decorrelates as much as possible BDDLSdiff from DURdiff. Moreover, non-linear correlations cannot be recovered from the PSD (the power spectrum only captures linear correlations) which implies that BDDLSdiff should contain information not present in PSDdiff if there is non-linearity in the system expressed in the bursting profiles.

We have made apparent that changes in temporal patterning of beta activity between medication states can be related to an increase in our burst duration specific non-linearity metric OFF medication, and that changes in the BDDLS metric are correlated with motor symptoms. Average burst duration profiles OFF medication rank higher on the BDDLS metric and can therefore be thought of as being generated by a more non-linear system than ON medication. To get a clearer idea of which specific dynamical changes could be at play between the ON and OFF states, we proceed to model one patient at each end of the BDDLS spectrum with biologically inspired models, and compare both dynamical systems.

3.5 Approaching dynamical changes using neural mass models

To investigate which particular changes to the dynamics of a biologically inspired model of the STN-GPe loop could account for the changes in the temporal patterning of beta oscillations between the OFF and ON condition, we fit WC models to patient data. We choose patients whose average burst duration profiles deviate the least and the most from their linear surrogates. These patients are patient 3, left hemisphere, in the ON state (lowest BDDLS for $\rho = 0$, see Supplementary Figure B.5 in Appendix B.6), and patient 6, right hemisphere, OFF medication (most striking deviation from its linear surrogate and greatest BDDLS for $\rho = 0$, see Figure 3.4). We denote these datasets patients 3L ON and 6R OFF, respectively. We note that the average burst duration profile of patient 3L ON is close to its linear surrogate (for $\rho = 0$). Since the average burst duration profiles of linear surrogates all closely match when z-scored (see Supplementary Figure B.10 in Appendix B.6), it is likely that patient 3L ON should also be representative of linear systems in general.

3.5.1 Fitting a linear Wilson-Cowan model to the lowest BDDLS patient

We start by fitting to patient 3L ON the time discretization of a linear WC model, which can be seen as a multivariate version of an ARMA model (equation (3.1)). This linear WC is a simplification of the WC model introduced in Section 1.2.3.1. The WC is a natural choice as it can be mapped onto the basal ganglia STN-GPe loop as shown in Figure 3.5 and reviewed in Section 1.2.3.3. The LFP recordings used in this study have been obtained from DBS electrodes implanted in the STN, and therefore we model the LFP signal by the activity of the excitatory population. The STN and GPe are reciprocally connected, and the STN receives a constant excitatory input from the cortex, while the GPe receives a constant inhibitory input from the striatum, and is also self-inhibiting. Uncorrelated inputs, specifically Gaussian white noise, are added to each population, and the STN activity, E, and

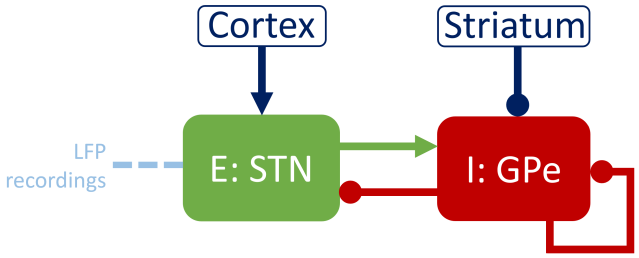

Figure 3.5: Mapping of the Wilson-Cowan model onto the STN-GPe loop. The excitatory population E and the inhibitory population I model respectively the basal ganglia STN and GPe. Arrows denote excitatory connections or inputs, whereas circles denote inhibitory connections or inputs. The DBS electrode is implanted in the STN (indicated by the dashed light blue line) and records the STN LFP. The STN also receives an excitatory input from the cortex, while the GPe receives an inhibitory input from the striatum, and also has a self-inhibitory loop.

the GPe activity, I, are described by the stochastic differential equations

$$\begin{cases} dE = \frac{1}{\Omega_E}\left(-E + f_\beta(\lambda_E - w_{IE}I)\right)dt + \zeta dW_E, \\ dI = \frac{1}{\Omega_I}\left(-I + f_\beta(-\lambda_I + w_{EI}E - w_{II}I)\right)dt + \zeta dW_I, \end{cases} \tag{3.3}$$

with w_{PR} the weight of the projection from population "P" to population "R", λ_P the constant input to population "P", Ω_P the time constant of populations "P", dW_E and dW_I are Wiener processes, and ζ the noise standard deviation. In this attempt to describe the simplest average burst duration profiles, we use a linear activation function simply given by $f_\beta(x) = \beta x$, parametrized by its slope β.

The time discretized model is fitted to two data features, namely the data PSD and the data average burst duration profile. How fitting is carried out is described in Section B.2 in Appendix B. As the model output E models the centered LFP recordings, a model of the beta envelope is obtained by considering the Hilbert amplitude of E.

The best fit to patient 3L ON is shown in the first row of Figure 3.6, and we report the corresponding model parameters in supplementary Table B.1 in Appendix B.5. The linear WC model is able to reproduce both the data PSD and average burst duration profile ($R^2 = 0.726$, see Figure 3.6, panels C1 and D1). The input parameters λ_E and λ_I only contribute to transients in the linear WC model, and are therefore set to zero here. They will have an influence on the model output when non-linearity is introduced.

We have shown that a linear WC model can fit to the lowest BDDLS patient, and we next fit increasingly complex WC models to patient 6R OFF to investigate the OFF medication case.

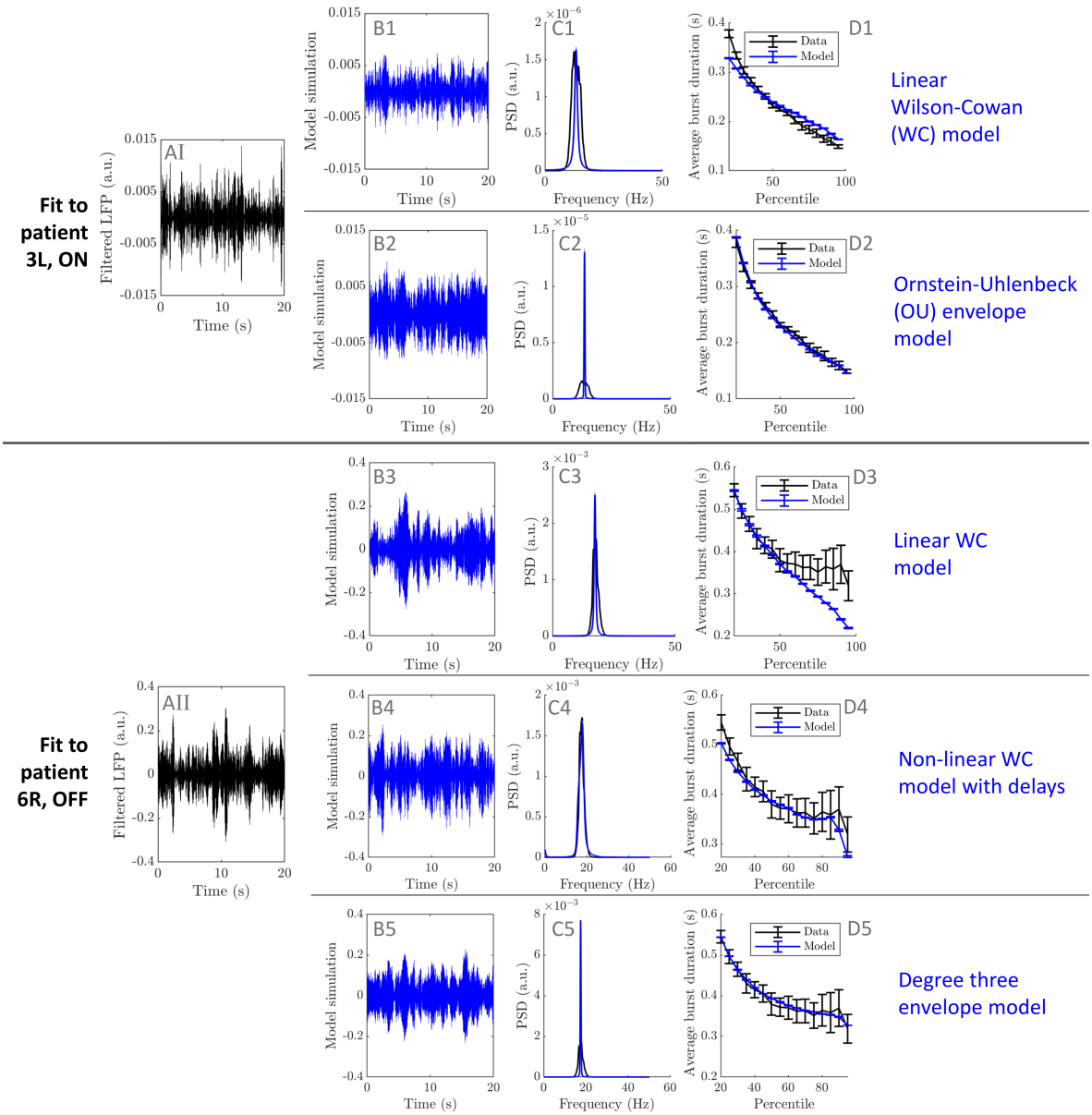

Figure 3.6: Best model fits. Showing best fits to patient 3L ON (first two rows), and patient 6R OFF (next three rows). Patient data is color coded in black, models in blue. Each row corresponds to a given model as labelled in blue. The first column shows twenty seconds of filtered LFP recording (A panels), while model oscillatory activity output is plotted in the second column (B panels). Data and model PSDs are compared in the third column (C panels), and data and model average burst duration profiles are shown in the last column (D panels, sem error bars).

3.5.2 Fitting Wilson-Cowan models to the highest BDDLS patient

The same procedure as before is used to fit the time discretized linear WC model to patient 6R OFF. The best fit is shown in Figure 3.6, third row, and we report the corresponding model parameters in Supplementary Table B.1 in Appendix B.5. The linear WC model is able to reproduce the data PSD but does not fit well to the data average burst duration profile ($R^2 = 0.312$ overall, see Figure 3.6, panels C3 and D3).

We next introduce the time discretization of a non-linear WC model, which is identical to the linear WC model (see Figure 3.5), except that its activation function

$$g_{\beta,\eta}(x) = \frac{\eta}{1 + e^{-\beta(x-1)}} \tag{3.4}$$

is non-linear and that connections carry a delay. The system of equations (3.3) is therefore modified as

$$\begin{cases} dE_t = \frac{1}{\Omega_E}\left(-E_t + g_{\beta,\eta}(\lambda_E - w_{IE} I_{t-\Delta_{IE}})\right) dt + \zeta dW_{E,t}, \\ dI_t = \frac{1}{\Omega_I}\left(-I_t + g_{\beta,\eta}(-\lambda_I + w_{EI} E_{t-\Delta_{EI}} - w_{II} I_{t-\Delta_{II}})\right) dt + \zeta dW_{I,t}, \end{cases} \tag{3.5}$$

where Δ_{PR} is the delay from population "P" to population "R", and η a scaling parameter.

The best fit to patient 6R OFF obtained with the same fitting methodology as before is shown in the fourth row of Figure 3.6, and we report the corresponding model parameters in Supplementary Table B.2 in Appendix B.5. The non-linear WC model with delays is able to reproduce well the data average burst duration profile and the data PSD ($R^2 = 0.91$, see Figure 3.6, panels C4 and D4).

In summary, this section has demonstrated that in a biologically inspired E/I model, reproducing the most striking average burst duration profile in the OFF condition requires the addition of delays and a non-linear (sigmoidal) activation function compared to typical ON profiles. The need for non-linearity agrees with the surrogate analysis carried out previously, but the present results also delineate the specific differences in dynamics of a biologically inspired model required to reproduce the two conditions studied.

In some cases, the envelope of E/I models can be related to what we call in this work "envelope models" (illustrated in Figure 3.1). Indeed, it was shown in (Powanwe and Longtin 2019) that the envelope of a linear WC model is a Rayleigh process, assuming the ratio of the E and I envelopes is constant, and the phase delay between E and I oscillations is also constant. A Rayleigh process is in fact a particular type of envelope model. We next investigate whether a conclusion similar to that of this section on E/I models holds for envelope models that provide a direct, simpler description of envelope dynamics. Additionally, we will study envelope models analytically to obtain additional insights.

3.6 Approaching dynamical changes using envelope models

To obtain the simplest polynomial dynamics describing the OFF and ON conditions (as represented by patient 6R OFF and patient 3L ON, respectively), we consider envelope models directly describing the LFP envelope and fit them to data. Further, to describe the dependence of burst duration on model parameters, we derive an approximate analytical expression for the average burst duration profile, and apply it to the model describing the ON condition.

3.6.1 Fitting envelope models to burst duration profiles

The time discretization of the simplest stochastic process with state dependent drift and uncorrelated white noise, the Ornstein-Uhlenbeck (OU) process, is in fact enough to model the average burst duration profile of patient 3L ON, which is representative of linear systems and of the ON condition. The OU process is described by the stochastic differential equation

$$dx = -\theta x dt + \zeta dW, \tag{3.6}$$

where W is a Wiener process, θ a positive decay parameter, and ζ the constant noise standard deviation. To illustrate the ability of such a system to also model

oscillatory activity, the phase equation

$$\dot{\phi} = 2\pi\nu \tag{3.7}$$

is added, where ν is a constant frequency. Oscillatory activity can then be generated as $z(t) = x(t)\cos\phi(t)$.

To reproduce the average burst duration profile of patient 6R OFF, we extend the drift function of the OU model to include non-linear polynomial terms. Since degree two polynomials could not fit the data (not shown), we are considering the time discretization of a degree three model

$$dx = \left(d_3x^3 + d_2x^2 + d_1x + d_0\right)dt + \zeta dW, \tag{3.8}$$

where d_0 to d_3 are constants. As before, the independent phase equation (3.7) is added to the envelope model.

The resulting models are fitted to the average burst duration profile of patient 3L ON, and patient 6R OFF, respectively. The frequencies ν are adjusted to match the data peak frequencies, and the models are scaled so the standard deviation of z roughly matches that of the data. In the simple OU model, the envelope is prevented from being negative by shifting it by the absolute value of its 0.1^{th} percentile, and setting values below that to zero. In the degree three model, a positive envelope is enforced by retaining only the absolute value of the next point at each integration step, which has a negligible impact on positive thresholds. Remaining model parameters are optimised (procedure in Section B.2 in Appendix B) to obtain the best fit of the data average burst duration profile with $x(t)$ directly modelling the beta envelope.

The best fits to patient 3L ON and 6R OFF are shown in the second and last row of Figure 3.6, and we report the corresponding model parameters in Supplementary Table B.3 and Table B.4 in Appendix B.5, respectively. The OU model is able to reproduce the data average burst duration profile of patient 3L ON well ($R^2 = 0.996$ for burst duration only, see panel D2 of Figure 3.6), and so is the degree three model for patient 6R OFF ($R^2 = 0.976$ for burst duration only, see panel D5 of

Figure 3.6). In both cases, oscillatory activity at the data peak frequency can be generated from the envelope model (Figure 3.6, panels C2 and C5).

As in the previous section, we conclude that reproducing the OFF average burst duration profile most strikingly different from its surrogate's profile requires the addition of non-linearity compared to typical ON profiles, which can be reproduced with an OU model. The non-linearity takes the form of a degree three polynomial drift function. We have shown that envelope models can successfully model patient average burst duration profiles, and we next study analytically how to express average burst duration profiles as a function of envelope model dynamics.

3.6.2 Average burst duration and exterior problem mean first passage time

In order to study the dependence of burst duration on envelope model parameters, we seek an analytical expression for the average burst duration profile of envelope models. As recently noted in (Powanwe and Longtin 2019), the concept of average burst duration is related to the concept of mean first passage time (MFPT, also known as mean exit time) in the exterior problem. Considering a threshold or boundary L and a starting point $x_0 = L + \delta$, with $\delta > 0$, we denote the continuous time MFPT from x_0 to L by $\tau_{x_0,L}$. It is defined by the expectation of the random variable $\inf\{t \geq 0 : x_t \leq L\}$. At this point it should be clarified that the average burst duration of a continuous time stochastic process with Gaussian noise is always zero, as all trajectories starting from the threshold L will cross it again in vanishingly short times. In addition, MFPTs in continuous time are systematically biased towards shorter first passage times since a continuous stochastic model is more likely to cross the boundary when close to it than its discrete time counterpart. However, we can adapt classical MFPT results from continuous time stochastic process literature to analytically approximate the average burst duration of the corresponding models in discrete time. In what follows, we use a tilde to distinguish quantities that can be measured readily in a time discretized system from the continuous system quantities.

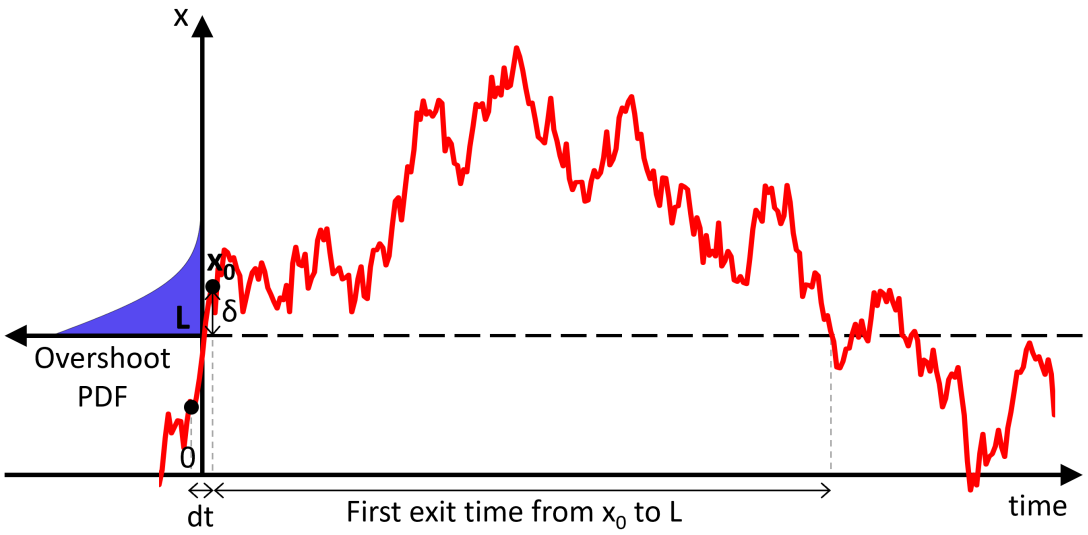

Figure 3.7: First exit time and overshoot distribution. Showing a discrete realisation of an OU process overshooting the threshold L by δ, with a sketch of the overshoot probability density at L in purple. The first exit time from x_0 to L is the time taken to get below L for the first time, starting from x_0.

To study the associated discrete time model with time step dt, we are considering the continuous case of a stochastic process

$$dx_t = \mu(x_t)dt + \zeta dW_t, \tag{3.9}$$

where we have assumed that the real valued drift function μ can depend on x_t, and that ζ is constant in time and space. Following a derivation similar to that reviewed in (Grebenkov 2014), we show in Appendix B (see Section B.3.1) that the MFPT of the continuous system is given by

$$\tau_{x_0,L} = \frac{2}{\zeta^2}\int_{x_0}^{L}\int_{x}^{+\infty} e^{\frac{2}{\zeta^2}\int_x^{x_1}\mu(x)dx} dx_1 dx. \tag{3.10}$$

For the integral to converge, it is necessary to have $\mu(x)$ be non-vanishing and negative at $+\infty$, which is necessarily the case in models describing neural oscillations. Equation (3.10) cannot be applied to white noise only, where $\mu(x) = 0$. From there, we derive the average burst duration for the discretized model with time step dt. We show in Appendix B (see Section B.3.2) how to correct for the systematic bias of the continuous model (Steps 1 and 2). We also detail therein how to relate average burst duration and MFPT (Step 3): when crossing a threshold L from below at

the start of a burst, a discrete model will always overshoot the threshold, and the average burst duration at threshold L can be related to MFPTs by taking into account the overshoot distribution at L (see Figure 3.7). We finally obtain to first order in $\sqrt{dt}$ the average burst duration $\widetilde{\tau}_L$ for the discrete time model as

$$\widetilde{\tau}_L \approx \frac{\sqrt{2\pi dt}}{\zeta} \int_L^{+\infty} e^{\frac{2}{\zeta^2}\int_L^{x_1}\mu(x)dx} dx_1. \tag{3.11}$$

Equation (3.11) provides a general relationship from drift function to average burst duration profile for the discretization of stochastic envelope models described by equation (3.9). As shown in Figure 3.8, this result applied to the OU model and the degree three model (equation (3.12) below and equation (B.33) in Appendix B) is very close to simulations.

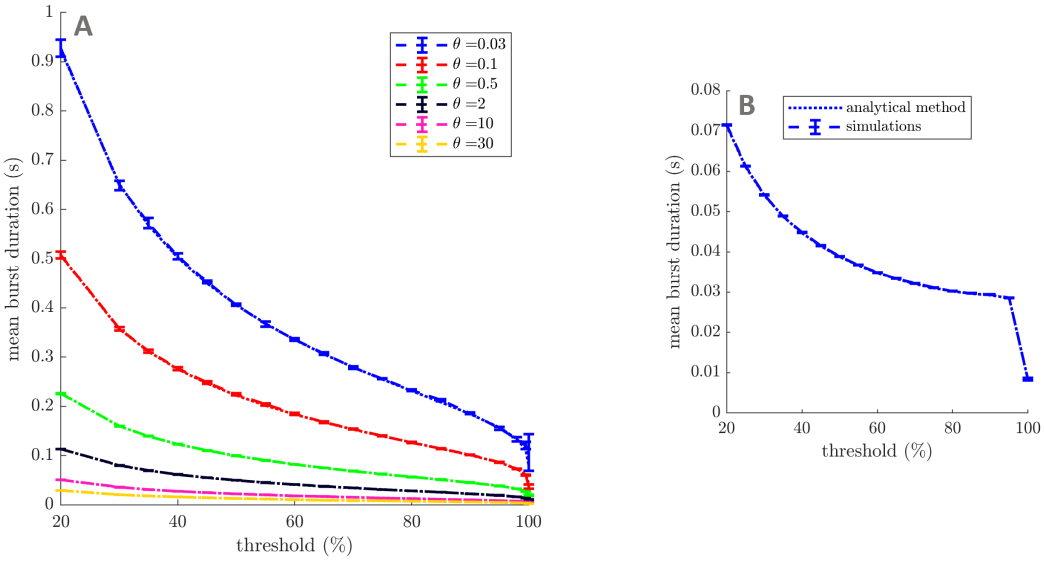

Figure 3.8: Simulations of average burst duration profiles for OU processes and the fitted degree three polynomial model. Average burst duration profiles from simulations of OU processes are compared to equation (3.12) for a range of decay parameters and $\zeta = 1$ in panel A. Similarly, average burst duration profiles from simulations of the fitted degree three polynomial envelope model are compared to equation (B.33) in panel B. Simulations are indicated by dashed lines (sem error bars), and analytical results by dotted lines. Simulations consist of five repeats of 10^5 s, with a time step of 1 ms (simulations of the OU process are done according to the exact updating equation (B.2)).

3.6.3 Increasing average burst duration in the OU model

Building on the previous result, we highlight the dependence of average burst duration on model parameters and show how bursts can be lengthened in the

discretized OU model, which is representative of the ON condition and of linear systems in general (see Supplementary Figure B.10 in Appendix B.6). We are considering here the discretization of an OU process centered on zero (equation (3.6)). Equation (3.11) gives, to first order in $\sqrt{dt}$,

$$\widetilde{\tau}_L \approx \pi \sqrt{\frac{dt}{2\theta}} e^{\frac{\theta L^2}{\zeta^2}} \operatorname{erfc}\left(\frac{\sqrt{\theta} L}{\zeta}\right), \tag{3.12}$$

where erfc is the complementary error function. The dependence of average burst duration on parameters is easier to see when L is expressed as a percentile of the time series values, which is also how we present average burst duration profiles. Because of this choice, the shift introduced earlier to ensure the envelope stays positive will have no impact on the result.

We express the average burst duration of a discrete OU process as a function of threshold percentile using the stationary probability distribution of the OU process (see Section B.3.3 in Appendix B). We obtain

$$\widetilde{\tau}_L \approx \pi \sqrt{\frac{2dt}{\theta}} \left(1 - L_{\%}\right) e^{\left\{\operatorname{erf}^{-1}(2L_{\%} - 1)\right\}^2}, \tag{3.13}$$

where $L_{\%}$ is the percentile rank (between 0 and 1) corresponding to threshold L. Equation (3.13) does not depend on the noise parameter ζ (which only scales trajectories), and makes apparent a simple dependence of the average burst duration on the decay parameter. We can conclude that increasing the average burst duration for a given threshold corresponds to decreasing the decay in the OU model, which is what is intuitively expected.

We demonstrated that discretized envelope models can reproduce patient average burst duration profiles, and provided the polynomial forms of the drift functions required. In addition, the average burst duration profile of discretized envelope models can be approximated analytically, which yields insights into how model parameters influence average burst duration profiles. This analytical result opens the question of a reverse link from average burst duration profile to dynamics, which we investigate next.

3.7 Average burst duration profiles are a signature of envelope dynamics

In this section, we establish that average burst duration profiles are a signature of envelope dynamics by showing that the envelope drift function can be recovered from the average burst duration profile. This clarifies how a change in the temporal patterning of beta oscillation signals a change in dynamics.

3.7.1 Relationship between envelope drift function and average burst duration profiles

To highlight the importance of burst duration profiles as a marker of dynamics, we establish a link for a general class of stochastic processes with additive noise between the average burst duration profile, the noise standard deviation, and dynamics. We are considering a time discretization (time step dt) of the stochastic process given by equation (3.9). As a reminder, we assume that the real valued drift function μ can depend on x_t, and that the diffusion term ζ is constant in time and space. We show in Section B.4 in Appendix B, that to first order in $\sqrt{dt}$,

$$\mu(L) \approx -\zeta \frac{\sqrt{\frac{\pi dt}{2}} + \frac{\zeta}{2}\frac{\partial \widetilde{\tau}_L}{\partial L}}{\widetilde{\tau}_L}. \tag{3.14}$$

Equation (3.14) highlights a direct relationship from average burst duration to envelope dynamics (drift function) in discrete time. This is essentially a local relationship (at threshold L), and the drift function can be estimated where the average burst duration profile is known. We call this estimation procedure the "passage method", and show next that it can recover envelope dynamics in synthetic data and patient data.

3.7.2 Inferring dynamics in synthetic data from envelope models and in patient data with the passage method

To validate the method, we first test the passage method on synthetic data. We are considering envelope time series of 250 s (roughly the same length as data) and of 1000 s generated from an OU envelope model (same parameters as best fit

to patient data, see Supplementary Table B.3 in Appendix B.5) and a degree five polynomial envelope model (see equation (B.35) in Appendix B, parameters given in Supplementary Table B.5). The degree five polynomial model provides more complex dynamics to infer than the degree three polynomial introduced earlier. Dynamics from these time series are recovered using the passage method. We are considering three hundred thresholds, and applying smoothing to $\widetilde{\tau}_L$ and its derivative (full details provided in Section B.4 in Appendix B). The results are shown in the first two rows of Figure 3.9. Approximations of the drift functions μ are recovered for the OU and degree five polynomial models (Figure 3.9, panels A1 and A2). The average burst duration profiles and inverse cumulative distribution functions (CDFs) obtained from simulating the recovered dynamics approximate the synthetic data well (Figure 3.9, panels B1 and B2, and panel C1 and C2, respectively). Dynamics and associated features recovered from longer time series are a better approximation than dynamics recovered from shorter time series. Performance is however reasonable for shorter time series, which are approximately the duration of patient data recordings.

Given its success on synthetic data, the method is tested on patient data. We pick the patient that scores the highest on our burst duration specific non-linearity measure, patient 6R OFF (as for non-linear fits), and the same patient and hemisphere ON medication for comparison. The method is applied as before, with the additional estimation of the noise parameter and the time step (specifics of the application of the method to patient data detailed in Section B.4 in Appendix B). The results are shown in the last two rows of Figure 3.9. There is no ground truth to compare the recovered dynamics against (Figure 3.9, panels A3 and A4), but the average burst duration profiles and inverse CDFs obtained from simulating the recovered dynamics are a good match to the data. We note that the dynamics inferred ON medication are closer to a straight line, which supports the hypothesis of more non-linearity OFF medication.

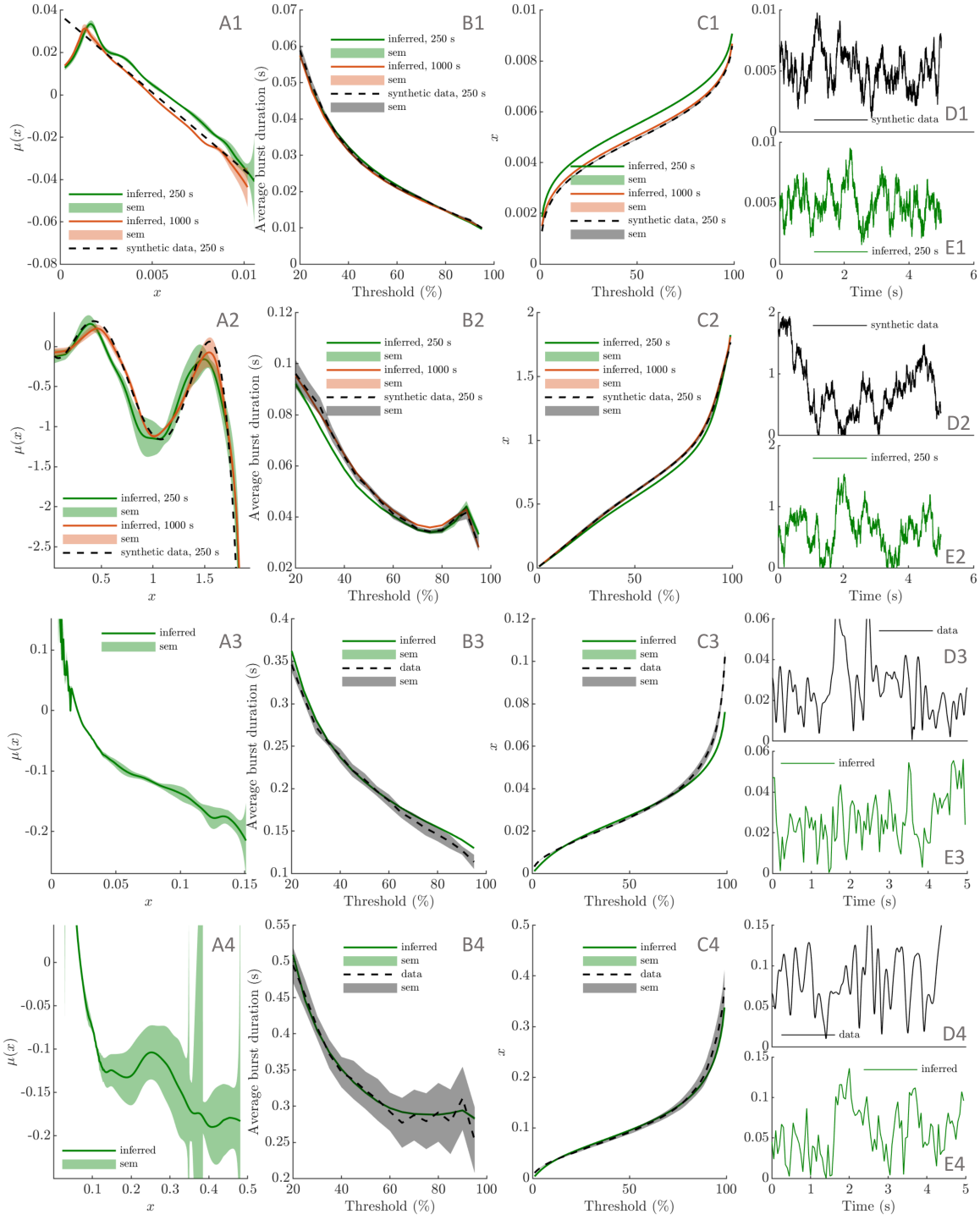

Figure 3.9: Recovering envelope dynamics with the passage method.The method is applied to synthetic data (OU model in the first row, degree five polynomial model in the second row), and patient data (patient 6, right, ON medication in the third row, and patient 6, right, OFF medication in the last row). The recovered drift functions (μ) are shown in the first column, and the average burst duration profiles and the inverse CDFs simulated from the recovered dynamics in the second and third column, respectively. Ground truths are provided when available (black dashed line). Synthetic data results are presented for 250 s and 1000 s of synthetic data. In the last column, 5 s of simulated data from the recovered dynamics is compared to training data (panels D and E share the same time axis).

3.7.3 Comparison of the passage method with a direct method

To evaluate the performance of the passage method in extracting envelope dynamics from data, we compare our method with a simpler envelope recovery method that directly tries to estimate time derivatives from the envelope time series. Specifically, time derivatives are calculated as a first order difference, and the data is binned in 300 bins of equal width (same number of bins as the number of thresholds in our method) within which derivative values are averaged.

Both the simple method and the passage method are applied to envelope time series of a range of durations from 100 s to 1000 s generated by the OU model and the degree five polynomial model used in previous tests. The passage method is applied as described in Section B.4 in Appendix B, expect that no smoothing is applied to either the passage method or the direct method for a fair comparison. The sum of the squared errors between the recovered drift function μ and the corresponding ground truth is calculated for both methods for each time series, and the results are presented in Figure 3.10. The passage method is at a slight advantage in the OU case as well as in the degree five polynomial case.

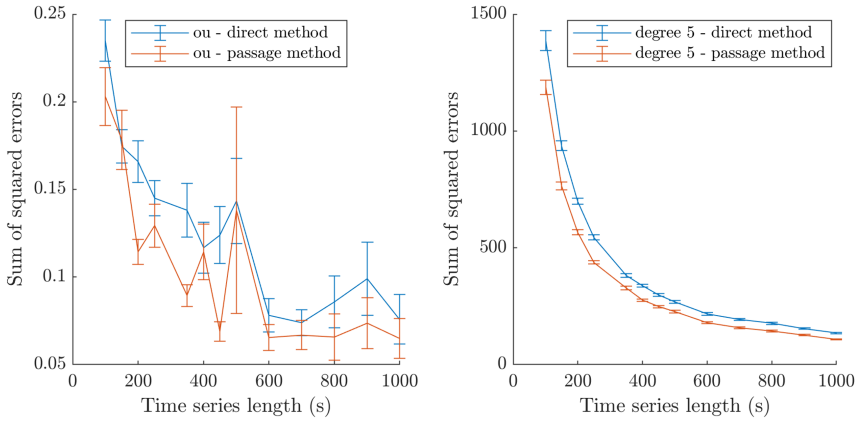

Figure 3.10: Comparison of the passage method and the direct method on synthetic data. Showing the sum of squared errors between the inferred μ function and the actual one for both methods as a function of the duration of synthetic data available. The training data were generated from an OU process (left) and a degree five polynomial (right). In both cases, the mean and sem errors are obtained for a large number of repeats (150 repeats from 100 s to 250 s, 100 repeats from 350 s to 450 s, and 50 repeats from 500 to 1000 s).

3.8 Discussion

In this study, we analysed PD patients' STN LFP recordings in the beta band and first motivated the choice of average burst duration as a marker of the differences in bursting activity ON and OFF medication. We found a burst duration specific measure of non-linearity based on linear surrogates to significantly increase from the ON to the OFF medication state, and the change in this non-linearity measure to be correlated with motor impairment. We further narrowed-down dynamical changes underlying the changes in beta oscillation temporal patterning between medication states by fitting models to data. The biologically inspired WC model could reproduce a typical ON average burst duration profile with a linear activation function, while the most striking OFF profile required a non-linear activation function and the addition of delays. Similarly, envelope models, where the beta envelope is directly described by the discretization of a stochastic process with constant noise, required a linear drift function (OU process), and a degree three polynomial drift function, respectively. The simplicity of envelope models allowed to derive an approximate expression for average burst duration profiles (equation (3.11)), which clarified how model parameters affect average burst duration in the linear case. Further, we showed that the non-linearity can be directly extracted from average burst duration profiles using our "passage method" (based on equation (3.14)), demonstrating that average burst duration profiles are a signature of envelope dynamics. This sheds light on why burst duration has been suggested in multiple studies as an important biomarker in PD.

Bursting features Average burst duration profiles are an insightful and exhaustive way of characterising bursting dynamics. Average profiles across thresholds benefit from information from a range of thresholds and capture more about the system than the burst duration distribution at one threshold (which may only integrate dynamical information, and predominantly above the threshold). In fact, we demonstrate that average burst duration profiles are closely related to the dynamics of the beta envelope. They can also provide insights into bursts

shape: the levelling of a burst duration profile at higher thresholds can be related to sharp and long bursts of high amplitude. Some previous studies have used wavelet amplitude as the beta envelope to study bursting features (Tinkhauser et al. 2017b; Tinkhauser et al. 2017a), while we used the Hilbert envelope of the filtered signal. We found little difference between the methods as far as average burst duration is concerned (not reported). While a number of recent studies define bursts as Hidden Markov Model states (Heideman et al. 2019; Quinn et al. 2019) or using support-vector machines (Schmidt et al. 2019), we aim at providing a more complete dynamical picture of beta dynamics.

Besides the PSD, our statistical analysis of patient STN LFP recordings identified burst duration across thresholds as the feature most suited to distinguish between burst dynamics in the ON and OFF states. We highlight the importance of individually z-scoring the filtered data when comparing average burst amplitude profiles between medication states to control for differences simply due to differences in mean beta power. A similar result has been reported in a non-human primate study (Deffains et al. 2018) where beta burst duration was found to be a better differentiator of healthy and pathological episodes in the STN. Deleting longer beta episodes resulted in a greater decrease of parkinsonian activity than deleting stronger episodes. In our patient analysis, the ON medication state gives an approximation to the physiological state. It is hypothesised that shorter bursts are more likely to be physiological, whereas longer burst are more likely to be pathological (Tinkhauser et al. 2017b; Tinkhauser et al. 2017a). Longer bursts are known to be associated with more synchronization in the STN, but also across the motor network (Tinkhauser et al. 2018). This results in less information coding capacity (Brittain and Brown 2014) and may underlie the motor symptoms.

Surrogate analysis Our burst duration specific measure of non-linearity, BDDLS, provides a new dimension that can be used to analyse LFP recordings. Non-linearity here should be understood as non-linear correlations in the time series of interest (a sinusoid is considered linear, as it can be represented by an ARMA model,

see Section 3.4.1). We showed that, in the case of PD, the difference in BDDLS between medication states in STN LFPs is correlated with motor impairment. The correlation for $\rho = 0$ to 0.5 was on par or better than the correlation obtained with the relative difference in power and the difference in burst duration. However this should be re-evaluated on larger datasets. Predicting burst duration based on PSD alone will not be accurate for patients who have different average burst duration profiles than their linear surrogates, which is the case for most patients OFF medication. This is because the PSD only reflects linear correlations. Changes between the ON and OFF states are of one of three types. The first one is mostly "linear" changes (e.g. patient 5, right, in Figure 3.4, where both the ON and OFF average burst duration profiles are close to their surrogates and there is a large difference between surrogates). The second one is mostly "non-linear" changes (e.g. patient 4, right, in Figure 3.4, where the ON profile matches its surrogate and the OFF surrogate, and the OFF profile differs from its surrogate). The third one is both "linear" and "non-linear" changes (e.g. patient 6, right, in Figure 3.4, where the ON profile is close to its surrogate, and there is a large difference between surrogates and between the OFF profile and its surrogate). These categories could provide a basis to stratify patients, in particular if similar results could be obtained from non-invasive EEG recordings. The scaling by the mean value of the surrogate profile that was applied to BDDLS helped decorrelate BDDLS from the difference in burst duration (DURdiff). We defined DURdiff as a difference between data burst duration profiles for simplicity, but it may be the case that defining DURdiff as the difference between linear surrogates decorrelates BDDLSdiff and DURdiff further and improves predictive power.

Surrogate testing has been used to explore non-linearity in brain recordings in pathological states. In particular it has been reported that epileptic seizures are associated with non-linear brain dynamics, while little non-linearity was found in Alzheimer's disease (reviewed in Stam 2005). In the context of PD, we found an increase in a burst duration specific measure of non-linearity in the pathological state compared to ON medication. From an information theoretic perspective,

non-linear correlations between frequencies within the beta band may further reduce information coding capacity, and impair motor function. On a related note, scalp EEG recordings over the sensorimotor cortex of PD patients were found to have more pronounced non-sinusoidal features in the beta band OFF medication compared to ON medication (Jackson et al. 2019) and OFF DBS compared to ON DBS (Cole et al. 2017). Non-linear correlations between different frequencies in STN LFP rhythms have been reported to be greater OFF than ON medication (Marceglia et al. 2006). STN LFPs were also described as more non-linear during resting tremor in PD (Camara et al. 2019), but our non-linearity measure is specific to burst duration in the beta band and may therefore be more specific to bradykinesia and rigidity.

Non-linear correlations are not seen in average power, and we showed that they are correlated with motor impairment, which has implication for aDBS in PD patients. A slow variant of aDBS provides stimulation according to average beta power on a 50 s time scale (Rosa et al. 2017a; Arlotti et al. 2018). Slow aDBS will not address selectively the aspect of the pathology we highlighted in this study, since average power cannot reflect non-linear correlations. Providing aDBS according to a predictive algorithm based on the frequency information contained in a 300 ms window before burst onset was reported in PD to be very close in performance to optimised aDBS, i.e. to threshold based stimulation (Moraud et al. 2018). Moreover, it appears that pathological synchronization is established earlier than common thresholds used to define beta bursts (Cagnan et al. 2019c). Non-linear information not present in the windowed power spectra studied in (Moraud et al. 2018) may provide additional predictive power, and linear surrogates estimated on a slower time scale than real time could provide a useful baseline to compare current recordings against. The computational cost of GWR surrogates rules them out, but computationally cheaper IAAFT surrogates may be better cut out for the task. Although GWR surrogates were used in our study to account for potential nonstationarity in LFP recordings, a correlation with clinical scores was observed for $\rho = 0$, which corresponds to IAAFT surrogates. Average burst duration profiles and BDDLSdiff have been studied on a slow time scale (about 250 s of data). How

little data can be used to reliably estimate BDDLSdiff remains to be explored, and other surrogate based non-linearity measures may be more suited to real-time use. Nevertheless, closed-loop DBS targeting non-linearity in the drift function might prove more selective in suppressing pathological oscillations than closed-loop DBS approaches based on amplitude. Additionally, amplitude thresholds in aDBS would need to change with medication and activity level, and a stimulation strategy not requiring an amplitude threshold would be simpler.

Modelling burst duration profiles As one could expect, linear models could fit to the average burst duration profile which scored the lowest on our burst duration specific measure of non-linearity. This profile was taken as a representative example of average burst duration profiles of linear systems, which were found to have a typical shape (potentially scaled and shifted). The linear models chosen were a linear WC model without delays and an OU envelope model. On the one hand, the architecture of the former can be mapped onto the STN and GPe populations (as reviewed in Section 1.2.3.3), and it only has a few parameters, making it easier to constrain and less likely to overfit the data. On the other hand, the latter is perhaps the simplest stochastic envelope model with a non constant drift term, and is a simplification of the Rayleigh envelope model, which has been shown to describe the envelope of the linear WC model under certain assumptions (Powanwe and Longtin 2019) as mentioned in the Section 3.5.

The data average burst duration profile that scores the highest on our burst duration specific measure of non-linearity could be modelled by more complex versions of the successful linear models, namely the non-linear WC with delays, and a degree three polynomial envelope model (the OU envelope model can be seen as a degree one polynomial model). Complexity was increased gradually to avoid overfitting. A linear WC model without delays could not fit the data, and a non-linear WC model without delays could not fit the data either (not shown), but the non-linear WC model with delays was successful. Similarly, a

degree two polynomial was found to not fit the data (not shown) before the degree three polynomial was introduced.

Dynamical changes identified in both models between medication states deserve further discussion. While it could be tempting to conclude from the WC fits that delays are necessary to reproduce the data from patient 6R OFF, the degree three polynomial envelope model suggests that non-linearity is enough to reproduce the data and that delays are not necessarily required in all models. The levelling off at high thresholds of an average burst duration profile such as that of patient 6R OFF could be explained by larger oscillations getting stability from an additional attractor. Multistability could be a dynamical interpretation of such features in the average burst duration profile, and could open the door to a dynamical definition of bursts as events in the vicinity of an attractor at larger amplitude. However multistability turns out to not be a requirement since the best fit degree three polynomial model to patient 6R OFF, and the dynamics inferred by the passage method applied to the same patient, do not exhibit multistability but produce an average burst duration profile close to the data (see Figure 3.6, and panels A4 and B4 of Figure 3.9). The "bump" seen in panel A4 of Figure 3.9 is not indicative of multistability since it does not cross the horizontal axis, but suggests an attractive influence at the corresponding amplitude level. It is unclear how this attractive influence could be interpreted in terms of physiological processes at this point.

It is well know that simple WC models of the STN-GPe loop can generate sustained beta oscillations without the need for correlated inputs (see Section 1.2.3.3), but whether it is the case for transient beta has not been reported. The finding that a simple STN-GPe WC model with uncorrelated noise as inputs can reproduce the most complex average burst duration profile of the dataset, i.e. realistic transient beta oscillations, is consistent with the theory that the STN-GPe loop could play a predominant role in the generation of pathological beta activity (Terman et al. 2002; Holgado et al. 2010; Tachibana et al. 2011; Pavlides et al. 2012).

Analytical expression of average burst duration in envelope models Standard first-passage results are available for continuous time stochastic processes (see for instance Grebenkov 2014), but their application to time-discretized systems is not immediate. While we derive in this study a three step correction to obtain the average burst duration profile of envelope models in discrete time (assuming time-independent but possible state dependent drift function and constant diffusion term across space and time), other related approaches are worth mentioning. Perhaps the most relevant is a continuity correction introduced in the financial literature to price continuous barrier options (Broadie et al. 1997). The correction consists in shifting the continuous barrier to account for discrete monitoring of prices, but is not applicable when the initial price is close to the barrier. As a result, this approach cannot be successfully used for bursts, since they start very close to the barrier (the distribution of initial points is given by the overshoot distribution). Alternatively, algorithms have been suggested to approximate continuous first passage time distributions with simulations (Taillefumier and Magnasco 2010; Drugowitsch 2016; Herrmann and Zucca 2019). In the specific case of the OU model, approximations are directly available for the first passage density of the discretized model, but their complexity makes them unpractical (Collin-Dufresne and Goldstein 2001; Larralde 2004).

Discrete models are required to model burst duration, however the dependence of our results on the time step is worth discussing. As mentioned in previously, discrete models are required to model burst duration since the average burst duration for a continuous stochastic process with Gaussian noise is always zero. As expected, the average burst duration given by equation (3.11) goes to zero as the time step goes to zero. Moreover, the dependence of average burst duration on the time step predicted by equation (3.11) matches what is observed when simulating the OU and degree three models for various time steps (not shown). Importantly, the square root of the time step is only a constant factor that scales the average burst duration as seen in equation (3.11), and it does not influence the shape of the profile. The time step can be seen as a parameter of the bursting model, and can be chosen

to match the roughness of the data envelope, which is done when applying the passage method to data. We also highlight that the analytical approach differs from the experimental approach in that the minimum burst duration of 100 ms considered for data analysis and fitting is not modelled.

Mean first passage time analysis in the context of gamma bursts has been used in (Powanwe and Longtin 2019), where an expression is given for the mean duration of a typical burst in a Rayleigh envelope model. A typical burst is arbitrarily defined therein as starting and ending at the envelope median, and peaking at the envelope mean plus one standard deviation. The present work contributes a result for a more general class of models, includes the influence of time-discretization and the dependence on the threshold used to define bursts, and does not rely on an arbitrary burst peak. In fact, equation (3.11) is applicable to the time-discretization of a Rayleigh model $dx = (-\theta x + \frac{\zeta^2}{2x})dt + \zeta dW$, and the corresponding average burst duration at threshold L is simply $\widetilde{\tau}_L = \sqrt{2\pi dt}\frac{\zeta}{2\theta L}$.

It is noteworthy that a simple analytical expression could be obtained for the average burst duration profile of OU processes (equation (3.13)), making the analysis of the influence of model parameters on average burst duration possible. Besides thresholds, only the decay parameter and the time step play a role in the expression. For a given time step, it is therefore possible to identify an envelope decay in a dataset by fitting an OU burst duration profile to its average burst duration profile. The decay could be assimilated to the real part of the eigenvalues of a broader class of linear envelope models. In the context of simple integrate and fire neuron models, firing can be related to the first passage of an OU process, and the associated decay parameter is estimated in (Ditlevsen and Lansky 2008) by considering inter-spike interval statistics. In our work, Equation (3.13) clarifies the role played by the decay parameter, and predicts that a linear system modelling beta bursts will be made more pathological when its decay parameter is reduced, which makes intuitive sense. This may correspond to changes in average burst duration described as "linear" in the "Surrogate analysis" part of the discussion. In the degree three model case, dependence on model parameters cannot be studied directly

contrary to the OU case, but the integral expression given by equation (B.33) could facilitate numerical analysis as it can be evaluated numerically much faster than the model can be simulated and subjected to burst duration quantification. Also of experimental interest, the burst duration distribution for a given threshold can be obtained analytically for OU processes as an infinite series, but is hard to evaluate numerically since it involves confluent hypergeometric functions of the second kind, their zeros and derivatives (equation (90) in Grebenkov 2014).

From average burst duration profiles to dynamics The link we established from average burst duration profiles to drift function suggests that average burst duration profiles are a window into envelope dynamics. As detailed in the introduction, burst duration has been experimentally identified as an important marker of pathology for PD, and our findings shed some light on the dynamical significance of burst duration. The uncovered link (equation (3.14)) is true for a general envelope model, with a general drift function that can depend on the position, and additive noise constant in time and space ("complicated dynamics, simple noise"). However, the model cannot include delays, and dynamics cannot be recovered in the vicinity of the derivative of the MFPT being zero at the threshold considered. As is manifest in equation (3.14), when average burst duration and its derivative are considered only at a given threshold, only local information on the dynamics is available.

The relationship naturally provides a method to infer envelope dynamics from data, which we call the passage method. We applied the passage method successfully to synthetic data, and recovered envelope dynamics from patient data for patient 6R, ON and OFF medication. In this case study, envelope dynamics OFF medication are found more linear than ON. The range of x values are lower for the ON state, and the OFF state is mostly linear in this region, which could suggest the ON state may correspond to a sub-regime of the OFF state, and non-linearity could come in when oscillations become larger.

The passage method favorably compared to a simple, direct method. The better performance of the passage method on synthetic data may be related to a better

robustness to noise. The noise parameter has to be estimated and is accounted for in the passage method, which is not the case in the direct method. This might be advantageous provided that constant additive noise is a good approximation for the dataset at hand. Comparison of the passage method with state of the art dynamics inference methods that account for stochasticity such as dynamical Bayesian inference (DBI, Smelyanskiy et al. 2005a; Smelyanskiy et al. 2005b; Stankovski et al. 2012) is out of the scope of this thesis, but would provide more insight into the performance of the passage method. DBI was not specifically designed to recover envelope time series, and assumes basis functions to represent dynamics, but could be applied to envelope dynamics inference. Additionally, the direct method can be improved using multiple linear regressions and derivative estimates with various time lags (Wilting and Priesemann 2018), in particular for linear dynamics. The passage method may find productive applications in other parts of the neurosciences – for instance in the field of memory, where beta and gamma bursts (Lundqvist et al. 2016), and the duration of sharp wave ripples (Fernández-Ruiz et al. 2019) have been found to be related to memory – and beyond.

4

Stimulating and measuring the effects of deep brain stimulation based on isostable amplitude in essential tremor patient models

Contents

4.1 Abstract

Medically refractory essential tremor can be treated with deep brain stimulation. Improving the therapy likely requires to be informed by modelling, as the space of possibilities is vast and cannot be fully explored experimentally. One goal of this modelling approach is to design stimulation to maximally reduce the Hilbert amplitude of a pathological signal such as tremor. Isostables provide a notion of amplitude related to convergence time to the attractor, which can be beneficial in model-based control problems. How isostable and Hilbert amplitude compare when measuring or optimising the amplitude response to stimulation in models constrained by data is unknown. Using models previously fitted to phase-locked deep brain stimulation data from essential tremor patients, we relate isostable amplitude response to the Hilbert amplitude response obtained as in experimental data. The resulting isostable response curves match the scale of the experimental method amplitude response across stimulation magnitude in synthetic data. From isostable amplitude, we predict the dependence of the amplitude response to stimulation on oscillation amplitude at the time of stimulation. This prediction is of interest to adaptive deep brain stimulation. Further, we report that for a simple closed-loop phase space stimulation strategy, stimulation based on isostable amplitude is in most cases on par or at a slight advantage compared to stimulation based on Hilbert amplitude. This suggests a potential benefit to using isostable amplitude more broadly for model-based optimisation of stimulation in neurological disorders.

4.2 Introduction

As described before, side-effects due to high frequency stimulation are the main clinical bottleneck of DBS (Section 1.2.2.1). This is why new closed-loop DBS strategies such as phase-locked DBS and aDBS have been explored to stimulate less while preserving clinical efficacy (Section 1.2.2.2). In Chapter 3, we related non-linearity in beta burst dynamics to pathology in PD. This adds to the evidence suggesting that indiscriminatingly suppressing beta oscillation amplitude may not

be the most beneficial strategy in PD (Tinkhauser et al. 2017b; Tinkhauser et al. 2017a). However, knowledge of how to target the pathology selectively based on the recorded signal is not available in ET. In such cases, the goal of closed-loop DBS is therefore to maximally suppress pathological oscillations with as little energy input as possible. How to do this is not clear, and is best explored in models (Wilson and Moehlis 2014; Haidar et al. 2016; Holt et al. 2016; Weerasinghe et al. 2019) since experimental testing is very limited. In Chapter 2, we quantified the efficacy of stimulation by changes in Hilbert amplitude or equivalent as in other modelling studies (see Section 1.2.3.4). This mirrors the amplitude measure commonly used in neurophysiological signals (Barnikol et al. 2008; Cagnan et al. 2013; Brittain et al. 2015; Cagnan et al. 2017; Tinkhauser et al. 2017a; Holt et al. 2019), and allows for meaningful predictions.

Isostables define a set of amplitude coordinates with codimension one associated with the decaying eigenvalues of an attractor (Mauroy et al. 2013). Trajectories starting on the same isostable approach the attractor synchronously. As reviewed in Section 1.2.4.1, isostables have been applied with great success to control the state of various systems (Mauroy et al. 2014; Wilson and Moehlis 2015; Wilson and Djouadi 2019), including coupled oscillators modelling pathological oscillations in PD (Wilson and Moehlis 2016b). Since isostable amplitude delineates convergence time to the attractor, it may provide additional information in model-based studies of DBS where the goal is to suppress pathological oscillations. However, how isostable and Hilbert amplitude compare when measuring or optimising the amplitude response to stimulation in DBS models constrained by data is unknown. In this work, using models fitted in Chapter 2 to phase-locked stimulation data from ET patients (Cagnan et al. 2017; Cagnan et al. 2019a), we ask the following questions. Can we relate the Hilbert amplitude response following a block of phase-locked stimulation to a change in isostable amplitude? Can phase-space stimulation based on isostable amplitude be advantageous in fitted patient models compared to phase-space stimulation simply based on Hilbert amplitude? Because of the transient character

of the data, best non-linear WC fits from Chapter 2 gave rise to stable foci. We will therefore consider isostable amplitude in stable foci (Mauroy et al. 2013).

The contributions of this chapter are twofold. Firstly, we define isostable amplitude response to stimulation in phase space. We relate an instantaneous change in isostable amplitude to a change in Hilbert amplitude later in time in the absence of noise. This allows to scale isostable amplitude response curves in such a way that they approximately match the scale of the Hilbert amplitude response to blocks of phase-locked stimulation in synthetic data from the fitted models. The isostable amplitude response provides predictions for the dependence of the Hilbert amplitude response on on-going oscillation amplitude at the time of stimulation (Section 4.4), which has implications for adaptive DBS. Secondly, on the basis of stimulation strategies benefiting from the knowledge of phase-space amplitude fields, we show that stimulation based on isostable amplitude is on par or at a slight advantage compared to stimulation based on Hilbert amplitude (Section 4.5). This suggests that, when dealing with the control goal of minimising the Hilbert amplitude of a model output, considering isostable amplitude may be beneficial. This opens opportunities for model-based optimisation of stimulation in neurological disorders.

4.3 Isostable coordinates of stable foci in 2D

We summarize the concept of isostables and isostable coordinates for stable fixed points presented in (Mauroy et al. 2013). Isostable coordinates will be used to obtain from the fitted foci models isostable amplitude response curves to be compared against synthetic data bARCs. On an intuitive level, the isostables of a stable fixed point can be defined as sets of points with the same asymptotic convergence to the fixed point, i.e. sets of points approaching the fixed point synchronously (Mauroy et al. 2013). This is illustrated in the example in Figure 4.1, where the animation shows that trajectories starting on the same isostable reach subsequent isostables at the same time. In what follows, we denote vectors in bold to distinguish

scalars and vectors more easily. To provide a precise definition of isostables, let us consider a dynamical system

$$\dot{\mathbf{X}} = F(\mathbf{X}), \tag{4.1}$$

where $\mathbf{X} \in \mathbb{R}^2$ for our purposes (for definitions in $\mathbb{R}^n$, see Mauroy et al. 2013), and the vector field F is analytic. The flow induced by equation (4.1) is denoted $\Phi_t(\mathbf{X})$. We assume that F has a stable fixed point $\mathbf{X}^*$, with a basin of attraction $\mathcal{B}(\mathbf{X}^*)$. We further assume that the Jacobian J of F at $\mathbf{X}^*$ has complex conjugate eigenvalues $\lambda_\pm = \sigma \pm i\omega$ with $\sigma < 0$. We denote by $\mathbf{v_1} = \mathbf{a} - i\mathbf{b}$ and $\mathbf{v_2}$ the right normalised eigenvectors associated with λ_+ and λ_-, respectively. The isostable $\mathcal{I}_\tau$ is defined in (Mauroy et al. 2013) when the leading eigenvalue is not real as the one-dimensional manifold

$$\mathcal{I}_\tau = \{\mathbf{X} \in \mathcal{B}(\mathbf{X}^*) | \exists \theta \in [0, 2\pi) \text{ s.t. } \lim_{t \to +\infty} e^{-\sigma t} \left\| \Phi_t(\mathbf{X}) - \mathbf{X}^* - \Re\left[\mathbf{v_1} e^{i(\omega t + \theta)}\right] e^{\sigma(t+\tau)} \right\| = 0 \Big\}, \tag{4.2}$$

where $\Re(z)$ is the real part of z. In equation (4.2), $\Phi_t(\mathbf{X}) - \mathbf{X}^*$ is the vector from the fixed point to the end point at time t of a trajectory with initial condition $\mathbf{X}$. The vector $\Re\left[\mathbf{v_1} e^{i(\omega t+\theta)}\right] e^{\sigma(t+\tau)}$ represents the asymptotic behavior at time t shared by trajectories with initial conditions on the isostable $\mathcal{I}_\tau$. These vectors both converge to $\mathbf{0}$. The distance in equation (4.2) is therefore scaled by the increasing function of time $e^{-\sigma t}$ to make the limit meaningful. For $\mathbf{X} \in \mathcal{I}_\tau$, the isostable coordinate of $\mathbf{X}$ is given by $r(\mathbf{X}) = e^{\sigma\tau}$ (Mauroy et al. 2013). We call $r(\mathbf{X})$ isostable amplitude. To provide further intuition, $r(\mathbf{X})$ is twice the modulus of the first coordinate of $\mathbf{Z}$ in the $\mathbb{C}^2$ basis $(\mathbf{v_1}, \mathbf{v_2})$, where $\mathbf{Z}$ is the initial condition of a trajectory sharing the same asymptotic evolution as $\Phi_t(\mathbf{x})$, but evolving according to the linearised dynamics $\dot{\mathbf{Z}} = J\mathbf{Z}$. As described in (Mauroy et al. 2013), isostables of linear systems are simpler to express. In $\mathbb{R}^2$, if F is linear, equation (4.2) simplifies to

$$\mathcal{I}_\tau = \{\mathbf{X} \in \mathcal{B}(\mathbf{X}^*) | \mathbf{X} = (\cos(\theta)\mathbf{a} + \sin(\theta)\mathbf{b})\, e^{\sigma\tau}, \theta \in [0, 2\pi)\}. \tag{4.3}$$

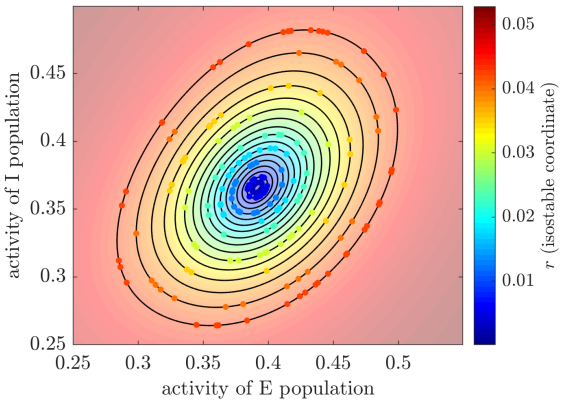

Figure 4.1: Isostables as sets of points with the same asymptotic convergence. The corresponding animation is available as supplementary material with this thesis and at https://tinyurl.com/isoSvideo. Trajectories starting on the same isostable are represented by dots of the same color and cross subsequent isostables at the same time. Isostables are depicted by black contours. This example shows the WC fit to patient 1. The state $\mathbf{X}$ corresponds to (E, I).

Isostables and isostable coordinates can be obtained by computing Laplace averages (more details in Mauroy et al. 2013), but we use in this work a simpler and more efficient computation method available for fixed points when the eigenvalue corresponding to the slowest direction is not real. This method is presented in Proposition 2 (ii) in (Mauroy et al. 2013), and we lay out how it is applied in this work. Isostable coordinates are computed using

$$r(\mathbf{X}) \approx \frac{e^{-\sigma n T}\sqrt{\left[(f_1 \circ \Phi_{nT})(\mathbf{X})\right]^2 + \left[(f_2 \circ \Phi_{nT})(\mathbf{X})\right]^2}}{|\langle \nabla f_1(\mathbf{X}^*), \mathbf{a}\rangle|}, \tag{4.4}$$

where $n \in \mathbb{N}$ is chosen such that $n \gg 1$ while avoiding numerical instability, $\langle \cdot, \cdot \rangle$ is the standard complex inner product, $T = \frac{2\pi}{\omega}$, and $f_1 : \mathbb{R}^2 \mapsto \mathbb{R}$ and $f_2 : \mathbb{R}^2 \mapsto \mathbb{R}$ are functions called observables. We define these observables as

$$f_1 = \left\langle \mathbf{X} - \mathbf{X}^*, \begin{bmatrix} b_2 \\ -b_1 \end{bmatrix} \right\rangle, \qquad f_2 = \left\langle \mathbf{X} - \mathbf{X}^*, \begin{bmatrix} a_2 \\ -a_1 \end{bmatrix} \right\rangle,$$

where $\mathbf{a} = \begin{bmatrix} a_1 \\ a_2 \end{bmatrix}$ and $\mathbf{b} = \begin{bmatrix} b_1 \\ b_2 \end{bmatrix}$. These definitions satisfy the three requirements on f_1 and f_2 of Proposition 2 (ii) in (Mauroy et al. 2013). Similarly to Laplace averages, this method allows to compute isostable coordinates in the entire basin of attraction of the fixed point, but is less prone to numerical instability. An explicit Runge-Kutta (4,5) method provided reliable estimates of isostable coordinates for

the three WC patient fits (Figure 4.2, panels A, B, and C). As n is increased, convergence of isostable coordinates happens before numerical instability sets in (this was not the case with the first order Euler's method). We use $n = 80$ for patient 1, $n = 60$ for patient 5, and $n = 120$ for patient 6. For these values, r has converged and there is no trace of numerical instability.

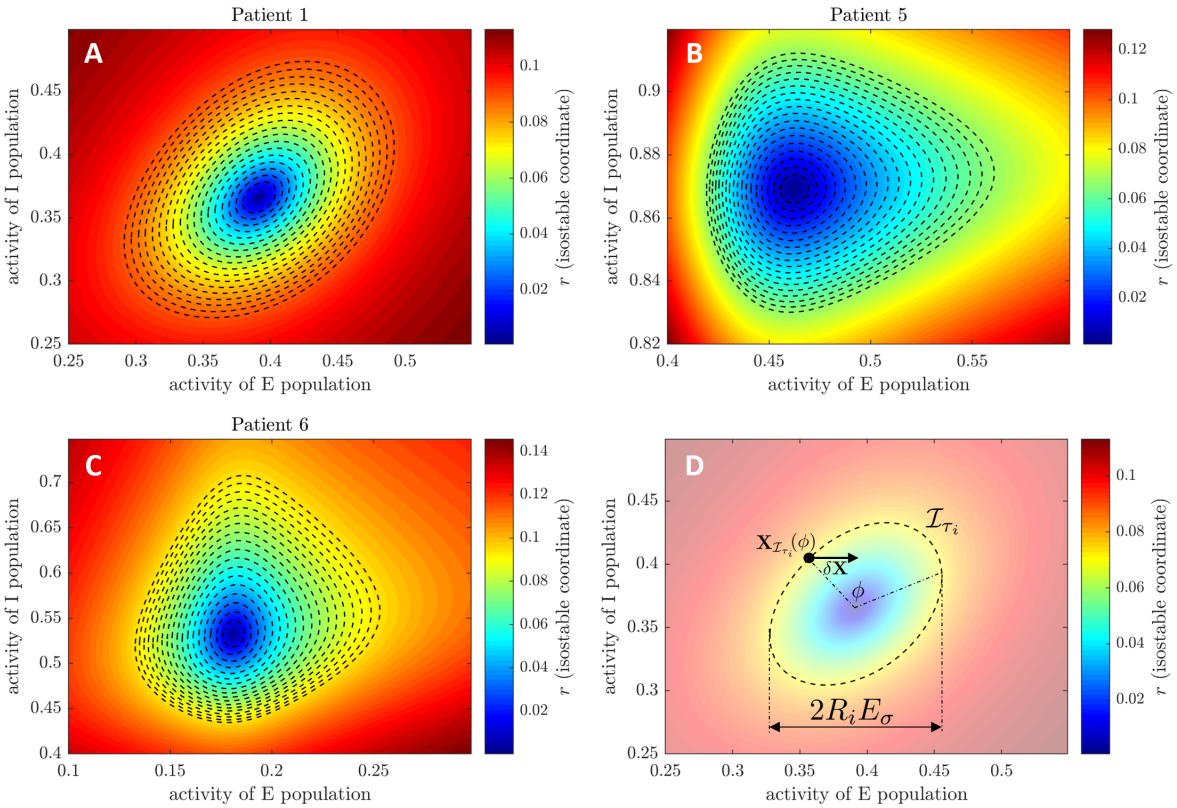

Figure 4.2: Isostable amplitude fields in patient fits. Isostable coordinates were obtained using equation (4.4) for the non-linear WC fits to patient 1 (panel A), patient 5 (panel B), and patient 6 (panel C). For the WC model, the state $\mathbf{X}$ corresponds to (E, I), where E is the activity of the excitatory population, and I the activity of the inhibitory population. In panels A to C, dashed lines represent isostables. Panel D illustrates how the partial asymptotic amplitude response curve $\text{aARC}_i(\phi, \delta\mathbf{X})$ corresponding to isostable $\mathcal{I}_{\tau_i}$ is obtained in phase space. The stimulation polar angle ϕ is referenced to the maximum of E, and $\delta\mathbf{X}$ is the stimulation vector (see text of Section 4.4.1).

4.4 Asymptotic amplitude response and block method amplitude response

Using isostable amplitude fields from the previous section, we derive in phase space isostable amplitude response curves which we call aARCs for "asymptotic amplitude

response curves". Analytical approximations were provided in Chapter 2 for first-order response curves, where the response is measured shortly after stimulation (at the end of the current period). Here, we demonstrate that a change in isostable amplitude can be related to a delayed measurement in Hilbert amplitude. In the block method used to measure the response to blocks of phase-locked stimulation (introduced in Section 2.3.1), bARCs are obtained by delaying Hilbert amplitude measurement to the end of the block. By scaling aARCs accordingly, we show that they can provide a scaling approximation of bARCs as stimulation magnitude is increased. We make use of this approximation to provide predictions for the dependence of the block response to stimulation on oscillation amplitude at the time of stimulation.

4.4.1 Stimulating in phase space

We lay out how we obtain aARCs in phase space, in particular how stimulation is applied at a given phase and amplitude, and how we integrate partial responses on amplitude contours to derive the overall response. Amplitude response curves are commonly defined as functions of stimulation phase, but not of the amplitude at which stimulation is applied (see for instance Cagnan et al. 2017). To approximate this notion in phase space, we start by providing stimulation on isostables parametrised by phase. Isostables play the role of amplitude contours, and we consider N such isostables spanning the range of amplitude values in phase-locked stimulation synthetic data. For simplicity, we measure the phase of stimulation along amplitude contours using a coarse approximation of the Hilbert phase. It is provided by the geometric phase in the (E, I) space, which we denote ϕ. We set the zero-phase of ϕ when E is maximum on the amplitude contour (see Figure 4.2, panel D). We only consider cases where the zero-phase point is a continuous function of isostable amplitude. For a stimulation $\delta\mathbf{X}$ at phase ϕ, we obtain the asymptotic amplitude response curve as the weighted sum

$$\mathrm{aARC}(\phi, \delta\mathbf{X}) = \sum_{i=1}^{N} w_i(\delta\mathbf{X})\, \mathrm{aARC}_i(\phi, \delta\mathbf{X}), \tag{4.5}$$

where aARC_i is the partial asymptotic amplitude response curve for the isostable $\mathcal{I}_{\tau_i}$ (contour of isostable amplitude $e^{\sigma\tau_i}$), and $w_i(\delta\mathbf{X})$ is the corresponding weight for a stimulation vector $\delta\mathbf{X}$ (more details below). We define the partial asymptotic amplitude response curve $\text{aARC}_i(\phi, \delta\mathbf{X})$ as the instantaneous change in isostable coordinate following stimulation

$$\text{aARC}_i(\phi, \delta\mathbf{X}) = r(\mathbf{X}_{\mathcal{I}_{\tau_i}}(\phi) + \delta\mathbf{X}) - r(\mathbf{X}_{\mathcal{I}_{\tau_i}}(\phi)), \tag{4.6}$$

with $\mathbf{X}_{\mathcal{I}_{\tau_i}}(\phi)$ the point of phase ϕ on the isostable $\mathcal{I}_{\tau_i}$ (see Figure 4.2, panel D). In line with fitted models (where stimulation is applied to the excitatory population which represents the most common target of DBS in ET), we will consider in what follows $\delta\mathbf{X} = \left[\begin{smallmatrix}\delta E\\ 0\end{smallmatrix}\right]$. We obtain the normalised weight $w_i(\delta\mathbf{X})$ for the isostable $\mathcal{I}_{\tau_i}$ from the PDF of Hilbert amplitudes in synthetic data with phase-locked stimulation $\delta\mathbf{X}$. Synthetic data is obtained as in Chapter 2 with all target stimulation phases equally represented, and is scaled by E_σ regardless of the stimulation level. We match the isostable $\mathcal{I}_{\tau_i}$ with an amplitude bin in the synthetic data Hilbert amplitude PDF by assigning to $\mathcal{I}_{\tau_i}$ the amplitude

$$R_i = \frac{1}{2E_\sigma}\left(\max_{\mathcal{I}_{\tau_i}}(E) - \min_{\mathcal{I}_{\tau_i}}(E)\right), \tag{4.7}$$

where E_σ is the standard deviation of synthetic data with no stimulation.

4.4.2 Relating a change in isostable amplitude to a change in Hilbert amplitude later in time

In the block method, the amplitude response is measured at the end of stimulation blocks, and to relate aARCs to bARCs, we show that a change in asymptotic amplitude corresponds to a change in Hilbert amplitude later in time (after m periods, with $m \gg 1$). We consider a stimulation $\delta\mathbf{X}$ applied to $\mathbf{X}^- \in \mathcal{I}_{\tau^-}$ at $t = 0$. The state of the system right after stimulation is $\mathbf{X}^+ \in \mathcal{I}_{\tau^+}$, with $\mathbf{X}^+ = \mathbf{X}^- + \delta\mathbf{X}$. To approximate the distance between $\Phi_{mT}(\mathbf{X}^+)$ and $\Phi_{mT}(\mathbf{X}^-)$ by a change in Hilbert amplitude when $m \gg 1$, we are going to use the fact that isochrons are approximately straight lines in the vicinity of the fixed point (isochrons were defined

in Section 1.2.4.2). We will choose one isochron in particular to obtain a change in Hilbert amplitude of the first coordinates. Because $\mathbf{X}^-$ and $\mathbf{X}^+$ are in general not on the same isochron, we consider instead $\widehat{\mathbf{X}}^+ \in \mathcal{I}_{\tau^+}$ and $\widehat{\mathbf{X}}^- \in \mathcal{I}_{\tau^-}$, such that $\widehat{\mathbf{X}}^+$ and $\widehat{\mathbf{X}}^-$ are both on the isochron of asymptotic phase Θ. In other words, while $\widehat{\mathbf{X}}^+$ and $\mathbf{X}^+$ as well as $\widehat{\mathbf{X}}^-$ and $\mathbf{X}^-$ have the same isostable coordinates (respectively), $\widehat{\mathbf{X}}^+$ and $\widehat{\mathbf{X}}^-$ have the same isochronal phase. This is illustrated in Figure 4.3, panel A. As a consequence of equation (4.2), we have for large times

$$\Phi_t(\widehat{\mathbf{X}}^-) \approx \mathbf{X}^* + \Re\left[\mathbf{v_1} e^{i(\omega t+\Theta)}\right] e^{\sigma t}\, r(\widehat{\mathbf{X}}^-), \tag{4.8}$$

$$\Phi_t(\widehat{\mathbf{X}}^+) \approx \mathbf{X}^* + \Re\left[\mathbf{v_1} e^{i(\omega t+\Theta)}\right] e^{\sigma t}\, r(\widehat{\mathbf{X}}^+), \tag{4.9}$$

where we have used that for $\mathbf{X} \in \mathcal{I}_\tau$, $r(\mathbf{X}) = e^{\sigma\tau}$ (see Section 4.3), and where the isochronal angle Θ is referenced to the direction of $\Re(\mathbf{v_1})$. The instantaneous change in isostable amplitude upon stimulation is $\Delta r = |r(\mathbf{X}^+) - r(\mathbf{X}^-)|$, and because of how we chose $\widehat{\mathbf{X}}^+$ and $\widehat{\mathbf{X}}^-$, we have $\Delta r = |r(\widehat{\mathbf{X}}^+) - r(\widehat{\mathbf{X}}^-)|$. It follows that for $t = mT$ with $m \gg 1$,

$$\left\|\Phi_{mT}(\widehat{\mathbf{X}}^+) - \Phi_{mT}(\widehat{\mathbf{X}}^-)\right\| \approx \left\|\Re\left(\mathbf{v_1} e^{i\Theta}\right)\right\| e^{\sigma mT} \Delta r. \tag{4.10}$$

Since isochrons are invariant under Φ_{mT}, both $\Phi_{mT}(\widehat{\mathbf{X}}^+)$ and $\Phi_{mT}(\widehat{\mathbf{X}}^-)$ are still on the same isochron (see Figure 4.3, panel A). This isochron's asymptotic phase Θ, which underlies the position of $\widehat{\mathbf{X}}^+$ and $\widehat{\mathbf{X}}^-$, can be chosen to obtain a convenient measure of distance. In our work, we choose $\Theta = \Theta_E$ such that, close to the fixed point, the isochron is aligned with the first dimension of $\mathbf{X}$, the direction of E (see example in Figure 4.3, panel A). With $\Theta = \Theta_E$, the norm $\left\|\Phi_{mT}(\widehat{\mathbf{X}}^+) - \Phi_{mT}(\widehat{\mathbf{X}}^-)\right\|$ is approximately a difference in the Hilbert amplitude of E at time mT after stimulation. Because they are on the same isostables, trajectories starting from $\Phi_{mT}(\widehat{\mathbf{X}}^+)$ and $\Phi_{mT}(\mathbf{X}^+)$, as well as from $\Phi_{mT}(\widehat{\mathbf{X}}^-)$ and $\Phi_{mT}(\mathbf{X}^-)$, share the same Hilbert amplitude, respectively. Therefore, the difference in Hilbert amplitude between $\Phi_{mT}(\mathbf{X}^+)$ and $\Phi_{mT}(\mathbf{X}^-)$, which we denote ΔE_m, is approximately equal to $\left\|\Phi_{mT}(\widehat{\mathbf{X}}^+) - \Phi_{mT}(\widehat{\mathbf{X}}^-)\right\|$ for $\Theta = \Theta_E$. We can write

$$\Delta E_m \approx C(m, \Theta_E)\Delta r, \tag{4.11}$$

where $C(m, \Theta_E) = \left\| \Re\left(\mathbf{v_1} e^{i\Theta_E}\right) \right\| e^{\sigma m T} = \|\Re(\mathbf{v_1})\cos\Theta_E - \Im(\mathbf{v_1})\sin\Theta_E\| \, e^{\sigma m T}$, with $\Im(z)$ the imaginary part of z. We have shown that an instantaneous change in isostable coordinates due to stimulation can be related to a change in distance in phase space later in time, which is approximately a change in the Hilbert amplitude of E with an appropriate choice of Θ in our setting.

To validate this claim, we test equation (4.10) numerically. We pick 30 stimulation points $\mathbf{X}^-$ at random in the phase space of the WC model fitted to patient 1 (Figure 4.3, panel B). In each case, stimulation is applied, and $\Phi_{mT}(\widehat{\mathbf{X}}^+)$ and $\Phi_{mT}(\widehat{\mathbf{X}}^-)$ are obtained for a range of Θ values spanning $[0, 2\pi)$ for various m. The isochronal phase Θ is obtained as detailed in Appendix C.1. Three times the fitted stimulation magnitude from Chapter 2 is used to limit the influence of numerical

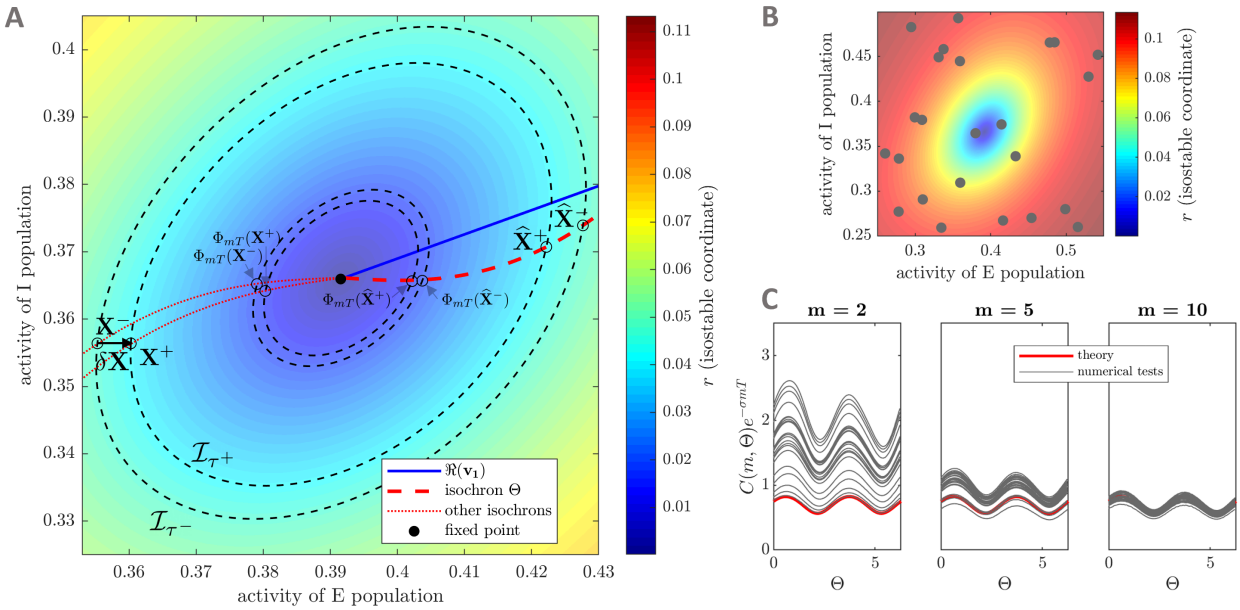

Figure 4.3: An instantaneous change in isostable coordinates due to stimulation can be related to a change in distance in state space later in time. Panel A presents a sketch of the setup used to relate $|r(\mathbf{X}^+) - r(\mathbf{X}^-)|$ to the distance between $\Phi_{mT}(\widehat{\mathbf{X}}^+)$ and $\Phi_{mT}(\widehat{\mathbf{X}}^-)$. In this example, we choose $\Theta = \Theta_E$, and the isochron shown by a dashed line is aligned with the direction of E in the vicinity of the fixed point. Isostables are shown as dashed black lines. Equation (4.10) is tested by picking 30 random stimulation points $\mathbf{X}^-$ (grey dots in panel B) in the phase space of the WC model fitted to patient 1. For each stimulation point, the numerical estimate given by equation (4.12) is then compared to the prediction of equation (4.10) for $m = 2$, 5, and 10 periods (panel C).

errors when measuring distances. The resulting numerical estimates of

$$G = \frac{\left\|\Phi_{mT}(\widehat{\mathbf{X}}^+) - \Phi_{mT}(\widehat{\mathbf{X}}^-)\right\|}{\Delta r} e^{-\sigma mT} \tag{4.12}$$

(grey lines in panel C of Figure 4.3) converge quickly to the red curve $C(m, \Theta_E)e^{-\sigma mT} = \left\|\Re\left(\mathbf{v_1}e^{i\Theta_E}\right)\right\|$ predicted by equation (4.10). A good convergence is obtained after $m = 10$ periods.

4.4.3 Predicting bARCs from asymptotic amplitude response

Using $C(m, \Theta_E)$ to turn an instantaneous change in isostable coordinates to a delayed change in Hilbert amplitude, we compare aARCs and bARCs in the three WC patient fits from Chapter 2, and study how these response curves scale with stimulation magnitude. We are considering stimulation levels $\delta E = p\delta E_0$, where $p \in \{0.1, 0.5, 1, 2, 3\}$, and δE_0 is the stimulation magnitude fitted to data in Chapter 2. bARCs are obtained from synthetic data as in Chapter 2. In addition to the scaling based on $C(m, \Theta_E)$, two adjustments are required for aARCs and bARCs to be comparable. Block amplitude response curves are computed on synthetic data generated by the fitted model, and the stimulation delay Δt_{stim} introduced in Chapter 2 has to be accounted for. Synthetic data used to compute bARCs was zscored using the standard deviation of synthetic data with no stimulation E_σ, so we additionally scale aARCs accordingly. The scaled and shifted in phase aARC, which we denote $\widetilde{\text{aARC}}$, is given by

$$\widetilde{\text{aARC}}(\phi - \Delta\phi_{\text{stim}}, \delta\mathbf{X}) = \frac{C(m_1, \Theta_E)}{E_\sigma} \text{aARC}(\phi, \delta\mathbf{X}), \tag{4.13}$$

where m_1 is chosen to be the number of periods corresponding to the Hilbert amplitude PDF range in synthetic data with no stimulation (from the maximum amplitude value seen in 600 trials of synthetic data down to 5% of it). This corresponds to $m_1 = 15$ for patient 1, $m_1 = 8$ for patient 5, and $m_1 = 20$ for patient 6. The phase shift $\Delta\phi_{\text{stim}}$ corresponding to the previsously fitted stimulation delay Δt_{stim} is obtained as

$$\Delta\phi_{\text{stim}} = 2\pi\Delta t_{\text{stim}}\overline{f_E}(\delta E) \pmod{2\pi}, \tag{4.14}$$

where $\overline{f_E}(\delta E)$ is the mean frequency of E synthetic data with phase-locked stimulation of magnitude δE. For simplicity when computing $C(m_1, \Theta_E)$, the isochronal angle Θ_E is approximated by the polar angle between $\Re(\mathbf{v_1})$ and the E direction. This is an acceptable approximation close to the fixed point ($m_1 \gg 1$) as isochrons become straight lines (see Supplementary Figure C.1 in Appendix C.1 as an example), and the zero-phase isochron is aligned with $\Re(\mathbf{v_1})$.

For the three fitted WC models, $\widetilde{\text{aARC}}$s provide an approximation of synthetic data bARCs shape, and scale similarly with stimulation magnitude as shown in Figure 4.4. The best phase to stimulate based on $\widetilde{\text{aARC}}$s is also in good agreement with what is predicted by synthetic data bARCs in most instances. However the magnitude of tremor suppression is generally overestimated by $\widetilde{\text{aARC}}$s compared to synthetic data bARCs, and in most cases the asymptotic amplitude response curves seem to be shifted towards negative values (see in particular patient 5 in Figure 4.4). The similarity in scaling as stimulation magnitude increases from $0.1\delta E_0$ to $3\delta E_0$ is further evidenced in panel A of Figure 4.5, where the scale of the amplitude response is measured by its standard deviation. Error bars on the scale of the amplitude response in synthetic data are obtained using error propagation (Ku 1966) on the standard deviation of the amplitude response as in (Weerasinghe et al. 2019).

4.4.4 Predicting the dependence of the block amplitude response on oscillation amplitude

The scaling approximation given by $\widetilde{\text{aARC}}$s presented in the previous section motivates the use of isostable amplitude to predict the dependence of the block amplitude response to stimulation on oscillation amplitude at the time of stimulation. Besides phase, oscillation amplitude at the time of stimulation may also have an effect on the block response to stimulation in patients. While this dependence is difficult to evaluate directly for blocks of phase-locked stimulation in data, it can be predicted using partial asymptotic amplitude response curves introduced in Section 4.4.1 (see equation (4.6)). Partial asymptotic amplitude response curves (aARC_i) are scaled as in equation (4.13), and we denote scaled partial asymptotic amplitude

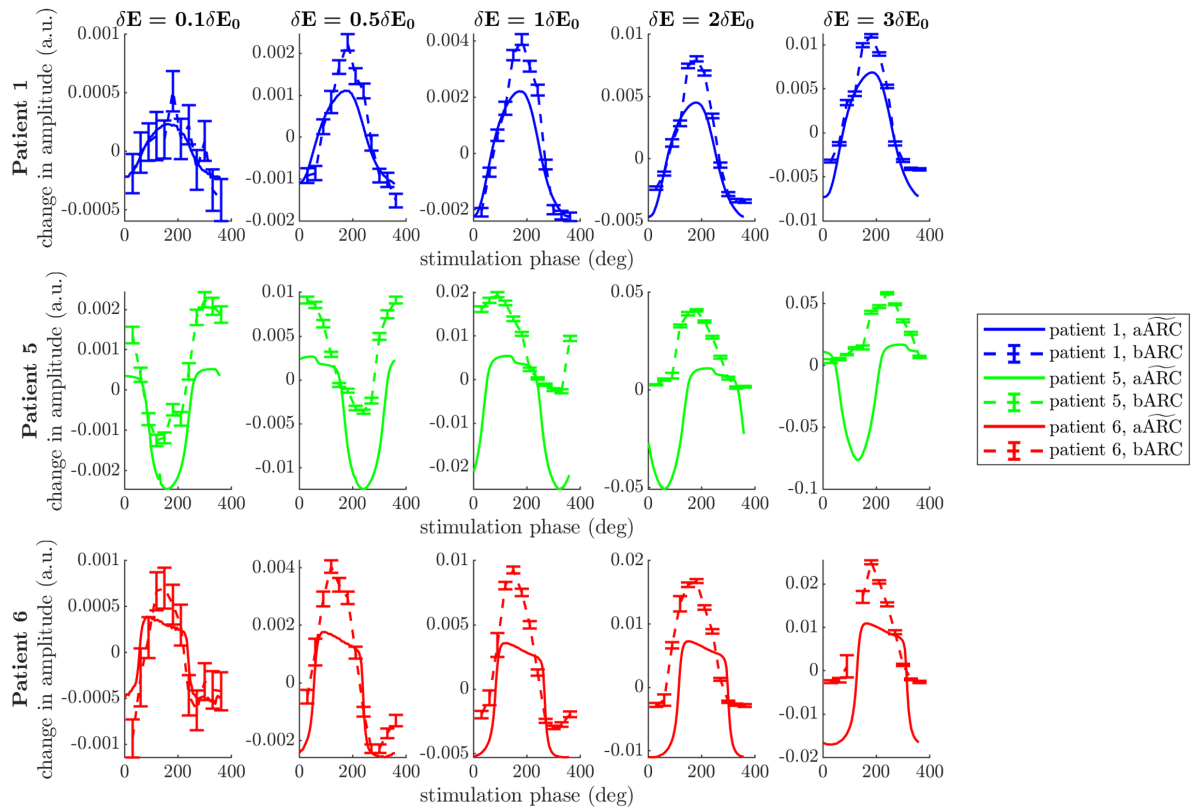

Figure 4.4: Asymptotic and block amplitude response curves for the three fitted patients. Each patient corresponds to a row, and each stimulation magnitude ratio $\delta E/\delta E_0$ to a column. Solid lines represent $\widetilde{\text{aARC}}$s obtained in phase space, and dashed lines bARCs from synthetic data (sem error bars). The number of amplitude contours used in phase space is $N = 78$.

response curves by $\widetilde{\text{aARC}}_i$. The partial asymptotic amplitude response curve $\widetilde{\text{aARC}}_i$ corresponds to stimulation at amplitude R_i (given by equation (4.7)). The scale (standard deviation) of partial asymptotic amplitude response curves decreases with the amplitude at which stimulation is applied (except for very low amplitudes in patient 5) as shown in Figure 4.5, panel B. The block method offers no simple way of measuring this dependence as stimulation is provided once per period in blocks of 5 s and amplitude is variable during the stimulation block. The bARC scale is therefore represented as a horizontal line in panel B of Figure 4.5 for scale comparison.

In this section, we have shown that isostable amplitude can be used to approximate the block amplitude response to phase-locked stimulation, and can provide a prediction for the dependence of the block amplitude response on oscillation amplitude at the time of stimulation. Since isostable amplitude can be related to

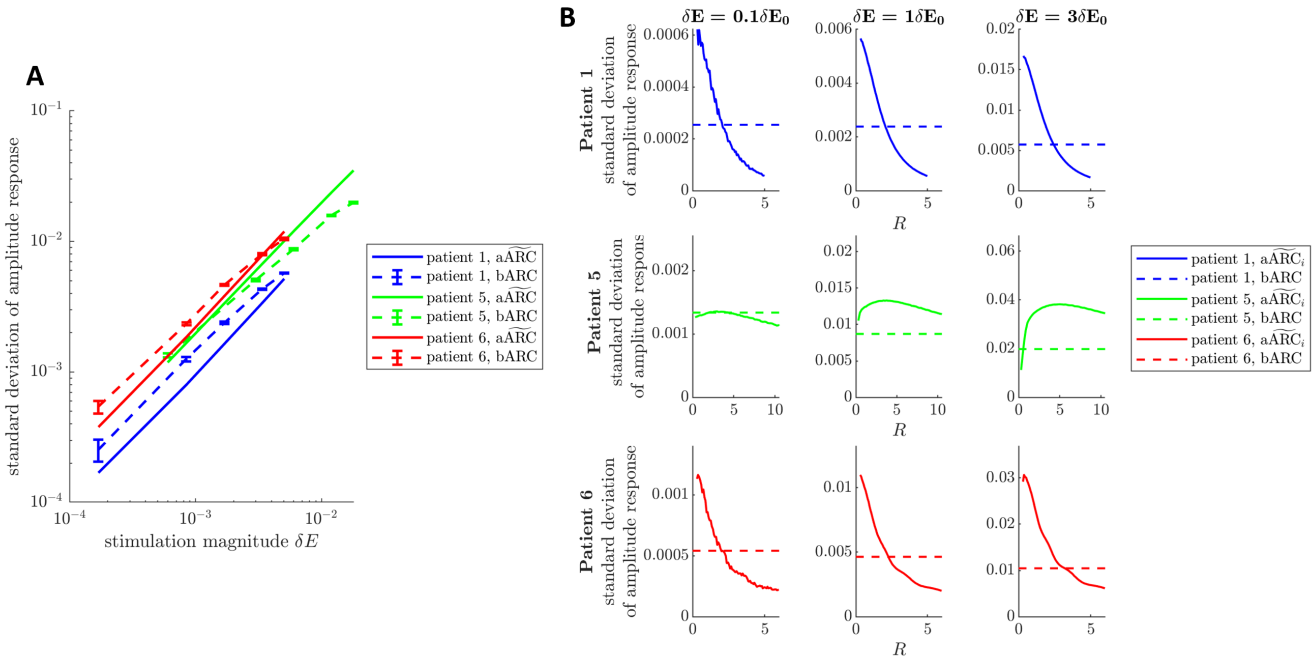

Figure 4.5: Scaling of block and amplitude responses as a function of stimulation magnitude (panel A) and of tremor amplitude at the time of stimulation (panel B). In both cases, scaling is obtained as the standard deviation of response curves. In panel B, each patient corresponds to a row, and each stimulation magnitude ratio $\delta E/\delta E_0$ to a column. The block method offers no amplitude resolution, and the bARC scale is represented as a horizontal line in panel B.

an experimental measurement technique of amplitude response, it is natural to investigate if providing stimulation in phase-space according to isostable amplitude could be advantageous.

4.5 Phase space closed-loop stimulation: isostable amplitude versus Hilbert amplitude

Here, we suggest a closed-loop stimulation strategy based on the state in phase space. The strategy relies on phase space amplitude fields, and we compare the performance of this strategy when the amplitude field used portrays isostable amplitude (Figure 4.2), to when it depicts Hilbert amplitude. We first describe how Hilbert amplitude fields are obtained, then detail the stimulation strategy, and finally compare results based on isostable and Hilbert amplitude for the three fitted models.

4.5.1 Stimulating using phase space amplitude fields

4.5.1.1 Obtaining Hilbert amplitude fields

To establish a basis for stimulation performance comparison, we obtain Hilbert amplitude fields through averaging of numerical simulations. Specifically, we randomly draw 2000 initial positions in the phase space region of interest. From these initial positions, we simulate the model (with noise) for 1000 periods. From each trajectory, we obtain the Hilbert amplitude of the E component after centering. We clip 0.5% of the trajectories and the Hilbert amplitude time series at both ends to remove edge effects. To reduce the effect of noise, we lightly smooth the trajectories and Hilbert amplitude time series (moving average spanning four time steps). The (E, I) region of interest is discretized, and for each point in each trajectory, the corresponding space bin is found, and the associated Hilbert amplitude value is added to the bin. The Hilbert amplitude field over the region of interest is finally obtained by averaging Hilbert amplitude values within space bins. Hilbert amplitude fields are obtained for the three WC patient fits, and Figure 4.6 highlights striking similarities in shape with asymptotic amplitude fields from Section 4.3 (Figure 4.2). While isostable coordinates can easily be computed anywhere in the basin of attraction of the fixed point, Hilbert amplitude could not be determined in white zones in Figure 4.6.

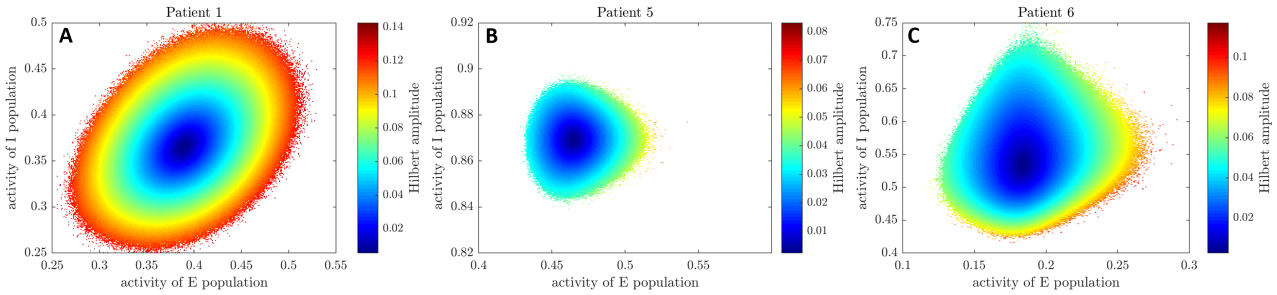

Figure 4.6: Hilbert amplitude fields for the three WC patient fits. Panel A shows patient 1, panel B patient 5, and panel C patient 6. Despite the simulation of two million periods with noise, the outer white zones are inaccessible and have no Hilbert amplitude values associated to them.

4.5.1.2 A phase space stimulation strategy drawing on amplitude fields

We describe a stimulation strategy that uses information from state space amplitude fields to decide whether it is more beneficial to stimulate now or at a later time of the ongoing period. The starting point is a phase space amplitude field $\Omega(\mathbf{X})$ (we will be using isostable coordinates in phase space as shown in Figure 4.2, or Hilbert amplitude fields as shown in Figure 4.6). From there, we define the corresponding "instantaneous amplitude response field" $\Gamma_0(\mathbf{X}) = \Omega(\mathbf{X}+\delta\mathbf{X}) - \Omega(\mathbf{X})$. Instantaneous amplitude response fields for isostable amplitude (Γ_0^{∞}) and Hilbert amplitude (Γ_0^{H}) are presented in Figure 4.7, panels A to C. In what we call an "augmented instantaneous amplitude response field" $\Gamma(\mathbf{X}, t)$, we embed the values of Γ_0 on deterministic trajectories starting at $\mathbf{X}$ from $t = 0$ to $t = T$. The information will be used to inform the decision to stimulate or not. We are considering the (E, I) phase space, and the range of interest of E and I are discretized into N_E and N_I values, respectively. Algorithm 1 describes how we obtain Γ from Γ_0 in discretized space and time. Stimulation is only beneficial when the amplitude response is negative (decrease in tremor magnitude). Positive values of the instantaneous amplitude response field are therefore of no interest and are logged in Γ as zeros.

Algorithm 1 Obtain Γ

for (i, j) in $\{1, .., N_E\} \times \{1, .., N_I\}$ **do**
  simulate trajectories $(E(t_k), I(t_k))_{k\in\{1,..,u\}}$ with $t_1 = 0$, $t_u = T$, $E(t_1) = E_i$, and $I(t_1) = I_j$.
  for k in $\{1, .., u\}$ **do**
    find $(p, q) \in \{1, .., N_E\} \times \{1, .., N_I\}$ s.t. (E_p, I_q) is the closest to $(E(t_k), I(t_k))$

    if $\Gamma_0(p, q) < 0$ and $\Gamma_0(p, q) \leq \Gamma_0(i, j)$ **then**
      $\Gamma(i, j, k) \leftarrow \Gamma_0(p, q)$
    else
      $\Gamma(i, j, k) \leftarrow 0$
    end if
  end for
end for

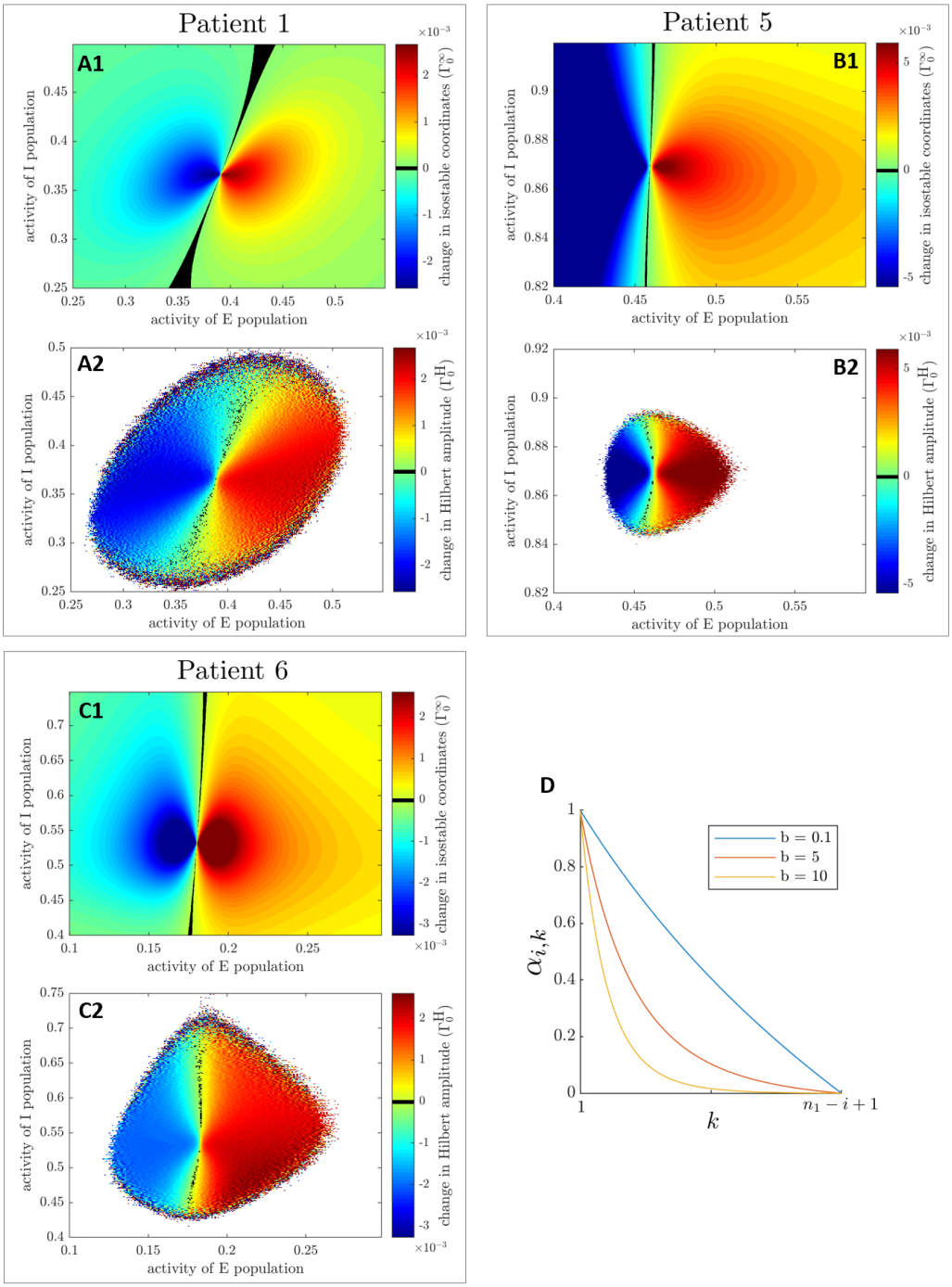

Figure 4.7: Instantaneous amplitude response fields for asymptotic amplitude (Γ_0^∞, panels A1, B1 and C1) and Hilbert amplitude (Γ_0^H, panels A2, B2, and C2) are shown for the three fitted WC models for $\delta E = \delta E_0$. White zones signify missing values. Negative values of the fields signify a decrease in amplitude (beneficial stimulation), positive values an increase in amplitude. A narrow range of values centered on zero is shown in black to separate positive and negative regions. Colour scales are matched on a patient basis. Panel D illustrates the $k-1$ step ahead discount factor $\alpha_{i,k}$ (given by equation (4.15)) at time t_i, for various values of the discounting parameter b. Time t_{n_1} corresponds to the predicted end of the current period.

Along with model integration, the decision to stimulate or not is made at each time step based on the current position in phase space (algorithm 2). Stimulation is provided at maximum once per period according to the scheme. We track zero-crossings and estimate the zero-crossing phase as done in Chapter 2 (more details in Appendix A.7). To prevent instability when zero-crossing tracking fails, we enforce a maximum stimulation frequency (corresponding to N_{lim} time steps in algorithm 2) of 10 Hz, which is roughly twice the tremor frequency. The benefit of stimulating at later times of the ongoing period is estimated by the values stored in Γ in the space bin corresponding to the current position. The estimated values are based on deterministic trajectories, whereas the model includes Gaussian white noise. As a result, the actual benefit of waiting to stimulate is uncertain and will deviate from the average (noiseless) trajectory prediction, while the benefit of stimulating now is known exactly. Future estimates must therefore be discounted. From time t_i, we define the $k-1$ step ahead discount factor $\alpha_{i,k}$ as

$$\alpha_{i,k} = \left[\frac{1}{(t_{i+k-1} - t_{n_0})^b} - \frac{1}{(t_{n_1} - t_{n_0})^b}\right]\left[\frac{1}{(t_i - t_{n_0})^b} - \frac{1}{(t_{n_1} - t_{n_0})^b}\right]^{-1}, \tag{4.15}$$

where b is the discounting parameter, n_0 is the index of the first time step of the current period, and n_1 is the index of the last time step of the current period. As shown in panel D of Figure 4.7, $\alpha_{i,k}$ is one at t_i (no discounting of the present value), and zero at the predicted end of the current period. It is also apparent that a larger b discounts more heavily future values. In algorithm 2, discount factors are not used if the current period end predicted by zero-crossing phase has been reached before the next zero-crossing is detected. In this case, stimulation is applied right then if beneficial.

Algorithm 2 decide to stimulate at time step t_i

if no stimulation for N_{lim} time steps and no stimulation yet in current period **then**
  find $(p, q) \in \{1, .., N_E\} \times \{1, .., N_I\}$ s.t. (E_p, I_q) is the closest to $(E(t_i), I(t_i))$
  if $\Gamma(p, q, 1) < 0$ **then**
    if predicted period end already reached **then**
      stimulate
    else
      if $\Gamma(p, q, 1) < \min_{k \in \{2,\ldots,n_1 - i + 1\}} (\alpha_{i,k} \Gamma(p, q, k))$ **then**
        stimulate
      end if
    end if
  end if
end if

4.5.2 Phase space stimulation based on isostable amplitude can be beneficial compared to phase space stimulation based on Hilbert amplitude

Using the three fitted patient models, we compare the performance of algorithm 2 when based on isostable amplitude or on Hilbert amplitude. We therefore apply algorithm 2 based on either Γ_0^{∞} or on Γ_0^{H} to the three fitted models for various stimulation magnitudes δE, and for various values of the discounting parameter b. Hilbert amplitude instantaneous response fields have space bins with missing values (white zones in Figure 4.7, panels A2, B2, and C2). For fair comparison, the corresponding space bins are emptied in isostable amplitude instantaneous response fields (not shown). For compatibility with algorithm 2, Γ_0 is set to zero in both cases for empty space bins, and stimulation will not be triggered at these locations. Smaller stimulation magnitude ratios $\delta E / \delta E_0$ are used for patient 5 because of the comparatively small size of the Hilbert amplitude field available for this patient. To compare Hilbert and isostable amplitude stimulation, we measure stimulation efficacy by integrating the stimulation data power spectrum density (PSD) in ten trials of 5000 s of stimulation.

Figure 4.8 shows that stimulation based on isostable amplitude is in most cases better or on par with stimulation based on Hilbert amplitude. The only exception is

the highest discounting parameter, highest stimulation case for patient 1. We note that noise at the boundaries of Γ_0^{H} (see Figure 4.7, panels A2, B2, and C2) is not responsible for differences between asymptotic and Hilbert amplitude as it is not present for large stimulations (not shown), where we observe the largest differences in favour of isostable stimulation for patient 5 and patient 6. While the observed differences in efficacy can be small depending on stimulation magnitude, they are statistically significant as evidenced by the size of the sem error bars in Figure 4.8. An

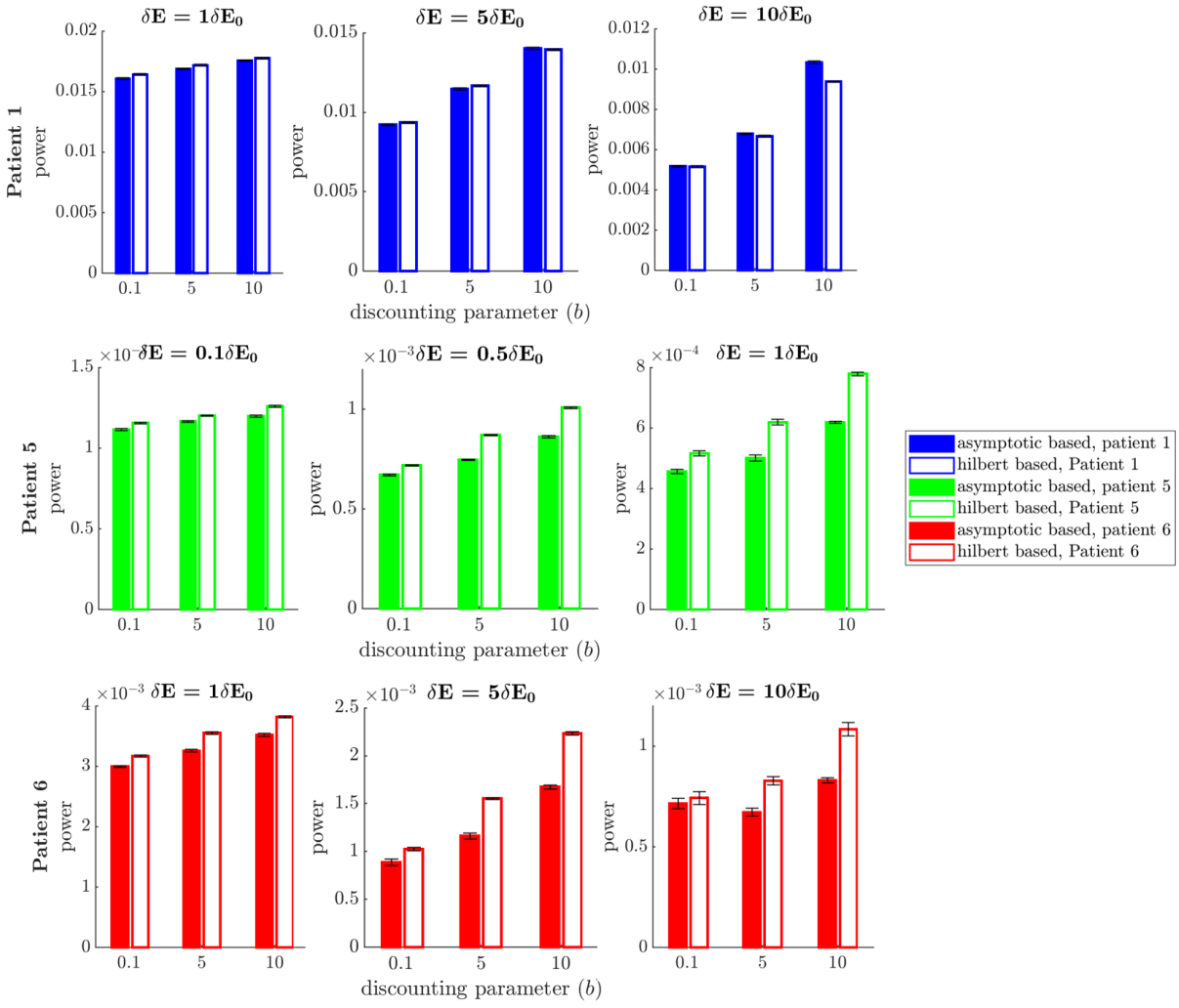

Figure 4.8: Comparison of the efficacy of a phase space stimulation strategy based on isostable amplitude fields (colored bars) and on Hilbert amplitude fields (white bars). Each row corresponds to a WC patient fit. Results are shown for a range of stimulation magnitude ratios $\delta E/\delta E_0$ (increasing from left to right), and a range of discounting parameters b. Efficacy is measured as the integral of the PSD of the corresponding signal. Averages correspond to ten trials of 5000 s of stimulation, and sem errorbars are shown in black.

additional, and perhaps more critical benefit of isostable coordinates is the relative simplicity with which isostable coordinates can be obtained everywhere in phase space to a high resolution. These results support the relevance of isostable amplitude fields to optimise model based stimulation strategies targeting Hilbert amplitude.

4.6 Discussion

In this study, we first investigated whether isostable amplitude response could be related to an experimental method measuring the Hilbert amplitude response to phase-locked deep brain stimulation, the block method. We based our work on models fitted to recordings of essential tremor patients undergoing phase-locked deep brain stimulation. Noting that in the block method, the amplitude response measurement is delayed to the end of the block, we showed that an instantaneous change in isostable amplitude can be converted to a change in Hilbert amplitude later in time. This allowed to scale the isostable amplitude response to approximate the experimental method response in synthetic data. Further, the dependence of the block amplitude response to phase-locked stimulation on the oscillation amplitude at the time of stimulation was predicted using isostable amplitude, which is of interest to adaptive deep brain stimulation.

Isostable amplitude measures convergence time to the attractor, which might be of importance to optimise stimulation. We report that for a simple phase space stimulation strategy, stimulation based on isostable amplitude was in most cases on par or at a slight advantage compared to stimulation based on Hilbert amplitude. This suggests that there might be a benefit to using more broadly isostable amplitude for model-based optimisation of stimulation in neurological disorders.

Isostable amplitude Isostables have been developed with model reduction in mind (Mauroy et al. 2013; Wilson and Ermentrout 2017; Shirasaka et al. 2017), but there are similarities between isostable amplitude and the Hilbert amplitude, which is one of the preferred measure of synchrony in experimental data. Trajectories starting from the same isostable converge synchronously to the attractor. In our

(E, I) model, trajectories starting from the same isostable share the same Hilbert amplitude (true regardless of whether the Hilbert amplitude is defined based on E or on I). This is reflected by the fact that isostable and Hilbert amplitude fields are strikingly similar (contrast Figure 4.2 with Figure 4.6). Although amplitude values and gradients are different, contours of equal amplitude have very similar shapes. In $\mathbb{R}^2$, a relationship might be revealed by studying the approximation of isostable coordinates given by equation (4.4), which can be interpreted as the norm of a 2D vector, similarly to the Hilbert amplitude. The Hilbert amplitude is indeed the norm of the vector formed by the real and the imaginary parts of the analytic signal.

Phase-amplitude reductions such as the isochron-isostable reduction are augmentations of classical phase reductions, and various techniques are available (for a recent review, see Pietras and Daffertshofer 2019). As reviewed in Section 1.2.4.1, not all techniques are based on isostable amplitude (Wedgwood et al. 2013; Castejón et al. 2013), but most are only applicable when the attractor is a limit cycle (Wedgwood et al. 2013; Castejón et al. 2013; Wilson and Moehlis 2016a; Wilson and Ermentrout 2017; Shirasaka et al. 2017; Mauroy and Mezić 2018), which is not the case in the present work. Benefits of the isostable method chosen here (Mauroy et al. 2013) include its computational efficiency, and its truly global character. Isotables can be computed everywhere in the basin of attraction of the fixed point without limitations. The theory behind isostables considers purely deterministic dynamical systems, whereas the fitted WC models employed in our study are stochastic. Theories have been developed to account for the effect of noise in isochrons (Schwabedal and Pikovsky 2013; Thomas and Lindner 2014; Cao et al. 2020), but isostables are lagging behind in this respect. However, isostable amplitude fields are similar to Hilbert amplitude fields which were obtained by averaging noisy trajectories. It therefore seems likely that isostable amplitude contours would not change substantially were noise accounted for.

Relationship between isostable amplitude response and block method amplitude response The relationship between isostable amplitude response to

stimulation and experimental measurement methods of amplitude response has not been investigated before. We relate isostable amplitude response to the Hilbert amplitude response following a block of stimulation measured as in a phase-locked DBS study in ET patients (Cagnan et al. 2017). The isostable amplitude response in phase space can be scaled to approximately match the block method response, in particular in terms of scale (Section 4.4.3). We base the scaling on relating an instantaneous change in isostable amplitude to a delayed change in Hilbert amplitude. An intuition for why this scaling is relevant to the block method is that the amplitude response measurement in the block method is not instantaneous, but rather delayed to the end of the 5 s stimulation block (which corresponds roughly to 25 periods of the tremor; see Figure 2.1, top panel). While the block method is not a perfect example of a delayed measurement paradigm (stimulation is delivered up until measurement, which happens after a finite time, relaxation time between blocks is only 1 s), our case study suggests that scaled isostable amplitude response may be suited to approximate delayed Hilbert amplitude response.

The differences between the scaled asymptotic amplitude response curves ($\widetilde{\text{aARCs}}$) and the block amplitude response curves (bARCs) observed in Figure 4.4 may be explained by several factors. Regarding the shape of the curves, $\widetilde{\text{aARCs}}$ are based on geometric phase referenced to the maximum of E, which is only a coarse approximation of the Hilbert phase used in bARCs. In the conversion of the stimulation delay used in synthetic data from a duration in time to a duration in phase, the average frequency of E is used (equation (4.14)). In synthetic data, the stimulation delay inevitably corresponds to a different phase duration for each cycle. Regarding the vertical shift of the curves and their scaling, bARCs are based on synthetic data generated from the stochastic WC fitted models, whilst $\widetilde{\text{aARCs}}$ are obtained in deterministic phase space. Noise might not affect isostable contours substantially, but could have a larger effect on the values of the isostable field and its gradient. Further, $\widetilde{\text{aARCs}}$ are derived from one stimulation pulse only, whereas bARCs are obtained for a block of phase-locked stimulation. This effect is lessened by considering the response divided by the number of pulses

in synthetic data, but the interaction of stimulation pulses within a block is not accounted for. Synthetic data is filtered before computing bARCS, which might also affect the scale and shift of the response.

Amplitude contours obtained from isostable coordinates allow to study the influence of tremor amplitude at the time of stimulation on the amplitude response (see Figure 4.5, panel B). This is a highly relevant topic to aDBS. Isostables can be computed with relative ease everywhere in the basin of attraction of the model, providing an exhaustive picture of the influence of tremor amplitude at the time of stimulation. With this new dependence, ARCs can be turned into amplitude response surfaces (not shown). The amplitude contours we used are based on isostables, but not the amplitude values associated with these contours (which are obtained from equation (4.7)). As mentioned before, isostable and Hilbert amplitude contours are similar in this study, therefore similar results would be obtained based on Hilbert amplitude contours.

Except for very low amplitudes for patient 5, the scale of the response to stimulation decreases when tremor amplitude at which stimulation is applied increases. An intuition for this is that for a given stimulation magnitude, the difference in convergence time to the attractor will be less when far from the attractor (i.e. at high amplitude). There, the decay is faster and the distance corresponding to stimulation will be covered in less time. This magnification of the amplitude response to stimulation at lower amplitude is also predicted by the population response of coupled phase oscillators whose time evolution follows Kuramoto equations (Weerasinghe et al. 2019, reviewed in Section 1.2.3.4), despite response to stimulation being measured therein as an instantaneous change in amplitude. The same dataset is used in our study, and evidence of a magnified amplitude response to stimulation at lower amplitudes is found for patient 5, but not in other datasets. These responses were however measured for individual pulses within stimulation blocks, which is not what is modelled in our study. The behavior of patient 5 at very low amplitude can be explained in our work by the fact that the maximum in isostable gradient magnitude is not as close to the fixed point as

in other patients (see Supplementary Figure C.2 in Appendix C.2). A hybrid DBS strategy was put forward in (Weerasinghe et al. 2019) whereby high-frequency DBS is applied at higher amplitudes and phase-locked stimulation at lower amplitudes, where its efficacy is greater. The predictions of our models fitted to patient data provide support to this stimulation strategy, with the caveat that the efficacy decrease at higher amplitudes might be small in some patients (here patient 5) and might not warrant the use of high-frequency DBS.

Comparing phase-space stimulation strategies based on isostable and Hilbert amplitude The closed-loop phase-space stimulation strategy suggested in Section 4.5.1.2 produces overall slightly better results when based on isostable amplitude than when based on Hilbert amplitude. Minimising isostable amplitude is minimising convergence time to the attractor. Knowledge of the future evolution of the (deterministic) non-linear system embedded in isostable coordinates may provide an advantage in controlling the Hilbert amplitude of the stochastic system. Stimulation based on isostable amplitude tends to happen a little later in phase, and tends to be more focal (see Supplementary Figure C.3 in Appendix C.2). While the former is due to differences in Γ_0, the latter may be due to the fact that Hilbert amplitude fields are not as smooth (contrast Figure 4.6 and Figure 4.2) since they are obtained by averaging stochastic trajectories. Additionally, boundaries between regions where stimulation is beneficial and where it is not differ in isostable and Hilbert amplitude response fields, particularly in patients 5 and 6 (see Figure 4.7, panels A to C). It is worth emphasizing that the resolution and coverage that can obtained for isostable amplitude fields is to our best knowledge out of reach for Hilbert amplitude fields. To obtain Hilbert amplitude fields, considering noisy trajectories is necessary to explore more of phase space, which drastically limits the resolution that can be obtained for a given number of simulations. To level the playing field for our comparison, the isostable amplitude field was masked to match the coverage of the Hilbert amplitude field, and the same resolution was used for both amplitude fields.

Isostable based stimulation for neurological disorders could be investigated further. Excessive synchrony in PD has been explored with isostables in a model of coupled neurons (Wilson and Moehlis 2016b), but not in a model constrained with experimental data. As shown in Chapter 3 and in previous studies (Gillies et al. 2002; Holgado et al. 2010; Pavlides et al. 2012; Merrison-Hort et al. 2013; Nevado-Holgado et al. 2014), the WC model can describe the feedback loop composed of the STN and the GPe, which plays a role in PD excessive beta synchrony. The low-dimensional WC can more easily by constrained with patient data as discussed in Section 1.2.3. Similarly to what was done in the present study, isostable based stimulation could be applied to WC focus models fitted to PD patients, and compared to simpler stimulation strategies. Such a strategy would not be selective to pathological activity, but given a way to discriminate between physiological and pathological activity, isostable control could be temporarily switched off to spare physiological activity. Because isostables are related to convergence properties of a system, isostable amplitude could be provided as an additional feature to complement Hilbert amplitude when trying to optimise stimulation with machine learning approaches. Furthermore, isostable coordinates are at present limited to situations where a model is available. Obtaining the Koopman operator from data is being researched (Marrouch et al. 2019; Korda et al. 2020), which could allow to recover isostables from data as there is a strong connection between Koopman operator and isostables (Mauroy et al. 2013). A method to directly obtain isostables from data has very recently been suggested (Wilson 2020), however it relies on limit cycle dynamics.

5 General discussion

Contents

‘

5.1 Summary of contributions

Before providing a general discussion, we summarize below the major contributions of this thesis to neurology and neuroscience on one hand, and to mathematical and computational neuroscience on the other hand.

Neurology and neuroscience

Contributions pertaining to ET (Chapter 2 unless otherwise stated)

- In patients receiving phase-locked stimulation, we showed that half of the datasets analysed (three out of six) had significant bPRCs and bARCs. In these patients, response curves had a dominant first harmonic, and the phase shift between them was between $\frac{\pi}{2}$ and π.

- A non-linear model including one feedback loop comprising excitatory and inhibitory populations was enough to reproduce realistic tremor dynamics and the effects of phase-locked DBS. This supports the hypothesis of an intermittently connected tremor network.
- Fitted models reproducing the phase dependence of the response to phase-locked DBS along with a phase-locked DBS simulator provide a synthetic data source which can be used to optimise and test stimulation strategies in individual patient models.
- Isostable amplitude provided a prediction for the dependence of the response to stimulation on the amplitude of the on-going oscillations (Chapter 4).

Contributions pertaining to PD (Chapter 3)

- We showed that average beta burst duration profiles are significantly different ON/OFF medication for a majority of patients, but the medication state does not significantly affect burst amplitude profiles (when accounting for the difference in mean power).
- We established that a beta burst duration specific measure of non-linearity was significantly greater OFF medication, and was correlated with motor symptoms. This implies that non-linearity could be a marker of pathology for closed-loop DBS.
- One feedback loop comprising excitatory and inhibitory populations was enough to reproduce the most non-linear beta burst duration profile of the dataset. This is consistent with the hypothesis of the STN-GPe loop playing a predominant role in the generation of beta oscillations.
- We demonstrated that burst duration profiles are a signature of envelope dynamics, which may underlie the success of burst duration as a biomarker in PD.
- We identified biologically inspired models and simpler envelope models of transient beta ON/OFF medication, which can provide a source of synthetic physiological and pathological filtered LFPs.

Mathematical and computational neuroscience

Contributions from Chapter 2

- Based on approximations of the Hilbert phase and amplitude, we derived approximate analytical expressions for the first order PRC and ARC of a linear two-dimensional model. For slow decay, the ARC is the opposite of a scaled version of the PRC derivative.
- We showed that a simple phase definition is approximately equivalent to the Hilbert phase of the first dimension in a linear two-dimensional model.

- Patient fits demonstrated that oscillatory activity in the datasets analysed was overall better described by stochastic models with stable focus dynamics than with limit cycle dynamics (also Chapter 3).
- We highlighted the ability of a canonical, mesoscale neuroscience model to fit to patient data in the context of movement disorders (also Chapter 3). We suggest the WC model as a candidate for further study of phase-locked DBS.

Contributions from Chapter 3

- We obtained an approximate analytical expression for average burst duration in envelope models.
- We proposed a method to infer envelope dynamics from a time series.

Contributions from Chapter 4

- We showed that model-based stimulation strategies aiming at suppressing the Hilbert amplitude of oscillations could benefit from using isostable amplitude.
- We related an instantaneous change in isostable amplitude to a change in Hilbert amplitude later in time in a two-dimensional model. This allowed to scale the isostable amplitude response to approximate the block method amplitude response in synthetic data.
- We reported that in a two-dimensional model, isostable amplitude fields are easier to obtain than Hilbert amplitude fields.

5.2 Common threads

Detailed discussions in the context of the relevant literature are provided in individual chapters, and in this section we focus on parallels between chapters.

In Chapter 2 and Chapter 4, we have presented ways of approximating from a dynamical system perspective definitions of phase and amplitude commonly used in neurophysiology, the Hilbert phase and amplitude. For linear two-dimensional foci, we have shown that a simple phase definition based on the frequency associated with the complex conjugate eigenvalues of the Jacobian at the fixed point is approximately equivalent to the Hilbert phase (Section 2.5.2). In Chapter 4, we related an instantaneous change in isostable amplitude to a change in Hilbert amplitude later in time under certain conditions (Section 4.4.2). In both chapters, bridging the gap between definitions used in models and in neurophysiology was a requirement to make predictions that are meaningful in a clinical setting. These

predictions were the shape of response curves and the phase shift between them in Chapter 2, and the dependence of the response to blocks of phase-locked stimulation on on-going oscillation amplitude in Chapter 4.

The complexity of models required to fit the data in Chapter 2 and Chapter 3 shows noteworthy similarities. Firstly, one WC model comprising one excitatory and one inhibitory population was sufficient to fit the data in both cases. As mentioned previously, this provides support for hypotheses related to the pathophysiology of ET and PD, respectively. However, reproducing the most non-linear burst duration profile in Chapter 3 required delays in the connections between and within populations. Secondly, non-linearity in the models was needed in both chapters to better reproduce the data. In Chapter 2, a non-linear WC model better described the shape of response curves and the phase shift between them than a linearisation of the model. Successive stimulation pulses have been reported to add non-linearly (Cagnan et al. 2013), which could partially explain this finding. In Chapter 3, whilst a linear WC model could reproduce linear burst duration profiles, a non-linear WC model was required to fit the most non-linear burst duration profile of the dataset. Although the brain is made up of a myriad of highly non-linear neurons, it does not necessarily follow that going beyond linear modelling will be useful to the study of mesoscale brain signals (Schreiber and Schmitz 2000). Chapter 2 and Chapter 3 provide evidence that non-linear models can bring practical benefits when modelling mesoscale recordings. Our approach in both chapters was to gradually increase the complexity of our models when fitting to data. The performance of linear models in reproducing the data was first deemed unsatisfactory before non-linearity was introduced. This contributed to addressing overfitting of the data.

In Chapter 2, Chapter 3, and Chapter 4, Gaussian white noise interacts with the models' vector field to reproduce the data. As mentioned before, model parameters play an integral part in shaping the resulting transient oscillations (see Appendix A.8 related to Chapter 2). Uncorrelated noise corresponds to contributions that we model as having no explanatory power. In Chapter 2, the transient nature of the fitted patients' tremor was better reproduced by stable focus dynamics rather than limit

cycle dynamics. Similarly, in Chapter 3, the best fit to patient 6R OFF was a non-linear WC model reaching a steady state in the absence of noise. As more complexity was not needed, only linear models (unable to give rise to limit cycle dynamics) were fitted to patient 3L ON. In contrast to pathological oscillation models fitted to data in this thesis, fitted envelope models (Chapter 3) exhibit one-dimensional fixed point dynamics where the fixed point is not located at zero. Such a fixed point in one dimension corresponds to a limit cycle in two-dimensional embeddings such as $(z, \mathcal{H}(z))$, where z is the oscillatory activity obtained from envelope models in Section 3.6.1. This is expected as envelopes are positive at all times.

Isostable amplitude introduced in Chapter 4 is related to convergence time to the attractor, and could in theory be used to predict burst duration studied in Chapter 3. Predictions at the beginning of a burst could help target longer bursts with DBS in PD. However this would require to identify from data high dimensional envelope models where the stochastic part of the dynamics is small compared to the deterministic part. My attempts to obtain these models from data using system identification techniques such as DBI (Smelyanskiy et al. 2005a; Smelyanskiy et al. 2005b; Stankovski et al. 2012) or sparse identification of nonlinear dynamics (SINDy, Brunton et al. 2016) have been unsuccessful (not shown).

5.3 Limitations

Sample sizes in this thesis are small (6 ET datasets and 8 PD patients). This is however typical of such studies, and reflects the considerable challenges in obtaining tremor recordings with phase-locked DBS in ET patients, and LFP recordings in PD patients. Patient fatigue limits recording length in ET patients as mentioned before. Although new wireless technology is becoming available for research (Swann et al. 2018), LFP recordings still require in most cases DBS leads to be accessible. This is only possible as part of a two-stage procedure where leads are externalized during electrode implantation surgery. There is an opportunity to record LFPs before the second surgery to implant a pulse generator in the chest. Although lead externalization has been reported to not increase the risk of infection (Rosa

et al. 2017b), it is not a universal practice, which limits patient recruitment. Further, surgeries are about a week apart, which leaves little time to schedule LFP recordings, considering surgery recovery time. In Chapter 2, fits were only performed for patients who had statistically significant response curves (significance criteria in Section 2.3.1), namely three datasets out of six. Chapter 4 relies on fitted models from Chapter 2, therefore the comparison between stimulation strategies based on isostable amplitude and Hilbert amplitude has only been carried out in three models. Correlations between motor impairment and degree of non-linearity presented in Chapter 3 are based on 8 patients. In all three chapters, conclusions should be re-evaluated as more datasets become available.

Features fitted to in Chapter 2 and Chapter 3 were carefully selected to capture key characteristics of the data. In Chapter 2, we considered three features to reproduce tremor dynamics, and bPRC to capture the response to phase-locked DBS (bARC is not fitted to, but predicted by the fitted models), see Section 2.6.1 for more details. In Chapter 3, we selected the data PSD as well as the average burst duration profile to reproduce bursting dynamic. This choice was motivated by the ability of average burst duration profile to capture envelope dynamics as discussed in Section 3.7. We acknowledge that progressively adding data features to fit to would necessarily gradually decrease the quality of the resulting fits. In this process, there will be a point at which two-population WC models will no longer fit to all the features well. Our models are therefore not reproducing the data, but key features of the data, which makes feature selection a crucial modelling step. Reproducing more features of the data may require more complex models, such as models with more than two WC populations. In models of beta oscillations in PD, this might reflect the need to model cortical populations using more than a constant input and uncorrelated noise (Pavlides et al. 2015). Another limitation related to fitting is non-identifiability of model parameters. Despite the relative simplicity of the mesoscale models used in Chapter 2 and Chapter 3, we suspect some level of non-identifiability. For this reason, our conclusions do not rely on the values of parameters obtained from fitting.

There are limitations to the correspondence between models presented in this thesis and the underlying biology. The price to pay for the simplicity of the WC model is the lack of a precise account of microscopic neuron dynamics. In particular, the WC model does not account for differences in neuron spiking patterns such as burst and tonic firing that have been implicated in ET, and can only give a network description (Yousif et al. 2017). Given the mesoscale level of the WC model and the fact that recordings fitted to in Chapter 2 are peripheral tremor, the suggested mapping to thalamic populations is only a plausible mapping as discussed in more details in Chapter 2. For simplicity, physiological conduction delays between populations are also not described in Chapter 2, which allows for mathematical analysis of the model. It should also be kept in mind that we model tremor in Chapter 2 as the output of a neural population model, which is justified by the high coherence between ventral thalamic activity and electromyographic recording of the contralateral wrist flexors (see Section 1.2.1.1 and Section 2.4). In Chapter 3, envelope models have no memory of past values for the same reason, and the passage method cannot accommodate models with memory. Non-linearity in the drift function of envelope models fitted to patient 6R OFF may be an interesting feature in the context of closed-loop DBS. However, the precise physiological interpretation of the non-linearity is unclear.

5.4 Implications

We discuss in this subsection some of the main implications of the results presented in this thesis. More details can be found in individual chapter discussions.

Our findings from Chapter 2 have implications for the pathophysiology of ET. Various brain structures have shown coherence with muscles giving rise to essential tremor, outlining a central network that could be involved in tremor generation (Schnitzler et al. 2009). However, coherence between the cortex and muscles involved in tremor was found to be intermittent, even at high tremor levels (Raethjen et al. 2007). This lead to the hypothesis that the central tremor network may be a distributed network, where a number of oscillators may be active at

different times and may intermittently entrain each other (Raethjen and Deuschl 2012). In Chapter 2, we concluded that a two-population feedback loop receiving constant inputs and uncorrelated noise can reproduce tremor dynamics and the phase-dependent effects of DBS. This supports the hypothesis of a distributed tremor network, where two coupled populations would be enough to generate tremor at any given time, and continuous interactions between populations would not be required. At present, pharmacological treatments given to ET patients are not specific to the disease, and improving our understanding of ET pathophysiology is a first step towards better drugs.

In Chapter 3, we showed that PD patient STN LFPs are more non-linear in the OFF medication state which is pathological, compared to the ON medication state which is more physiological. Although different techniques were used, this finding echoes earlier studies reporting more non-linearity in the pathological state at the subcortical (Marceglia et al. 2006), and cortical level (Cole et al. 2017; Jackson et al. 2019). We further demonstrated in Chapter 3 that the degree of non-linearity is correlated with motor impairment. It follows that non-linearity could provide a measure of pathology to closed-loop DBS in PD. While more work is needed to assess the feasibility of this approach, non-linearity might prove a more specific target of pathology than beta amplitude which aDBS is currently based on. Such a measure of pathology may also be more robust to changes in beta oscillation amplitude caused by medication and activity, which would require an amplitude threshold to be adjusted. Further, the correlation between non-linearity and motor impairment can contribute to the debate regarding slow aDBS (Rosa et al. 2017a; Arlotti et al. 2018) and fast aDBS (Little et al. 2013; Little et al. 2016). Slow aDBS based on beta power averaged over 50 s cannot respond to non-linear correlations since they are not reflected in average power. In contrast, fast aDBS based on beta power averaged over 300 ms could, at least in principle, have more of a differential effect on non-linearity because of its rapidly changing dynamics.

The results of Chapter 4 offer two main implications. Firstly, the predicted dependence of amplitude response on on-going oscillation amplitude partially

supports the hybrid DBS strategy suggested in (Weerasinghe et al. 2019). Hybrid DBS is based on the premise that phase-locked DBS is more effective at low tremor amplitude. This behaviour was predicted in Chapter 4 in two out of three cases. Secondly, isostable amplitude may prove beneficial to oscillation amplitude control in model-based approaches to DBS in various neurological disorders. This follows from a measurable advantage of isostable amplitude over Hilbert amplitude in most comparisons of phase space stimulation performed in Chapter 4.

5.5 Future work

To comment on the values of fitted parameters in an effort to understand ET pathophysiology, parameter identifiability of the non-linear WC model from Chapter 2 could be investigated in future work. A first step would be fitting to synthetic data generated by the model to check that model parameters can be recovered in representative parts of parameter space. Further, approximate Bayesian computation (ABC) methods can provide an estimate of the posterior distribution over parameters for intractable likelihoods, indicating which parts of parameter space are consistent with the data (for a recent review, see Beaumont 2019). However, because of sensitivity to parameter prior distributions, these methods should be tested with care. Whether ABC methods could successfully tackle a complicated landscape and provide more meaningful insight on fitted model parameters in the setting of the present work is an interesting avenue for further research.

Importantly, optimal stimulation strategies could be further studied in silico based on fitted ET patient models from Chapter 2. For instance, global optimisation could be used to explore parametric stimulation strategies where stimulation is not simply a pulse (only pulses were used in Chapter 4). As more data become available, the comparison between stimulation strategies based on isostable amplitude and on Hilbert amplitude (Chapter 4) should be repeated with models fitted to the new data.

The work described in Chapter 3 should be extended in several ways. Firstly, the non-linearity analysis (Section 3.4) should be repeated ON and OFF DBS. We hypothesize that the same conclusions would apply, namely more non-linearity OFF

DBS, and a correlation between the degree of non-linearity and motor impairment. Moreover, drift functions inferred from data using the passage method could provide a signature of how various types of experimental DBS protocols affect envelope dynamics. Modelling the effects of stimulation in envelope models would allow these models to be used in control strategies.

Secondly, more work is needed to assess the feasibility of using non-linearity in STN LFPs as a target for closed loop stimulation. While other authors have suggested considering waveform shape (Cole et al. 2017; Jackson et al. 2019), online statistical comparison with linear surrogates computed periodically could be investigated. This should first be evaluated offline using existing data. One appeal of targeting LFP non-linearity is that it could be overall more robust than threshold-based aDBS to changes in beta levels due to movement. This should be evaluated using existing movement task data.

Thirdly, to elucidate the physiological basis of envelope model non-linear drift functions, a link from envelope model to population model could be explored. Powanwe and Longtin (2019) have transformed a linear WC model to a Rayleigh envelope model and a phase model under certain assumptions. Starting from envelope models with non-linear drift functions such as the degree three polynomial fitted to patient 6R OFF in Chapter 3 and a simple phase model, similar assumptions as in (Powanwe and Longtin 2019) could be made to obtain dynamics of an excitatory and an inhibitory population. The resulting population model could then be contrasted with a linear WC model.

Both ET and PD are heterogeneous diseases (Louis and Ferreira 2010; Van Rooden et al. 2010), and identifying disease subtypes would allow to provide more targeted therapies. Models individually fitted to patient pathological oscillations could assist in identifying patient clusters, provided model parameters are identifiable. In the case of PD, the non-linearity measure introduced in Chapter 3 or envelope models inferred from LFP recordings could be used to stratify patients, given a larger sample than what was available in Chapter 3.

In future work, pathological oscillations in PD and ET could be modelled with so-called "next-generation neural masses" to provide a more realistic description of microscopic neuron dynamics with a moderate increase in complexity (for a recent review, see Bick et al. 2020). In these models, theta neurons or equivalently quadratic integrate and fire (QIF) neurons provide a spiking neuron description at the microscopic level. Simple equations for mesoscale activity are obtained through mean-field reduction in the thermodynamic limit (Montbrió et al. 2015; Laing 2017; Pietras et al. 2019). Theta neurons can spike periodically or remain in an excitable state depending on input. They are therefore better neuron models than simple phase oscillators used in the Kuramoto model, and are still amenable to mean-field reduction. Mean-field reductions of networks of QIF neurons have been used to model beta changes related to movement (Byrne et al. 2017; Byrne et al. 2020), and to investigate the emergence of phase-locking in coupled populations (Dumont and Gutkin 2019).

5.6 Concluding remarks

In this thesis, we have provided insights relevant to the improvement of therapies for ET and PD and contributed to bridge the gap between dynamical systems and patient data. Some of the theoretical developments presented in this thesis in the context of ET and PD are more general, such as the relationship between PRC and ARC in linear two-dimensional models, the analytical expression for burst duration in envelope models, the passage method, and the comparison between isostable and Hilbert amplitude. Thus, these contributions may prove useful to optimising the delivery of brain stimulation in various contexts. Further, next-generation DBS systems are likely to include more stimulation contacts (Schüpbach et al. 2017). Maximizing their clinical benefit will require sophisticated algorithms, and we can expect mathematical models to play an increasing role in developing these algorithms. Although there are considerable challenges ahead, non-invasive DBS is being developed (Grossman et al. 2017), and the use of brain stimulation as a therapeutic tool is likely to grow in the future.

Appendices

A

Appendix to response curve phase-dependence chapter

Contents

In this appendix pertaining to Chapter 2, we include technicalities on approximating the Hilbert phase in the linearisation (Section A.1), details of the derivations leading to response curve analytical expressions in the linearised system (Sections A.2 to A.4), and the procedure used to obtain WC parameters from a given Jacobian (Section A.5). We also present details of the two-step optimisation used for fitting to patient data (Section A.6), the implementation of live-phase tracking and stimulation

(Section A.7), as well as an analytical expression for the standard deviation of the tremor for the stationary linearised model (Section A.8). Supplementary figures and supplementary tables make up Section A.9 and Section A.10, respectively.

A.1 Hilbert transforms of sine and cosine exponential decays with error terms

The goal here is to show that $\mathcal{H}(s(t)s_j(t)) \approx s(t)\mathcal{H}(s_j(t))$ for $j = c, n$, with $s(t) = e^{\sigma|t|}$, $s_c(t) = \cos\omega t$, and $s_n(t) = \sin\omega t$. The Bedrosian identity (Bedrosian 1963) states that the Hilbert transform of the product of a low-pass and a high-pass signal with non-overlapping spectra is the product of the low-pass signal and the Hilbert transform of the high-pass signal. The spectrum support of s is $\mathbb{R}$ and therefore overlaps with the spectra of s_c and s_n, but for low decay compared to the rotation, the spectrum of s is very small where it overlaps with the spectra of s_c or s_n. Because of the overlaps, the equality given by the Bedrosian identity is not exact and turns into an approximation, and inspired by the proof in (Bedrosian 1963), we can calculate error terms. Let S and S_c be the Fourier transforms of s and s_c respectively:

$$s(t)s_c(t) = \frac{1}{(2\pi)^2}\int_{-\infty}^{\infty}\int_{-\infty}^{\infty} S(u)S_c(v)e^{i(u+v)t}dudv, \tag{A.1}$$

$$\mathcal{H}(s(t)s_c(t)) = \frac{1}{(2\pi)^2}\int_{-\infty}^{\infty}\int_{-\infty}^{\infty} S(u)S_c(v)i\operatorname{sgn}(u+v)e^{i(u+v)t}dudv. \tag{A.2}$$

The Fourier transform of s_c is given by $S_c(v) = \pi\left[\delta(v-\omega) + \delta(v+\omega)\right]$, so

$$\mathcal{H}(s(t)s_c(t)) = \frac{1}{(2\pi)^2}\int_{-\infty}^{\infty} S(u)e^{iut}\Gamma(u)du \tag{A.3}$$

where $\Gamma(u) = \frac{\pi}{i}\left[\operatorname{sgn}(u+\omega)e^{i\omega t} + \operatorname{sgn}(u-\omega)e^{-i\omega t}\right]$. This can be simplified as

$$\Gamma(u) = 2\pi\sin\omega t + \begin{cases} 0 & |u| < \omega \\ -\frac{2\pi}{i}e^{i\omega t} & u < -\omega \\ \frac{2\pi}{i}e^{-i\omega t} & u > \omega \end{cases}.$$

The Fourier transform $S(u) = \frac{2\sigma}{\sigma^2+u^2}$ is even, therefore

$$\mathcal{H}(s(t)s_c(t)) = \frac{\sin(\omega t)}{(2\pi)^2}\int_{-\infty}^{\infty} S(u)e^{iut}du + \frac{1}{2\pi i}\int_{\omega}^{\infty} S(u)\left(e^{i(u-\omega)t} - e^{-i(u-\omega)t}\right)du, \tag{A.4}$$

$$\mathcal{H}(s(t)s_c(t)) = s(t)\mathcal{H}(s_c(t)) + \mathcal{I}_{s_c}, \tag{A.5}$$

with

$$\mathcal{H}(s_c(t)) = \sin \omega t,$$
$$\mathcal{I}_{s_c} = \frac{2}{\pi} \int_{\omega}^{\infty} \frac{\sigma}{\sigma^2 + u^2} \sin{(u - \omega)t} du.$$

A similar derivation provides

$$\mathcal{H}(s(t)s_n(t)) = s(t)\mathcal{H}(s_n(t)) + \mathcal{I}_{s_n} \tag{A.6}$$

with

$$\mathcal{H}(s_n(t)) = -\cos \omega t,$$
$$\mathcal{I}_{s_n} = \frac{2}{\pi} \int_{\omega}^{\infty} \frac{\sigma}{\sigma^2 + u^2} \cos{(u - \omega)t} du.$$

Numerical integration demonstrates that for $\omega \gg |\sigma|$, and in particular in the case of the patients we are interested in, $\mathcal{I}_{s_c}$ and $\mathcal{I}_{s_n}$ are under 5% of the signal scale for about 12 periods (see Figure A.1). This is more than enough for our purposes as only one period is needed to derive response curves. It is therefore reasonable to ignore $\mathcal{I}_{s_c}$ and $\mathcal{I}_{s_n}$.

A.2 Reference trajectory without stimulation

Let us find the coefficients K_{ref} and K'_{ref} of the trajectory starting at $t = 0$ at a maximum of the first coordinate $X_1 = X_1^0 > 0$. With the choice $\phi = \omega t$, this will ensure we are referencing the phase to the maximum of X_1. It should be noted at this point that we are not using the Jacobian in what follows as we are interested in the dependence of the response on the rotation ω and the decay σ. From the initial condition at $t = 0$,

$$K_{ref} a_1 + K'_{ref} b_1 = X_1^0. \tag{A.7}$$

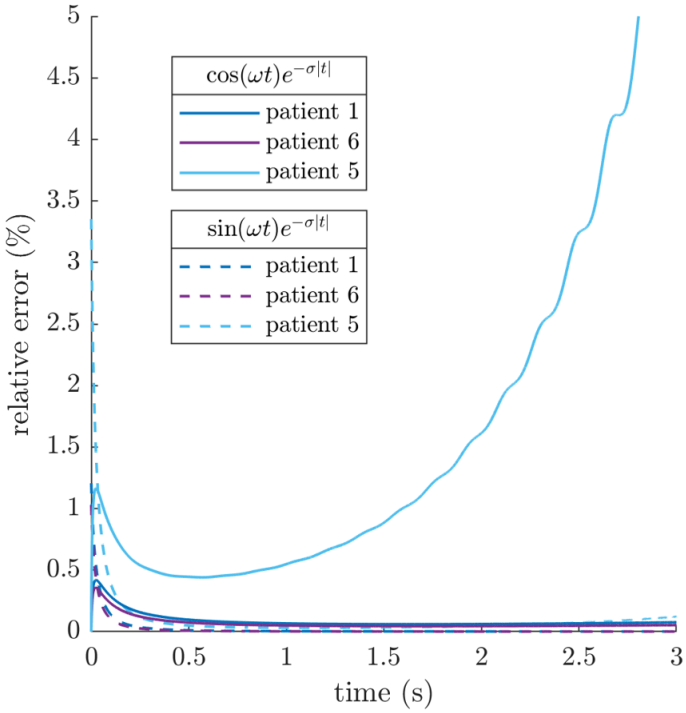

Figure A.1: Relative error made across patients in estimating $\mathcal{H}(s(t)s_c(t))$ by $s(t)\mathcal{H}(s_c(t))$ (solid lines) and $\mathcal{H}(s(t)s_n(t))$ by $s(t)\mathcal{H}(s_n(t))$ (dashed lines). The error is calculated as the ratio of $\mathcal{I}_{s_c}$ (respectively $\mathcal{I}_{s_n}$) over the modulus of the numerical Hilbert transform of the signal, which is the envelope of the signal. The relative error is under 5% in all cases for at least 12 periods.

Additionally, X_1^0 being a maximum requires that $\frac{dX_1}{dt} = 0$ at $t = 0$, therefore

$$\frac{dX_1}{dt} = e^{\sigma t}\left[-\omega(K_{ref}a_1 + K'_{ref}b_1)\sin\omega t + \omega(-K_{ref}b_1 + K'_{ref}a_1)\cos\omega t + \right.$$
$$\left.\sigma\left\{(K_{ref}a_1 + K'_{ref}b_1)\cos\omega t + (-K_{ref}b_1 + K'_{ref}a_1)\sin\omega t\right\}\right]. \quad \text{(A.8)}$$

Using the condition at $t = 0$,

$$K_{ref}(\sigma a_1 - \omega b_1) + K'_{ref}(\sigma b_1 + \omega a_1) = 0, \quad \text{(A.9)}$$

$$\text{(A.7)} + \text{(A.9)} \implies \begin{aligned} K_{ref} &= \tfrac{\sigma b_1 + \omega a_1}{\omega(a_1^2 + b_1^2)} X_1^0, \\ K'_{ref} &= \tfrac{-\sigma a_1 + \omega b_1}{\omega(a_1^2 + b_1^2)} X_1^0. \end{aligned} \quad \text{(A.10)}$$

We are excluding the case where the denominator in (A.10) is equal to zero, which corresponds to both a_1 and b_1 being zero, which would imply $X_1(t) = 0$. Also note that by picking a positive X_1^0, we are ensuring that the null derivative corresponds to a maximum of X_1 rather than a minimum.

A.3 Trajectory with stimulation

Let us determine what the coefficients K_{stim} and K'_{stim} are for the stimulated trajectory (still constrained by the dynamics of equation (2.10)). We have

$$\mathbf{X}^{\mathbf{1}^+} = \{K_{stim}\,(\mathbf{a}\cos\phi_0 - \mathbf{b}\sin\phi_0) + K'_{stim}\,(\mathbf{a}\sin\phi_0 + \mathbf{b}\cos\phi_0)\}\,e^{\sigma\frac{\phi_0}{\omega}}. \tag{A.11}$$

Solving for K_{stim} gives

$$K_{stim} = \frac{X_2^{1^-}(a_1\sin\phi_0 + b_1\cos\phi_0) - (X_1^{1^-} + \delta X_1)(a_Y\sin\phi_0 + b_2\cos\phi_0)}{a_2b_1 - a_1b_2}e^{-\sigma\frac{\phi_0}{\omega}}. \tag{A.12}$$

Plugging in $X_1^{1^-}$, $X_2^{1^-}$, and the expressions for K_{ref} and K'_{ref} yields

$$K_{stim} = \frac{\omega a_1 + \sigma b_1}{\omega(a_1^2 + b_1^2)}X_1^0 - \frac{a_2\sin\phi_0 + b_2\cos\phi_0}{a_2b_1 - a_1b_2}\delta X_1 e^{-\sigma\frac{\phi_0}{\omega}}. \tag{A.13}$$

Similarly for K'_{stim}, using the previous result:

$$K'_{stim} = \frac{X_2^{1-}e^{-\sigma\frac{\phi_0}{\omega}} - K_{stim}(a_1\cos\phi_0 - b_1\sin\phi_0)}{a_1\sin\phi_0 + b_1\cos\phi 0}, \tag{A.14}$$

$$K'_{stim} = \frac{-\sigma a_1 + \omega b_1}{\omega(a_1^2 + b_1^2)}X_1^0 + \frac{a_2\cos\phi_0 - b_2\sin\phi_0}{a_2b_1 - a_1b_2}\delta X_1 e^{-\sigma\frac{\phi_0}{\omega}}. \tag{A.15}$$

A.4 Phase at the next maximum of X_1 on the stimulated trajectory

We are looking for ϕ_{max} such that $\frac{dX_1^{stim}}{dt} = 0$ at $\omega t = \phi_{max}$. This give us

$$e^{\sigma\frac{\phi_{max}}{\omega}}\,[-\omega(K_{stim}a_1 + K'_{stim}b_1)\sin\phi_{max} + \omega(-K_{stim}b_1 + K'_{stim}a_1)\cos\phi_{max} +$$
$$\sigma\,\{(K_{stim}a_1 + K'_{stim}b_1)\cos\phi_{max} + (-K_{stim}b_1 + K'_{stim}a_1)\sin\phi_{max}\}] = 0, \tag{A.16}$$

$$\tan\phi_{max} = \frac{K_{stim}(\sigma a_1 - \omega b_1) + K'_{stim}(\sigma b_1 + \omega a_1)}{K_{stim}(\sigma b_1 + \omega a_1) + K'_{stim}(-\sigma a_1 + \omega b_1)}. \tag{A.17}$$

The phase ϕ_{max} is returned by the arctan function in $\left(-\frac{\pi}{2}, \frac{\pi}{2}\right)$, and corresponds to the previous peak on the stimulated trajectory extended backwards. The next peak has the same phase (mod 2π) as the expression in square brackets in equation (A.16) is 2π-periodic.

A.5 Finding WC parameters corresponding to a given Jacobian

The Jacobian of (2.7) evaluated at (E^*, I^*) can be simplified by making use of $f'(x) = \beta f(x)(1 - f(x))$. We also have

$$f(\Theta_1) = E^*, \tag{A.18}$$

$$f(\Theta_2) = I^*, \tag{A.19}$$

with

$$\Theta_1 = w_{EE}E^* - w_{IE}I^* + \theta_E,$$
$$\Theta_2 = w_{EI}E^* + \theta_I.$$

The Jacobian of (2.7) evaluated at (E^*, I^*) is therefore given by

$$J_{WC} = \frac{1}{\tau}\begin{bmatrix} w_{EE}f'(\Theta_1) - 1 & -w_{IE}f'(\Theta_1) \\ w_{EI}f'(\Theta_2) & -1 \end{bmatrix} = \frac{1}{\tau}\begin{bmatrix} w_{EE}\beta E^*(1-E^*) - 1 & -w_{IE}\beta I^*(1-I^*) \\ w_{EI}\beta E^*(1-E^*) & -1 \end{bmatrix}. \tag{A.20}$$

We are interested in finding WC parameters so that the linearisation of the WC model at the fixed point will be characterised by a given Jacobian matrix

$$J = \begin{bmatrix} J_{11} & J_{12} \\ J_{21} & J_{22} \end{bmatrix}. \tag{A.21}$$

If we pick values for β, E^* and I^*, the remaining parameters can be obtained by equating (A.20) and (A.21), and by re-arranging equations (A.18) and (A.19). Parameters in Supplementary Table A.1 were obtained using this method, which yields

$$\begin{aligned} \tau &= -\frac{1}{J_{22}}, \\ w_{EE} &= \frac{\tau J_{11} + 1}{\beta E^*(1 - E^*),} \\ w_{IE} &= -\frac{\tau J_{12}}{\beta E^*(1 - E^*)}, \\ w_{EI} &= \frac{\tau J_{21}}{\beta I^*(1 - I^*)}, \\ \theta_E &= 1 - \frac{1}{\beta}\ln\left(\frac{1}{E^*} - 1\right) - w_{EE}E^* + w_{IE}I^*, \\ \theta_I &= 1 - \frac{1}{\beta}\ln\left(\frac{1}{I^*} - 1\right) - w_{EI}E^*. \end{aligned}$$

A.6 Two-step optimisation

The optimisation procedure is as follows. For each patient, random sets of parameters are picked from uniform distributions (bounds in Supplementary Table A.3). To improve the efficiency of the optimisation, we accept parameters only if the PSD peak of the corresponding model (without stimulation) is within 1 Hz and 25% in magnitude of the data PSD peak. Once 2500 parameter sets have been accepted, we put them through local optimisations. Local optimisations are carried out using a direct search algorithm called the generalized pattern search algorithm (Torczon 1997; Audet and Dennis 2003). The pattern is a set of fixed vectors in parameter space. At each step, points to be polled (the mesh) are generated by adding a scaled version of the pattern to the current best point. If a point with a lower value of the objective function is found, this point becomes the new best point, and a scaled up version of the pattern is used next. If not, a scaled down version of the pattern is used next. Parameters supplied to pattern search are put on a similar scale to improve search robustness, and hard limits are given to the optimiser (see Supplementary Table A.3 in Appendix A.10). Optimisations are performed in parallel on a supercomputer. A time step of 1 ms is used for the fits (a period is about 200 ms). At the end of this process, the 20 best performing sets of parameters were put through more local optimisations with a finer time step of 0.1 ms and stop criteria leaving room for more steps. The finer time step is also used to produce the results shown in Section 2.6.2).

The implementation of the generalized pattern search algorithm used is Matlab's patternsearch optimiser with the poll method "positive basis 2N" and the following stop criteria:

- main optimisation (time step of 1 ms): mesh size of 10^{-4}, function call budget of 800,
- second optimisation (time step of 0.1 ms): mesh size of 10^{-5}, function call budget of 1000.

A.7 Live phase tracking and stimulation

One simulation consists of 600 trials with 12 blocks of phase-locked stimulation each. As in the experimental paradigm, blocks last 5s, and inter-block intervals are 1s. Inter-trial intervals are 5s, and the first trial starts after about 200 periods. During this initial time, the mean of E and the standard deviation of E, σ_{sim}, are obtained from about 20 periods after a ramp-up of about 40 periods. Phase-tracking subsequently starts: E is centered and a threshold $T = 0.2\sigma_{sim}$ is used to track positive zero-crossings. We define a positive zero-crossing as happening when

$$\begin{cases} E(n) < -T, \\ E(p) > T, \\ p > n, \\ \forall i \in \{n+1, ..., p-1\}, E(i) \in [-T, T]. \end{cases} \tag{A.22}$$

These conditions are constantly monitored, and if found true, a positive zero-crossing is declared to have happened at time step $\chi = \frac{n+p}{2}$. The threshold T was found critical to handle the noise included in the model, as it prevents situations where a negative zero-crossing very closely follows a positive zero-crossing (or vice-versa) from interfering. We evolve the zero-crossing phase according to a frequency based on the previous period, and if χ_k is the last positive zero-crossing to have occurred, the current value of the zero-crossing phase is given by

$$\varphi = \frac{2\pi}{t_{\chi_k} - t_{\chi_{k-1}}}(t - t_{\chi_k}). \tag{A.23}$$

If the value of 2π is reached, the phase value is set to 0 until the next positive zero-crossing is detected. Stimulation is provided after φ reaches the target phase for the block, and the stimulation trigger is recorded Δt_{stim} before stimulation occurs. If the zero-crossing phase has not reached the target stimulation phase yet when the next positive zero-crossing is detected, stimulation is provided right then. As in (Cagnan et al. 2017), a pulse of stimulation consists of six quick bursts at 130 Hz.

A.8 Stationary standard deviation of the first coordinate in the linearised model

In the absence of stimulation, the stationary covariance matrix P^∞ of the linearised model (equation (2.25)) must satisfy (see Särkkä and Solin 2019)

$$JP^\infty + P^\infty J^\mathrm{T} + \begin{bmatrix} \zeta^2 & 0 \\ 0 & \zeta^2 \end{bmatrix} = 0. \tag{A.24}$$

Solving for P^∞ and following the notation in equation (A.21), we can write the stationary standard deviation of the first coordinate in the linearised model as

$$\sqrt{P^\infty_{11}} = \zeta \sqrt{\frac{J_{12}^2 + J_{22}^2 + J_{11}J_{22} - J_{12}J_{21}}{2(J_{11} + J_{22})(J_{12}J_{21} - J_{11}J_{22})}}. \tag{A.25}$$

A.9 Supplementary figures

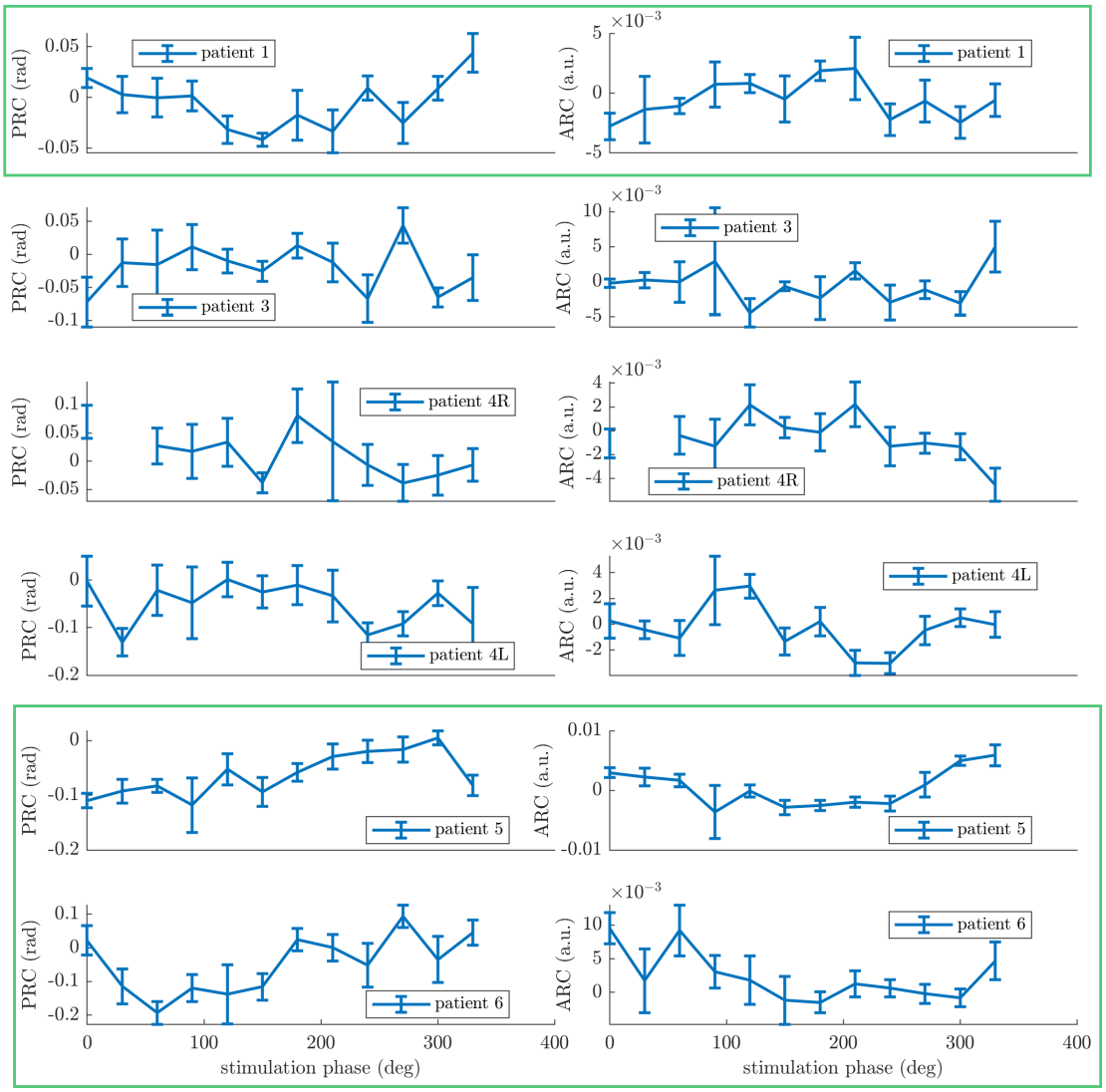

Supplementary Figure A.2: Patients' bPRCs (first column) and bARCs (second column) obtained as described in Section 2.3.1. Datasets with both response curves significant according to at least one of our statistical tests under FDR control are highlighted with green rectangles.

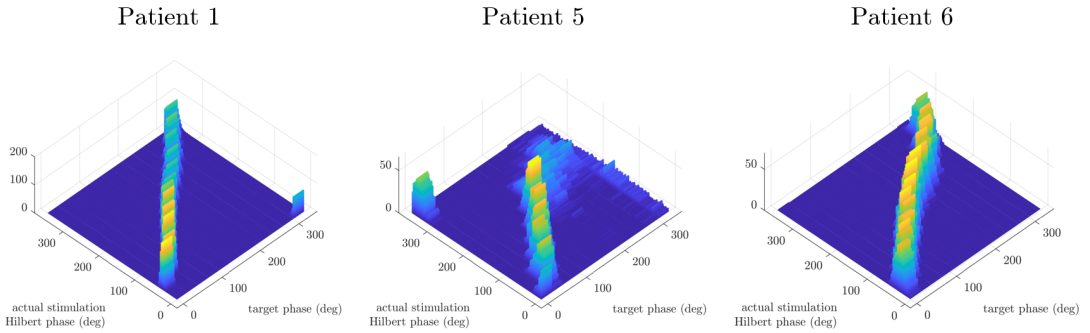

Supplementary Figure A.3: Phase tracking illustrated in the three fitted patients by histograms of the pair (target stimulation phase for the stimulation block, average of actual Hilbert phase at stimulation for the stimulation block). The actual Hilbert phase is obtained post-hoc after filtering. A block average includes averaging across bursts and within the block. Averages are obtained using circular means. The effect of the stimulation delay was removed, and phases are referenced to positive zero-crossings. Phase tracking is satisfactory for all patients, although tracking is less precise for later phases in patient 5.

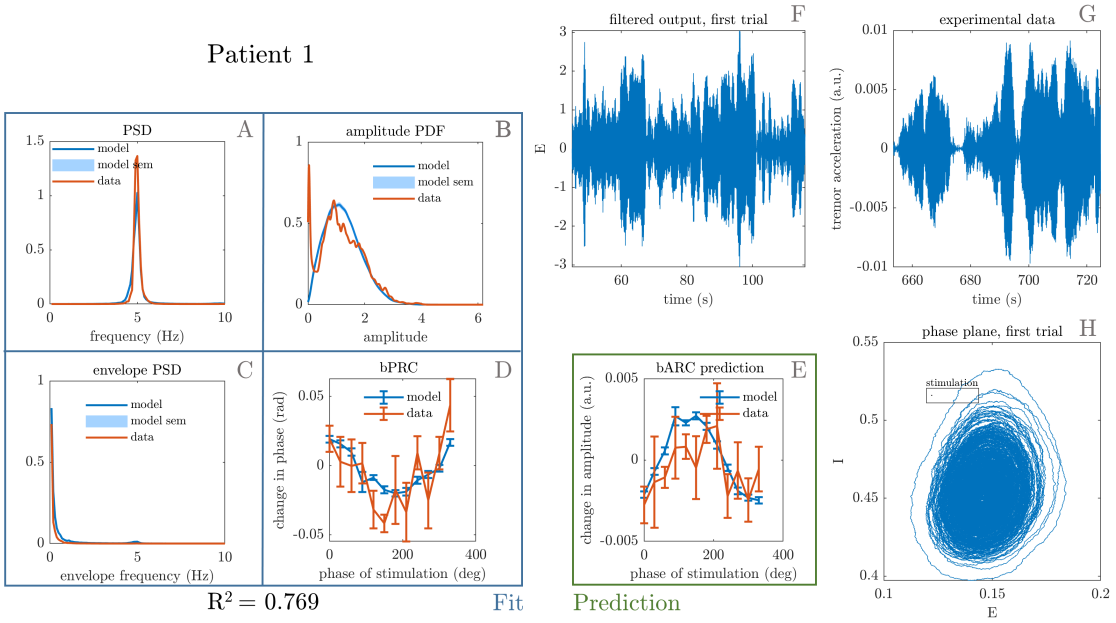

Supplementary Figure A.4: Fit to patient 1 showing the best PRC-ARC shift. The four features that were included in the cost function are shown on the left, namely tremor PSD (A), tremor envelope PDF (B), tremor envelope PSD (C) and bPRC (D). The model better predicts the data bARC (E) thanks to a PRC-ARC shift closer to that of the data (equivalent PRC alignment between the model and the data, but better ARC alignment). The model phase plane is shown in H, and the model tremor time-series (F) is shown next to the patient tremor time series (G). The framed black bar in H indicates the fitted stimulation magnitude to scale.

A.10 Supplementary tables

Parameter	Symbol	J_{circ}^{slow}	J_{circ}^{fast}	J_{ellip}
I to E weight	w_{IE}	200	5	1
E to I weight	w_{EI}	200	5	2
E to E weight	w_{EE}	0	0	2
Sigmoid steepness parameter	β	4	4	4
Time constant (s)	τ	200	5	1
Constant input to E	θ_E	101	3.5	0.5
Constant input to I	θ_I	-99	-1.5	0

Supplementary Table A.1: WC parameters corresponding to the Jacobians presented in Section 2.5.7. The steepness parameter β was set to 4, E^* and I^* to 0.5, and parameters were determined according the method presented in Appendix A.5.

	patient 1	patient 5	patient 6
$\frac{\lvert\sigma\rvert}{\omega}$	1.9%	5.1%	1.6%

Supplementary Table A.2: $|\sigma|/\omega$ ratios in the linearisation of patient fits.

Parameter	Symbol	Initial parameter distribution		Hard limits enforced by optimizer	
		Lower bound	Upper bound	Lower bound	Upper bound
I to E weight	w_{IE}	0	10	0	30
E to I weight	w_{EI}	0	10	0	30
E to E weight	w_{EE}	0	10	0	30
Sigmoid steepness parameter	β	0	10	0	30
Time constant (s)	τ	0	0.3	0	0.5
Constant input to E	θ_E	-2	10	-30	30
Constant input to I	θ_I	-10	2	-30	30
Noise standard deviation	ζ	0	0.1	0	0.3
Stimulation magnitude	δE	0	0.02	0	0.1
Stimulation delay (ms)	Δt_{stim}	0	250	0	500

Supplementary Table A.3: Lower and upper bounds of parameters uniform distributions used to generate initial parameters for fitting, and hard limits enforced by pattern search during the optimization process.

B

Appendix to beta burst dynamics chapter

Contents

In this appendix pertaining to Chapter 3, we include some methodological details on GWR surrogates (Section B.1), on model fitting (Section B.2), on the derivation of average burst duration in envelope models (Section B.3), and on the passage method (Section B.4). We also present supplementary tables (Section B.5) and supplementary figures (Section B.6).

B.1 GWR surrogates

The GWR method is based on a maximal overlap discrete wavelet transform (MODWT) implementation of the IAAFT algorithm first described in (Keylock 2006) and later refined in (Keylock 2007). The algorithm details are available in

(Keylock 2010), but the basic ingredients are fixing a proportion of the MODWT wavelet coefficients, and applying the IAAFT algorithm to each scale and to the dataset as a whole. Surrogates can be computed along a continuum parametrised by ρ, where $\rho = 0$ corresponds to IAAFT surrogates, and $\rho = 1$ corresponds to the data. The fixed coefficients are related to ρ as follows. The energy of a signal of length $N = 2^J$ is proportional to

$$\Xi = \sum_{j=1}^{J} \sum_{i=1}^{N} W_{j,i}^2 \tag{B.1}$$

where $W_{j,i}$ is the wavelet coefficient at scale j and temporal position i. Let us define an energy threshold $\Xi_0 = \rho\Xi$. Going from the largest to the smallest, squared wavelet coefficients are summed irrespective of scale and position until Ξ_0 is reached. Coefficients that contributed to the sum are fixed for this level of ρ. An example of surrogates for a range of ρ values is given in Figure B.1.

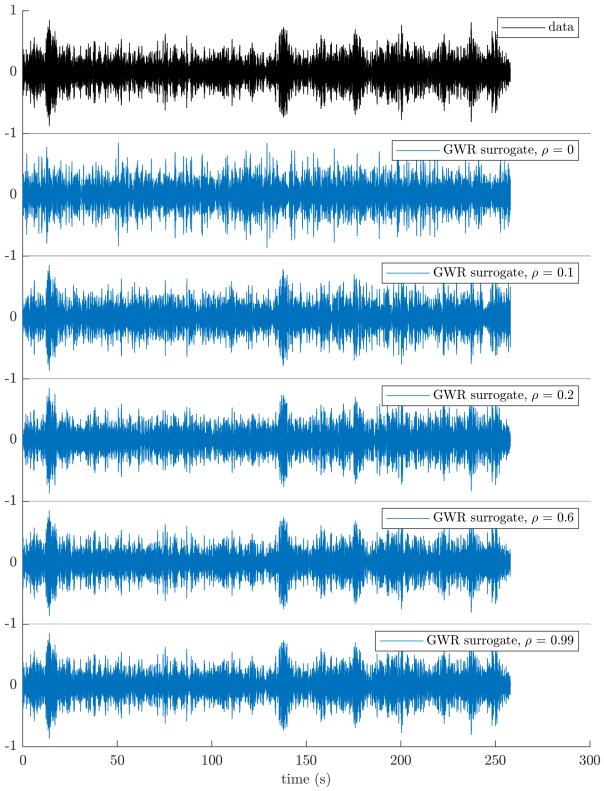

Supplementary Figure B.1: Filtered LFP for patient 6L OFF (black), and corresponding GWR surrogates for a range of ρ levels (blue). Most of the data temporal variability is already accounted for at $\rho = 0.1$. The plots share the same time axes.

B.2 Fitting procedures

We describe in this section the fitting procedure used to fit all the models of Chapter 3 to data. Slight differences between models will be highlighted when applicable. The general fitting procedure is similar to what was used in Chapter 2. For each fit, random sets of model parameters are generated from uniform distributions with appropriate bounds. For envelope models, all parameters are accepted. For WC models, parameters impacting the PSD and the average burst duration profile are coupled, and to improve optimisation efficiency, parameters are accepted when the PSD peak of the corresponding model is within 1 Hz and 30% in magnitude of the data PSD peak. The first 5000 sets of parameters are optimised in parallel on a supercomputer with the generalized pattern search algorithm (Torczon 1997; Audet and Dennis 2003). We use Matlab's implementation of the algorithm with the "positive basis 2N" poll method. Parameters are put on a similar scale to improve search robustness. A mesh size of 10^{-5}, and a function call budget of 600 calls are used. At each optimisation step, the optimiser returns the cost given by equation (2.23) in Chapter 2. For envelope models, the PSD is not considered in the optimisation, while for other models both the PSD and the average burst duration profiles are considered. At the end of the procedure, the fit with the highest $R^2 = 1 - c$ is deemed the best fit. Model simulations are performed with a Euler–Maruyama scheme, except for the OU model which is simulated according to the exact updating equation (Gillespie 1996)

$$x(t + \delta t) = x(t)e^{-\theta \delta t} + n\sqrt{\frac{\zeta^2}{2\theta}\left(1 - e^{-2\theta \delta t}\right)} \tag{B.2}$$

where n are independent samples of the standard normal distribution. The time step used in all cases was 10^{-3} s, roughly equivalent to the data sampling rate. At each optimisation step, the features (average burst duration for all models, plus PSD for WC models) are computed on five repeats of 1000 s and are averaged over the five repeats. The average burst duration profiles are computed from the model envelope (model output for envelope models, modulus of the analytic signal

of the model output for WC models), based on the same thresholds and minimum burst duration as for data analysis (see Section 3.3.2).

B.3 Average burst duration in an envelope model

B.3.1 Continuous model MFPT

To derive the average burst duration of the time discretization of the stochastic process described by equation (3.9), we start by drawing on classic results for the continuous time stochastic process itself. We consider the MFPT problem on $[L, +\infty)$ with a single boundary at $x = L$, and a reflective boundary at $x = +\infty$. The backward Fokker-Planck operator corresponding to the continuous time stochastic process reads

$$\mathcal{L}^*_{x_0} = \mu(x_0)\partial x_0 + \frac{\zeta^2}{2}\partial^2 x_0. \tag{B.3}$$

As reviewed in (Grebenkov 2014), the MFPT from x_0 to L which we denote $\tau_{x_0,L}$ can be found as the solution of the differential equation

$$\mathcal{L}^*_{x_0}\tau_{x_0,L} = -1, \tag{B.4}$$

where $\mathcal{L}^*_{x_0}$ is the backward Fokker-Planck operator acting on the starting point x_0. Equation (B.4) is a first order differential equation in $T(x_0) = \frac{\partial \tau_{x_0,L}}{\partial x_0}$

$$\frac{\partial T}{\partial x_0} + \frac{2\mu(x_0)}{\zeta^2}T = -\frac{2}{\zeta^2}, \tag{B.5}$$

whose solution reads

$$T(x_0) = \left(A - \frac{2}{\zeta^2}\int_{+\infty}^{x_0} e^{\frac{2}{\zeta^2}\int^{x_1}\mu(x)dx}dx_1\right) e^{-\frac{2}{\zeta^2}\int^{x_0}\mu(x)dx}, \tag{B.6}$$

where A is an integration constant, which is zero in the continuous case (reflective boundary at $+\infty$). We can therefore write T as

$$T(x_0) = \frac{2}{\zeta^2}\int_{x_0}^{+\infty} e^{\frac{2}{\zeta^2}\int_{x_0}^{x_1}\mu(x)dx}dx_1. \tag{B.7}$$

Integrating $T(x_0)$, we obtain the MFPT as

$$\tau_{x_0,L} = \int_L^{x_0} T(x)dx, \tag{B.8}$$

where we have used the absorbing boundary condition at L ($\tau_{L,L} = 0$). This leads to the expression for the MFPT in the continuous model presented in Section 3.6.2 (equation (3.10)). Finally, for $x_0 = L + \delta$ and $\delta \ll L$, the mean first passage time close to the boundary $\tau_{L+\delta,L}$ can be approximated by

$$\tau_{L+\delta,L} \approx \delta T(L). \tag{B.9}$$

B.3.2 Discretized model

We now consider a time discretization of the stochastic process described by equation (3.9) with time step dt, and derive an expression for the average burst duration of the discretized model in three steps. We correct for the systematic bias of the continuous model MFPT and MFPT derivative in steps 1 and 2, respectively. In step 3, we relate average burst duration and MFPT. We remind the reader we use a tilde to distinguish quantities that can be measured readily in a discretized system from the continuous system quantities introduced earlier. For clarity of exposition, we also denote with a hat and double hat intermediate quantities that will be introduced as the derivation progresses. The three steps will make use of the transition probability for small $dt = t - t'$ to first order in $\sqrt{dt}$,

$$p(x, t' + dt|x', t') \approx \frac{1}{\sqrt{2\pi dt}\zeta} \exp\left\{-\frac{(x - x')^2}{2dt\zeta^2}\right\}. \tag{B.10}$$

Step 1: MFPT bias When close to the boundary $x = L$, the continuous model is more likely to cross the boundary earlier, which makes for a systematic underestimation of the discrete MFPT by the continuous model. The first correction to the continuous MFPT $\tau_{x_0,L}$ is therefore to add a constant correction $\hat{\tau}_{L,L}$ to it, which describes the average additional time taken by the discrete model once close to the boundary:

$$\hat{\tau}_{x_0,L} = \tau_{x_0,L} + \hat{\tau}_{L,L}. \tag{B.11}$$

Another way of looking at it is that in the continuous model, all trajectories starting from the threshold will cross the boundary in vanishingly short times, which is reflected by the boundary condition $\tau_{L,L} = 0$. This is not the case for the discrete

model, as some trajectories starting at L will end up above L a time step later. In fact, by considering trajectories starting at L and the transition probability for one time step dt, $\hat{\tau}_{L,L}$ can be estimated as

$$\hat{\tau}_{L,L} = \int_{-\infty}^{0} \frac{dt}{2} p^0(z)dz + \int_0^{+\infty} (\hat{\tau}_{L+z,L} + dt)p^0(z)dz, \tag{B.12}$$

where $p^x(z) = p(L + x + z, t' + dt|L + x, t')$, and the burst duration of a trajectory starting at L but ending below L a time step later has been approximated by $\frac{dt}{2}$. Using equation (B.11), we find

$$\hat{\tau}_{L,L} = (1 - \alpha)\frac{dt}{2} + \int_0^{+\infty} \tau_{L+z,L} p^0(z)dz + \alpha\hat{\tau}_{L,L} + \alpha dt, \tag{B.13}$$

with $\alpha = \int_0^{+\infty} p^0(z)dz$. Therefore

$$\hat{\tau}_{L,L} = \frac{1 + \alpha}{1 - \alpha}\frac{dt}{2} + \frac{1}{1 - \alpha}\int_0^{+\infty} \tau_{L+z,L} p^0(z)dz. \tag{B.14}$$

As p^0 decays quickly away from L for small dt, we use equation (B.9), and obtain to first order in $\sqrt{dt}$

$$\hat{\tau}_{L,L} = \frac{T(L)}{1 - \alpha}\int_0^{+\infty} z p^0(z)dz. \tag{B.15}$$

To first order in $\sqrt{dt}$, $p^0(z) = p(L + z, t' + dt|L, t')$ is even (see equation (B.10)) and $1 - \alpha = \alpha$. Therefore,

$$\hat{\tau}_{L,L} = T(L)\frac{\int_0^{+\infty} z p^0(z)dz}{\int_0^{+\infty} p^0(z)dz} = \bar{\Gamma}T(L), \tag{B.16}$$

where $\bar{\Gamma}$ is the average step above L starting from L. To first order in $\sqrt{dt}$, Γ does not depend on μ and L and is given by

$$\bar{\Gamma} \approx \sqrt{\frac{2dt}{\pi}}\zeta. \tag{B.17}$$

Step 2: MFPT derivative As the discrete model is less likely to cross the boundary when close to it, the derivative of the MFPT at the boundary will also be affected. We model this effect with a correction to the continuous model through a non-zero A (integration constant in equation (B.6)). We define

$$A_0 = A\left(\frac{2}{\zeta^2}\int_L^{+\infty} e^{\frac{2}{\zeta^2}\int^{x_1}\mu(x)dx} dx_1\right)^{-1}, \tag{B.18}$$

in such a way that the corrected MFPT derivative at the boundary $\widetilde{T}(L)$ equals $(A_0+1)T(L)$. To show that A_0 should not be zero in the discrete time case and provide an approximation of its value, we are going to approximate $\widetilde{T}(L)$ by

$$\left.\frac{\partial \hat{\tilde{\tau}}_{L+\delta,L}}{\partial \delta}\right|_{\delta=0},$$

where $\hat{\tilde{\tau}}_{L+\delta,L}$ is defined next and will explicitly take into account the distribution of the first time step from $L+\delta$, similarly to what was done in the previous paragraph. We are assuming here that most of the difference in the derivative with the continuous case comes from the first time step, and that the MFPT will subsequently evolve according to equation (B.11). Starting from $L+\delta$ and considering explicitly the first time step and its associated transition probability, we can write

$$\hat{\tilde{\tau}}_{L+\delta,L} = \int_{-\infty}^{-\delta} \frac{dt}{2} p^{\delta}(z)dz + \int_{-\delta}^{+\infty} (\hat{\tau}_{L+\delta+z,L} + dt)p^{\delta}(z)dz. \tag{B.19}$$

With the change of variable $x = \delta + z$, we obtain to first order in $\sqrt{dt}$,

$$\hat{\tilde{\tau}}_{L+\delta,L} = \int_{0}^{+\infty} \hat{\tau}_{L+x,L} p^{\delta}(x-\delta)dx. \tag{B.20}$$

Making use of $\hat{\tau}_{L+x,L} = xT(L) + \bar{\Gamma}T(L)$ (see equations (B.9), (B.11), and (B.16)), we express

$$\hat{\tilde{\tau}}_{L+\delta,L} = \int_{0}^{+\infty} (x+\bar{\Gamma})T(L)p^{\delta}(x-\delta)dx. \tag{B.21}$$

From there, we obtain to zeroth order in $\sqrt{dt}$ (A_0+1 will multiply a $\sqrt{dt}$ factor in the final expression)

$$\left.\frac{\partial \hat{\tilde{\tau}}_{L+\delta,L}}{\partial \delta}\right|_{\delta=0} = \left(\frac{1}{2} + \frac{1}{\pi}\right) T(L), \tag{B.22}$$

which yields $A_0 = \frac{1}{\pi} - \frac{1}{2} \approx -0.18$. This provides a rationale for a non-zero A_0 in the discretization and a good approximation of the optimal value of A_0, which was found empirically to be $A_0 = \frac{\pi-4}{\pi+4} \approx -0.12$ (the discrepancy may come from considering only the contribution from the first time step). We use this latter value in what follows, and obtain for the MFPT in the discretized model

$$\tilde{\tau}_{L+x,L} \approx x\widetilde{T}(L) + \bar{\Gamma}\widetilde{T}(L) = \frac{2\pi}{\pi+4}(x+\bar{\Gamma})T(L), \tag{B.23}$$

for $x \ll L$, with $T(L)$ given by equation (B.7).

Step 3: overshoot distribution We have just obtained an approximation for the MFPT in the discretized model (equation (B.23)), and the last step is to derive from this result the average burst duration for the discretized model as a function of the threshold L. In the discretization, unless simulations are started exactly at L before every single burst is analysed (which is not compatible with modelling data), the distribution of boundary overshoots from below has to be taken into account (see Figure 3.7 in Chapter 3). Averaging equation (B.23) over the overshoot distribution of density χ gives the average burst duration $\widetilde{\tau}_L$ that can be measured from one long time series of the discretized model as

$$\widetilde{\tau}_L = \int_L^{+\infty} \widetilde{\tau}_{x_0,L} \chi_L(x_0) dx_0. \tag{B.24}$$

Contrary to $\widetilde{\tau}_{L,L}$, the notation $\widetilde{\tau}_L$ does not imply an exact start of trajectories from L before each burst. We also note that the contribution of boundary overshoots from above when getting back to L at the end of the burst is negligible compared to stopping exactly at the threshold as it cannot change $\widetilde{\tau}_L$ by more than a time step. This is not the case at the beginning of a burst as the further away from the threshold, the less likely a premature end of the burst is, which has a drastic influence on burst duration. As χ_L decays quickly away from L for small dt (the average overshoot scales with $\sqrt{dt}$ as we will see in equation (B.28)), equation (B.24) can be approximated by

$$\widetilde{\tau}_L \approx \widetilde{T}(L) \int_0^{+\infty} \delta \chi_L(L+\delta) d\delta + \widetilde{\tau}_{L,L} = \left(\bar{\Delta}_L + \bar{\Gamma}\right) \widetilde{T}(L), \tag{B.25}$$

where $\bar{\Delta}_L$ is the average overshoot at threshold L. An approximation for the average overshoot can be obtained by considering the probability of the state x given that dt before, the state was anywhere below L, which is given by

$$p_L(x, dt) = \int_{-\infty}^{L} p(x, t' + dt | x', t') p_\infty(x') dx', \tag{B.26}$$

where $p_\infty(x)$ is the stationary probability density of the process normalised by its integral over $(-\infty, L]$ and p is the transition probability to first order in $\sqrt{dt}$ introduced earlier (equation (B.10)). The overshoot density is

$$\chi_L(x_0) = \frac{p_L(x_0, dt)}{\int_L^{+\infty} p_L(x, dt) dx}. \tag{B.27}$$

For small dt the stationary probability density contribution reduces to a constant that cancels out in the overshoot density. The average overshoot is obtained to first order in $\sqrt{dt}$ as

$$\bar{\Delta}_L \approx \frac{1}{2}\sqrt{\frac{\pi dt}{2}}\zeta, \tag{B.28}$$

which does not depend on the drift function μ (to first order in $\sqrt{dt}$) and as a result does not depend on L either. We will therefore drop the subscript L and simply denote the average burst duration by $\bar{\Delta}$.

This leads to a direct relationship between $\widetilde{\tau}_L$ and $T(L)$,

$$\widetilde{\tau}_L \approx \left(\bar{\Delta} + \bar{\Gamma}\right)\widetilde{T}(L) \approx \sqrt{\frac{\pi dt}{2}}\zeta T(L), \tag{B.29}$$

and the full expression presented in Section 3.6.2 for the average burst duration of a discretized envelope model to first order in $\sqrt{dt}$ is

$$\widetilde{\tau}_L \approx \frac{\sqrt{2\pi dt}}{\zeta}\int_L^{+\infty} e^{\frac{2}{\zeta^2}\int_L^{x_1}\mu(x)dx}dx_1.$$

B.3.3 Application to two envelope models

OU We are considering here the discretization of an OU process centered on zero (equation (3.6)). To highlight the dependence of average burst duration on parameters, we are going to express equation (3.12) with L as a percentile of the time series values. Equation (3.12) is found in Section 3.6.2, and is a direct application of the previous result. The stationary probability density for our centered OU process is

$$p_\infty(x) = \sqrt{\frac{\theta}{\pi\zeta^2}}e^{-\frac{\theta x^2}{\zeta^2}}, \tag{B.30}$$

and the associated CDF Φ reads

$$\Phi(x) = \frac{1}{2}\left\{1 + \mathrm{erf}\left(\frac{\sqrt{\theta}x}{\zeta}\right)\right\}, \tag{B.31}$$

where erf is the error function. Let us denote by $L_\%$ the percentile rank (between 0 and 1) corresponding to the threshold L. By definition, $\Phi(L) = L_\%$, and therefore

$$\frac{\sqrt{\theta}L}{\zeta} = \mathrm{erf}^{-1}\left(2L_\% - 1\right). \tag{B.32}$$

This leads to an expression for the average burst duration of a discrete OU process as a function of threshold percentile rank:

$$\widetilde{\tau}_L \approx \pi \sqrt{\frac{2dt}{\theta}} \left(1 - L_{\%}\right) e^{\left\{\mathrm{erf}^{-1}(2L_{\%}-1)\right\}^2}.$$

Degree three polynomial We are considering here the discretization of a degree three polynomial envelope model (equation (3.8)). The direct application of the general expression for $\widetilde{\tau}_L$ obtained previously provides an approximation for the average burst duration of this model to first order in $\sqrt{dt}$, which reads

$$\widetilde{\tau}_L \approx \frac{\sqrt{2\pi dt}}{\zeta} \int_L^{+\infty} e^{\frac{2}{\zeta^2}(\Lambda(x)-\Lambda(L))} dx, \tag{B.33}$$

with

$$\Lambda(x) = \frac{d_3}{4}x^4 + \frac{d_2}{3}x^3 + \frac{d_1}{2}x^2 + d_0 x$$

The average burst duration expression for the degree three polynomial model is not as simple as in the OU case, but it can easily be evaluated numerically.

B.4 Passage method

From average burst duration profile to envelope dynamics We are concerned here with the time discretization of the continuous-time stochastic process described by equation (3.9), where we are assuming the real valued drift function μ can depend on x_t, and the diffusion term ζ is constant in time and space. Provided that the derivative of the first passage time $T(x_0)$ is never zero, the differential equation satisfied by T (equation (B.5)) can be re-arranged into

$$\mu(x_0) = -\frac{1 + \frac{1}{2}\zeta^2 \frac{\partial T}{\partial x_0}}{T(x_0)}. \tag{B.34}$$

We have shown previously that in the discretized system considered, there is a simple relationship to first order in $\sqrt{dt}$ between the average burst duration $\widetilde{\tau}_L$ at threshold L and $T(L)$ (equation (B.29)). Thus, to first order in $\sqrt{dt}$,

$$\mu(L) \approx -\zeta \frac{\sqrt{\frac{\pi dt}{2}} + \frac{\zeta}{2}\frac{\partial \widetilde{\tau}_L}{\partial L}}{\widetilde{\tau}_L},$$

which we discuss in Section 3.7.1.

Preparation of synthetic data Simulation of the synthetic data used to test envelope dynamics recovery was performed with the same methods as in Section B.2. Synthetic data were generated by the OU model introduced before, and by a degree five polynomial model given by

$$dx = \gamma x \prod_{i=1}^{4}(x - x_i) + \zeta dW, \tag{B.35}$$

where γ is a coefficient, the x_i are roots, and ζ a constant noise parameter (parameters values given in supplementary Table B.5 in Appendix B.5). OU synthetic data were shifted as before, while for the degree five model, only the absolute value of the next point was retained at each integration step. For patient data the envelope was obtained as the Hilbert amplitude of the filtered data as in Section 3.3.2.

Envelope dynamics recovery Three hundred thresholds equally spaced from one fiftieth to 90% of the maximum envelope value are considered (extreme thresholds will not yield reliable measures). At each threshold, the average burst duration $\widetilde{\tau}_L$ is obtained, and the resulting curve is smoothed across thresholds (LOWESS method, which stands for locally weighted scatterplot smoothing, smoothing span of threshold range divided by eight). The derivative of $\widetilde{\tau}_L$ is then estimated numerically and smoothed (LOWESS, smoothing span of threshold range divided by five). In the case of patient data, the first 10% to 20% of both $\widetilde{\tau}_L$ and its derivative are not smoothed as the fast decay of $\widetilde{\tau}_L$ at the left edge of the profile is not handled properly by the smoothing function. Finally, the drift function μ is reconstructed based on equation (3.14). The noise parameter ζ is simply taken as the known value used to generate the envelope for synthetic data, and is estimated for data (24% and 27% of the time series standard deviation, for OFF medication and ON medication, respectively). These values were obtained for patient data by adjusting the noise parameter so the burst duration profile and the envelope inverse CDF of the inferred dynamics best match the data. The time step dt is taken as the time step used for forward simulation for synthetic data, and as the time scale of variation of the envelope for data (roughly a beta cycle, 0.05 s). The mean of the

drift function is inferred by considering all the data available, while sem error bars are obtained by dividing all the data available in four segments and repeating the process on each segment (noise parameter fixed to the value used for the mean).

Simulation of inferred envelope dynamics The inferred dynamics are known at 300 equally spaced points between x_{min} and x_{max}, so we define

$$\mu(x(i)) = \begin{cases} \mu(x_{min}) & x(i) < x_{min}, \\ \mu(x_{max}) & x(i) > x_{max}, \\ \mu_x^{interp} & otherwise, \end{cases} \tag{B.36}$$

where μ_x^{interp} is the linear interpolation of μ between the closest x points framing $x(i)$ at which μ is known. Forward simulations of the inferred envelope dynamics are then performed according to equation (3.9) with a Euler–Maruyama scheme (the time step is taken as dt). Additionally, at each integration step, only the absolute value of the next point $x(i+1)$ is retained to prevent the envelope from becoming negative. Five repeats of ten times the data duration are simulated. The resulting envelopes are used to compute the mean and sem error bars of the average burst duration profile and the inverse CDF of the inferred envelope dynamics.

B.5 Supplementary tables

Parameter	Symbol	Best fit values	
		Patient 3LON	Patient 6ROFF
I to E weight	w_{IE}	13.636	21.349
E to I weight	w_{EI}	9.140	26.810
I to I weight	w_{II}	0.502	0.0986
Steepness parameter	β	3.188	2.439
E time constant (s)	Ω_E	0.418	0.556
I time constant (s)	Ω_I	0.437	0.519
Constant input to E	λ_E	0	0
Constant input to I	λ_I	0	0
Noise standard deviation	ζ	0.00644	0.131

Supplementary Table B.1: Best parameters for fits of the linear WC model.

Parameter	Symbol	Best fit values
I to E weight	w_{IE}	1.215
E to I weight	w_{EI}	2.118
I to I weight	w_{II}	1.144
Scaling parameter	η	4.100
Steepness parameter	β	4.777
E time constant (s)	Ω_E	0.0170
I time constant (s)	Ω_I	0.165
Constant input to E	λ_E	2.662
Constant input to I	λ_I	2.304
Delay from I to E (s)	Δ_{IE}	0.0039
Delay from E to I (s)	Δ_{EI}	0.0005
Delay from I to I (s)	Δ_{II}	0.0445
Noise standard deviation	ζ	0.0710

Supplementary Table B.2: Best parameters for the fit of the non-linear WC model with delays to patient 6ROFF.

Parameter	Symbol	Best fit values
Decay parameter	θ	7.353
Rotation frequency	ν	13.5
Noise standard deviation	ζ	0.006

Supplementary Table B.3: Best parameters for the OU model fit to patient 3LON.

Parameter	Symbol	Best fit values
Coefficient of x^3	d_3	-119.577
Coefficient of x^2	d_2	74.6519
Coefficient of x^1	d_1	-15.329
Coefficient of 1	d_0	0.892
Rotation frequency	ν	17.46
Noise standard deviation	ζ	0.110

Supplementary Table B.4: Best parameters for the degree three polynomial model fit to patient 6ROFF.

Parameter	Symbol	Value
Leading coefficient	γ	-12.67
First root	x_1	0.199
Second root	x_2	0.633
Third root	x_3	1.496
Fourth root	x_4	1.597
Noise standard deviation	ζ	0.828

Supplementary Table B.5: Parameters used to generate training data to test the passage method (degree five polynomial).

B.6 Supplementary figures

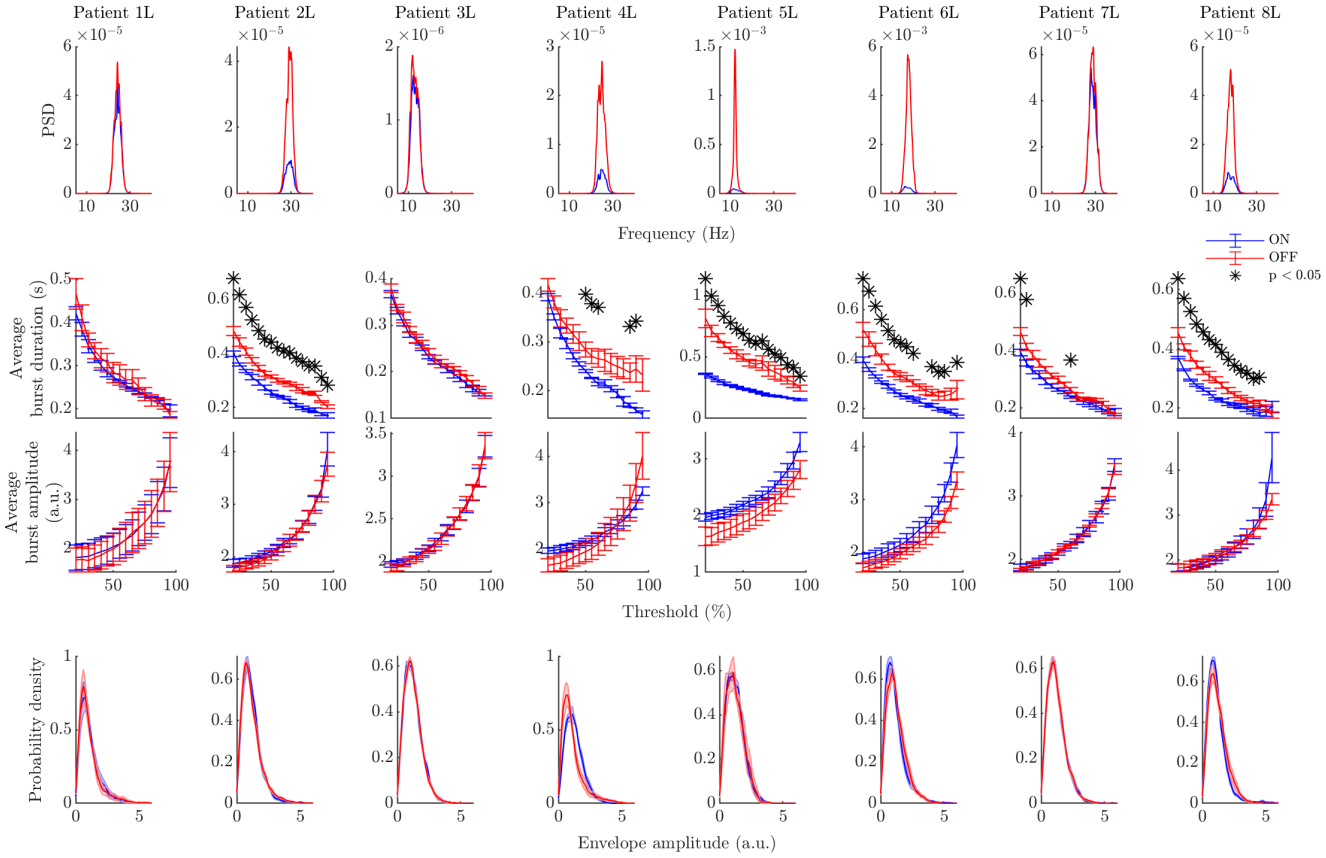

Supplementary Figure B.2: Power spectra and bursting features ON and OFF Levodopa (left hemispheres). Each column corresponds to the left hemisphere of one of the eight patients. Each row corresponds to a bursting feature, the ON state is always in blue, and the OFF state in red. The first row shows power spectra, the second row average burst duration profiles, the third row average burst amplitude profiles, and last row envelope amplitude PDFs. Statistically significant differences under FDR control are indicated by black stars (three bursting features only).

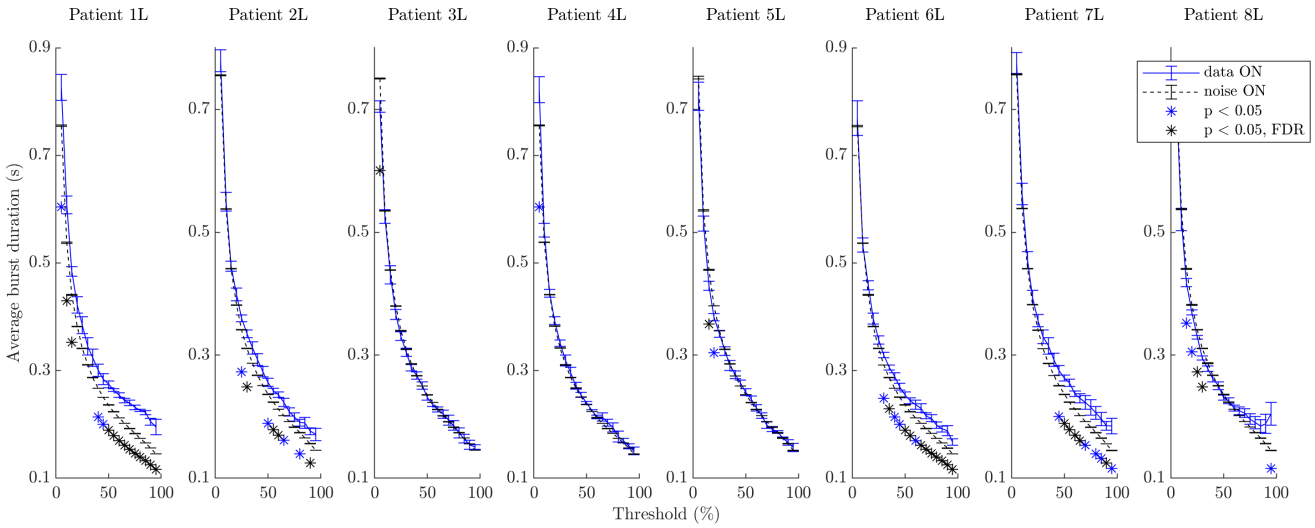

Supplementary Figure B.3: Average burst duration ON Levodopa compared to average burst duration of filtered white noise (left hemispheres). Each column corresponds to the left hemisphere of one of the eight patients. The ON state is shown by blue lines, filtered white noise by dashed black lines. Statistically significant differences under FDR control are indicated by black stars. Cases not significant under FDR control where $p < 0.05$ are indicated by blue stars.

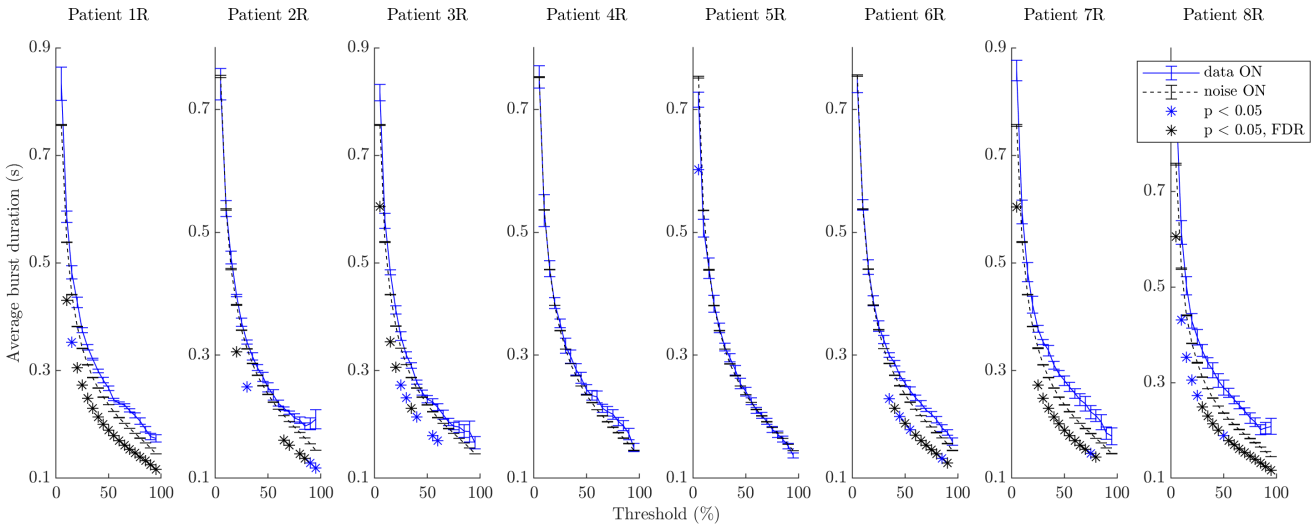

Supplementary Figure B.4: Average burst duration ON Levodopa compared to average burst duration of filtered white noise (right hemispheres). Each column corresponds to the right hemisphere of one of the eight patients. The ON state is shown by blue lines, filtered white noise by dashed black lines. Statistically significant differences under FDR control are indicated by black stars. Cases not significant under FDR control where $p < 0.05$ are indicated by blue stars.

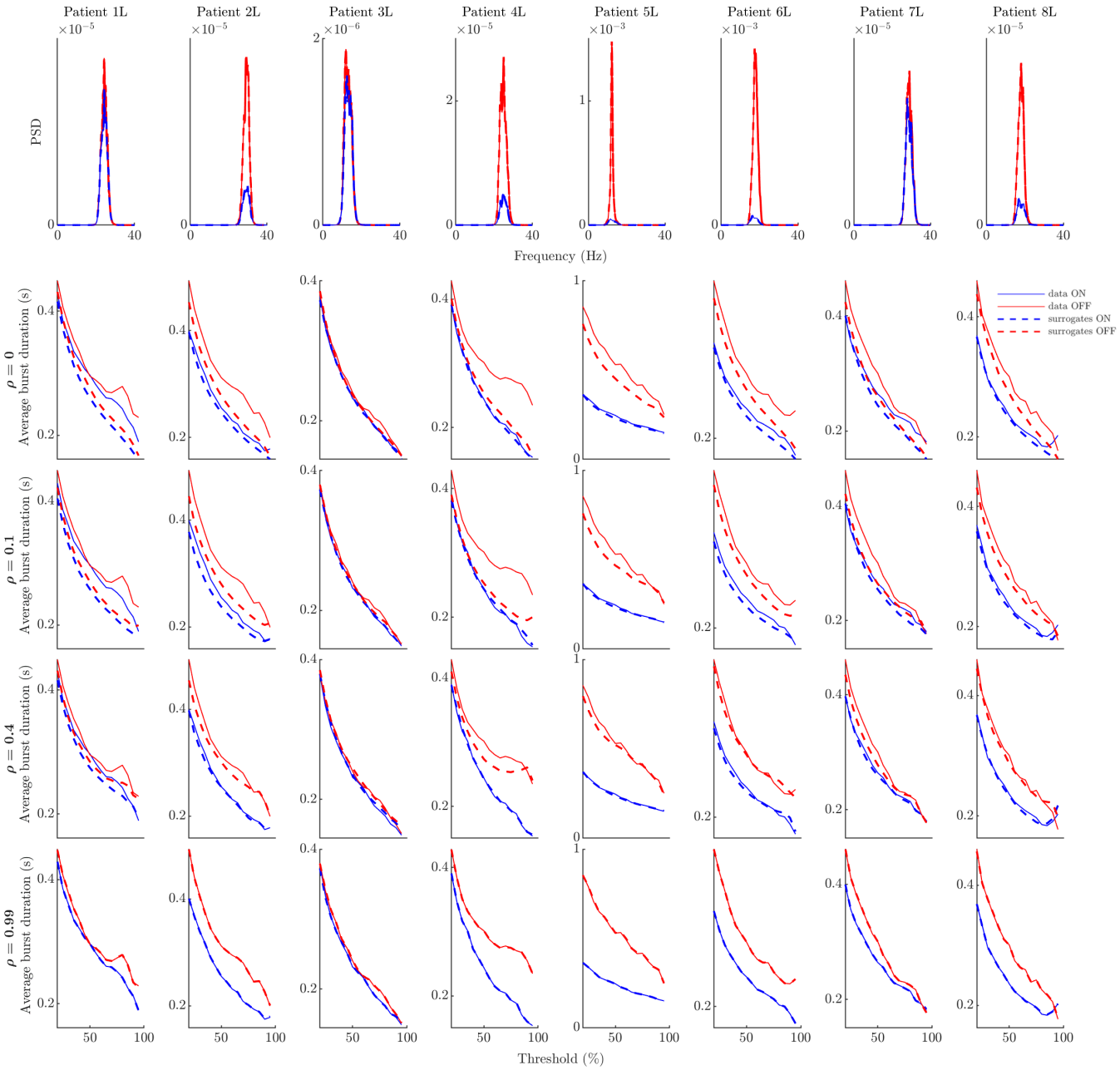

Supplementary Figure B.5: Power spectra and average burst duration profiles ON and OFF medication for data and GWR surrogates for a range of ρ values (left hemispheres). Each column corresponds to the left hemisphere of one of the eight patients. In all panels, data profiles are solid lines, while surrogate profiles are dashed lines. The OFF medication state is indicated in red, and the ON state in blue. Power spectra are shown in the first row (data and surrogates overlap as expected). Average burst duration profiles for various ρ values are provided in the next rows. Surrogate profiles match data profiles for ρ close to one as expected.

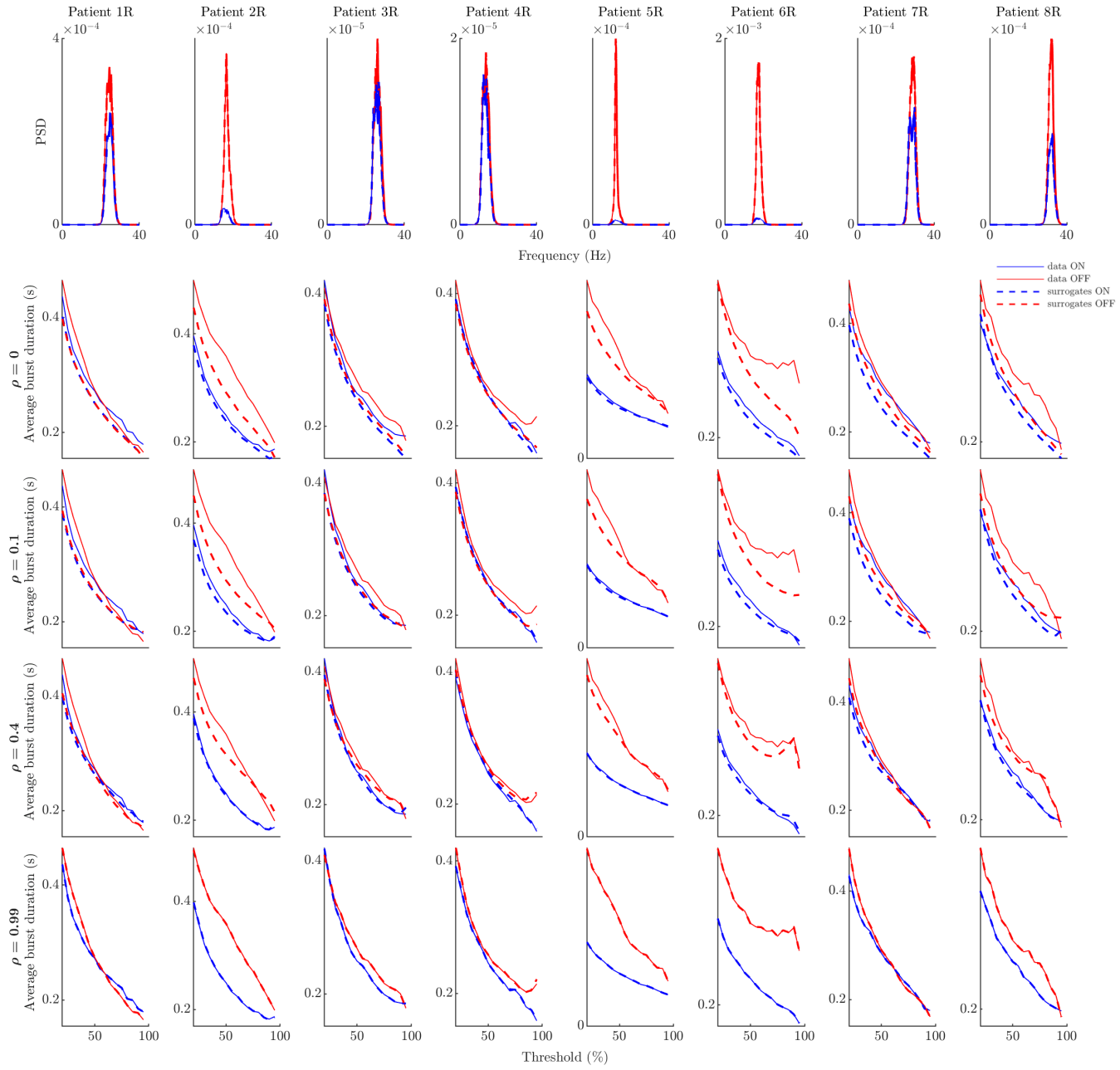

Supplementary Figure B.6: Power spectra and average burst duration profiles ON and OFF medication for data and GWR surrogates for a range of ρ values (right hemispheres). Each column corresponds to the right hemisphere of one of the eight patients. In all panels, data profiles are solid lines, while surrogate profiles are dashed lines. The OFF medication state is indicated in red, and the ON state in blue. Power spectra are shown in the first row (data and surrogates overlap as expected). Average burst duration profiles for various ρ values are provided in the next rows. Surrogate profiles match data profiles for ρ close to one as expected.

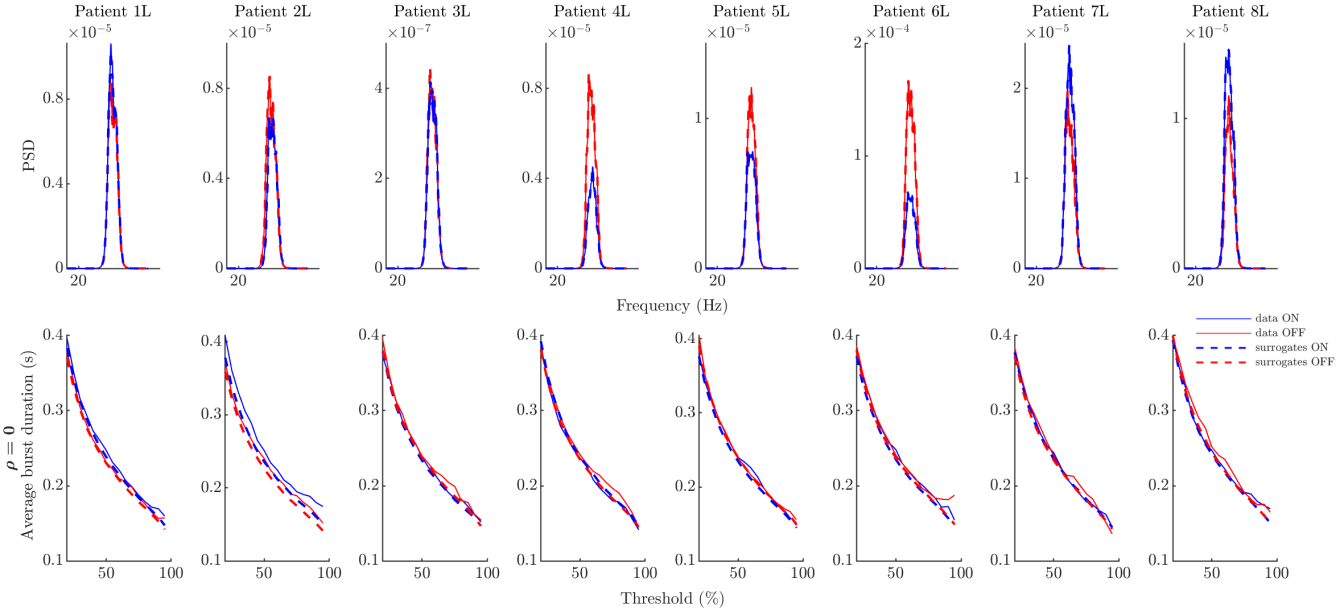

Supplementary Figure B.7: 35 Hz controls (left hemispheres): power spectra and average burst duration profiles ON and OFF medication. Each column corresponds to the left hemisphere of one of the eight patients. In all panels, data profiles are solid lines, while surrogate profiles are dashed lines. The OFF medication state is indicated in red, and the ON state in blue. Power spectra are shown in the first row (data and surrogates overlap as expected). Average burst duration profiles for $\rho = 0$ are presented in the second row.

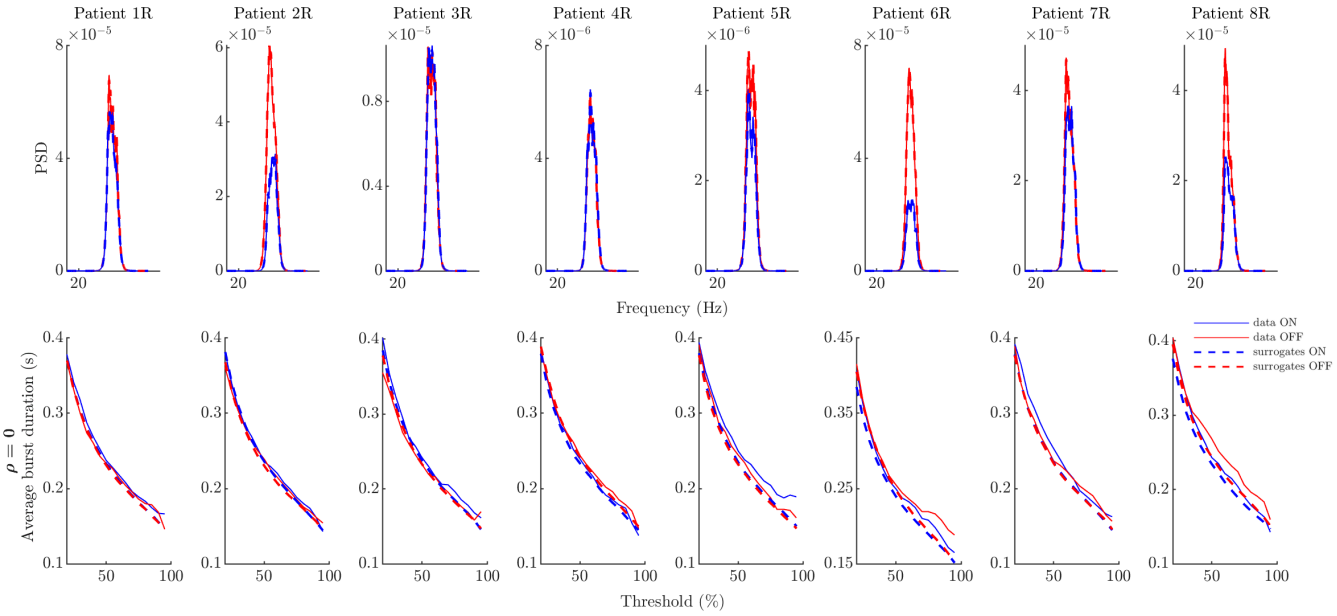

Supplementary Figure B.8: 35 Hz controls (right hemispheres): power spectra and average burst duration profiles ON and OFF medication. Each column corresponds to the right hemisphere of one of the eight patients. In all panels, data profiles are solid lines, while surrogate profiles are dashed lines. The OFF medication state is indicated in red, and the ON state in blue. Power spectra are shown in the first row (data and surrogates overlap as expected). Average burst duration profiles for $\rho = 0$ are presented in the second row.

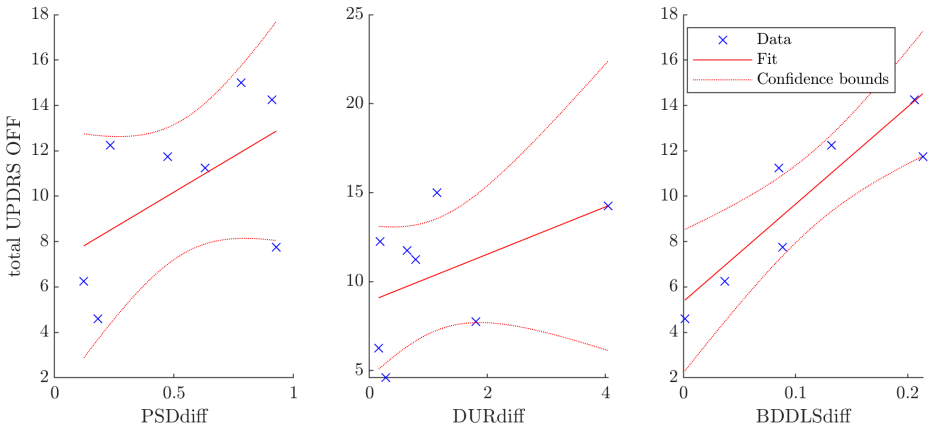

Supplementary Figure B.9: Total UPDRS score OFF medication as a function of the three predictors. Spearman's correlations of 0.500, p = 0.216 (PSDdiff), 0.476, p = 0.243 (DURdiff), and 0.810, p = 0.0037* (BDDLSdiff), where * denotes significance under FDR correction. BDDLSdiff is taken at $\rho = 0.2$. Confidence bounds are at 95%.

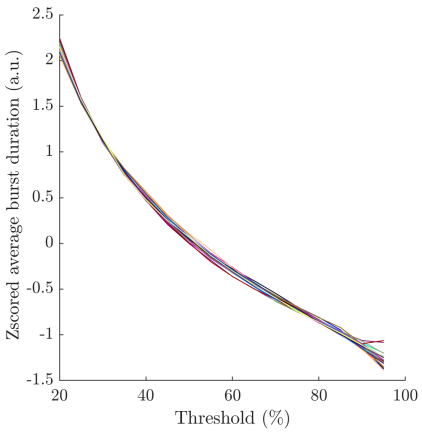

Supplementary Figure B.10: Z-scored average burst duration profiles of data linear surrogates ($\rho = 0$). Shown for all patients and hemispheres available. The 16 average burst duration profiles closely match, highlighting that average burst duration profiles of linear systems are the same shape (potentially scaled and shifted).

C

Appendix to isostable amplitude chapter

Contents

In this appendix pertaining to Chapter 4, we include details on isochron computation (Section C.1), and supplementary figures (Section C.2).

C.1 Isochron computation

In this Chapter 4, we use the Fourier average method (Mauroy and Mezic 2012) to obtain the isochrons (Figure C.1) of the model used in the numerical tests presented in Section 4.4.2. The Fourier average method can readily be applied to stable foci models using the frequency ω associated with the stable fixed point (as defined in Section 4.3) instead of the limit cycle frequency. We also implement truncation as described in (Mauroy et al. 2014) to improve computational efficiency. Explicitly, we obtain isochronal phase as

$$\Theta(\mathbf{X}) \approx \angle \left(\frac{1}{n_1 T - n_2 T} \int_{n_2 T}^{n_1 T} (f \circ \Phi_t)(\mathbf{X}) e^{-i\omega t} dt \right), \tag{C.1}$$

where in $\mathbb{R}^2$, we choose the observable $f : \mathbb{R}^2 \mapsto \mathbb{R}$ defined by $f\left(\begin{bmatrix} X_1 \\ X_2 \end{bmatrix}\right) = X_1 + X_2$, and $\angle(z)$ designates the argument of the complex number z. The number of periods n_1 is chosen so that Θ has converged and there is no trace of numerical instability, and n_2 is the truncation index.

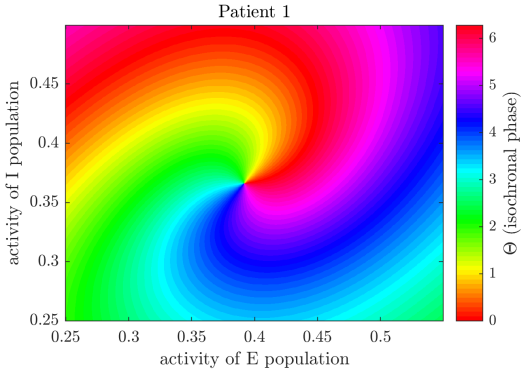

Supplementary Figure C.1: Isochronal phase obtained for the WC fit to patient 1 using the Fourier average method ($n_1 = 30$ $n_2 = 25$).

C.2 Supplementary figures

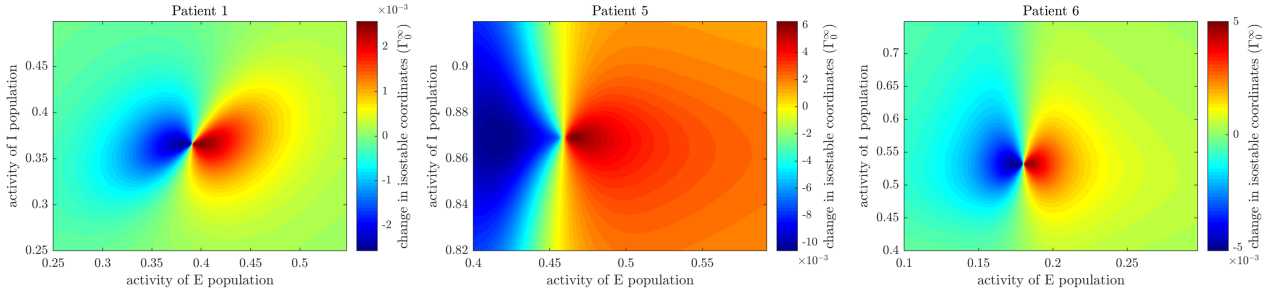

Supplementary Figure C.2: Instantaneous asymptotic amplitude response fields of the three fitted models, (full colour scale), shown for $\delta E = \delta E_0$. The minimum of the response field is not as close to the fixed point in patient 5 as in other patients.

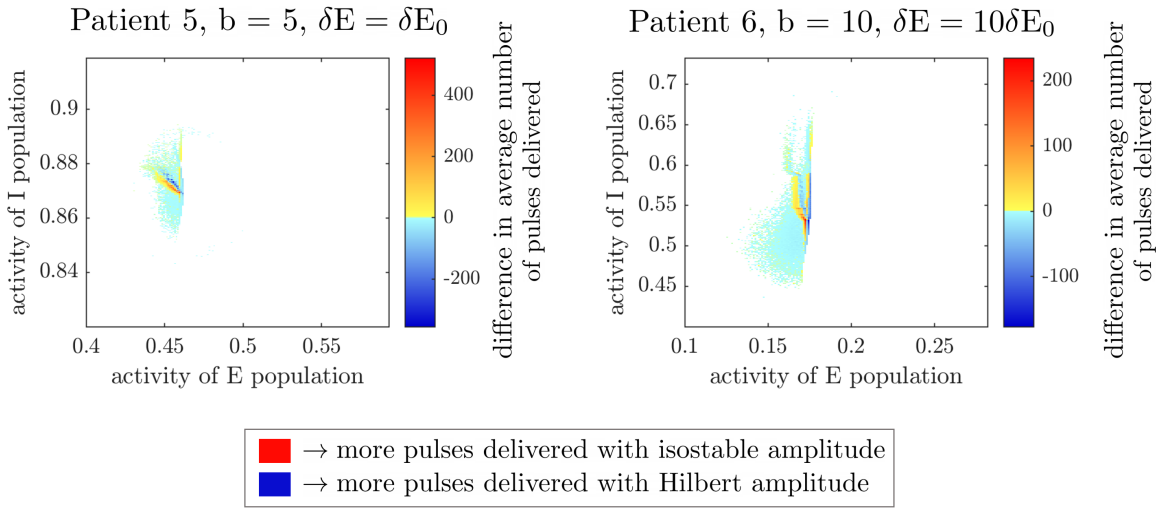

Supplementary Figure C.3: Difference in average number of pulses delivered in phase space between stimulation based on isostable amplitude and on Hilbert amplitude. A positive difference (yellow to red) means that more pulses were delivered with the strategy based on isostable amplitude at this location. The stimulation strategy described in Section 4.5 was used. Two combinations of patient, discount parameter (b), and stimulation magnitude are shown as examples. These results were obtained with 10 trials of 5000 s of stimulation.

References

Achuthan, S. and C. C. Canavier (2009). "Phase-resetting curves determine synchronization, phase locking, and clustering in networks of neural oscillators". In: *Journal of Neuroscience* 29.16, pp. 5218–5233. DOI: 10.1523/JNEUROSCI.0426-09.2009.

Adamchic, I., C. Hauptmann, U. B. Barnikol, N. Pawelczyk, O. Popovych, T. T. Barnikol, A. Silchenko, J. Volkmann, G. Deuschl, W. G. Meissner, M. Maarouf, V. Sturm, H. J. Freund, and P. A. Tass (2014). "Coordinated reset neuromodulation for Parkinson's disease: proof-of-concept study". In: *Mov Disord* 29.13, pp. 1679–1684. DOI: 10.1002/mds.25923.

Ahn, S., S. E. Zauber, R. M. Worth, and L. L. Rubchinsky (2016). "Synchronized beta-band oscillations in a model of the globus pallidus-subthalamic nucleus network under external input". In: *Frontiers in computational neuroscience* 10, p. 134. DOI: 10.3389/fncom.2016.00134.

Ahn, S., S. E. Zauber, R. M. Worth, T. Witt, and L. L. Rubchinsky (2018). "Neural synchronization: Average strength vs. temporal patterning". In: *Clinical Neurophysiology* 129.4, pp. 842–844. DOI: 10.1016/j.clinph.2018.01.063.

Albin, R. L., A. B. Young, and J. B. Penney (1989). "The functional anatomy of basal ganglia disorders". In: *Trends in Neurosciences* 12.10, pp. 366–375. DOI: 10.1016/0166-2236(89)90074-X.

Anidi, C. M., J. J. O'Day, R. W. Anderson, M. F. Afzal, J. Syrkin-Nikolau, A. Velisar, and H. M. Bronte-Stewart (2018). "Neuromodulation targets pathological not physiological beta bursts during gait in Parkinson's disease". In: *Neurobiology of disease* 120, pp. 107–117. DOI: 10.1016/j.nbd.2018.09.004.

Arlotti, M., S. Marceglia, G. Foffani, J. Volkmann, A. M. Lozano, E. Moro, F. Cogiamanian, M. Prenassi, T. Bocci, F. Cortese, P. Rampini, S. Barbieri, and A. Priori (Mar. 2018). "Eight-hours adaptive deep brain stimulation in patients with Parkinson disease". In: *Neurology* 90.11, e971–e976. DOI: 10.1212/WNL.0000000000005121.

Ashwin, P., S. Coombes, and R. Nicks (2016). "Mathematical Frameworks for Oscillatory Network Dynamics in Neuroscience". In: *J Math Neurosci* 6.1, p. 2. DOI: 10.1186/s13408-015-0033-6.

Atasoy, S., I. Donnelly, and J. Pearson (2016). "Human brain networks function in connectome-specific harmonic waves". In: *Nature Communications* 7. DOI: 10.1038/ncomms10340.

Audet, C. and J. E. Dennis (2003). "Analysis of generalized pattern searches". In: *SIAM Journal on Optimization* 13.3, pp. 889–903. DOI: 10.1137/S1052623400378742.

Barnikol, U. B., O. V. Popovych, C. Hauptmann, V. Sturm, H. J. Freund, and P. A. Tass (Oct. 2008). "Tremor entrainment by patterned low-frequency stimulation". In: *Philosophical Transactions of the Royal Society A: Mathematical, Physical and Engineering Sciences* 366.1880, pp. 3545–3573. DOI: 10.1098/rsta.2008.0104.

Beaumont, M. A. (2019). "Approximate Bayesian Computation". In: *Annual Review of Statistics and Its Application* 6.1, null. DOI: 10.1146/annurev-statistics-030718-105212.

Bedrosian, E. (1963). "A product theorem for Hilbert transforms". In: *Proceedings of the IEEE* 51.5, pp. 868–869.

Bellman, R. and K. J. Åström (Apr. 1970). "On structural identifiability". In: *Mathematical Biosciences* 7.3-4, pp. 329–339. DOI: 10.1016/0025-5564(70)90132-X.

Benabid, A. L., P. Pollak, A. Louveau, S. Henry, and J. De Rougemont (1987). "Combined (thalamotomy and stimulation) stereotactic surgery of the vim thalamic nucleus for bilateral parkinson disease". In: *Applied Neurophysiology* 50.1-6, pp. 344–346. DOI: 10.1159/000100803.

Benabid, A. L., S. Chabardes, J. Mitrofanis, and P. Pollak (Jan. 2009). *Deep brain stimulation of the subthalamic nucleus for the treatment of Parkinson's disease*. DOI: 10.1016/S1474-4422(08)70291-6.

Benjamini, Y., A. M. Krieger, and D. Yekutieli (2006). "Adaptive linear step-up procedures that control the false discovery rate". In: *Biometrika* 93.3, pp. 491–507. DOI: 10.1093/biomet/93.3.491.

Bhatia, K. P., P. Bain, N. Bajaj, R. J. Elble, M. Hallett, E. D. Louis, J. Raethjen, M. Stamelou, C. M. Testa, and G. Deuschl (Jan. 2018). "Consensus Statement on the classification of tremors. from the task force on tremor of the International Parkinson and Movement Disorder Society". In: *Movement Disorders* 33.1, pp. 75–87. DOI: 10.1002/mds.27121.

Bick, C., M. Goodfellow, C. R. Laing, and E. A. Martens (2020). "Understanding the dynamics of biological and neural oscillator networks through exact mean-field reductions: a review". In: *The Journal of Mathematical Neuroscience* 10.1, p. 9. DOI: 10.1186/s13408-020-00086-9.

Borisyuk, G. N., R. M. Borisyuk, A. I. Khibnik, and D. Roose (1995). "Dynamics and bifurcations of two coupled neural oscillators with different connection types". In: *Bulletin of mathematical biology* 57.6, pp. 809–840. DOI: 10.1007/BF02458296.

Borisyuk, R. M. and A. B. Kirillov (1992). "Bifurcation analysis of a neural network model". In: *Biological Cybernetics* 66.4, pp. 319–325. DOI: 10.1007/bf00203668.

Børretzen, M. N., S. Bjerknes, T. Sæhle, M. Skjelland, I. M. Skogseid, M. Toft, and E. Dietrichs (2014). "Long-term follow-up of thalamic deep brain stimulation for essential tremor – patient satisfaction and mortality". In: *BMC Neurology* 14.1, p. 120. DOI: 10.1186/1471-2377-14-120.

Bressloff, P. C., J. D. Cowan, M. Golubitsky, P. J. Thomas, and M. C. Wiener (2002). "What geometric visual hallucinations tell us about the visual cortex". In: *Neural Computation* 14.3, pp. 473–489. DOI: 10.1162/089976602317250861.

Brittain, J. S. and P. Brown (2014). "Oscillations and the basal ganglia: motor control and beyond". In: *Neuroimage* 85 Pt 2, pp. 637–647. DOI: 10.1016/j.neuroimage.2013.05.084.

Brittain, J. S., H. Cagnan, A. R. Mehta, T. A. Saifee, M. J. Edwards, and P. Brown (2015). "Distinguishing the central drive to tremor in Parkinson's disease and essential tremor". In: *J Neurosci* 35.2, pp. 795–806. DOI: 10.1523/JNEUROSCI.3768-14.2015.

Brittain, J. S., P. Probert-Smith, T. Z. Aziz, and P. Brown (2013). "Tremor suppression by rhythmic transcranial current stimulation". In: *Curr Biol* 23.5, pp. 436–440. DOI: 10.1016/j.cub.2013.01.068.

Broadie, M., P. Glasserman, and K. Steven (1997). "A continuity correction for discrete barrier options". In: *Mathematical Finance* 7.4, pp. 325–349. DOI: 10.1111/1467-9965.00035.

Brown, E., J. Moehlis, and P. Holmes (Apr. 2004). "On the phase reduction and response dynamics of neural oscillator populations". In: *Neural Computation* 16.4, pp. 673–715. DOI: 10.1162/089976604322860668.

Brown, P. (2003). "Oscillatory nature of human basal ganglia activity: relationship to the pathophysiology of Parkinson's disease". In: *Movement Disorders* 18.4, pp. 357–363. DOI: 10.1002/mds.10358.

Brown, P., A. Oliviero, P. Mazzone, A. Insola, P. Tonali, and V. Di Lazzaro (2001). "Dopamine dependency of oscillations between subthalamic nucleus and pallidum in Parkinson's disease". In: *Journal of Neuroscience* 21.3, pp. 1033–1038. DOI: 10.1523/jneurosci.21-03-01033.2001.

Bruns, A. (Aug. 2004). "Fourier-, Hilbert- and wavelet-based signal analysis: Are they really different approaches?" In: *Journal of Neuroscience Methods* 137.2, pp. 321–332. DOI: 10.1016/j.jneumeth.2004.03.002.

Brunton, S. L., J. L. Proctor, and J. N. Kutz (2016). "Discovering governing equations from data by sparse identification of nonlinear dynamical systems". In: *Proceedings of the National Academy of Sciences* 113.15, pp. 3932–3937.

Butterworth, S. (1930). "On the theory of filter amplifiers". In: *Wireless Engineer* 7.6, pp. 536–541.

Byrne, Á., M. J. Brookes, and S. Coombes (2017). "A mean field model for movement induced changes in the beta rhythm". In: *Journal of Computational Neuroscience* 43.2, pp. 143–158. DOI: 10.1007/s10827-017-0655-7.

Byrne, Á., R. D. O'Dea, M. Forrester, J. Ross, and S. Coombes (2020). "Next-generation neural mass and field modeling". In: *Journal of neurophysiology* 123.2, pp. 726–742. DOI: 10.1152/jn.00406.2019.

Cabral, J., H. Luckhoo, M. Woolrich, M. Joensson, H. Mohseni, A. Baker, M. L. Kringelbach, and G. Deco (Apr. 2014). "Exploring mechanisms of spontaneous functional connectivity in MEG: How delayed network interactions lead to structured amplitude envelopes of band-pass filtered oscillations". In: *NeuroImage* 90, pp. 423–435. DOI: 10.1016/j.neuroimage.2013.11.047.

Cagnan, H., J. S. Brittain, S. Little, T. Foltynie, P. Limousin, L. Zrinzo, M. Hariz, C. Joint, J. Fitzgerald, A. L. Green, T. Aziz, and P. Brown (2013). "Phase dependent modulation of tremor amplitude in essential tremor through thalamic stimulation". In: *Brain* 136.Pt 10, pp. 3062–3075. DOI: 10.1093/brain/awt239.

Cagnan, H., S. Little, T. Foltynie, P. Limousin, L. Zrinzo, M. Hariz, B. Cheeran, J. Fitzgerald, A. L. Green, T. Aziz, and P. Brown (2014). "The nature of tremor circuits in parkinsonian and essential tremor". In: *Brain* 137.Pt 12, pp. 3223–3234. DOI: 10.1093/brain/awu250.

Cagnan, H., D. Pedrosa, S. Little, A. Pogosyan, B. Cheeran, T. Aziz, A. Green, J. Fitzgerald, T. Foltynie, P. Limousin, L. Zrinzo, M. Hariz, K. J. Friston, T. Denison, and P. Brown (2017). "Stimulating at the right time: phase-specific deep brain stimulation". In: *Brain* 140.Pt 1, pp. 132–145. DOI: 10.1093/brain/aww286.

Cagnan, H., G. Weerasinghe, and P. Brown (2019a). *Tremor data measured from essential tremor patients subjected to phase-locked deep brain stimulation*. Oxford. DOI: 10.5287/bodleian:xq24eN2Km.

Cagnan, H., T. Denison, C. McIntyre, and P. Brown (Sept. 2019b). "Emerging technologies for improved deep brain stimulation". In: *Nature Biotechnology* 37.9, pp. 1024–1033. DOI: 10.1038/s41587-019-0244-6.

Cagnan, H., E. P. Duff, and P. Brown (2015). "The relative phases of basal ganglia activities dynamically shape effective connectivity in Parkinson's disease". In: *Brain* 138.Pt 6, pp. 1667–1678. DOI: 10.1093/brain/awv093.

Cagnan, H., N. Mallet, C. K. E. Moll, A. Gulberti, A. B. Holt, M. Westphal, C. Gerloff, A. K. Engel, W. Hamel, P. J. Magill, P. Brown, and A. Sharott (Aug. 2019c). "Temporal evolution of beta bursts in the parkinsonian cortical and basal ganglia network". In: *Proceedings of the National Academy of Sciences* 116.32, pp. 16095–16104. DOI: 10.1073/pnas.1819975116.

Calabresi, P., B. Picconi, A. Tozzi, V. Ghiglieri, and M. Di Filippo (2014). *Direct and indirect pathways of basal ganglia: A critical reappraisal*. DOI: 10.1038/nn.3743.

Camara, C., N. P. Subramaniyam, K. Warwick, L. Parkkonen, T. Aziz, and E. Pereda (2019). "Non-Linear Dynamical Analysis of Resting Tremor for Demand-Driven Deep Brain Stimulation". In: *Sensors* 19.11, p. 2507. DOI: 10.3390/s19112507.

Cao, A., B. Lindner, and P. J. Thomas (July 2020). "A Partial Differential Equation for the Mean–Return-Time Phase of Planar Stochastic Oscillators". In: *SIAM Journal on Applied Mathematics* 80.1, pp. 422–447. DOI: 10.1137/18m1218601. arXiv: 1908.00487.

Cassidy, M., P. Mazzone, A. Oliviero, A. Insola, P. Tonali, V. Di Lazzaro, and P. Brown (2002). "Movement-related changes in synchronization in the human basal ganglia". In: *Brain* 125.6, pp. 1235–1246. DOI: 10.1093/brain/awf135.

Castejón, O., A. Guillamon, and G. Huguet (2013). "Phase-Amplitude response functions for Transient-State stimuli". In: *Journal of Mathematical Neuroscience* 3.1, pp. 1–26. DOI: 10.1186/2190-8567-3-13.

Chen, L. L., R. Madhavan, B. I. Rapoport, and W. S. Anderson (2013). "Real-time brain oscillation detection and phase-locked stimulation using autoregressive spectral estimation and time-series forward prediction". In: *IEEE transactions on Biomedical Engineering* 60.3, pp. 753–762. DOI: 10.1109/TBME.2011.2109715.

Cheng, H. C., C. M. Ulane, and R. E. Burke (2010). *Clinical progression in Parkinson disease and the neurobiology of axons*. DOI: 10.1002/ana.21995.

Chossat, P. (2020). "The hyperbolic model for edge and texture detection in the primary visual cortex". In: *Journal of Mathematical Neuroscience* 10.1. DOI: 10.1186/s13408-020-0079-y.

Chow, C. C. and Y. Karimipanah (Mar. 2020). "Before and beyond the Wilson-Cowan equations". In: *Journal of Neurophysiology*. DOI: 10.1152/jn.00404.2019. arXiv: 1907.07821.

Cole, S. R., R. van der Meij, E. J. Peterson, C. de Hemptinne, P. A. Starr, and B. Voytek (2017). "Nonsinusoidal beta oscillations reflect cortical pathophysiology in parkinson's disease". In: *Journal of Neuroscience* 37.18, pp. 4830–4840. DOI: 10.1523/JNEUROSCI.2208-16.2017.

Collin-Dufresne, P. and R. S. Goldstein (2001). "Do credit spreads reflect stationary leverage ratios?" In: *Journal of Finance* 56.5, pp. 1929–1957. DOI: 10.1111/0022-1082.00395.

Crodelle, J., S. H. Piltz, M. H. Hagenauer, and V. Booth (2019). "Modeling the daily rhythm of human pain processing in the dorsal horn". In: *PLoS Computational Biology* 15.7. DOI: 10.1371/journal.pcbi.1007106.

Deffains, M., L. Iskhakova, S. Katabi, Z. Israel, and H. Bergman (2018). "Longer β oscillatory episodes reliably identify pathological subthalamic activity in Parkinsonism". In: *Movement Disorders* 33.10, pp. 1609–1618. DOI: 10.1002/mds.27418.

De Lau, L. M. and M. M. Breteler (June 2006). *Epidemiology of Parkinson's disease*. DOI: 10.1016/S1474-4422(06)70471-9.

Deuschl, G., C. Schade-Brittinger, P. Krack, J. Volkmann, H. Schäfer, K. Bötzel, C. Daniels, A. Deutschländer, U. Dillmann, W. Eisner, D. Gruber, W. Hamel, J. Herzog, R. Hilker, S. Klebe, M. Kloß, J. Koy, M. Krause, A. Kupsch, D. Lorenz, S. Lorenzl, H. M. Mehdorn, J. R. Moringlane, W. Oertel, M. O. Pinsker, H. Reichmann, A. Reuß, G. H. Schneider, A. Schnitzler, U. Steude, V. Sturm, L. Timmermann, V. Tronnier, T. Trottenberg, L. Wojtecki, E. Wolf, W. Poewe, and J. Voges (Aug. 2006). "A randomized trial of deep-brain stimulation for Parkinson's disease". In: *New England Journal of Medicine* 355.9, pp. 896–908. DOI: 10.1056/NEJMoa060281.

Ditlevsen, S. and P. Lansky (2008). "Comparison of statistical methods for estimation of the input parameters in the Ornstein-Uhlenbeck neuronal model from first-passage times data". In: *AIP Conference Proceedings*. Vol. 1028, pp. 171–185. DOI: 10.1063/1.2965085.

Drugowitsch, J. (2016). "Fast and accurate Monte Carlo sampling of first-passage times from Wiener diffusion models". In: *Scientific Reports* 6. DOI: 10.1038/srep20490.

Duchet, B., F. Ghezzi, G. Weerasinghe, G. Tinkhauser, A. A. Kuhn, P. Brown, C. Bick, and R. Bogacz (Apr. 2020a). "Average beta burst duration profiles provide a signature of dynamical changes between the ON and OFF medication states in Parkinson's disease". In: *bioRxiv*, p. 2020.04.27.064246. DOI: 10.1101/2020.04.27.064246.

Duchet, B., G. Weerasinghe, H. Cagnan, P. Brown, C. Bick, and R. Bogacz (2020b). "Phase-dependence of response curves to deep brain stimulation and their relationship: from essential tremor patient data to a Wilson–Cowan model". In: *The Journal of Mathematical Neuroscience* 10.1, p. 4. DOI: 10.1186/s13408-020-00081-0.

Dumont, G. and B. Gutkin (2019). "Macroscopic phase resetting-curves determine oscillatory coherence and signal transfer in inter-coupled neural circuits". In: *PLoS Computational Biology* 15.5. DOI: 10.1371/journal.pcbi.1007019.

Engel, A. K., C. Gerloff, C. C. Hilgetag, and G. Nolte (2013). "Intrinsic coupling modes: multiscale interactions in ongoing brain activity". In: *Neuron* 80.4, pp. 867–886. DOI: 10.1016/j.neuron.2013.09.038.

Eusebio, A., W. Thevathasan, L. D. Gaynor, A. Pogosyan, E. Bye, T. Foltynie, L. Zrinzo, K. Ashkan, T. Aziz, and P. Brown (2011). "Deep brain stimulation can suppress pathological synchronisation in parkinsonian patients". In: *Journal of Neurology, Neurosurgery & Psychiatry* 82.5, pp. 569–573. DOI: 10.1136/jnnp.2010.217489.

Fasano, A. and R. C. Helmich (Aug. 2019). "Tremor habituation to deep brain stimulation: Underlying mechanisms and solutions". In: *Movement Disorders* 34.12, pp. 1761–1773. DOI: 10.1002/mds.27821.

Feingold, J., D. J. Gibson, B. Depasquale, and A. M. Graybiel (Nov. 2015). "Bursts of beta oscillation differentiate postperformance activity in the striatum and motor cortex of monkeys performing movement tasks". In: *Proceedings of the National Academy of Sciences of the United States of America* 112.44, pp. 13687–13692. DOI: 10.1073/pnas.1517629112.

Fernández-Ruiz, A., A. Oliva, E. F. de Oliveira, F. Rocha-Almeida, D. Tingley, and G. Buzsáki (2019). "Long-duration hippocampal sharp wave ripples improve memory". In: *Science* 364.6445, pp. 1082–1086. DOI: 10.1126/science.aax0758.

Finger, H., M. Bönstrup, B. Cheng, A. Messé, C. Hilgetag, G. Thomalla, C. Gerloff, and P. König (Aug. 2016). "Modeling of Large-Scale Functional Brain Networks Based on Structural Connectivity from DTI: Comparison with EEG Derived Phase Coupling Networks and Evaluation of Alternative Methods along the Modeling Path". In: *PLoS Computational Biology* 12.8, e1005025. DOI: 10.1371/journal.pcbi.1005025.

Fischer, P., H. Tan, A. Pogosyan, and P. Brown (2016). "High post-movement parietal low-beta power during rhythmic tapping facilitates performance in a stop task". In: *European Journal of Neuroscience* 44.5, pp. 2202–2213. DOI: 10.1111/ejn.13328.

Frank, M. J., J. Samanta, A. A. Moustafa, and S. J. Sherman (Nov. 2007). "Hold your horses: Impulsivity, deep brain stimulation, and medication in Parkinsonism". In: *Science* 318.5854, pp. 1309–1312. DOI: 10.1126/science.1146157.

Fries, P. (2015). "Rhythms for cognition: communication through coherence". In: *Neuron* 88.1, pp. 220–235. DOI: 10.1016/j.neuron.2015.09.034.

Galtier, M. N. and J. Touboul (2013). "Macroscopic equations governing noisy spiking neuronal populations with linear synapses". In: *PloS one* 8.11, e78917. DOI: 10.1371/journal.pone.0078917.

Gillespie, D. T. (1996). "Exact numerical simulation of the Ornstein-Uhlenbeck process and its integral". In: *Physical Review E* 54.2, p. 2084. DOI: 10.1103/PhysRevE.54.2084.

Gillies, A., D. Willshaw, and Z. Li (2002). "Subthalamic-pallidal interactions are critical in determining normal and abnormal functioning of the basal ganglia". eng. In: *Proc Biol Sci* 269.1491, pp. 545–551. DOI: 10.1098/rspb.2001.1817.

Giné, J. and M. Grau (2005). "Characterization of isochronous foci for planar analytic differential systems". In: *Royal Society of Edinburgh - Proceedings A*. Vol. 135. 5, pp. 985–998. DOI: 10.1017/S0308210500004236.

Gironell, A. (July 2014). "The GABA Hypothesis in Essential Tremor: Lights and Shadows". eng. In: *Tremor and other hyperkinetic movements (New York, N.Y.)* 4, p. 254. DOI: 10.7916/D8SF2T9C.

Glass, L. and M. C. Mackey (1988). *From clocks to chaos: the rhythms of life*. Princeton, NJ: Princeton University Press.

Grebenkov, D. S. (2014). "First exit times of harmonically trapped particles: a didactic review". In: *Journal of Physics A: Mathematical and Theoretical* 48.1, p. 13001. DOI: 10.1088/1751-8113/48/1/013001.

Grill, W. M., A. N. Snyder, and S. Miocinovic (May 2004). "Deep brain stimulation creates an informational lesion of the stimulated nucleus". In: *NeuroReport* 15.7, pp. 1137–1140. DOI: 10.1097/00001756-200405190-00011.

Grossman, N., D. Bono, N. Dedic, S. B. Kodandaramaiah, A. Rudenko, H. J. Suk, A. M. Cassara, E. Neufeld, N. Kuster, L. H. Tsai, A. Pascual-Leone, and E. S. Boyden (June 2017). "Noninvasive Deep Brain Stimulation via Temporally Interfering Electric Fields". In: *Cell* 169.6, 1029–1041.e16. DOI: 10.1016/j.cell.2017.05.024.

Guckenheimer, J. (1975). "Isochrons and phaseless sets". In: *Journal of Mathematical Biology* 1.3, pp. 259–273.

Guillamon, A. and G. Huguet (2009). "A computational and geometric approach to phase resetting curves and surfaces". In: *SIAM Journal on Applied Dynamical Systems* 8.3, pp. 1005–1042. DOI: 10.1137/080737666.

Haidar, I., W. Pasillas-Lepine, A. Chaillet, E. Panteley, S. Palfi, and S. Senova (2016). "Closed-loop firing rate regulation of two interacting excitatory and inhibitory neural populations of the basal ganglia". In: *Biol Cybern* 110.1, pp. 55–71. DOI: 10.1007/s00422-015-0678-y.

Hammond, C., H. Bergman, and P. Brown (2007). *Pathological synchronization in Parkinson's disease: networks, models and treatments.* DOI: 10.1016/j.tins.2007.05.004.

Harary, M., D. J. Segar, M. T. Hayes, and G. R. Cosgrove (June 2019). "Unilateral Thalamic Deep Brain Stimulation Versus Focused Ultrasound Thalamotomy for Essential Tremor". In: *World Neurosurgery* 126, e144–e152. DOI: 10.1016/j.wneu.2019.01.281.

Hariz, M. (2017). "My 25 Stimulating Years with DBS in Parkinson's Disease". In: *Journal of Parkinson's Disease* 7.s1, S35–S43. DOI: 10.3233/JPD-179007.

Harris, J. D. and B. Ermentrout (2018). "Traveling waves in a spatially-distributed Wilson–Cowan model of cortex: From fronts to pulses". In: *Physica D: Nonlinear Phenomena* 369, pp. 30–46. DOI: 10.1016/j.physd.2017.12.011.

Hay, S. I., S. P. Jayaraman, T. Truelsen, R. J. D. Sorensen, A. Millear, G. Giussani, and E. Beghi (2017). "GBD 2015 disease and injury incidence and prevalence collaborators. Global, regional, and national incidence, prevalence, and years lived with disability for 310 diseases and injuries, 1990-2015: a systematic analysis for the global burden of disease stud". In: *Lancet* 389.10064, E1–E1. DOI: 0.1016/S0140-6736(16)31678-6.

Hebb, A. O., F. Darvas, and K. J. Miller (Jan. 2012). "Transient and state modulation of beta power in human subthalamic nucleus during speech production and finger movement". In: *Neuroscience* 202, pp. 218–233. DOI: 10.1016/j.neuroscience.2011.11.072.

Heideman, S. G., A. J. Quinn, M. W. Woolrich, F. van Ede, and A. C. Nobre (2019). "Dissecting beta-state changes during timed movement preparation in Parkinson's disease". In: *Progress in Neurobiology*, p. 101731. DOI: 10.1016/j.pneurobio.2019.101731.

Herrmann, S. and C. Zucca (2019). "Exact Simulation of the First-Passage Time of Diffusions". In: *Journal of Scientific Computing* 79.3, pp. 1477–1504. DOI: 10.1007/s10915-018-00900-3. arXiv: 1705.06881.

Herz, D. M., S. Little, D. J. Pedrosa, G. Tinkhauser, B. Cheeran, T. Foltynie, R. Bogacz, and P. Brown (2018). "Mechanisms Underlying Decision-Making as Revealed by Deep-Brain Stimulation in Patients with Parkinson's Disease". In: *Current Biology* 28.8, 1169–1178.e6. DOI: 10.1016/j.cub.2018.02.057.

Hines, K. E., T. R. Middendorf, and R. W. Aldrich (Mar. 2014). "Determination of parameter identifiability in nonlinear biophysical models: A bayesian approach". In: *Journal of General Physiology* 143.3, pp. 401–416. DOI: 10.1085/jgp.201311116.

Hoang, K. B., I. R. Cassar, W. M. Grill, and D. A. Turner (2017). "Biomarkers and Stimulation Algorithms for Adaptive Brain Stimulation". In: *Frontiers in Neuroscience* 11. DOI: 10.3389/fnins.2017.00564.

Holgado, A. J., J. R. Terry, and R. Bogacz (2010). "Conditions for the generation of beta oscillations in the subthalamic nucleus-globus pallidus network". In: *J Neurosci* 30.37, pp. 12340–12352. DOI: 10.1523/JNEUROSCI.0817-10.2010.

Holt, A. B., D. Wilson, M. Shinn, J. Moehlis, and T. I. Netoff (2016). "Phasic Burst Stimulation: A Closed-Loop Approach to Tuning Deep Brain Stimulation Parameters

for Parkinson's Disease". In: *PLoS Comput Biol* 12.7, e1005011. DOI: 10.1371/journal.pcbi.1005011.

Holt, A. B., E. Kormann, A. Gulberti, M. Pötter-Nerger, C. G. McNamara, H. Cagnan, M. K. Baaske, S. Little, J. A. Köppen, and C. Buhmann (2019). "Phase-dependent suppression of beta oscillations in Parkinson's disease patients". In: *Journal of Neuroscience* 39.6, pp. 1119–1134. DOI: 10.1523/JNEUROSCI.1913-18.2018.

Houston, B. C., M. C. Thompson, J. G. Ojemann, A. L. Ko, and H. J. Chizeck (2017). "Classifier-based closed-loop deep brain stimulation for essential tremor". In: *Neural Engineering (NER), 2017 8th International IEEE/EMBS Conference on*. IEEE, pp. 316–320.

Hua, S. E., F. A. Lenz, T. A. Zirh, S. G. Reich, and P. M. Dougherty (1998). "Thalamic neuronal activity correlated with essential tremor". In: *Journal of Neurology Neurosurgery and Psychiatry* 64.2, pp. 273–276. DOI: 10.1136/jnnp.64.2.273.

Hua, S. E. and F. A. Lenz (2005). "Posture-related oscillations in human cerebellar thalamus in essential tremor are enabled by voluntary motor circuits". In: *Journal of Neurophysiology* 93.1, pp. 117–127. DOI: 10.1152/jn.00527.2004.

Izhikevich, E. M. (2007). *Dynamical systems in neuroscience*. Cambridge, MA: MIT press.

Jackson, N., S. R. Cole, B. Voytek, and N. C. Swann (2019). "Characteristics of Waveform Shape in Parkinson's Disease Detected with Scalp Electroencephalography". In: *eNeuro*, ENEURO. 0151–19.2019. DOI: 10.1523/ENEURO.0151-19.2019.

Jansen, B. H. and V. G. Rit (1995). "Electroencephalogram and visual evoked potential generation in a mathematical model of coupled cortical columns". In: *Biological Cybernetics* 73.4, pp. 357–366. DOI: 10.1007/BF00199471.

Kalia, L. V. and A. E. Lang (2015). "Parkinson's disease". In: *The Lancet* 386.9996, pp. 896–912. DOI: 10.1016/S0140-6736(14)61393-3.

Keylock, C. J. (2006). "Constrained surrogate time series with preservation of the mean and variance structure". In: *Physical Review E - Statistical, Nonlinear, and Soft Matter Physics* 73.3. DOI: 10.1103/PhysRevE.73.036707.

— (2010). "Characterizing the structure of nonlinear systems using gradual wavelet reconstruction". In: *Nonlinear Processes in Geophysics* 17.6, pp. 615–632. DOI: 10.5194/npg-17-615-2010.

— (2019). "Hypothesis Testing for Nonlinear Phenomena in the Geosciences Using Synthetic, Surrogate Data". In: *Earth and Space Science* 6.1, pp. 41–58. DOI: 10.1029/2018EA000435.

Keylock, C. J. (2007). "A wavelet-based method for surrogate data generation". In: *Physica D: Nonlinear Phenomena* 225.2, pp. 219–228. DOI: 10.1016/j.physd.2006.10.012.

Khawaldeh, S., G. Tinkhauser, S. A. Shah, K. Peterman, I. Debove, T. A. K. Nguyen, A. Nowacki, M. L. Lachenmayer, M. Schuepbach, C. Pollo, P. Krack, M. Woolrich, and P. Brown (Feb. 2020). "Subthalamic nucleus activity dynamics and limb movement prediction in Parkinson's disease". In: *Brain* 143.2, pp. 582–596. DOI: 10.1093/brain/awz417.

Kiss, Z. H. (2007). "Bilateral pallidal neurostimulation - Long-term motor and cognitive effects in primary generalized dystonia". In: *Nature Clinical Practice Neurology* 3.9, pp. 482–483. DOI: 10.1038/ncpneuro0555.

Kitzbichler, M. G., M. L. Smith, S. R. Christensen, and E. Bullmore (Mar. 2009). "Broadband criticality of human brain network synchronization". In: *PLoS Computational Biology* 5.3, e1000314. DOI: 10.1371/journal.pcbi.1000314.

Klinger, N. V. and S. Mittal (Jan. 2016). "Clinical efficacy of deep brain stimulation for the treatment of medically refractory epilepsy". In: *Clinical Neurology and Neurosurgery* 140, pp. 11–25. DOI: 10.1016/j.clineuro.2015.11.009.

Koller, W. C., K. E. Lyons, S. B. Wilkinson, A. I. Troster, and R. Pahwa (May 2001). "Long-term safety and efficacy of unilateral deep brain stimulation of the thalamus in essential tremor". In: *Movement Disorders* 16.3, pp. 464–468. DOI: 10.1002/mds.1089.

Korda, M., M. Putinar, and I. Mezić (Mar. 2020). "Data-driven spectral analysis of the Koopman operator". In: *Applied and Computational Harmonic Analysis* 48.2, pp. 599–629. DOI: 10.1016/j.acha.2018.08.002. arXiv: 1710.06532.

Kordower, J. H., C. W. Olanow, H. B. Dodiya, Y. Chu, T. G. Beach, C. H. Adler, G. M. Halliday, and R. T. Bartus (2013). "Disease duration and the integrity of the nigrostriatal system in Parkinson's disease". In: *Brain* 136.8, pp. 2419–2431. DOI: 10.1093/brain/awt192.

Kralemann, B., L. Cimponeriu, M. Rosenblum, A. Pikovsky, and R. Mrowka (2008). "Phase dynamics of coupled oscillators reconstructed from data". In: *Physical Review E* 77.6, p. 66205. DOI: 10.1103/PhysRevE.77.066205.

Ku, H. (1966). "Notes on the use of propagation of error formulas". In: *Journal of Research of the National Bureau of Standards, Section C: Engineering and Instrumentation* 70C.4, p. 263. DOI: 10.6028/jres.070c.025.

Kuhn, A. A., A. Kupsch, G. H. Schneider, and P. Brown (2006). "Reduction in subthalamic 8-35 Hz oscillatory activity correlates with clinical improvement in Parkinson's disease". In: *Eur J Neurosci* 23.7, pp. 1956–1960. DOI: 10.1111/j.1460-9568.2006.04717.x.

Kühn, A. A., A. Tsui, T. Aziz, N. Ray, C. Brücke, A. Kupsch, G. H. Schneider, and P. Brown (Feb. 2009). "Pathological synchronisation in the subthalamic nucleus of patients with Parkinson's disease relates to both bradykinesia and rigidity". In: *Experimental Neurology* 215.2, pp. 380–387. DOI: 10.1016/j.expneurol.2008.11.008.

Kühn, A. A., D. Williams, A. Kupsch, P. Limousin, M. Hariz, G. H. Schneider, K. Yarrow, and P. Brown (Apr. 2004). "Event-related beta desynchronization in human subthalamic nucleus correlates with motor performance". In: *Brain* 127.4, pp. 735–746. DOI: 10.1093/brain/awh106.

Kühn, A. A., F. Kempf, C. Brücke, L. G. Doyle, I. Martinez-Torres, A. Pogosyan, T. Trottenberg, A. Kupsch, G. H. Schneider, M. I. Hariz, W. Vandenberghe, B. Nuttin, and P. Brown (June 2008). "High-frequency stimulation of the subthalamic nucleus suppresses oscillatory β activity in patients with Parkinson's disease in parallel with improvement in motor performance". In: *Journal of Neuroscience* 28.24, pp. 6165–6173. DOI: 10.1523/JNEUROSCI.0282-08.2008.

Kumar, A., S. Cardanobile, S. Rotter, and A. Aertsen (2011). "The role of inhibition in generating and controlling Parkinson's disease oscillations in the Basal Ganglia". In: *Front Syst Neurosci* 5, p. 86. DOI: 10.3389/fnsys.2011.00086.

Kumar, R., A. M. Lozano, E. Sime, and A. E. Lang (2003). "Long-term follow-up of thalamic deep brain stimulation for essential and parkinsonian tremor". eng. In: *Neurology* 61.11, pp. 1601–1604. DOI: 10.1212/01.wnl.0000096012.07360.1c.

Kuramoto, Y. (1975). "Self-entrainment of a population of coupled non-linear oscillators". In: *International symposium on mathematical problems in theoretical physics*. Springer, pp. 420–422.

Laing, C. R. (Sept. 2017). "Phase Oscillator Network Models of Brain Dynamics". In: *Computational Models of Brain and Behavior*. John Wiley & Sons, Ltd, pp. 505–517. DOI: 10.1002/9781119159193.ch37.

Lancaster, G., D. Iatsenko, A. Pidde, V. Ticcinelli, and A. Stefanovska (2018). "Surrogate data for hypothesis testing of physical systems". In: *Physics Reports*. DOI: 10.1016/j.physrep.2018.06.001.

Larralde, H. (Mar. 2004). "A first passage time distribution for a discrete version of the Ornstein-Uhlenbeck process". In: *Journal of Physics A: Mathematical and General* 37.12, pp. 3759–3767. DOI: 10.1088/0305-4470/37/12/003.

Lawrence Marple, S. (Sept. 1999). "Computing the discrete-time analytic signal via fft". In: *IEEE Transactions on Signal Processing* 47.9, pp. 2600–2603. DOI: 10.1109/78.782222.

Lea-Carnall, C. A., M. A. Montemurro, N. J. Trujillo-Barreto, L. M. Parkes, and W. El-Deredy (2016). "Cortical Resonance Frequencies Emerge from Network Size and Connectivity". In: *PLoS Computational Biology* 12.2, p. 1004740. DOI: 10.1371/journal.pcbi.1004740.

Leblois, A., T. Boraud, W. Meissner, H. Bergman, and D. Hansel (2006). "Competition between feedback loops underlies normal and pathological dynamics in the basal ganglia". In: *Journal of Neuroscience* 26.13, pp. 3567–3583. DOI: 10.1523/JNEUROSCI.5050-05.2006.

Lee, S., D. J. Segar, W. Asaad, and S. Jones (June 2019). "Biophysical modeling of VIM to assess contributions of oscillatory activity to essential tremor". In: *bioRxiv*, p. 339846. DOI: 10.1101/339846.

Li, M. C. H. and M. J. Cook (Feb. 2018). "Deep brain stimulation for drug-resistant epilepsy". In: *Epilepsia* 59.2, pp. 273–290. DOI: 10.1111/epi.13964.

Little, S., A. Pogosyan, S. Neal, B. Zavala, L. Zrinzo, M. Hariz, T. Foltynie, P. Limousin, K. Ashkan, J. FitzGerald, A. L. Green, T. Z. Aziz, and P. Brown (2013). "Adaptive deep brain stimulation in advanced Parkinson disease". In: *Ann Neurol* 74.3, pp. 449–457. DOI: 10.1002/ana.23951.

Little, S., E. Tripoliti, M. Beudel, A. Pogosyan, H. Cagnan, D. Herz, S. Bestmann, T. Aziz, B. Cheeran, L. Zrinzo, M. Hariz, J. Hyam, P. Limousin, T. Foltynie, and P. Brown (2016). "Adaptive deep brain stimulation for Parkinson's disease demonstrates reduced speech side effects compared to conventional stimulation in the acute setting". In: *J Neurol Neurosurg Psychiatry*. DOI: 10.1136/jnnp-2016-313518.

Little, S., J. Bonaiuto, G. Barnes, and S. Bestmann (2019). "Human motor cortical beta bursts relate to movement planning and response errors". In: *PLoS biology* 17.10, e3000479. DOI: 10.1371/journal.pbio.3000479.

Little, S. and P. Brown (Feb. 2020). "Debugging Adaptive Deep Brain Stimulation for Parkinson's Disease". In: *Movement Disorders* 35.4, pp. 555–561. DOI: 10.1002/mds.27996.

Liu, Q., A. Ulloa, and B. Horwitz (2017). "Using a large-scale neural model of cortical object processing to investigate the neural substrate for managing multiple items in short-term memory". In: *Journal of Cognitive Neuroscience* 29.11, pp. 1860–1876. DOI: 10.1162/jocn_a_01163.

Lofredi, R., H. Tan, W.-J. Neumann, C.-H. Yeh, G.-H. Schneider, A. A. Kühn, and P. Brown (2019). "Beta bursts during continuous movements accompany the velocity decrement in Parkinson's disease patients". In: *Neurobiology of disease*. DOI: 10.1016/j.nbd.2019.03.013.

Louis, E. D. and J. J. Ferreira (2010). "How common is the most common adult movement disorder? Update on the worldwide prevalence of essential tremor". In: *Movement Disorders* 25.5, pp. 534–541. DOI: 10.1002/mds.22838.

Louis, E. D. (2005). *Essential tremor*. DOI: 10.1016/S1474-4422(05)00991-9.

Lozano, A. M., N. Lipsman, H. Bergman, P. Brown, S. Chabardes, J. W. Chang, K. Matthews, C. C. McIntyre, T. E. Schlaepfer, M. Schulder, Y. Temel, J. Volkmann, and J. K. Krauss (Mar. 2019). *Deep brain stimulation: current challenges and future directions*. DOI: 10.1038/s41582-018-0128-2.

Lundqvist, M., J. Rose, P. Herman, S. L. L. Brincat, T. J. J. Buschman, and E. K. K. Miller (Apr. 2016). "Gamma and Beta Bursts Underlie Working Memory". In: *Neuron* 90.1, pp. 152–164. DOI: 10.1016/j.neuron.2016.02.028.

Marceglia, S., G. Foffani, A. M. Bianchi, G. Baselli, F. Tamma, M. Egidi, and A. Priori (2006). "Dopamine-dependent non-linear correlation between subthalamic rhythms in Parkinson's disease". In: *Journal of Physiology* 571.3, pp. 579–591. DOI: 10.1113/jphysiol.2005.100271.

Marconi, R., D. Lefebvre-Caparros, A.-M. .-M. Bonnet, M. Vidailhet, B. Dubois, and Y. Agid (1994). "Levodopa-induced dyskinesias in Parkinson's disease phenomenology and pathophysiology". In: *Movement Disorders* 9.1, pp. 2–12. DOI: 10.1002/mds.870090103.

Marrouch, N., J. Slawinska, D. Giannakis, and H. L. Read (Nov. 2019). "Data-driven Koopman operator approach for computational neuroscience". In: *Annals of Mathematics and Artificial Intelligence*, pp. 1–19. DOI: 10.1007/s10472-019-09666-2.

Mauroy, A. and I. Mezic (2012). "On the use of Fourier averages to compute the global isochrons of (quasi)periodic dynamics". In: *Chaos* 22.3, p. 33112. DOI: 10.1063/1.4736859.

Mauroy, A. and I. Mezić (July 2018). "Global computation of phase-amplitude reduction for limit-cycle dynamics". In: *Chaos* 28.7, p. 073108. DOI: 10.1063/1.5030175.

Mauroy, A., I. Mezić, and J. Moehlis (2013). "Isostables, isochrons, and Koopman spectrum for the action-angle representation of stable fixed point dynamics". In: *Physica D: Nonlinear Phenomena* 261, pp. 19–30. DOI: 10.1016/j.physd.2013.06.004.

Mauroy, A. (2014). "Converging to and escaping from the global equilibrium: Isostables and optimal control". In: *Proceedings of the IEEE Conference on Decision and Control*. Vol. 2015-Febru. February. Institute of Electrical and Electronics Engineers Inc., pp. 5888–5893. DOI: 10.1109/CDC.2014.7040311.

Mauroy, A., B. Rhoads, J. Moehlis, and I. Mezić (2014). "Global Isochrons and Phase Sensitivity of Bursting Neurons". In: *SIAM Journal on Applied Dynamical Systems* 13.1, pp. 306–338. DOI: 10.1137/130931151.

McCarthy, M. M., C. Moore-Kochlacs, X. Gu, E. S. Boyden, X. Han, and N. Kopell (July 2011). "Striatal origin of the pathologic beta oscillations in Parkinson's disease". In: *Proceedings of the National Academy of Sciences of the United States of America* 108.28, pp. 11620–11625. DOI: 10.1073/pnas.1107748108.

McIntyre, C. C. and R. W. Anderson (2016). "Deep brain stimulation mechanisms: the control of network activity via neurochemistry modulation". In: *J Neurochem* 139 Suppl, pp. 338–345. DOI: 10.1111/jnc.13649.

McIntyre, C. C., W. M. Grill, D. L. Sherman, and N. V. Thakor (Apr. 2004). "Cellular Effects of Deep Brain Stimulation: Model-Based Analysis of Activation and Inhibition". In: *Journal of Neurophysiology* 91.4, pp. 1457–1469. DOI: 10.1152/jn.00989.2003.

McIntyre, C. C. and P. J. Hahn (June 2010). *Network perspectives on the mechanisms of deep brain stimulation*. DOI: 10.1016/j.nbd.2009.09.022.

Merrison-Hort, R., N. Yousif, F. Njap, U. G. Hofmann, O. Burylko, and R. Borisyuk (2013). "An interactive channel model of the basal ganglia: Bifurcation analysis under healthy and Parkinsonian conditions". In: *Journal of Mathematical Neuroscience* 3.1, pp. 1–29. DOI: 10.1186/2190-8567-3-14.

Miller, K. J., S. Zanos, E. E. Fetz, M. Den Nijs, and J. G. Ojemann (2009). "Decoupling the cortical power spectrum reveals real-time representation of individual finger movements in humans". In: *Journal of Neuroscience* 29.10, pp. 3132–3137. DOI: 10.1523/JNEUROSCI.5506-08.2009.

Mirzaei, A., A. Kumar, D. Leventhal, N. Mallet, A. Aertsen, J. Berke, and R. Schmidt (Nov. 2017). "Sensorimotor processing in the basal ganglia leads to transient beta oscillations during behavior". In: *Journal of Neuroscience* 37.46, pp. 11220–11232. DOI: 10.1523/JNEUROSCI.1289-17.2017.

Monga, B., D. Wilson, T. Matchen, and J. Moehlis (2018). "Phase reduction and phase-based optimal control for biological systems: a tutorial". In: *Biological Cybernetics*, pp. 1–36. DOI: 10.1007/s00422-018-0780-z.

Montbrió, E., D. Pazó, and A. Roxin (2015). "Macroscopic description for networks of spiking neurons". In: *Physical Review X* 5.2. DOI: 10.1103/PhysRevX.5.021028. arXiv: 1506.06581.

Mor, D. E., M. J. Daniels, and H. Ischiropoulos (Feb. 2019). *The usual suspects, dopamine and alpha-synuclein, conspire to cause neurodegeneration*. DOI: 10.1002/mds.27607.

Moraud, E. M., G. Tinkhauser, M. Agrawal, P. Brown, and R. Bogacz (2018). "Predicting beta bursts from local field potentials to improve closed-loop DBS paradigms in Parkinson's patients". In: *2018 40th Annual International Conference of the IEEE Engineering in Medicine and Biology Society (EMBC)*. IEEE, pp. 3766–3796. DOI: 10.1109/EMBC.2018.8513348.

Mücke, D., A. Hermes, T. B. Roettger, J. Becker, H. Niemann, T. A. Dembek, L. Timmermann, V. Visser-Vandewalle, G. R. Fink, M. Grice, and M. T. Barbe (Jan. 2018). "The effects of thalamic deep brain stimulation on speech dynamics in patients with essential tremor: An articulographic study". In: *PLoS ONE* 13.1. DOI: 10.1371/journal.pone.0191359.

Neumann, W. J., F. Staub, A. Horn, J. Schanda, J. Mueller, G. H. Schneider, P. Brown, and A. A. Kühn (Jan. 2016). "Deep brain recordings using an implanted pulse generator in Parkinson's disease". In: *Neuromodulation* 19.1, pp. 20–23. DOI: 10.1111/ner.12348.

Neumann, W. J., F. Staub-Bartelt, A. Horn, J. Schanda, G. H. Schneider, P. Brown, and A. A. Kühn (2017). "Long term correlation of subthalamic beta band activity with motor impairment in patients with Parkinson's disease". In: *Clinical Neurophysiology* 128.11, pp. 2286–2291. DOI: 10.1016/j.clinph.2017.08.028.

Nevado-Holgado, A. J., N. Mallet, P. J. Magill, and R. Bogacz (Apr. 2014). "Effective connectivity of the subthalamic nucleus-globus pallidus network during Parkinsonian oscillations". In: *Journal of Physiology* 592.7, pp. 1429–1455. DOI: 10.1113/jphysiol.2013.259721.

Nutt, J. G. and N. H. Holford (May 1996). *The response to levodopa in Parkinson's disease: Imposing pharmacological law and order*. DOI: 10.1002/ana.410390504.

Onslow, A. C., M. W. Jones, and R. Bogacz (2014). "A canonical circuit for generating phase-amplitude coupling". In: *PloS one* 9.8, e102591. DOI: 10.1371/journal.pone.0102591.

Oprisan, S. A. (2017). "A Consistent Definition of Phase Resetting Using Hilbert Transform". In: *International scholarly research notices* 2017. DOI: 10.1155/2017/5865101.

Ott, E. and T. M. Antonsen (2008). "Low dimensional behavior of large systems of globally coupled oscillators". In: *Chaos: An Interdisciplinary Journal of Nonlinear Science* 18.3, p. 37113. DOI: 10.1063/1.2930766.

Pahwa, R., K. E. Lyons, S. B. Wilkinson, R. K. Simpson, W. G. Ondo, D. Tarsy, T. Norregaard, J. P. Hubble, D. A. Smith, R. A. Hauser, and J. Jankovic (2006). "Long-term evaluation of deep brain stimulation of the thalamus". In: *Journal of Neurosurgery* 104.4, pp. 506–512. DOI: 10.3171/jns.2006.104.4.506.

Palva, J. M., S. Palva, and K. Kaila (2005). "Phase synchrony among neuronal oscillations in the human cortex". In: *Journal of Neuroscience* 25.15, pp. 3962–3972. DOI: 10.1523/JNEUROSCI.4250-04.2005.

Pavlides, A., S. J. Hogan, and R. Bogacz (2012). "Improved conditions for the generation of beta oscillations in the subthalamic nucleus–globus pallidus network". In: *Eur J Neurosci* 36.2, pp. 2229–2239. DOI: 10.1111/j.1460-9568.2012.08105.x.

— (2015). "Computational Models Describing Possible Mechanisms for Generation of Excessive Beta Oscillations in Parkinson's Disease". In: *PLoS Comput Biol* 11.12, e1004609. DOI: 10.1371/journal.pcbi.1004609.

Pedrosa, D. J., E.-L. Quatuor, C. Reck, K. A. M. Pauls, C. A. Huber, V. Visser-Vandewalle, and L. Timmermann (2014). "Thalamomuscular coherence in essential tremor: hen or egg in the emergence of tremor?" In: *Journal of Neuroscience* 34.43, pp. 14475–14483. DOI: 10.1523/JNEUROSCI.0087-14.2014.

Pereira, T., M. S. Baptista, and J. Kurths (Feb. 2007). "Phase and average period of chaotic oscillators". In: *Physics Letters, Section A: General, Atomic and Solid State Physics* 362.2-3, pp. 159–165. DOI: 10.1016/j.physleta.2006.09.099.

Pietras, B. and A. Daffertshofer (2019). "Network dynamics of coupled oscillators and phase reduction techniques". In: *Physics Reports*. DOI: 10.1016/j.physrep.2019.06.001.

Pietras, B., F. Devalle, A. Roxin, A. Daffertshofer, and E. Montbrió (2019). "Exact firing rate model reveals the differential effects of chemical versus electrical synapses in spiking networks". In: *Physical Review E* 100.4. DOI: 10.1103/PhysRevE.100.042412. arXiv: 1905.01917.

Pina, J. E., M. Bodner, and B. Ermentrout (2018). "Oscillations in working memory and neural binding: A mechanism for multiple memories and their interactions". In: *PLoS Computational Biology* 14.11. DOI: 10.1371/journal.pcbi.1006517.

Pogosyan, A., L. D. Gaynor, A. Eusebio, and P. Brown (2009). "Boosting cortical activity at beta-band frequencies slows movement in humans". In: *Current biology* 19.19, pp. 1637–1641. DOI: 10.1016/j.cub.2009.07.074.

Pollina, B., D. Benardete, and V. W. Noonburg (2003). "A Periodically Forced Wilson–Cowan System". In: *SIAM Journal on Applied Mathematics* 63.5, pp. 1585–1603. DOI: 10.1137/s003613990240814x.

Ponce-Alvarez, A., G. Deco, P. Hagmann, G. L. Romani, D. Mantini, and M. Corbetta (Feb. 2015). "Resting-State Temporal Synchronization Networks Emerge from Connectivity Topology and Heterogeneity". In: *PLoS Computational Biology* 11.2. Ed. by C. C. Hilgetag, e1004100. DOI: 10.1371/journal.pcbi.1004100.

Popovych, O. V., C. Hauptmann, and P. A. Tass (2006). "Control of neuronal synchrony by nonlinear delayed feedback". In: *Biological Cybernetics* 95.1, pp. 69–85. DOI: 10.1007/s00422-006-0066-8.

Popovych, O. V., B. Lysyansky, and P. A. Tass (2017). "Closed-loop deep brain stimulation by pulsatile delayed feedback with increased gap between pulse phases". In: *Scientific Reports* 7.1, p. 1033. DOI: 10.1038/s41598-017-01067-x.

Powanwe, A. S. and A. Longtin (Dec. 2019). "Determinants of Brain Rhythm Burst Statistics". In: *Scientific Reports* 9.1, pp. 1–28. DOI: 10.1038/s41598-019-54444-z.

Quinn, A. J., F. van Ede, M. J. Brookes, S. G. Heideman, M. Nowak, Z. A. Seedat, D. Vidaurre, C. Zich, A. C. Nobre, and M. W. Woolrich (2019). "Unpacking Transient Event Dynamics in Electrophysiological Power Spectra." In: *Brain topography* 32, pp. 1020–1034. DOI: 10.1007/s10548-019-00745-5.

Rabinovich, M. I., R. Huerta, P. Varona, and V. S. Afraimovich (2008). "Transient cognitive dynamics, metastability, and decision making". In: *PLoS Computational Biology* 4.5, p. 1000072. DOI: 10.1371/journal.pcbi.1000072.

Radulescu, A., J. Herron, C. Kennedy, and A. Scimemi (2017). "Global and local excitation and inhibition shape the dynamics of the cortico-striatal-thalamo-cortical pathway". In: *Sci Rep* 7.1, p. 7608. DOI: 10.1038/s41598-017-07527-8.

Raethjen, J. and G. Deuschl (2012). "The oscillating central network of essential tremor". In: *Clinical Neurophysiology* 123.1, pp. 61–64. DOI: 10.1016/j.clinph.2011.09.024.

Raethjen, J., R. B. Govindan, F. Kopper, M. Muthuraman, and G. Deuschl (May 2007). "Cortical involvement in the generation of essential tremor". In: *Journal of Neurophysiology* 97.5, pp. 3219–3228. DOI: 10.1152/jn.00477.2006.

Roberts, J. A., L. L. Gollo, R. G. Abeysuriya, G. Roberts, P. B. Mitchell, M. W. Woolrich, and M. Breakspear (2019). "Metastable brain waves". In: *Nature Communications* 10.1. DOI: 10.1038/s41467-019-08999-0.

Rodriguez-Oroz, M. C., J. A. Obeso, A. E. Lang, J. L. Houeto, P. Pollak, S. Rehncrona, J. Kulisevsky, A. Albanese, J. Volkmann, M. I. Hariz, N. P. Quinn, J. D. Speelman, J. Guridi, I. Zamarbide, A. Gironell, J. Molet, B. Pascual-Sedano, B. Pidoux, A. M. Bonnet, Y. Agid, J. Xie, A. L. Benabid, A. M. Lozano, J. Saint-Cyr, L. Romito, M. F. Contarino, M. Scerrati, V. Fraix, and N. Van Blercom (Oct. 2005). "Bilateral deep brain stimulation in Parkinson's disease: A multicentre study with 4 years follow-up". In: *Brain* 128.10, pp. 2240–2249. DOI: 10.1093/brain/awh571.

Rosa, M., M. Arlotti, S. Marceglia, F. Cogiamanian, G. Ardolino, A. D. Fonzo, L. Lopiano, E. Scelzo, A. Merola, M. Locatelli, P. M. Rampini, and A. Priori (Apr. 2017a). *Adaptive deep brain stimulation controls levodopa-induced side effects in Parkinsonian patients*. DOI: 10.1002/mds.26953.

Rosa, M., E. Scelzo, M. Locatelli, G. Carrabba, V. Levi, M. Arlotti, S. Barbieri, P. Rampini, and A. Priori (Jan. 2017b). "Risk of Infection After Local Field Potential Recording from Externalized Deep Brain Stimulation Leads in Parkinson's Disease". In: *World Neurosurgery* 97, pp. 64–69. DOI: 10.1016/j.wneu.2016.09.069.

Rosenbaum, R., A. Zimnik, F. Zheng, R. S. Turner, C. Alzheimer, B. Doiron, and J. E. Rubin (2014). "Axonal and synaptic failure suppress the transfer of firing rate oscillations, synchrony and information during high frequency deep brain stimulation". In: *Neurobiology of disease* 62, pp. 86–99. DOI: 10.1016/j.nbd.2013.09.006.

Rosin, B., M. Slovik, R. Mitelman, M. Rivlin-Etzion, S. N. Haber, Z. Israel, E. Vaadia, and H. Bergman (Oct. 2011). "Closed-loop deep brain stimulation is superior in ameliorating parkinsonism". In: *Neuron* 72.2, pp. 370–384. DOI: 10.1016/j.neuron.2011.08.023.

Rubin, J. E. and D. Terman (2004). "High frequency stimulation of the subthalamic nucleus eliminates pathological thalamic rhythmicity in a computational model". eng. In: *J Comput Neurosci* 16.3, pp. 211–235. DOI: 10.1023/b:jcns.0000025686.47117.67.

Rubin, J. E. (Oct. 2017). *Computational models of basal ganglia dysfunction: the dynamics is in the details*. DOI: 10.1016/j.conb.2017.08.011.

Sabatini, M. (2003). "Non-periodic isochronous oscillations in plane differential systems". In: *Annali di Matematica Pura ed Applicata* 182.4, pp. 487–501. DOI: 10.1007/s10231-003-0078-0.

Salanova, V., T. Witt, R. Worth, T. R. Henry, R. E. Gross, J. M. Nazzaro, D. Labar, M. R. Sperling, A. Sharan, E. Sandok, A. Handforth, J. M. Stern, S. Chung, J. M. Henderson, J. French, G. Baltuch, W. E. Rosenfeld, P. Garcia, N. M. Barbaro, N. B. Fountain, W. J. Elias, R. R. Goodman, J. R. Pollard, A. I. Tröster, C. P. Irwin, K. Lambrecht, N. Graves, and R. Fisher (2015). "Long-term efficacy and safety of thalamic stimulation for drug-resistant partial epilepsy". In: *Neurology* 84.10, pp. 1017–1025. DOI: 10.1212/WNL.0000000000001334.

Särkkä, S. and A. Solin (2019). *Applied Stochastic Differential Equations*, p. 316. DOI: 10.1017/9781108186735.

Schmidt, R., K. J. LaFleur, M. A. de Reus, L. H. van den Berg, and M. P. van den Heuvel (2015). "Kuramoto model simulation of neural hubs and dynamic synchrony in the human cerebral connectome". In: *BMC Neuroscience* 16.1, p. 54. DOI: 10.1186/s12868-015-0193-z.

Schmidt, S. L., J. J. Peters, D. A. Turner, and W. M. Grill (2019). "Continuous deep brain stimulation of the subthalamic nucleus may not modulate beta bursts in patients with Parkinson's disease". In: *Brain Stimulation* 13.2, pp. 433–443. DOI: 10.1016/j.brs.2019.12.008.

Schnitzler, A., C. Munks, M. Butz, L. Timmermann, and J. Gross (2009). "Synchronized brain network associated with essential tremor as revealed by magnetoencephalography". In: *Mov Disord* 24.11, pp. 1629–1635. DOI: 10.1002/mds.22633.

Schreiber, T. and A. Schmitz (1996). "Improved surrogate data for nonlinearity tests". In: *Physical Review Letters* 77.4, pp. 635–638. DOI: 10.1103/PhysRevLett.77.635.

— (2000). "Surrogate time series". In: *Physica D: Nonlinear Phenomena* 142.3-4, pp. 346–382. DOI: 10.1016/S0167-2789(00)00043-9.

Schroll, H. and F. H. Hamker (2016). "Basal Ganglia dysfunctions in movement disorders: What can be learned from computational simulations". In: *Movement Disorders* 31.11, pp. 1591–1601. DOI: 10.1002/mds.26719.

Schüpbach, W. M., S. Chabardes, C. Matthies, C. Pollo, F. Steigerwald, L. Timmermann, V. Visser Vandewalle, J. Volkmann, and P. R. Schuurman (Oct. 2017). "Directional

leads for deep brain stimulation: Opportunities and challenges". In: *Movement Disorders* 32.10, pp. 1371–1375. DOI: 10.1002/mds.27096.

Schwabedal, J. T. and A. Pikovsky (2013). "Phase description of stochastic oscillations". In: *Phys Rev Lett* 110.20, p. 204102. DOI: 10.1103/PhysRevLett.110.204102.

Sherman, M. A., S. Lee, R. Law, S. Haegens, C. A. Thorn, M. S. Hämäläinen, C. I. Moore, and S. R. Jones (Aug. 2016). "Neural mechanisms of transient neocortical beta rhythms: Converging evidence from humans, computational modeling, monkeys, and mice". In: *Proceedings of the National Academy of Sciences of the United States of America* 113.33, E4885–E4894. DOI: 10.1073/pnas.1604135113.

Shin, H., R. Law, S. Tsutsui, C. I. Moore, and S. R. Jones (Nov. 2017). "The rate of transient beta frequency events predicts behavior across tasks and species". In: *eLife* 6. DOI: 10.7554/eLife.29086.

Shirasaka, S., W. Kurebayashi, and H. Nakao (2017). "Phase-amplitude reduction of transient dynamics far from attractors for limit-cycling systems". In: *Chaos* 27.2, p. 23119. DOI: 10.1063/1.4977195.

Smelyanskiy, V. N., D. G. Luchinsky, A. Stefanovska, and P. V. E. McClintock (2005a). "Inference of a Nonlinear Stochastic Model of the Cardiorespiratory Interaction". In: *Physical review letters* 94.9, p. 98101. DOI: 10.1103/PhysRevLett.94.098101.

Smelyanskiy, V. N., D. G. Luchinsky, D. A. Timucin, A. Bandrivskyy, D. A. Timuçin, and A. Bandrivskyy (2005b). "Reconstruction of stochastic nonlinear dynamical models from trajectory measurements". In: *Physical Review E* 72.2, p. 26202. DOI: 10.1103/PhysRevE.72.026202.

Stam, C. J. (Oct. 2005). "Nonlinear dynamical analysis of EEG and MEG: Review of an emerging field". In: *Clinical Neurophysiology* 116.10, pp. 2266–2301. DOI: 10.1016/j.clinph.2005.06.011.

Stankovski, T., A. Duggento, P. V. E. McClintock, and A. Stefanovska (2012). "Inference of time-evolving coupled dynamical systems in the presence of noise". In: *Physical review letters* 109.2, p. 24101. DOI: 10.1103/PhysRevLett.109.024101.

Steiner, L. A., W.-J. Neumann, F. Staub-Bartelt, D. M. Herz, H. Tan, A. Pogosyan, A. A. Kuhn, and P. Brown (2017). "Subthalamic beta dynamics mirror Parkinsonian bradykinesia months after neurostimulator implantation". In: *Movement Disorders* 32.8, pp. 1183–1190. DOI: 10.1002/mds.27068.

Storey, J. D., J. E. Taylor, and D. Siegmund (2004). "Strong control, conservative point estimation and simultaneous conservative consistency of false discovery rates: a unified approach". In: *Journal of the Royal Statistical Society: Series B (Statistical Methodology)* 66.1, pp. 187–205. DOI: 10.1111/j.1467-9868.2004.00439.x.

Su, F., K. Kumaravelu, J. Wang, and W. M. Grill (Sept. 2019). "Model-Based Evaluation of Closed-Loop Deep Brain Stimulation Controller to Adapt to Dynamic Changes in Reference Signal". In: *Frontiers in Neuroscience* 13, p. 956. DOI: 10.3389/fnins.2019.00956.

Swann, N. C., C. De Hemptinne, S. Miocinovic, S. Qasim, J. L. Ostrem, N. B. Galifianakis, M. S. Luciano, S. S. Wang, N. Ziman, R. Taylor, and P. A. Starr (Feb. 2018). "Chronic multisite brain recordings from a totally implantable bidirectional neural interface: Experience in 5 patients with Parkinson's disease". In: *Journal of Neurosurgery* 128.2, pp. 605–616. DOI: 10.3171/2016.11.JNS161162.

Sydow, O., S. Thobois, F. Alesch, and J. D. Speelman (Oct. 2003). "Multicentre European study of thalamic stimulation in essential tremor: A six year follow up". In:

Journal of Neurology, Neurosurgery and Psychiatry 74.10, pp. 1387–1391. DOI: 10.1136/jnnp.74.10.1387.

Tachibana, Y., H. Iwamuro, H. Kita, M. Takada, and A. Nambu (Nov. 2011). "Subthalamo-pallidal interactions underlying parkinsonian neuronal oscillations in the primate basal ganglia". In: *European Journal of Neuroscience* 34.9, pp. 1470–1484. DOI: 10.1111/j.1460-9568.2011.07865.x.

Taillefumier, T. and M. O. Magnasco (2010). "A Fast Algorithm for the First-Passage Times of Gauss-Markov Processes with Hölder Continuous Boundaries". In: *Journal of Statistical Physics* 140.6, pp. 1130–1156. DOI: 10.1007/s10955-010-0033-6.

Tan, H., J. Debarros, S. He, A. Pogosyan, T. Z. Aziz, Y. Huang, S. Wang, L. Timmermann, V. Visser-Vandewalle, D. J. Pedrosa, A. L. Green, and P. Brown (July 2019). "Decoding voluntary movements and postural tremor based on thalamic LFPs as a basis for closed-loop stimulation for essential tremor". In: *Brain Stimulation* 12.4, pp. 858–867. DOI: 10.1016/j.brs.2019.02.011.

Tan, H., N. Jenkinson, and P. Brown (2014). "Dynamic neural correlates of motor error monitoring and adaptation during trial-to-trial learning". In: *Journal of Neuroscience* 34.16, pp. 5678–5688. DOI: 10.1523/JNEUROSCI.4739-13.2014.

Tan, H., A. Pogosyan, A. Anzak, T. Foltynie, P. Limousin, L. Zrinzo, K. Ashkan, M. Bogdanovic, A. L. Green, T. Aziz, and P. Brown (Feb. 2013). "Frequency specific activity in subthalamic nucleus correlates with hand bradykinesia in Parkinson's disease". In: *Experimental Neurology* 240.1, pp. 122–129. DOI: 10.1016/j.expneurol.2012.11.011.

Tass, P. A. (Aug. 2003). *A model of desynchronizing deep brain stimulation with a demand-controlled coordinated reset of neural subpopulations*. DOI: 10.1007/s00422-003-0425-7.

Terman, D., J. E. Rubin, A. C. Yew, and C. J. Wilson (2002). "Activity Patterns in a Model for the Subthalamopallidal Network of the Basal Ganglia". In: *Journal of Neuroscience* 22.7, pp. 2963–2976. DOI: 10.1523/jneurosci.22-07-02963.2002.

Theiler, J., S. Eubank, A. Longtin, B. Galdrikian, and J. D. Farmer (1992). "Testing for nonlinearity in time series: the method of surrogate data". In: *Physica D: Nonlinear Phenomena* 58.1-4, pp. 77–94. DOI: 10.1016/0167-2789(92)90102-S.

Thomas, P. J. and B. Lindner (2014). "Asymptotic phase for stochastic oscillators". In: *Physical review letters* 113.25, p. 254101. DOI: 10.1103/PhysRevLett.113.254101.

Tiesinga, P. and T. J. Sejnowski (2009). "Cortical enlightenment: are attentional gamma oscillations driven by ING or PING?" In: *Neuron* 63.6, pp. 727–732.

Tinkhauser, G., A. Pogosyan, S. Little, M. Beudel, D. M. Herz, H. Tan, and P. Brown (2017a). "The modulatory effect of adaptive deep brain stimulation on beta bursts in Parkinson's disease". In: *Brain* 140.4, pp. 1053–1067. DOI: 10.1093/brain/awx010.

Tinkhauser, G., A. Pogosyan, H. Tan, D. M. Herz, A. A. Kühn, and P. Brown (2017b). "Beta burst dynamics in Parkinson's disease off and on dopaminergic medication". In: *Brain* 140.11, pp. 2968–2981. DOI: 10.1093/brain/awx252.

Tinkhauser, G., F. Torrecillos, Y. Duclos, H. Tan, A. Pogosyan, P. Fischer, R. Carron, M.-L. Welter, C. Karachi, and W. Vandenberghe (2018). "Beta burst coupling across the motor circuit in Parkinson's disease". In: *Neurobiology of disease* 117, pp. 217–225. DOI: 10.1016/j.nbd.2018.06.007.

Torczon, V. (1997). "On the convergence of pattern search algorithms". In: *SIAM Journal on Optimization* 7.1, pp. 1–25. DOI: 10.1137/S1052623493250780.

Torrecillos, F., J. Alayrangues, B. E. Kilavik, and N. Malfait (2015). "Distinct modulations in sensorimotor postmovement and foreperiod β-band activities related to error salience processing and sensorimotor adaptation". In: *Journal of Neuroscience* 35.37, pp. 12753–12765. DOI: 10.1523/JNEUROSCI.1090-15.2015.

Torrecillos, F., G. Tinkhauser, P. Fischer, A. L. Green, T. Z. Aziz, T. Foltynie, P. Limousin, L. Zrinzo, K. Ashkan, and P. Brown (2018). "Modulation of beta bursts in the subthalamic nucleus predicts motor performance". In: *Journal of Neuroscience* 38.41, pp. 8905–8917. DOI: 10.1523/JNEUROSCI.1314-18.2018.

Ueta, T. and G. Chen (2003). "On Synchronization and Control of Coupled Wilson–Cowan Neural Oscillators". In: *International Journal of Bifurcation and Chaos* 13.01, pp. 163–175. DOI: 10.1142/s0218127403006406.

Van Rooden, S. M., W. J. Heiser, J. N. Kok, D. Verbaan, J. J. Van Hilten, and J. Marinus (June 2010). *The identification of Parkinson's disease subtypes using cluster analysis: A systematic review.* DOI: 10.1002/mds.23116.

Velarde, O. M., G. Mato, and D. Dellavale (2017). "Mechanisms for pattern specificity of deep-brain stimulation in Parkinson's disease". In: *PloS one* 12.8, e0182884. DOI: 10.1371/journal.pone.0182884.

Velisar, A., J. Syrkin-Nikolau, Z. Blumenfeld, M. H. Trager, M. F. Afzal, V. Prabhakar, and H. Bronte-Stewart (July 2019). "Dual threshold neural closed loop deep brain stimulation in Parkinson disease patients". In: *Brain Stimulation* 12.4, pp. 868–876. DOI: 10.1016/j.brs.2019.02.020.

Venda, L. L., S. J. Cragg, V. L. Buchman, and R. Wade-Martins (Dec. 2010). *α-Synuclein and dopamine at the crossroads of Parkinson's disease.* DOI: 10.1016/j.tins.2010.09.004.

Volkmann, J., J. Mueller, G. Deuschl, A. A. Kühn, J. K. Krauss, W. Poewe, L. Timmermann, D. Falk, A. Kupsch, A. Kivi, G. H. Schneider, A. Schnitzler, M. Südmeyer, J. Voges, A. Wolters, M. Wittstock, J. U. Müller, S. Hering, W. Eisner, J. Vesper, T. Prokop, M. Pinsker, C. Schrader, M. Kloss, K. Kiening, K. Boetzel, J. Mehrkens, I. M. Skogseid, J. Ramm-Pettersen, G. Kemmler, K. P. Bhatia, J. L. Vitek, and R. Benecke (2014). "Pallidal neurostimulation in patients with medication-refractory cervical dystonia: A randomised, sham-controlled trial". In: *The Lancet Neurology* 13.9, pp. 875–884. DOI: 10.1016/S1474-4422(14)70143-7.

Wang, Y., A. J. Trevelyan, A. Valentin, G. Alarcon, P. N. Taylor, and M. Kaiser (2017). "Mechanisms underlying different onset patterns of focal seizures". In: *PLoS Computational Biology* 13.5. DOI: 10.1371/journal.pcbi.1005475.

Wedgwood, K. C., K. K. Lin, R. Thul, and S. Coombes (2013). "Phase-amplitude descriptions of neural oscillator models". In: *J Math Neurosci* 3.1, p. 2. DOI: 10.1186/2190-8567-3-2.

Weerasinghe, G., B. Duchet, H. Cagnan, P. Brown, C. Bick, and R. Bogacz (Aug. 2019). "Predicting the effects of deep brain stimulation using a reduced coupled oscillator model". In: *PLOS Computational Biology* 15.8. Ed. by J. Rubin, e1006575. DOI: 10.1371/journal.pcbi.1006575.

Weickenmeier, J., M. Jucker, A. Goriely, and E. Kuhl (2019). "A physics-based model explains the prion-like features of neurodegeneration in Alzheimer's disease, Parkinson's disease, and amyotrophic lateral sclerosis". In: *Journal of the Mechanics and Physics of Solids* 124, pp. 264–281. DOI: 10.1016/j.jmps.2018.10.013.

Weickenmeier, J., E. Kuhl, and A. Goriely (2018). "Multiphysics of Prionlike Diseases: Progression and Atrophy". In: *Physical Review Letters* 121.15. DOI: 10.1103/PhysRevLett.121.158101.

Wendling, F., J. J. Bellanger, F. Bartolomei, and P. Chauvel (2000). "Relevance of nonlinear lumped-parameter models in the analysis of depth-EEG epileptic signals". In: *Biological Cybernetics* 83.4, pp. 367–378. DOI: 10.1007/s004220000160.

Wessel, J. R. (Jan. 2020). "β-Bursts Reveal the Trial-to-Trial Dynamics of Movement Initiation and Cancellation". In: *The Journal of neuroscience : the official journal of the Society for Neuroscience* 40.2, pp. 411–423. DOI: 10.1523/JNEUROSCI.1887-19.2019.

Wilson, D. and B. Ermentrout (2017). "Greater accuracy and broadened applicability of phase reduction using isostable coordinates". In: *J Math Biol*. DOI: 10.1007/s00285-017-1141-6.

Wilson, D. (2020). "A data-driven phase and isostable reduced modeling framework for oscillatory dynamical systems". In: *Chaos* 30.1, p. 13121. DOI: 10.1063/1.5126122.

Wilson, D. and S. Djouadi (2019). "Isostable Reduction and Boundary Feedback Control for Nonlinear Convective Flows". In: *2019 IEEE 58th Conference on Decision and Control (CDC)*, pp. 2138–2143. DOI: 10.1109/cdc40024.2019.9029951.

Wilson, D. and B. Ermentrout (2018). "An operational definition of phase characterizes the transient response of perturbed limit cycle oscillators". In: *SIAM Journal on Applied Dynamical Systems* 17.4, pp. 2516–2543. DOI: 10.1137/17M1153261.

Wilson, D. and J. Moehlis (2014). "Optimal Chaotic Desynchronization for Neural Populations". In: *SIAM Journal on Applied Dynamical Systems* 13.1, pp. 276–305. DOI: 10.1137/120901702.

— (2015). "Extending phase reduction to excitable media: theory and applications". In: *SIAM Review* 57.2, pp. 201–222. DOI: 10.1137/140952478.

— (2016a). "Isostable reduction of periodic orbits". In: *Physical Review E* 94.5, p. 52213. DOI: 10.1103/PhysRevE.94.052213.

— (2016b). "Isostable reduction with applications to time-dependent partial differential equations". In: *Physical Review E* 94.1, p. 12211. DOI: 10.1103/PhysRevE.94.012211.

Wilson, H. R. and J. D. Cowan (1973). "A mathematical theory of the functional dynamics of cortical and thalamic nervous tissue". In: *Kybernetik* 13.2, pp. 55–80. DOI: 10.1007/BF00288786.

Wilson, H. R. and J. D. Cowan (1972). "Excitatory and inhibitory interactions in localized populations of model neurons". In: *Biophysical journal* 12.1, pp. 1–24. DOI: 10.1016/S0006-3495(72)86068-5.

Wilson, H. R. (Dec. 2019). "Hyperchaos in Wilson–Cowan oscillator circuits". In: *Journal of Neurophysiology* 122.6, pp. 2449–2457. DOI: 10.1152/jn.00323.2019.

Wilting, J. and V. Priesemann (2018). "Inferring collective dynamical states from widely unobserved systems". In: *Nature Communications* 9.1. DOI: 10.1038/s41467-018-04725-4. arXiv: 1608.07035.

Winfree, A. T. (2001). *The geometry of biological time*. Vol. 12. New York, NY: Springer Science & Business Media.

Yang, H., W. L. Shew, R. Roy, and D. Plenz (2012). "Maximal variability of phase synchrony in cortical networks with neuronal avalanches". In: *Journal of Neuroscience* 32.3, pp. 1061–1072. DOI: 10.1523/JNEUROSCI.2771-11.2012.

Yao, L., P. Brown, and M. Shoaran (Jan. 2020). "Improved detection of Parkinsonian resting tremor with feature engineering and Kalman filtering". In: *Clinical Neurophysiology* 131.1, pp. 274–284. DOI: 10.1016/j.clinph.2019.09.021.

Yousif, N., M. Mace, N. Pavese, R. Borisyuk, D. Nandi, and P. Bain (2017). "A Network Model of Local Field Potential Activity in Essential Tremor and the Impact of Deep Brain Stimulation". In: *PLoS Comput Biol* 13.1, e1005326. DOI: 10.1371/journal.pcbi.1005326.

Yousif, N., P. G. Bain, D. Nandi, and R. Borisyuk (Mar. 2020). "A Population Model of Deep Brain Stimulation in Movement Disorders From Circuits to Cells". In: *Frontiers in Human Neuroscience* 14. DOI: 10.3389/fnhum.2020.00055.

Zirh, T. A., F. A. Lenz, S. G. Reich, and P. M. Dougherty (1998). "Patterns of bursting occurring in thalamic cells during parkinsonian tremor". In: *Neuroscience* 83.1, pp. 107–121. DOI: 10.1016/S0306-4522(97)00295-9.